TECHNICAL DIGEST

IEEE

SOLID-STATE SENSOR AND ACTUATOR

Workshop

Sponsored by the IEEE Electron Devices Society

1988

Hilton Head Island, South Carolina

June 6-9

IEEE Catalog Number — 88TH0215-4
Library of Congress Number — 87-83469

UNCLASSIFIED MASTER COPY - FOR REPRODUCTION PURPOSES

SECURITY CLASSIFICATION OF THIS PAGE

REPORT DOCUMENTATION PAGE

1a. REPORT SECURITY CLASSIFICATION Unclassified	1b. RESTRICTIVE MARKINGS
2a. SECURITY CLASSIFICATION AUTHORITY	3. DISTRIBUTION/AVAILABILITY OF REPORT Approved for public release; distribution unlimited.
2b. DECLASSIFICATION/DOWNGRADING SCHEDULE	
4. PERFORMING ORGANIZATION REPORT NUMBER(S)	5. MONITORING ORGANIZATION REPORT NUMBER(S) ARO 26222.1-EL-CF
6a. NAME OF PERFORMING ORGANIZATION IEEE 6b. OFFICE SYMBOL (If applicable)	7a. NAME OF MONITORING ORGANIZATION U. S. Army Research Office
6c. ADDRESS (City, State, and ZIP Code) 345 Scarborough Road Briarcliff Manor, NY 10510	7b. ADDRESS (City, State, and ZIP Code) P. O. Box 12211 Research Triangle Park, NC 27709-2211
8a. NAME OF FUNDING/SPONSORING ORGANIZATION U. S. Army Research Office 8b. OFFICE SYMBOL (If applicable)	9. PROCUREMENT INSTRUMENT IDENTIFICATION NUMBER DAAL03-88-G-0029
8c. ADDRESS (City, State, and ZIP Code) P. O. Box 12211 Research Triangle Park, NC 27709-2211	10. SOURCE OF FUNDING NUMBERS PROGRAM ELEMENT NO. / PROJECT NO. / TASK NO. / WORK UNIT ACCESSION NO.

11. TITLE (Include Security Classification)
Workshop on Solid-State Sensor and Actuator

12. PERSONAL AUTHOR(S)
Richard S. Muller

13a. TYPE OF REPORT	13b. TIME COVERED	14. DATE OF REPORT (Year, Month, Day)	15. PAGE COUNT
Final	FROM 5/16/88 TO 5/15/89	1988	153

16. SUPPLEMENTARY NOTATION
The view, opinions and/or findings contained in this report are those of the author(s) and should not be construed as an official Department of the Army position, policy, or decision, unless so designated by other documentation.

17. COSATI CODES		
FIELD	GROUP	SUB-GROUP

18. SUBJECT TERMS (Continue on reverse if necessary and identify by block number)
Solid-State Sensor Workshop, Actuator Workshop, Workshop

19. ABSTRACT (Continue on reverse if necessary and identify by block number)
The Proceedings of the Workshop have been published by IEEE.

20. DISTRIBUTION/AVAILABILITY OF ABSTRACT ☐ UNCLASSIFIED/UNLIMITED ☐ SAME AS RPT. ☐ DTIC USERS	21. ABSTRACT SECURITY CLASSIFICATION Unclassified
22a. NAME OF RESPONSIBLE INDIVIDUAL	22b. TELEPHONE (Include Area Code) / 22c. OFFICE SYMBOL

DD FORM 1473, 84 MAR 83 APR edition may be used until exhausted. All other editions are obsolete.

SECURITY CLASSIFICATION OF THIS PAGE
UNCLASSIFIED

1988 SOLID STATE SENSOR and ACTUATOR WORKSHOP

Hilton Head Island, SC

June 6-9, 1988

General Chairman:	**Richard Muller** **University of California, Berkeley**
Technical Program Chairman:	**Ben Hocker** **Honeywell**
Local Arrangements Chairman:	**Tom Poteat** **AT&T Bell Laboratories**
Financial Chairman:	**Joe Giachino** **Ford Motor Company**
Technical Digest:	**Dave Eddy** **General Motors**
Committee Meeting Chairman:	**Bob Huber** **University of Utah**

Program Committee:

Henry Baltes **University of Alberta**	**Phil Barth** **NovaSensor**
Henry Guckel **University of Wisconsin**	**Wen Ko** **Case Western Reserve**
Bob Sulouff **Allied Bendix**	**Steve Senturia** **MIT**
Ken Wise **University of Michigan**	**Henry Wohltjen** **Microsensor Systems**

Additional Support Provided By:

US Army Research Office, Research Triangle Park, NC

National Science Foundation

IEEE Catalog Number 88TH0215-4

Library of Congress Number 87-83469

1988 SOLID-STATE SENSOR & ACTUATOR WORKSHOP
HILTON HEAD ISLAND, SC, JUNE 6-9, 1988

Welcome to Hilton Head Island for this third American workshop on sensors and actuators.

As in previous workshops we will have opportunity this week for idea exchange and sociability-- a chance to renew and to form new friendships as well as to compare plans and results. A shared unspoken agreement in a cooperative spirit has marked our meetings at Hilton Head since the first gathering in 1984. We are at Hilton Head again this year as the popular choice of participants in 1986. When polled at the conclusion of that meeting, those attending also favored the schedule adopted for the 1988 workshop and endorsed the traditions of not running competing technical sessions and of encouraging a reasoned discussion of each paper presented. To make your influence felt on the next workshop, keep notes of ideas, reactions and suggestions you have about this, **your** workshop and pass them on to the committee when you return your questionnaire on Thursday.

The Hilton Head Workshop is one of the regional meetings (others are being held this year in Europe and Japan) that alternate in even-numbered years with TRANSDUCERS, the international conference series on sensors and actuators. TRANSDUCERS '87 was held last June in Tokyo and TRANSDUCERS '89 is scheduled for June 25-30, 1989 in Montreux, Switzerland. TRANSDUCERS '91 will take place June 24-28, 1991 at the Hyatt Regency Hotel in San Francisco.

The 1988 Sensors and Actuators Workshop would not have been possible without a financial guarantee extended by the IEEE Electron Devices Society. We thank the National Science Foundation and George Hazelrigg for responding generously to our request for travel-assistance funds. This support will enable more students than in any previous sensors and actuators workshop to join with us at Hilton Head. We are grateful to the US Army Research Office and Mike Stroscio for underwriting a portion of the publication expense for the technical digest. We also thank the General Motors Corporation which has continued to contribute to these workshops by offering publication services at very generous rates. Dave Eddy has contributed his efforts to make this come about.

All of the committee has worked hard to make this a successful workshop. Our preview of the papers submitted has whet an appetite to learn more and to participate in lively discussion. With all of you, we look forward to getting underway. Enjoy your workshop!

Sincerely,

Richard S. Muller

Richard Muller
General Chairman: 1988 Workshop

PROGRAM

SUNDAY, JUNE 5
7:00PM INFORMAL GET-TOGETHER, CASH BAR
THE BUOY BAR

****

SESSION 1
MONDAY MORNING, JUNE 6
PHYSICAL SENSORS AND NEW PROCESSES

Chairman: K. Wise
Co-Chairman: H. Guckel

7:30 **BREAKFAST**

8:30 **Welcome**

8:40 **Announcements**

8:50 **LIGA Process: Sensor Construction Techniques via X-Ray Lithography**
W. Ehrfeld, F. Gotz, D. Munchmeyer, W. Schelb, and D. Schmidt
- Kernforschungszentrum Karlsruhe Gmbh 1

9:30 **Cesium Hydroxide (CsOH): A Useful Etchant for Micromachining Silicon**
Lloyd D. Clark Jr., Jennifer L. Lund, and David J. Edell
- Massachusetts Institute of Technology 5

10:00 - 10:30 **BREAK**

10:30 **Plasma Polymerization of Methyl Methacrylate: A Photoresist for 3D Applications**
Henry Guckel, Jay Uglow, Ming Lin, Denice Denton, Jeff Tobin, Kathleen Euch, and Michael Juda
- University of Wisconsin 9

11:00 **Micro-Structures**
Wayne E. Feely
- Rohm and Haas Co. 13

11:30 **A Miniature Fabry-Perot Interferometer Fabricated Using Silicon Micromachining Techniques**
J.H. Jerman, S.R. Mallinson
- IC Sensors - British Telecom Research Laboratories 16

12:00 - 1:00 **LUNCH**

1:00 A Twin-Interferometer Fiber-Optic Readout For Diaphragm Pressure Transducers
Albert M. Young, James E. Goldsberry, Joseph H. Haritonidis,
Rosemary L. Smith, and Stephen D. Senturia
- Massachusetts Institute of Technology 19

SESSION 2
MONDAY AFTERNOON, JUNE 6
CHEMICAL SENSORS

Chairman: R. Huber
Co-Chairman: W. Ko

1:30 Acoustic Plate Mode Devices As Liquid Phase Sensors
A.J. Ricco, S.J. Martin, G.C. Frye, and T.M. Niemczyk
- Sandia National Laboratories 23

2:00 Silicon-Based Ultrasonic Lamb-Wave Multisensors
Stuart W. Wenzel and Richard M. White
- University of California, Berkeley 27

2:30 Theoretical Description of Gas/Film Interaction on SnO_x
Jay N. Zemel
- University of Pennsylvania 31

****

SESSION 3
TUESDAY MORNING, JUNE 7
PHYSICAL SENSORS II

Chairman: T. Poteat
Co-Chairman: H. Wohltjen

7:30 **BREAKFAST**

8:00 **A Monolithic Silicon Accelerometer With Integral Air Damping And Overrange Protection**
Philip W. Barth, Farzad Pourahmadi, Robert Mayer, John Poydock, Kurt Petersen
- NovaSensor 35

8:30 **Nonplanar Silicon Strain Sensors**
Robert W. Bower, Richard R. Spencer and Derfu D. Lee
- University of California, Davis 39

9:00 **A Constant-Temperature Gas Flowmeter with a Silicon Micromachined Package**
C.H. Mastrangelo and R.S. Muller
- University of California, Berkeley 43

9:30 **A Thermally Isolated Microstructure Suitable for Gas Sensing Applications**
Michael A. Huff, Sephen D. Senturia and Roger T. Howe
- Massachusetts Institute of Technology 47

10:00 - 10:30 **BREAK**

SESSION 4
POLYSILICON

Chairman: S. Senturia
Co-Chairman: H. Baltes

10:30 **Processing Conditions for Polysilicon Films with Tensile Strain for Large Aspect Ratio Microstructures**
H. Guckel, D.W. Burns, H. A. C. Tilmans, C.C.G. Visser, D.W. DeRoo, T.R. Christenson, P.J. Klomberg, J. J. Sniegowski and D. H. Jones
- University of Wisconsin 51

11:00 **As-Deposited Low-Strain LPCVD Polysilicon**
L.S. Fan and R.S. Muller
- University of California, Berkeley 55

11:30 **Surface Micromachining Processes for Electrostatic Microactuator Fabrication**
Theresa A. Lober and Roger T. Howe
- Massachusetts Institute of Technology 59

12:00 - 1:00 LUNCH

THE AFTERNOON HOURS ARE FREE FOR YOU TO USE AS YOU WISH.
SESSIONS WILL BEGIN AGAIN WEDNESDAY MORNING, JUNE 8.

A BANQUET WILL BE HELD THIS EVENING AT THE SHOREHOUSE, 7:00 PM

****

SESSION 5
WEDNESDAY MORNING, JUNE 8
SYSTEMS AND ARRAYS
Chairman: Phil Barth
Co-Chairman: Ben Hocker

7:30 BREAKFAST

8:30 Gnat Robots: A Low-Intelligence, Low-Cost Approach
Anita Flynn
- Massachusetts Institute of Technology 63

9:10 Integrated Relative Humidity Sensor
S.V. Silverthorne, C.W. Watson, R.D. Baxter
- Leeds & Northrup Company 67

9:40 - 10:10 BREAK

10:10 CMOS Magnetic Sensor Arrays
James J. Clark
- Harvard University 72

10:40 An Architecture and Interface for VLSI Sensors
N. Najafi, K.W. Clayton, W. Baer, and K.D. Wise
- University of Michigan 76

11:10 Fiber Optic Data Bus for Solid State Sensors
Jim Lenz, Paul Bjork, Kyuri Fujiwara
- Honeywell Systems & Research Center 80

12:00 - 1:00 LUNCH

SESSION 6
WEDNESDAY AFTERNOON, JUNE 8
MATERIALS AND CHARACTERIZATION

Chairman: Dave Eddy
Co-Chairman: Ben Hocker

1:00 **Calibrated Measurements of Elastic Limit, Modulus, and the Residual Stress of Thin Films Using Micromachined Suspended Membranes**
Fariborz Maseeh, Martin A. Schmidt, Mark G. Allen, and Stephen D. Senturia
- Massachusetts Institute of Technology 84

1:30 **Fracture Strain of LPCVD Polysilicon**
Y. C. Tai and R. S. Muller
- University of California, Berkeley 88

2:00 **Characterization of the Mechanisms Producing Bending Moments in Polysilicon Micro-Cantilever Beams by Interferometric Deflection Measurements**
Theresa A. Lober, Jiahua Huang, Martin A. Schmidt, and Stephen D. Senturia
- Massachusetts Institute of Technology 92

2:30 **Mechanical Properties of Fine Grained Polysilicon - The Repeatability Issue**
H. Guckel, D.W. Burns, H.A.C. Tilmans, D. W. DeRoo and C. R. Rutigliano
- University of Wisconsin 96

SESSION 7
WEDNESDAY, JUNE 8
POSTER SESSION
OPEN 12:00 - 9:00 PM
AUTHORS PRESENT 7:30 - 8:30 PM
ROOM TO BE ANNOUNCED

o **Reoxidized Nitrided Oxides as Gate Dielectrics for High Temperature Integrated Sensor MOS Devices**
Wei-Tsun Shaiu and Fred L. Terry, Jr.
- University of Michigan 100

o **Mesa Structure Formation Using Potassium Hydroxide and Ethylene Diamine Based Etchants**
Shih-Chia Chang and David B. Hicks
- General Motors Research Laboratories 102

o **Noise Correlations In Magnetic Field Sensitive Transistors**
Henry P. Baltes, Arokia Nathan, and Davide R. Briglio
- University of Alberta 104

o **Bipolar Integrated Pressure Transducer**
Ronald E. Brown, Dennis M. Koglin
- General Motors Hughes Electronics Corporation 106

o A Broad Range Absolute Pressure Microsensor
S.D. James, R. G. Johnson, and R.E. Higashi
- Honeywell Sensors and Signal Processing Laboratory 107

o Mechanisms of Anodic Bonding of Silicon to Pyrex Glass
Kevin Albaugh
- IBM Corporation 109

o Edge Erosion Effects in Double Sided Silicon Micromachining
M. Zanini, M. Mikkor, R. C. Elder, L. W. Cathey, J. L. Bomback, and B. E. Artz
- Ford Motor Company 111

o A Miniature Silicon Accelerometer With Built-in Damping
Stephen Terry
- IC Sensors, Inc. 114

o A CMOS Process for High Temperature Sensors and Circuits
R.B. Brown and K.C. Wu - University of Michigan
M. Ghezzo and D.M. Brown - General Electric Company 117

o An Advanced Solid State Pressure Transducer For High Reliability SSME Applications
G. E. Gustafson and J.J. Shea
- Honeywell Solid State Electronics Division 119

o New Generation Of Disposable Blood Pressure Sensors Brings On-Chip Digital Laser Trimming
Janusz Bryzek, Robert Mayer, Phillip Barth
- NovaSensor 121

o An Innovative Design Approach To Packaging Of Microsensors
Joseph R. Mallon Jr., Janusz Bryzek, Jeff Ramsey, Graham Tomblin, Farzad Pourahamdi
- NovaSensor 123

o Use of Time Dependent Chemical Sensor Signals for Selective Identification
Joseph R. Stetter and G. Jordan Maclay
- Transducer Research Inc. - University of Illinois 125

RUMP SESSION
8:30 PM
JOE GIACHINO
ROOM TO BE ANNOUNCED

****

SESSION 8
THURSDAY MORNING, JUNE 9
MICROMECHANISMS

Chairman: Joe Giachino
Co-Chairman: H. Guckel

7:30 **BREAKFAST**

8:00 **Toward the Design of Successful Electric Micromotors**
Jeffrey H. Lang and Stephen F. Bart
- Massachusetts Institute of Technology 127

8:40 **The Modelling of Electrostatic Forces in Small Electrostatic Actuators**
Richard H. Price, John E. Wood, and Stephen C. Jacobsen
- University of Utah 131

9:10 **Constant Flow-Rate Microvalve Actuator Based On Silicon And Micromachining Technology**
Sekwang Park, Wen H. Ko and Joseph M. Prahl
- Case Western Reserve University 136

9:40 - 10:00 **BREAK**

SESSION 9
THURSDAY MORNING, JUNE 9
PROCESSING TECHNIQUES

Chairman: Bob Suloff
Co-Chairman: S. Senturia

10:00 **A New Silicon-On-Glass Process for Integrated Sensors**
L.J. Spangler and K.D. Wise
- University of Michigan 140

10:30 **Silicon Fusion Bonding for Pressure Sensors**
Kurt Petersen, Phillip Barth, John Poydock, Joseph Mallon Jr., Janusz Bryzek
- NovaSensor 144

11:00 **Polysilicon Microbridge Fabrication Using Standard CMOS Technology**
M. Parameswaran, H.P. Baltes and A.M. Robinson
- University of Alberta 148

11:30 **Preferred Crystallographic Directions of Pore Propagation in Porous Silicon Layers**
S.F. Chuang and R.L. Smith
- Massachusetts Institute of Technology 151

12:00 **ADJOURN**

AUTHOR INDEX

Albaugh, K., 109
Allen, M. G., 84
Artz, B. E., 111

Baer, W., 76
Baltes, H. P., 104, 148
Bart, S. F., 127
Barth, P. W., 35, 121, 144
Baxter, R. D., 67
Bjork, P., 80
Bomback, J. L., 111
Bower, R. W., 39
Briglio, D. R., 104
Brown, D. M., 117
Brown, J., 144
Brown, R. B., 117
Brown, R. E., 106
Bryzek, J., 121, 123, 144
Burns, D. W., 51, 96

Cade, P. E., 109
Chang, S. -C., 102
Cathey, L. W., 111
Christenson, T. R., 51
Chuang, S. -F., 151
Clark, J. J., 72
Clark, L. D., 5
Clayton, K. W., 76

Denton, D., 9
DeRoo, D. W., 51, 96

Edell, D. J., 5
Ehreld, W., 1
Elder, R. C., 111
Euch, K., 9

Fan, L. S., 55
Feeley, W. E., 13
Flynn, A., 63
Frye, G. C., 23
Fujiwara, K., 80

Ghezzo, M., 117
Goldsberry, J. E., 19
Gotz, F., 1
Guckel, H., 9, 51, 96
Gustafson, G. E., 119

Haritonidis, J. H., 19
Hicks, D. B., 102
Higashi, R. E., 107
Howe, R. T., 47, 59
Huang, J., 92
Huff, M. A., 47

Jacobson, S. C., 131
James, S. D., 107
Jerman, J. H., 16
Johnson, R. G., 107
Jones, D. H., 51
Juda, M., 9

Klomberg, P. J., 51
Ko, W. H., 136
Koglin, D. M., 106

Lang, J. H., 127
Lee, D. D., 39
Lenz, J., 80
Lin, M., 9
Lober, T. A., 59, 92
Lund, J. L., 5

Maclay, G. J., 125
Mallinson, S. R., 16
Mallon, J. R., 123, 144
Martin, S. J., 23
Maseeh, F., 84
Mastrangelo, C. H., 43
Mayer, R., 35, 121
Mikkor, M., 111
Muller, R. S., 43, 55, 88
Munchmeyer, D., 1

Najafi, K., 76
Najafi, M., 76
Nathan, A., 104
Niemczyk, T. M., 23

Parameswaran, M., 148
Park, S., 136
Petersen, K., 35, 144
Prahl, J. M., 136
Price, R. H., 131
Pourahmadi, F., 35, 123
Poydock, J., 35, 144

Ramsey, J., 123
Rasmussen, D. H., 109
Ricco, A. J., 23
Robinson, A. M., 148
Rutigliano, C. R., 96

Schelb, W., 1
Schmidt, D., 1
Schmidt, M. A., 84, 92
Senturia, S. D., 19, 47, 84, 92
Shea, J. J., 119
Shiau, W.-T., 100
Silverthorne, S. V., 67
Smith, R. L., 19, 151
Sniegowski, J. J., 51
Spangler, L. J., 140
Spencer, R. R., 39
Stetter, J. R., 125

Tai, Y. C., 88
Terry, F. L., 100
Terry, S., 114
Tilmans, H. A. C., 51, 96
Tobin, J., 9
Tomblin, G., 123

Uglow, J., 9

Visser, C. C. G., 51

Watson, C. W., 67
Wenzel, S. W., 27
White, R. M., 27
Wise, K. D., 76, 140
Wood, J. E., 131
Wu, K. C., 117

Young, A. M., 19

Zanini, M., 111
Zemel, J. N., 31

LIGA PROCESS: SENSOR CONSTRUCTION TECHNIQUES VIA X-RAY LITHOGRAPHY

W. Ehrfeld [1], F. Götz [2], D. Münchmeyer [1], W. Schelb [1], D. Schmidt [1]

[1] Kernforschungszentrum Karlsruhe GmbH,
Institut für Kernverfahrenstechnik, P.O. Box 3640,
D-7500 Karlsruhe 1, Federal Republic of Germany

[2] Steag AG, P.O. Box 10 37 62, D-4300 Essen 1,
Federal Republic of Germany

Abstract

A large variety of microsensors and components for microactuators can be fabricated by the so-called LIGA method which is based on deep-etch X-ray lithography, electroforming and molding processes (in German: Lithographie, Galvanoformung, Abformung). This microfabrication technique allows to generate devices with minimal lateral dimensions in the micrometer range and structural heights of several hundred micrometers from metallic and plastic materials. In contrast to orientation dependent etching of monocrystalline silicon there are no restrictions in the cross-sectional shape of the microstructures. Various concepts of sensors for measuring vibration, acceleration, position, spectral distribution, radiation, composition of mixtures etc are presented.

Introduction

Technological advances in lithography continue to drive the level of integration and the reduction in minimum feature size of semiconductor products. In the laboratory scale, optical lithography which is by far the most important technique in present production lines has reached the 0.5 µm range required for the fabrication of 16 Mbit memory chips. For mass production of 64 Mbit and even more advanced devices, X-ray lithography is expected to become the preferred technique [1]. It is capable to generate minimum dimensions in the 0.2 µm range.

Besides semiconductor devices, a large number of other microstructure products may be fabricated by means of X-ray lithography. The so-called LIGA process which is based on deep-etch X-ray lithography with high quantum energy synchrotron radiation, electroforming and molding processes (in German: Lithographie, Galvanoformung, Abformung) allows to produce microstructures with lateral dimensions in the micrometer range and structural heights of several hundred micrometers from a variety of materials [2, 3]. Its application potential covers microelectronics, sensors, microoptics, micromechanics and biotechnology [4].

This paper gives a short overview of the LIGA process and its application potential for fabricating microsensors.

Microfabrication Process

The principle of the LIGA method is evident from the process sequence shown in Figure 1. A polymeric material (resist) which changes its dissolution rate in a liquid solvent (developer) under high-energy irradiation, is exposed through an X-ray mask to highly intensive parallel X-rays. The radiation source is an electron synchrotron or an electron storage ring which, at present, is the only possibility to generate the highly collimated photon flux in the spectral range required for precise deep-etch X-ray lithography in thick resist layers. If one considers a thickness between 10 and 1000 µm for the resist layers to be structured, the optimum critical wavelength of the synchrotron radiation source ranges from some 0.1 to 1 nm for typical resist materials.

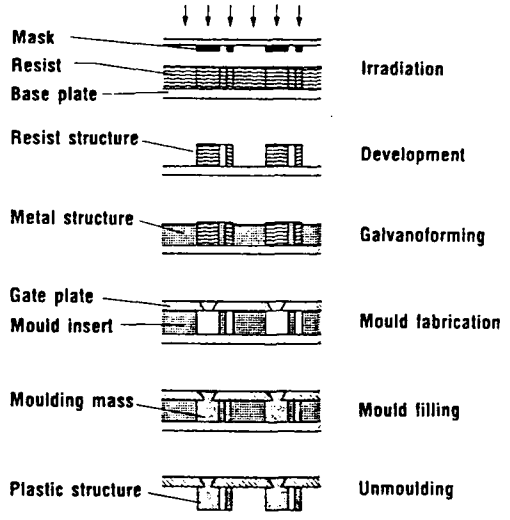

Fig. 1: Schematic representation of a process sequence of the LIGA method for mass fabrication of micro-devices.

In the next step, the resist structure is used as a template in an electroforming process where metal is deposited onto the electrically conductive substrate. In this way, a complementary metallic structure is obtained which can be either the final microstructure product or can be used as a microtool (mold insert) for multiple reproduction by means of a molding process.

The micromolding process has been optimized using methacrylate based casting resins with a special internal mold release agent. In the process sequence shown in Fig. 1 the mold material is introduced into the mold cavities through the holes of a gate plate. This plate which has a formlocking connection with the polymeric microstructures after hardening of the resin serves as an electrode in a second electroforming process for generating secondary metallic microstructures. It has been demonstrated by many experiments that, in spite of an aspect ratio of about 100 and minimum lateral dimensions of only some micrometers, a yield of approximately 100 % can be obtained in the micromolding process.

The secondary structures are perfect copies of the primary structures. Consequently, mass production of plastic and metallic microstructures should be feasible without a continuous utilization of a synchrotron radiation source which is only necessary for fabricating mold inserts.

Sensors

The development of modern sensors aims at miniaturization, more complex or array structures and integration with electronic signal conditioning. Furthermore, the expenditure for adjustment, trimming and replacement should be minimized and, accordingly, the manufacturing tolerances should be as small as possible. In this respect,

TH0215-4/88/0000-0001$1.00

the LIGA meth[illegible], number of advantages which will be illustrated by [illegible]scription of several sensor devices in the following.

Measurement of vibration and acceleration:

A LIGA configuration for measuring vibration or acceleration is shown schematically in Figure 2. By means of deep-etch X-ray lithography a template is generated which allows to manufacture a spring plate and a rigid stationary electrode directly upon a microelectronic circuit or, correspondingly, a multitude of such arrangements upon a completely processed silicon wafer. The change in capacity and the corresponding voltage change, respectively, may change directly the electric potential of the gate electrode of a MOSFET circuit

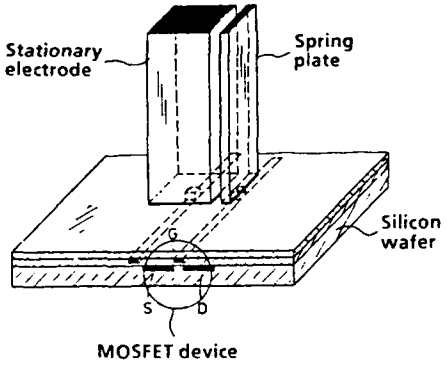

Fig. 2: Schematic representation of a LIGA sensor for measuring vibration or acceleration.

Compared to orientation dependent etching of monocrystalline silicon which is a well-known and proven technique for fabricating similar integrated sensors for vibration measurement, the LIGA technique should have several advantages. In particular, the fabrication of the electronic circuits can be fully completed prior to the fabrication of the sensor structure. Therefore, no mixing between micromechanical and microelectronic process steps occurs and a separate optimization is possible for the different fabrication procedures. Since the sensor element is arranged vertically upon the electronic circuit, the space requirement is minimized. This should be a further advantage compared to silicon micromechanics where the spring plates are usually fabricated in a plane parallel to the surface of the wafer. Nevertheless, the LIGA method allows also to produce cantilever structures which are arranged parallel to the wafer surface. Moreover, a two-axis sensor arrangement can be simply realized.

Measurement of position, displacement and magnetic fields:

For measuring position, displacement, small distances or changes of a magnetic field, sensor devices using inductive circuits are used in a large number of configurations. The LIGA method allows to generate small coils or complex coil arrays from materials with high electrical conductivity as well as microstructures with high aspect ratio from ferroelectric materials. Because of the large structural height attainable by the LIGA process, a low electrical resistance can be realized for small coils, which is an obvious advantage compared to corresponding configurations generated by thin film techniques whereas, compared to thick film techniques, much smaller dimensions and tolerances can be obtained.

Figure 3 shows a scanning electron micrograph of a helical structure generated by X-ray lithography. It is used for fabricating two intermeshing coils by electrodeposition which serve as the transmitting and receiving unit, respectively.

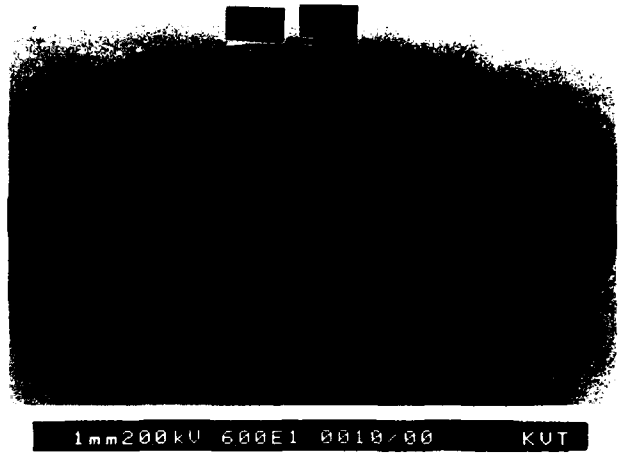

Fig. 3: Scanning electron micrograph of a resist template for fabricating two intermeshing microcoils.

Microoptical devices and spectrometry:

In the field of microoptics, the LIGA process could be used for fabricating waveguides, gratings, small prisms and small cylindrical lenses, zone plates, polarizers and spectral filters for the infrared range, spatial filters, modulators and many other optical devices and structures. More or less arbitrarily, one may discriminate between two basic configurations. One is represented by a perforated, self-supporting membrane of plate structure which is put into the path of rays and where the optical effect is determined by the special pattern of perforation. The other configuration may be characterized by the fact that optical structures are generated on a stable substrate where the path of rays is parallel to the surface of the substrate and partially determined by a waveguide structure. In the following, two special examples of these basic configurations will be described.

Figure 4 illustrates the principle of a small simultaneous spectrometer. It has a Rowland configuration with a curved reflective grating and comprises a slab waveguide consisting of three layers of transparent X-ray resist with matched refractive indices. In spite of the relatively low resolution of this microspectrometer, it might be a cheap and reliable sensor for photometric analysis of mixtures, chromatic testing, optical film thickness measurement, etc. In the field of communication technology, this device can be applied as a low-cost wavelength division multiplexer/demultiplexer.

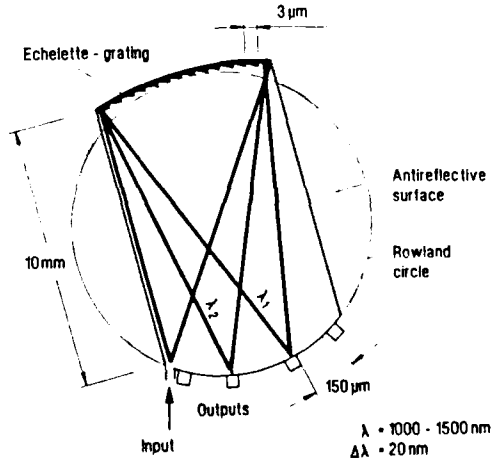

Fig. 4: Schematic representation of a simultaneous microspectrometer.

In the field of infrared spectroscopy, bandpass or cut-off filters can be realized as a so-called resonant mesh, i.e. by a metallic membrane with a multitude of cross-shaped, Y-shaped or circular openings whose dimensions and distances correspond to the wavelength to be transmitted [5, 6]. Such self-supporting membranes with the desired configuration of the openings can be fabricated by X-ray lithography and electroforming as demonstrated by Figure 5.

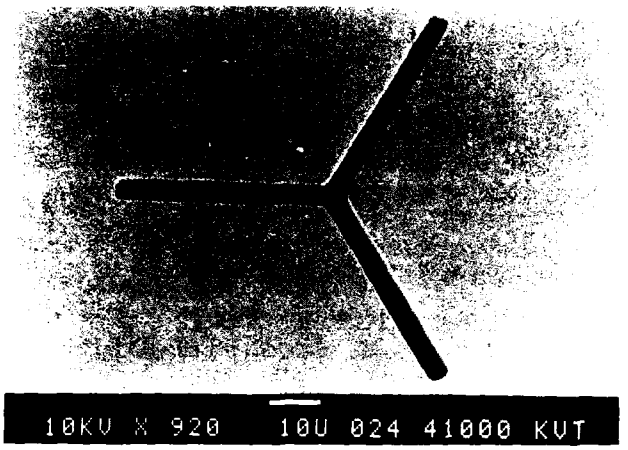

Fig. 5: Scanning electron micrograph of a Y-shaped opening with a slit width of 5 µm in a nickel membrane with a thickness of 300 µm.

Further development work deals with the fabrication of highly precise supporting and positioning elements for fiber optical sensors and with lithographic generation of waveguide elements from transparent X-ray resists.

Fluidic devices:

The first development work on the LIGA process aimed at the fabrication of micron-sized slit-shaped nozzles for uranium isotope separation as shown in Figure 6. Consequently, other flow devices and, in particular, fluidic sensors for measuring position, gas density, composition of mixtures etc. can be produced. Because of the small dimensions, a favorably low response time should be obtainable and such devices would be applicable even under conditions where microelectronic devices are difficult to operate, e. g. at a high radiation level. Further flow devices might be columns for chromatography, micro-cooling systems based on the Joule-Thompson effect, anemometric sensors, sieves for determining the size distribution of particles, micro-valves etc.

Measurement of radiation:

Concepts have been worked out for fabricating micro-channel plates and arrays of secondary electron multipliers. In contrast to the standard processes for producing channel plates, the tolerances of the dimensions can be reduced and the positions can be exactly determined. As a result, single channels or groups of channels can be matched directly to other discrete microstructures at the input or output of a micro-channel plate. In the case of miniaturized electron multiplier arrays, the dynodes can be arranged in a ring-shaped or any other curved configuration required in an experiment.

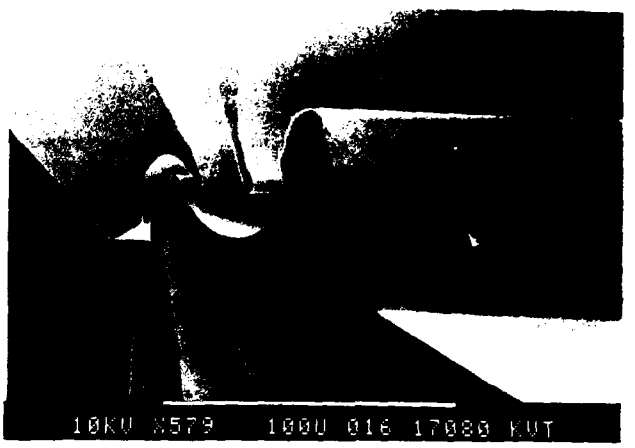

Fig. 6: Scanning electron micrograph of a double deflecting separation nozzle electroformed from nickel. The minimum slit width of the curved nozzle is 3 µm, the slit length is about 300 µm.

Electrical and Optical Microconnectors

The continuous increase of logic functions in microprocessor chips and the decrease in critical dimensions results in a corresponding demand for high density electrical connections with subminiaturized dimensions. A similar trend will probably be observable in the near future in optical communication technology, where the interconnection of optical waveguides, e. g. in the case of multiple monomode fiber connectors, requires micromechanical fabrication methods with submicron tolerances. Analogous requirements exist in modern sensor technology when sensor arrays have to be connected to VLSI chips.

Figure 7 shows an enlarged view of a part of a multi-pin plug with 100 poles per cm. The device is equipped with stable integrated guide pins which are fabricated in the same process sequence and ensure a simple insertion of the plugs.

Actuators

Since the LIGA method obviously allows to fabricate precise micromechanical components from various materials, its potential range of application also includes the fabrication of microacturators. Consequently, the current development work aims at the production of simple mechanical parts like gear wheels, bearings, joint couplings etc. and tests of various materials provided for fabrication of such devices. Moreover, feasibility studies are beginning which deal with the utilization of the LIGA process for fabricating micromotors and complete microactuator and positioning systems.

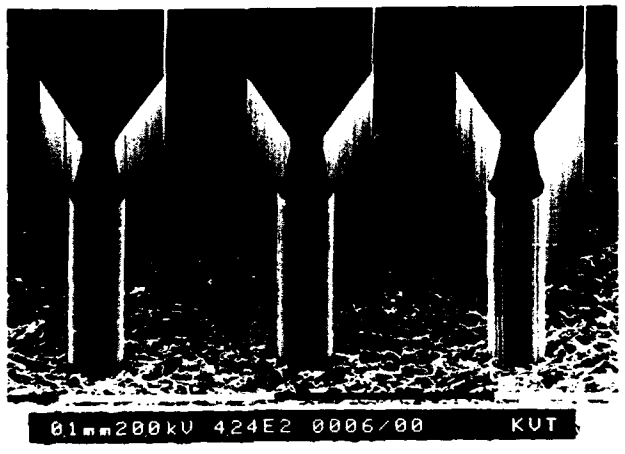

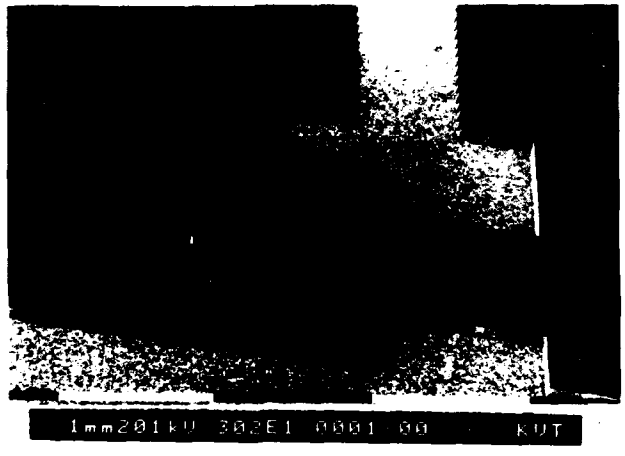

Fig. 7: Scanning electron micrographs of a multi-pin plug with 100 poles per cm.

Conclusions

The development work on the LIGA process is carried out by the Karlsruhe Nuclear Research Center in cooperation with the German industrial companies Steag AG, Essen, and Degussa AG, Frankfurt. The authors would like to emphasize that the feasibility of the process has been proven in the laboratory-scale only and large efforts are still necessary for commercialization. However, it is to be expected that this new microfabrication method will be superior to other processes if, in mass production of microstructures, specific requirements are imposed on the spatial resolution, the aspect ratio, the structural height, the parallelism of the structure walls and, in particular, if an unrestricted design of the cross-sectional shape and an optimum selection of the material required for the various microdevices has to be ensured.

These arguments should be important, above all, in the field of sensor technology where a precise mass fabrication of micromechanical, microoptical and microelectronic elements should result in favourable cost and where a trend exists in producing more and more smart and complex sensor elements. Moreover, the LIGA process should be also applicable in the field of microactuators. Thus, in connection with other microfabrication methods and semiconductor technology, the LIGA process might contribute to the future production of complete autonomous microsystems.

References

[1] A.D. Wilson, X-Ray Lithography: Can it be Justified?, Solid State Technology, Vol. 29, pp. 249-255, May 1986.

[2] E.W. Becker, W. Ehrfeld, P. Hagmann, A. Maner, D. Münchmeyer: Fabrication of microstructures with high aspect ratios and great structural heights by synchrotron radiation lithography, galvanoforming, and plastic moulding (LIGA process), Microelectronic Engineering, Vol. 4, pp. 35-56, 1986.

[3] W. Ehrfeld and E.W. Becker, Das LIGA-Verfahren zur Herstellung von Mikrostrukturkörpern mit großem Aspektverhältnis und großer Strukturhöhe, KfK-Nachrichten, Vol. 19, No. 4, pp. 167-179, 1987

[4] W. Ehrfeld, P. Bley, F. Götz, P. Hagmann, A. Maner, J. Mohr, H.O. Moser, D. Münchmeyer, W. Schelb, D. Schmidt, E.W. Becker, Fabrication of Microstructures Using the LIGA Process, Micro Robots and Teleoperators Workshop, Hyannis, Massachusetts, Nov. 9-11, 1987, Proc. IEEE Catalog Number 87 TH 0240-8

[5] F. Keilmann, Infrared High-Pass Filter with High Contrast, International Journal of Infrared and Millimeter Waves, Vol. 2, No. 2, pp. 259-271, 1981

6] H.-P. Gemünd, Filter für den submm-Bereich, Kleinheubacher Berichte, Vol. 29, pp. 501-505, 1986

CESIUM HYDROXIDE (CsOH): A USEFUL ETCHANT FOR MICROMACHINING SILICON

Lloyd D. Clark, Jr., Jennifer L. Lund, and David J. Edell
Massachusetts Institute of Technology, Room 20A-127
77 Massachusetts Avenue, Cambridge, Mass. 02139

Abstract

The $CsOH:H_2O$ etchant system was studied over a range of concentrations (10%–76% by weight) and temperatures (25°C–90°C). The etch rates of (110) silicon, (111) silicon, silicon dioxide, silicon nitride, and tantalum were experimentally determined. It was found that the $CsOH:H_2O$ etchant system has significant advantages over other commonly-used anisotropic silicon etchants (KOH, NaOH, EDP, and hydrazine). By proper choice of the $CsOH:H_2O$ temperature and concentration, an etchant system with a large (110)/(111) Si etch ratio and a small SiO_2 etch rate can be created, allowing silicon dioxide to be used as a masking material. For example, 60% CsOH at 50°C has a (110)/(111) Si etch ratio of 200 and a (110)/SiO_2 etch ratio of 5500. These data imply that a 1000Å SiO_2 mask would be sufficient for etching up to 550μm of (110) silicon. Cesium hydroxide also exhibits low tantalum etch rates, allowing tantalum to be used as part of an outer metallization system on micromachined structures.

Introduction

Our research group is currently involved in the development of an insertable neural signal transducer. This is a micromechanical device which can be inserted into living tissue for the purpose of converting neural signals into externally-available electrical signals [1]. Previous versions of the device were fabricated by anisotropically etching silicon in an aqueous solution of potassium hydroxide [2]. A new process sequence which used a trilayer (tantalum-platinum-gold) outer metallization system was incompatible with potassium hydroxide selective etch. Thus a new, selective etch was sought with better Ta etch characteristics. Preliminary tests of sodium hydroxide and ammonium hydroxide indicated a lower selectivity than potassium hydroxide. In fact, weaker bases in general seem to exhibit lower selectivity. Cesium hydroxide is the strongest base known, so it was conceivable that it would be more selective. Further, as noted by Hooley [3], SiO_2 etches more slowly in CsOH than in the other group I hydroxides (LiOH, NaOH, KOH, and RbOH). During our KOH studies [2], we observed a threshold phenomenon for KOH etching of tantalum. Below certain etch concentrations and temperatures, tantalum grew an oxide rather than etching. Since CsOH did not etch SiO_2 rapidly, perhaps it would also not etch Ta_2O_5 rapidly which could be important in the self-protection of Ta from the etchant.

The behavior of the $CsOH:H_2O$ etchant system was studied over a range of concentrations and temperatures. The etch rates of (110) silicon, (111) silicon, silicon dioxide, silicon nitride, and tantalum (in a Ta/Pt/Au metal system) were experimentally determined. These materials were chosen for study since they are directly relevant to the development of a successful fabrication sequence for insertable neural signal transducers as well as other micromachined sensors and actuators which must reliably operate in hostile environments.

Etching Experiments

The $CsOH:H_2O$ etching experiments were performed using four etch rate test structures which have been described previously [2]. The sequence of steps performed for each etching experiment was as follows:

1. The desired $CsOH:H_2O$ solution was mixed from deionized H_2O and solid CsOH (99.9% pure, metals basis). It is important to note that solid CsOH contains a significant amount of H_2O, which must be taken into consideration when calculating the true CsOH concentration of a solution. One lot of solid CsOH used in our experiments was 80.4% CsOH by weight, and a second lot was 78.8% CsOH by weight.

2. The $CsOH:H_2O$ solution was heated to the desired temperature in a feedback-controlled oven. Glass thermometers were used for temperature measurement. A closed polypropylene beaker was used to contain the etch solution. Stability of the temperatures was within ±0.2°C.

3. The etch test structure was placed in the $CsOH:H_2O$ solution. The (110) Si and (111) Si etch test structures were given 30 second dips in 10:1 H_2O:HF just prior to the etch to remove any oxide on the silicon, since the presence of a thin oxide layer on the silicon could have caused severe errors in the silicon etch rate measurement when the SiO_2 etch rate was slow [4].

4. The etch test structure was removed from the solution and measured using the following techniques: (a) (110) Si etch distance was measured to an accuracy of 1μm (2%) by taking the difference in focal plane height of a microscope focused first on the unetched silicon nitride and then on the etched silicon; (b) (111) Si etch distance was measured to an accuracy of 0.1μm (2%) with linewidth measurement equipment; (c) SiO_2 etch distance was measured to an accuracy of 10Å (1%) with an interferometric thin film measurement instrument; (d) Si_3N_4 etch distance was measured to an accuracy of 10Å (5%) with an interferometric thin film measurement instrument; (e) Ta etch distance was determined to an accuracy of 100Å (20%) with a mechanical step height measurement instrument. The etch rate was computed from the etch distance and etch time.

Experimental Results

Table 1 provides the etch rate data in units of either μ/hour or Å/hour. It also provides the etch rate data in terms of ratios relative to the (110) Si etch rate, which is useful for micromachining applications.

A series of graphs is provided (Figures 1–8) to aid in the interpretation of this data. Figures 1–4 display etch rates as a function of CsOH concentration, while Figures 5–7 display etch

TH0215-4/88/0000-0005$1.00

CsOH wt. pct.	temp. °C	(110) Si μ/hr	(111) Si μ/hr	SiO_2 Å/hr	Si_3N_4 Å/hr	Ta Å/hr	(110) ÷ (111)	(110) ÷ SiO_2	(110) ÷ Si_3N_4	(110) ÷ Ta
10%	50	0.89	0.56	5.7			1.6	1600		
10%	60	0.62	0.61	19			1.0	330		
10%	70	1.2	1.2	43			1.0	280		
30%	50	0.68	0.59	7.0			1.2	970		
30%	60	1.3	0.77	24			1.7	540		
30%	70	5.4	1.1	70			4.9	770		
40%	50	2.6	0.36	9.0			7.2	2900		
40%	60	4.0	0.53	30			7.5	1300		
40%	70	5.9	0.71	66			8.3	890		
45%	50	10	0.22	11			45	9100		
45%	60	22	0.40	32			55	6900		
45%	70	52	0.88	110			59	4700		
50%	25	2.7	0.025	0.86		oxide	110	31000		oxide
50%	50	13	0.12	13		23	110	10000		5700
50%	60	28	0.21	39		44	130	7200		6400
50%	70	46	0.38	86			120	5300		
50%	90	120	0.84	870		320	140	1400		3800
60%	25	1.3	0.0070	0.94		3.7	190	14000		3500
60%	50	8.3	0.042	15		29	200	5500		2900
60%	60	15	0.088	34		33	170	4400		4500
60%	70	27	0.15	85			180	3200		
60%	90	92	0.58	970	15	310	160	950	61000	3000
64%	25	1.1	0.0063	0.81		6.2	170	14000		1800
64%	50	6.3	0.037	14		23	170	4500		2700
64%	60	11	0.079	33		34	140	3300		3200
64%	70	19	0.14	72			140	2600		
64%	90	63	0.51	930	11	310	120	680	57000	2000
68%	25	0.30	0.0021	0.39		7.6	140	7700		390
68%	50	2.2	0.019	6.5		27	120	3400		810
68%	70	11	0.084	48			130	2300		
76%	50	0.56	0.010				56			

Table 1. $CsOH:H_2O$ etch rates and ratios.

CsOH wt. pct.	(110) Si E_A eV	(111) Si E_A eV	SiO_2 E_A eV	Ta E_A eV
10%		0.36	0.97	
30%	0.99	0.30	1.10	
40%	0.39	0.32	0.95	
45%	0.79	0.66	1.10	
50%	0.55	0.51	0.98	0.67
60%	0.61	0.63	0.97	0.62
64%	0.58	0.63	0.98	0.56
68%	0.70	0.72	0.94	

Table 2. $CsOH:H_2O$ activation energies.

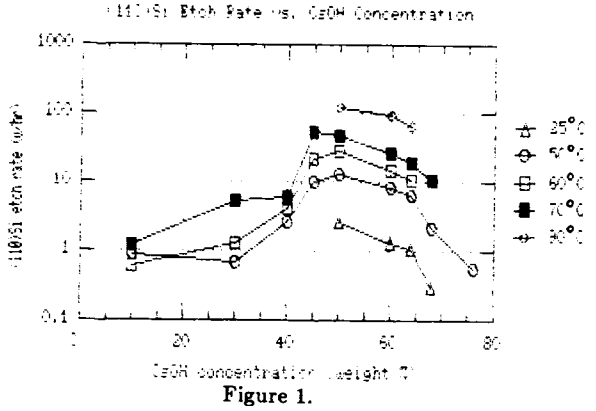

Figure 1.

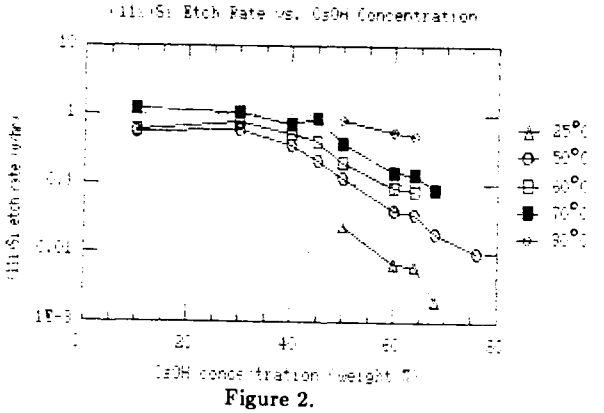

Figure 2.

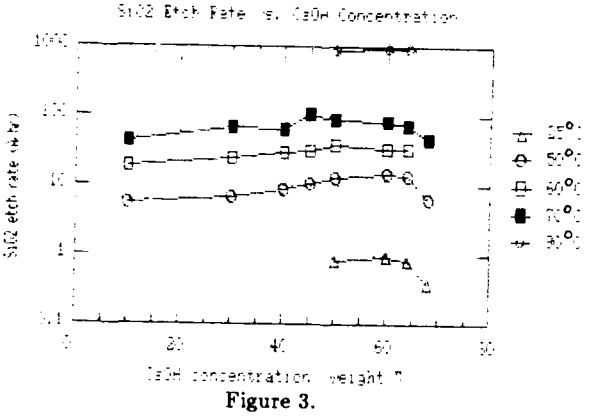

Figure 3.

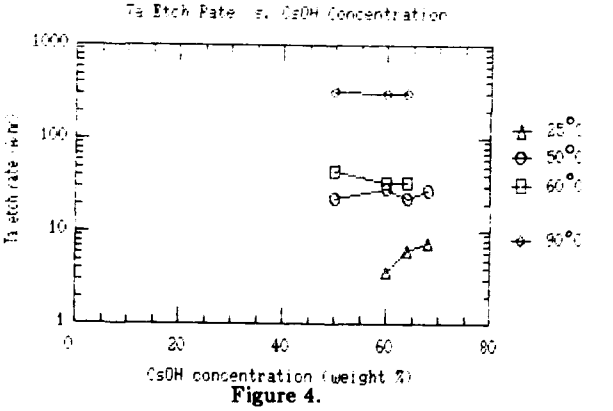

Figure 4.

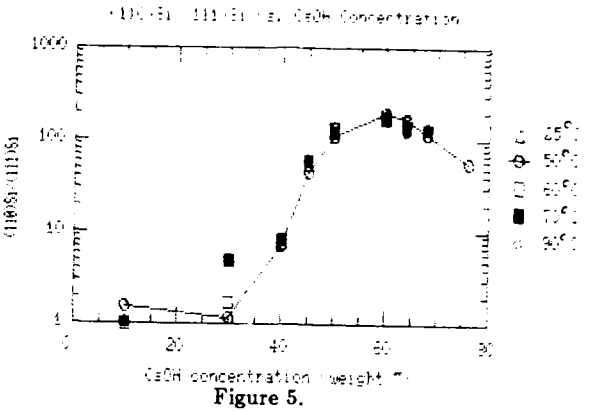

Figure 5.

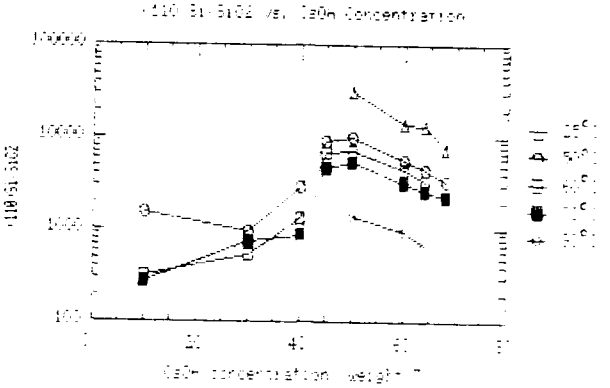

Figure 6.

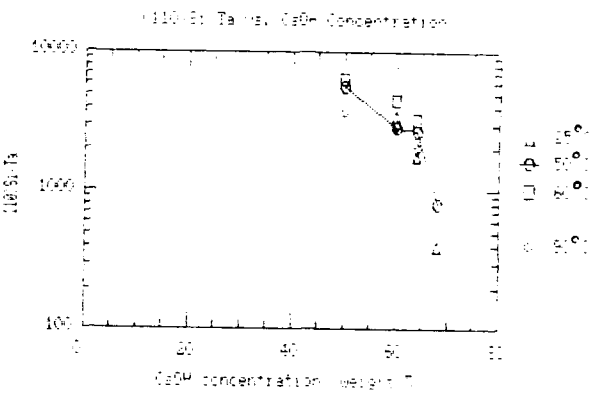

Figure 7.

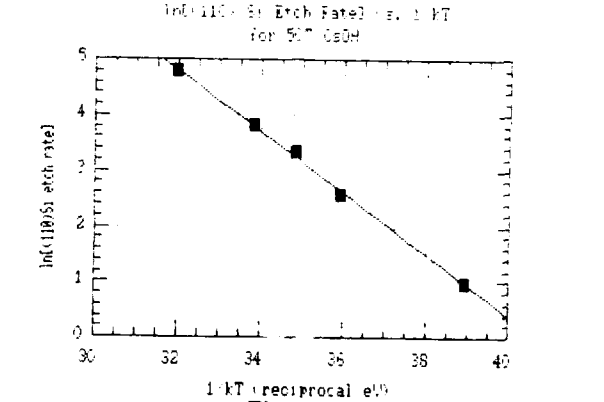

Figure 8.

ratios. Activation energies (see Table 2) were determined from the etch data using least-squares regression fits such as the one shown in Figure 8.

It was observed during the course of the etching experiments that there was a general relationship between the CsOH concentration of an etchant system and the smoothness of the (110) Si surface produced by the etchant system. Lower concentrations produced (110) surfaces which were very rough—more than 10μm of peak-to-peak roughness was observed. The highest concentrations produced (110) Si surfaces which were much smoother. Peak-to-peak roughness values of less than 1μm were observed via microscope focal plane height variation.

Discussion of Results

Hooley's 1961 study [3] determined an activation energy value of 0.95eV for CsOH:H_2O etching of SiO_2. This value is in good agreement with our values, which average 1.00eV. Hooley proposed the following sequence of reactions for SiO_2 etching:

$$SiO_2(s) + 2H_2O(l) \rightarrow SiO_2 \cdot 2H_2O(s) \quad (1)$$

$$SiO_2 \cdot 2H_2O(s) + 2OH^- \rightarrow [Si(OH)_6]^{-2} \quad (2)$$

As Hooley pointed out, at low hydroxide concentration (and therefore high water concentration) reaction (2) should be the rate-limiting step and the rate should increase as hydroxide concentration is increased. At high hydroxide concentration (and therefore low water concentration) reaction (1) should become the rate-limiting step and the rate should decrease as hydroxide concentration increases. Thus, the proposed reactions correctly predict a maximum in the plot of SiO_2 rate vs. CsOH concentration.

Various reaction mechanisms have been proposed for Si etching in alkali solutions. Finne and Klein [5] suggested the reaction:

$$Si + 4H_2O + 2(OH)^- \rightarrow Si(OH)_6^{-2} + 2H_2 \quad (3)$$

Palik [6] proposed the reaction:

$$Si + 2H_2O + 2(OH)^- \rightarrow Si(OH)_2(O^-)_2 + 2H_2 \quad (4)$$

Kendall [7] proposed:

$$Si + 3H_2O + OH^- \rightarrow Si(OH)_4^- + \frac{3}{2}H_2 \quad (5)$$

On the basis of the (110) and (111) Si etch data obtained in this study, we have not conclusively determined that any of the above reactions can be ruled out.

The phenomenon of smoother etched Si surfaces with increasing etchant concentration has been noted previously in the cases of hydrazine [4] and KOH:H_2O [7,2].

Applications to Micromechanical Structure Fabrication

A notable feature of the CsOH:H_2O etch system is the ability to achieve a large (110)/(111) Si selectivity while simultaneously allowing a silicon dioxide mask to be used. For example, 60% CsOH at 50°C has a (110)/(111) Si etch ratio of 200 and a (110)/SiO_2 etch ratio of 5500. This implies that a 1000Å SiO_2 mask would be sufficient for etching up to 550μm of (110) silicon. Kendall [7] presents a variety of micromechanical structures which can be fabricated by anisotropically etching (110) silicon wafers with KOH:H_2O. If instead CsOH is utilized as the anisotropic etchant, those structures can be created using oxide masks.

Conclusions

The etch ratios in Table 1 should allow a CsOH:H_2O etch system to be chosen for a particular application when specifications such as (110)/(111) selectivity, oxide etch ratio, and tantalum etch ratio must be met. The information regarding the relationship between CsOH concentration and surface smoothness should be useful in the fabrication of microstructures which require flat surfaces. Finally, it is worth noting that CsOH is relatively non-toxic and easy to work with when compared to other anisotropic Si etchants such as hydrazine and ethylene diamine.

Acknowledgments

This work was supported by the Whitaker Health Sciences Foundation and a NSF Graduate Fellowship. We wish to thank Vince McNeil for performing some of the etching and Bayla Fine for assistance in the use of linewidth measurement equipment. We also wish to thank Paul Maciel, Manager of the MIT Microsystems Technology Laboratory, for his continuing assistance.

References

[1] David J. Edell. A peripheral nerve information transducer for amputees: long-term multichannel recordings from rabbit peripheral nerves. *IEEE Transactions on Biomedical Engineering*, BME-33(2):203–214, February 1986.

[2] Lloyd D. Clark Jr. and David J. Edell. KOH:H_2O etching of (110) Si, (111) Si, SiO_2, and Ta: an experimental study. In *IEEE Micro Robots and Teleoperators Workshop*, 1987.

[3] J.G. Hooley. The kinetics of the reaction of silica with group I hydroxides. *Canadian Journal of Chemistry*, 39:1221–1230, 1961.

[4] D.B. Lee. Anisotropic etching of silicon. *Journal of Applied Physics*, 40(11):4569–4574, October 1969.

[5] R.M. Finne and D.L. Klein. A water-amine-complexing agent system for etching silicon. *Journal of the Electrochemical Society: Solid State Science*, 114(9):965–970, September 1967.

[6] E.D. Palik, V.M. Bermudez, and O.J. Glembocki. Ellipsometric study of bias-dependent etching and the etch-stop mechanism for silicon in aqueous KOH. In C.D. Fung, P.W. Cheung, W.H. Ko, and D.G. Fleming, editors, *Micromachining and Micropackaging of Transducers*, pages 135–149, 1985.

[7] Don L. Kendall and G. R. deGuel. Orientations of the third kind: the coming of age of (110) silicon. In C.D. Fung, P.W. Cheung, W.H. Ko, and D.G. Fleming, editors, *Micromachining and Micropackaging of Transducers*, pages 107–124, 1985.

PLASMA POLYMERIZATION OF METHYL METHACRYLATE: A PHOTORESIST FOR 3D APPLICATIONS

Henry Guckel, Jay Uglow*, Ming Lin#, Denice Denton, Jeff Tobin, Kathleen Euch, and Michael Juda

Wisconsin Center for Applied Microelectronics
Department of Electrical and Computer Engineering
University of Wisconsin
1415 Johnson Drive
Madison, WI 53706-1691

*Currently employed at Texas Instruments, Dallas, TX
#Currently employed at Intel, Santa Clara, CA

Abstract

Great efforts are being made to fabricate micromechanical sensors and actuators using approaches compatible with standard IC processing techniques [1-3]. Because these devices are fundamentally three-dimensional in nature, patterning steps must be carried out using photoresists capable of coating rapidly changing contours. This rules out the use of conventional spin-on resists for many applications. We are investigating the use of plasma polymerized methyl methacrylate (PPMMA) as a deep UV photoresist which fills this critical need. By depositing a light sensitive polymer film from a plasma, very irregular surfaces can be coated and patterned. Other key parameters for a photoresist are photosensitivity, stability, selectivity, and resolution. We have used these parameters as a means of optimizing the plasma process, exposure, and development cycle. The optimum process sequence results in stable films which withstand subsequent exposure to acetone and isopropyl alcohol, have a line width resolution of at least 1.5 μm, and have a selectivity of at least 70%.

Introduction

Plasmas have been used commercially to polymerize monomeric materials for several decades. An excellent review article on plasma polymerization has been written by Vinogradov [4]. He discusses experimental foundations, modelling, and characterization techniques of plasma polymerized films. Another comprehensive review article is that of Biederman [5]. The mechanisms for plasma polymerization are not well understood. Attempts underway to develop models include the work of Gazicki and Yasuda [6].

We are interested in the use of plasma polymerization in microelectronic fabrication. One of the goals of VLSI fabrication is to develop a dry lithography process. Previous work on the use of PPMMA to achieve this goal is summarized here. Hattori et al. [7] describe a vacuum lithography process using PPMMA and E-Beam patterning. Earlier work in plasma initiated polymerization of MMA was done by Osada et al. [8]. Kinzig and Smardzewski [9] characterized PPMMA films using FTIR spectroscopy. Ohno et al. [10] discuss possible mechanisms for crosslinking in plasma polymerization of MMA.

We describe here a lithography process using deep UV exposure of PPMMA. Previous work on deep UV exposure of spin-on PMMA films is reported by Lin [11] and Mimura et al. [12]. Efforts have been made to increase the sensitivity of spin-on PMMA by the addition of an aromatic azide compound [13]. The sensitivity has also been increased by exposing irradiated PMMA films to acrylic acid [14].

Plasma polymerized MMA films differ significantly from spin-on films. Use of plasma polymerization allows better control of the polymer structure and morphology. The PPMMA films are uniform and highly crosslinked and consequently pinhole free and highly adhesive [15]. Early work on PPMMA films was reported by Morita et al. [16]. Efforts have been made to enhance the sensitivity of PPMMA resist films by copolymerizing them with tetramethyltin [17].

Previous work on the use of PPMMA as a photoresist for IC fabrication has focussed on the use of high energy E-Beam and X-Ray exposure techniques [15-17]. Fong et al. [18] report the use of plasma polymerized styrene as a negative resist for V groove MOS (VMOS) using high energy sources. In the present work, we investigate the exposure of PPMMA films using a lower energy deep UV source with an emphasis on 3D fabrication.

Experimental Procedure

The plasma polymerization of MMA was done in the reactor system shown schematically in Fig. 1. It consists of a Tegal Plasma Inline 700 etcher modified slightly to perform plasma deposition. The PIL-700 operates at a frequency of 13.56 MHz and is capable of delivering a maximum power of 110 Watts to the reactor chamber. The parallel plate electrodes are circular with a diameter of 4 inches and a plate spacing of 1.5 inches. The substrate electrode temperature can be varied from 20°C to 90°C. The reactor chamber is evacuated using a vacuum pump and is instrumented with a Baratron pressure gauge. The MMA monomer is poured into a pressure can and the flow rate of the monomer vapor into the chamber is controlled via a flow meter as shown. Nitrogen can be introduced into the vacuum line to set the desired chamber pressure.

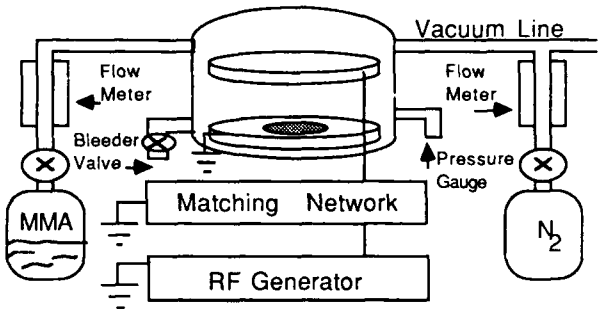

Fig. 1 Schematic Diagram of Plasma Deposition System

PPMMA was deposited onto silicon substrates which were coated with a chromium layer. The 0.1 μm chromium layer was sputter deposited using a Varian system. The MMA monomer (Aldrich M5, 590-9) was 99% pure with 10 ppm MEQH inhibitor. After putting the monomer into the pressure can, a freeze-pump-thaw cycle was performed to remove dissolved gases from the liquid. This was achieved by submerging the pressure can in liquid nitrogen to freeze the MMA solution and degassing the pressure can line using the vacuum

TH0215-4/88/0000-0009 © 1988 IEEE

pump. The monomer was then allowed to thaw and the process was repeated twice more. A chromium-coated wafer was then placed into the chamber and the system was pumped down to the base pressure of 50 mT. The monomer vapor was then introduced and the flow rate was allowed to stabilize. In some cases, nitrogen was used to throttle the pump to set the desired pressure. The RF power was then applied to the parallel plates to deposit the PPMMA onto the chromium surface.

A test mask (chromium on quartz substrate) with feature sizes from 1.5 μm to 180 μm was used to characterize the resolution of the PPMMA. The experimental procedure is shown schematically in Fig. 2. First, the thickness of the plasma deposited PPMMA was measured using an Alpha-Step Profilometer. The test mask was then placed in intimate contact with the wafer surface and the PPMMA was exposed using a Hybrid Technology Group 1000 Watt Deep UV Source (200-260nm). The exposed PPMMA was then developed in either acetone or KTI PMMA Developer I (74% methyl ethyl ketone and 26% ethanol). The wafer was then rinsed in DI water and dried. The resolution was determined by identifying the smallest pattern that was successfully transferred to the PPMMA material. The thickness of the developed PPMMA was also measured using the surface profilometer. The selectivity is defined as the ratio of the developed PPMMA thickness to the as-deposited PPMMA thickness, Y/X (see Fig. 2).

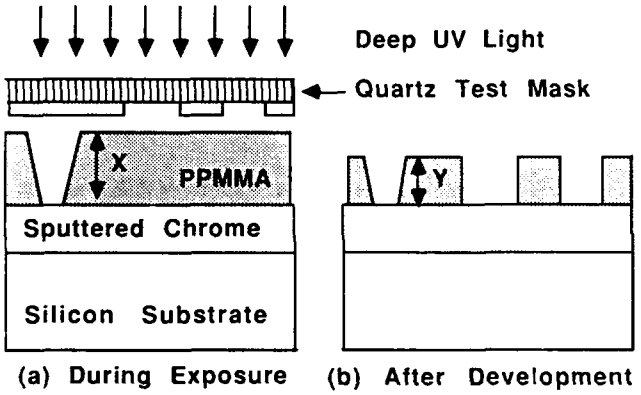

Fig. 2 Schematic Cross Section of Resolution Test Structure X and Y are the PPMMA depth before and after development.

Experimental Results

The objective of this study was to optimize the plasma process parameters (substrate temperature, chamber pressure, flow rate of monomer, reaction time, and forward power) and the PPMMA development parameters (exposure time, developer, and developer time). The algorithm used to choose the optimum parameters was to maximize the resolution, selectivity, and stability of the PPMMA films. The optimum process parameters were found empirically to be a substrate temperature of 50°C, a chamber pressure of 120 mT, flow rate of monomer of 0.05 standard liters/minute, reaction time of 20 minutes, and a forward power of 18 Watts. Under these conditions, the deposition rate of PPMMA on chromium was found to be 60 A/minute. PPMMA film thicknesses ranged from 1000A to 3000A depending on reaction time. The optimum deep UV exposure time for the Hybrid Technology Group Source was 15 minutes and the KTI developer was found to be superior to acetone. The system was relatively insensitive to developer time - we standardized on 60 seconds. Using these process and development parameters, the minimum test mask feature size of 1.5 μm was successfully transferred to the PPMMA film. The selectivity was at least 70 % and the developed films withstood exposure to acetone and isopropyl alcohol.

Because plasma polymerization is not well understood, it is interesting to explore the effect of the process parameters on the stability, resolution, and selectivity of the PPMMA film. Preliminary results indicate that higher RF power leads to higher film stability and lower resolution. This is to be expected since films deposited at higher powers are more heavily crosslinked. We also note a correlation between reactor pressure and resolution. Lower reactor pressure leads to higher resolution. These qualitative observations are being investigated using a statistical factorial experiment. These results will be published separately.

3D Fabrication

A feasibility study was done to verify the conformal nature of the PPMMA films. PPMMA was used to pattern freestanding silicon micromechanical structures held in place by aluminum beams in the bottom of 350 μm wells in a silicon substrate.

The process flow is outlined briefly here. A silicon nitride layer is deposited on both sides of a silicon wafer. The nitride is etched in the areas where wells are to be opened in the silicon substrate. A KOH anisotropic etch is used to remove the silicon in the well regions leaving a 25 μm thick silicon layer. Next, 1000A of chromium is sputter deposited on the backside of the silicon wafer. Then, PMMA and KTI 809 are spun successively on the backside and patterned to remain in the regions where the thinned silicon is to be etched. PPMMA is then plasma deposited on the backside and acetone is used to lift off the PPMMA and open up holes through which the chromium is etched. Aluminum is deposited on the front side of the wafer and patterned to form the beam structures. Finally, the thinned silicon is RIE etched to release the freestanding devices. One such structure, shown in Fig. 3, is a freestanding ring (25 μm thick) held in place by aluminum beams. Fig. 4 shows a square diaphragm held by aluminum beams.

Conclusion

A successful process for the plasma polymerization, exposure, and development of polymethyl methacrylate has been demonstrated. The fabrication of micromechanical structures confirms the feasibility of the use of PPMMA in three-dimensional applications.

Acknowledgement

Denice Denton is supported by the National Science Foundation via Presidential Young Investigator Award ECS-8747404.

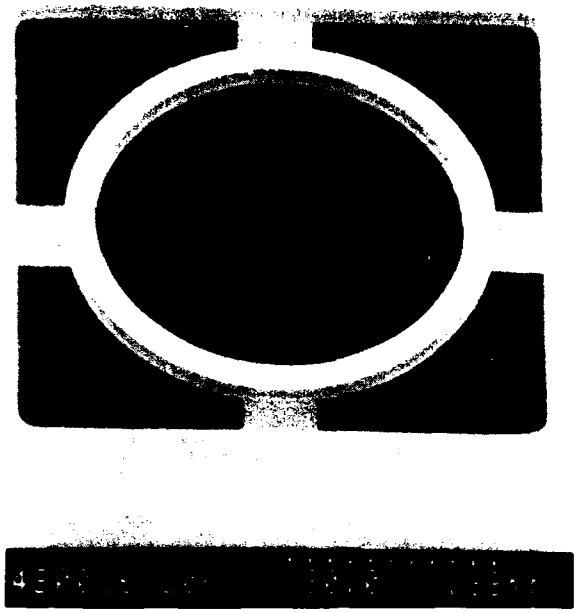

Fig. 3 Single Crystal Silicon Ring Structure Supported by Aluminum Beams.

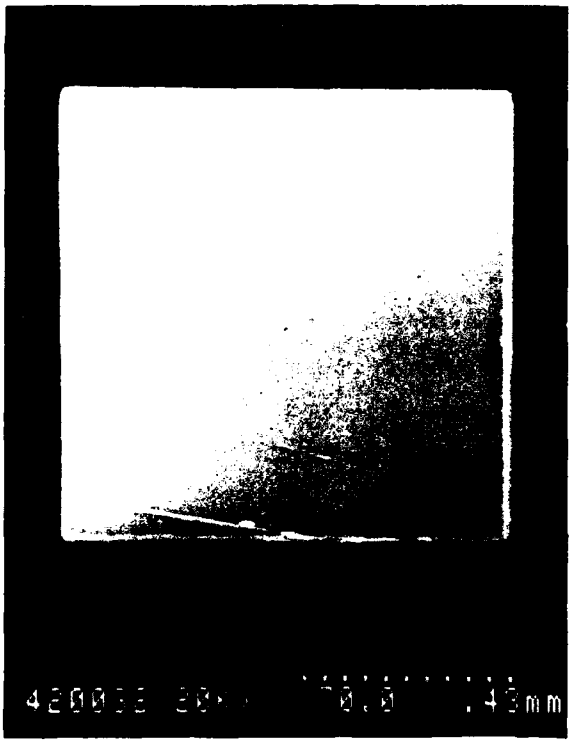

Fig. 4 Single Crystal Silicon Diaphragm Supported by Aluminum Beams.

References

[1] L.-S. Fan, Y.-C. Tai and R.S. Muller, "Pin Joints, Gears, Springs, Cranks, and other Novel Mechanical Structures," Transducers '87, pp. 849-852.

[2] K.J. Gabriel, W.S.N. Trimmer and M. Mehregany, "Micro Gears and Turbines Etched from Silicon," Transducers '87, pp. 853-856.

[3] H. Guckel, D.W. Burns, C.R. Rutigliano, D.K. Showers and J. Uglow, "Fine Grained Polysilicon and Its Application to Planar Pressure Transducers," Transducers '87, pp. 277-282.

[4] G.K. Vinogradov, "Plasma Polymerization (Review)," Translated from Khimiya Vysokikh Energii, vol. 20, no. 3, pp. 195-214, May-June, 1986.

[5] H. Biederman, "Polymer Films Prepared by Plasma Polymerization and their Potential Application," Vacuum, vol. 37, nos. 3-4, pp. 367-373, 1987.

[6] M. Gazicki and H. Yasuda, "An Atomic Aspect of Plasma Polymerization: the Role of Elemental Composition of the Monomer," J. Applied Polymer Sci.: Applied Polymer Symposium, vol. 38, pp. 35-44, 1984.

[7] S. Hattori, M. Yamada, J. Tamano, M. Ieda, S. Morita, K. Yoneda, S. Ikeda and S. Ishibashi, "Application of Plasma-Polymerized Film to Electron Beam Lithography," J. Applied Polymer Sci.: Applied Polymer Symposium, vol. 38, pp. 127-135, 1984.

[8] Y. Osada, A.T. Bell, and M. Shen, "Plasma-Initiated Polymerization of Methyl Methacrylate," J. Poly. Sci.: Poly. Letters Ed., vol. 6, pp. 309-311, 1978.

[9] B.J. Kinzig and R.R. Smardzewski, "Plasma-Polymerized Thin Coatings from Methyl-Methacrylate, Styrene and Tetrafluoroethylene," Surface Technology, vol. 14, pp. 3-16, 1981.

[10] M. Ohno, K. Ohno and J. Sohma, "Product Analyses and Crosslink Mechanism of Plasma-Polymerized Methyl Methacrylate," J. Polymer Sci.: Part A: Polymer Chem., vol. 25, pp. 1273-1284, 1987.

[11] B.J. Lin, "Deep UV Lithography," J. Vacuum Sci. Technol., vol. 12, no. 6, pp. 1317-1320, Nov.-Dec., 1975.

[12] Y. Mimura, T. Ohkubo, T. Takeuchi and K. Sekikawa, "Deep-UV Photolithography," Japanese J. Applied Phys., vol. 17, no. 3, pp. 541-550, March, 1978.

[13] C.C. Han and J.C. Corelli, "Azide-Poly(methylmethacrylate) Photoresist for Ultraviolet Lithography," J. Vacuum Sci. Technol. B, vol. 6, no. 1, pp. 219-223, Jan.-Feb., 1988.

[14] S.Y. Kim, J. Choi, D. Pulver, J.A. Moore, J.C. Corelli, A.J. Steckl and J.N. Randall, "Optimization of Solvent Development in Radiation Induced Graph Lithography of Poly(methylmethacrylate)," J. Vacuum Sci. Technol. B, vol. 4, no. 1, pp. 403-407, Jan.-Feb., 1986.

[15] S.A. Gangal, M. Hori, S. Morita and S. Hattori, "Plasma-Polymerized Electron Beam Resists Prepared from Methyl Methacrylate Using Various Carrier Gases," Thin Solid Films, vol. 149, pp. 341-350, 1987.

[16] S. Morita, J. Tamano, S. Hattori and M. Ieda, "Plasma Polymerized Methyl-Methacrylate as an Electron-Beam Resist, J. Applied Phys., vol. 51, no. 7, pp. 3938-3941, 1980.

[17] M. Hori, S. Hattori, T. Yoneda and S. Morita, "Effect of Sn in Plasma Copolymerized Methyl-methacrylate and Tetramethyltin (MMA-TMT) Resist on Plasma Development for X-ray Irradiation," J. Vacuum Sci. Technol. B, vol. 4, no. 2, pp. 500-504, March-April, 1986.

[18] F.O. Fong, H.C. Kuo, J.C. Wolfe and J.N. Randall, "Plasma Polymerized Styrene: A Negative Resist," J. Vacuum Sci. Technol. B, vol. 6, no. 1, pp. 375-378, Jan.-Feb., 1988.

MICRO-STRUCTURES

Wayne E. Feely
Rohm and Haas Co.
Spring House, PA 19477

Abstract

Three dimensional micron scale structures can be prepared from an acid hardening photoreist by the use of a special photomask. Positive mode structures have surface relief features while the negative mode produces tunnels, chambers and cantilever beams. The resist chemistry and process are versatile and can be tailored to specific applications.

Introduction

During the investigation of acid hardening photoresists for high resolution microlithography applications, it was found that three dimensional micro-structures could be prepared using a light attenuating photomask [1,2]. This paper describes our exploratory work in preparing microstructures and proposes possible applications.

Acid Hardening Photoresists

A typical acid hardening photoresist consists of a novolak resin and an amino resin together with a diazoquinone sensitizer. When exposed to near UV radiation, the latter is converted to an acid. In the unexposed state, the diazoquinone sensitizer functions as a dissolution inhibitor in retarding dissolution of the unexposed resist in aqueous alkaline developer. In the exposed areas, where the diazoquinone has been converted to an acid, dissolution in aqueous developer occurs readily. It is the difference in dissolution rate of the exposed and unexposed areas which permit the formation of positive images.

Positive images are formed when the areas exposed to light are removed in development and negative images are formed when the exposed areas remain and the unexposed are removed in development.

If a negative image is desired, the exposed resist, which contains an acidic latent image, can be heated to cause an acid catalyzed cross-linking reaction to occur in the exposed areas. Crosslinking insolubilizes the exposed areas and the entire resist can then be flood exposed and developed with aqueous base to reveal the negative image.

Negative mode imaging has several interesting features. At the time of development, the crosslinked image is insoluble in developer and thus, capable of higher resolution and wider processing latitude than in positive mode imaging. The crosslinked nature of the image imparts resistance to swelling and dissolution by both aqueous and organic solvents as well as dimensional and thermal stability to temperatures >300°C.

After the positive image is developed it can be easily crosslinked by flood exposing and then heating.

3-D Images

As the diazoquinone sensitizer is converted to an acid, photobleaching also occurs to produce sharp boundaries between exposed and unexposed areas both horizontally and vertically.

If a mask is constructed with clear, opaque and light attenuating areas, then exposure of an acid hardening photoresist produces a three dimensional acidic latent image, as shown in Figure 1. This latent image can be processed by

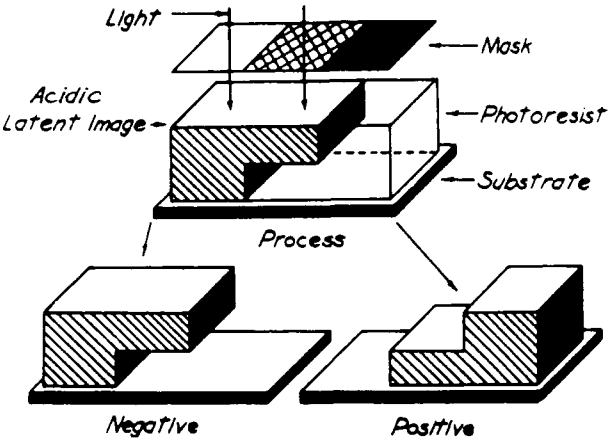

Latent Image Formation & Processing

Figure 1

the steps described above to give either a positive or negative three dimensional image.

The positive images have surface relief features in the partially exposed areas. The negative images are undercut where partially exposed, and are capable of forming cantilever beams, hollow chambers and tunneled structures.

In principle, a resist on a transparent substrate could be exposed to light on either the top or the bottom surface. Since the acidic latent image forms from the exposed surface downward, then changing from top to bottom imaging, inverts the images as well as changing its mode from negative to positive or vice-versa. Figure 2 shows how an acidic latent image would form on a top vs. bottom surface.

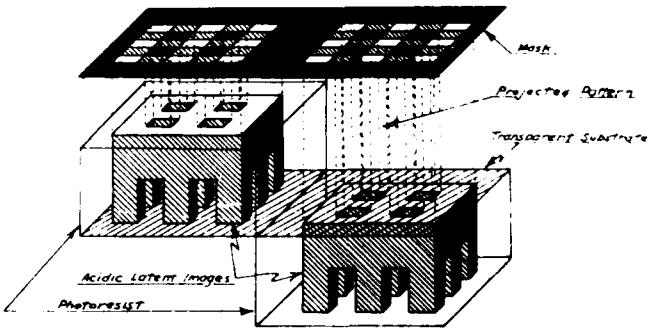

Top & Bottom Imaging with a Transparent Substrate

Figure 2

Figure 3 shows the structures that could be formed with simple checkerboard patterns.

TH0215-4/88/0000-0013$1.00

Checkerboard Mask Pattern & 3D Images

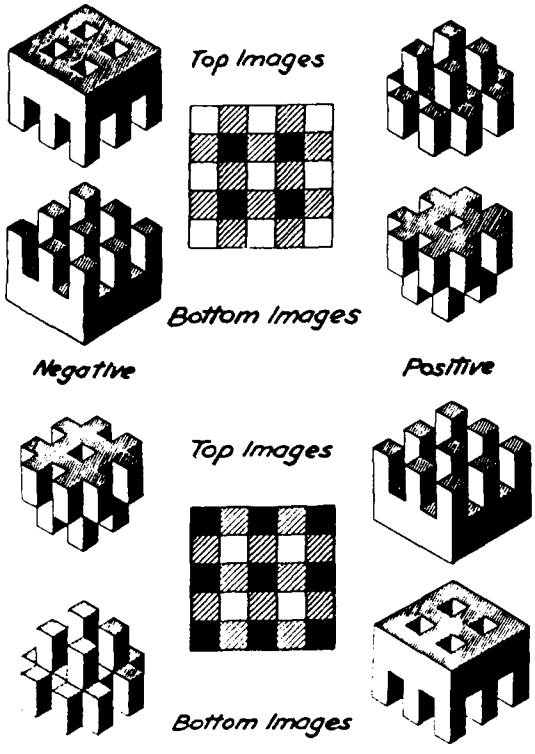

Figure 3

Mask patterns for preparing image clusters are shown in Figure 4. The light and dark margin masks are

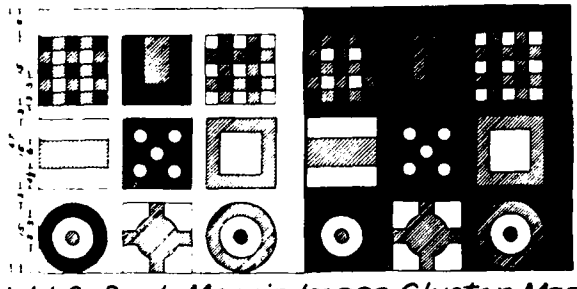

Light & Dark Margin Image Cluster Mask

Figure 4

necessary to isolate individual images in both positive and negative modes. The clusters from the two masks are shown in Figure 5 and the scale of images in Figure 6.

Figure 7 is the negative image pattern from the mask shown in Figure 4 and Figures 8, 9 and 10 show details of its structural features. Figure 11 shows images on a silicon wafer that has been heated to 300°C for 30 min.

A corresponding positive cluster from the same mask but at double the image dimensions can be seen in Figure 12. Notice that the positive image is simply what is missing from the negative image. Figure 13 illustrates some thick 225-250um images and Figure 14 shows free standing images that have been released from the wafer during development. Figure 6 shows a size comparison of these images with a hair.

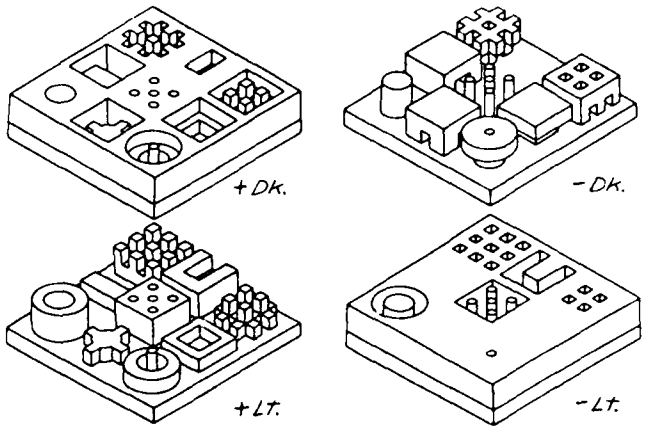

Positive & Negative Image Clusters with Lt & Dk Margin Masks

Figure 5

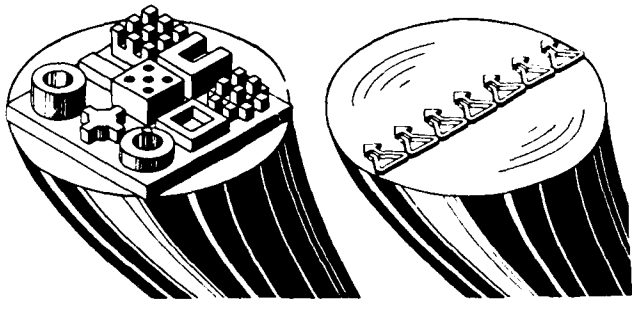

Comparative Size of Images and a Hair

Figure 6

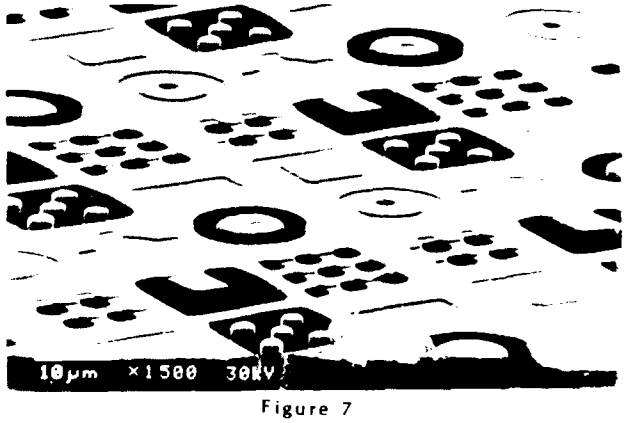

Figure 7

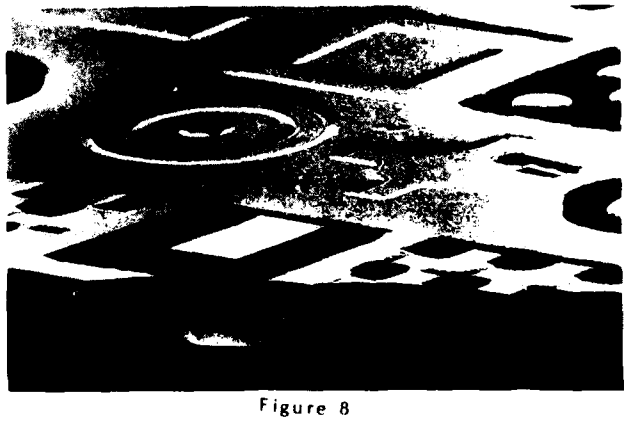

Figure 8

Figure 9

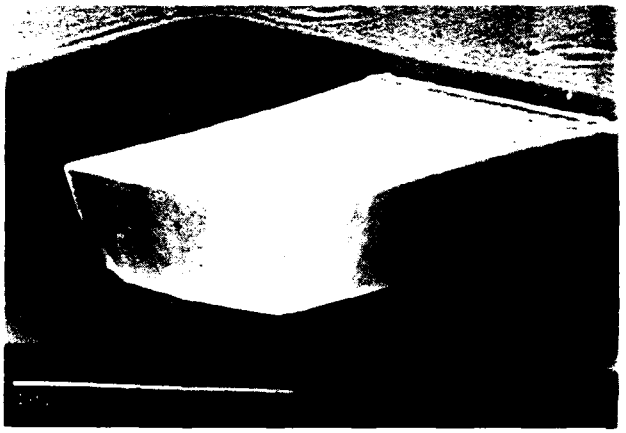

Figure 10

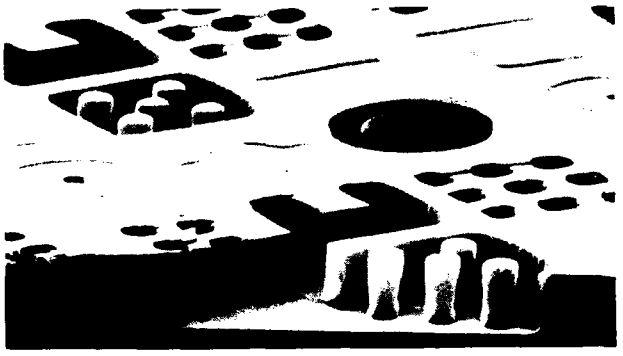

Figure 11

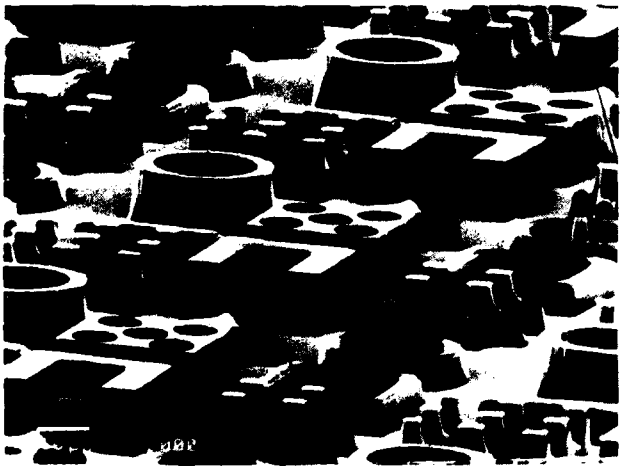

Figure 12

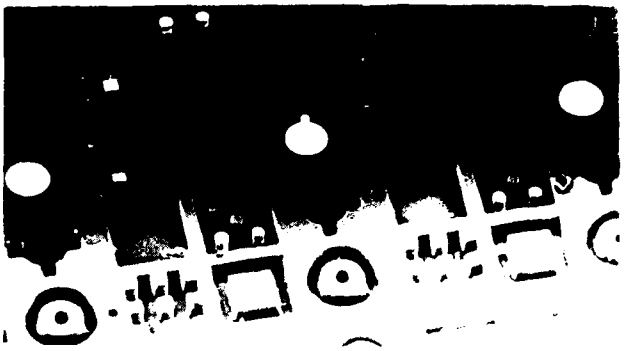

Figure 13

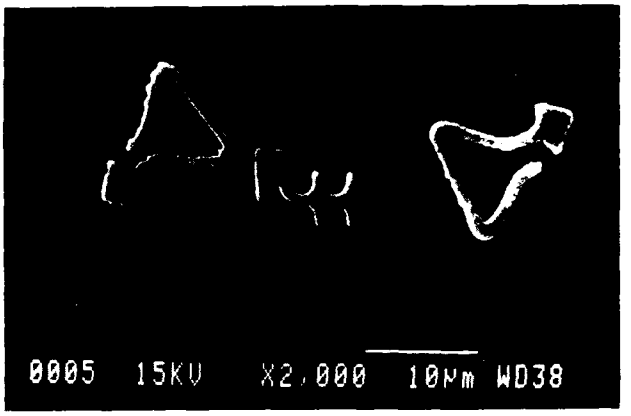

Figure 14

Potential uses for the micro-structures might be as components of miniature chemical, electrical, mechanical, and optical devices. Transparent elements such as lenses, prisms, filters and gratings could be tailored to specific requirements. The structures could also be used as molds for casting metals, plastics and ceramics or for the vapor deposition of metals or silicon dioxide. Free standing plastic and rubber objects are prepared by processing the resist over a water soluble release coating.

We welcome comments and suggestions.

References

1) W.E. Feely, J.C. Imhof, C.M. Stein, "The Role of the Latent Image in a New Dual Image, Aqueous Developable, Thermally Stable Photoresist", Polym. Eng. Sci. 26 1101(1986)

2) W.E. Feely, "Microplastic Structures", SPIE 631 48(1986)

A Miniature Fabry-Perot Interferometer Fabricated Using Silicon Micromachining Techniques

J. H. Jerman
IC Sensors, 1701 McCarthy Blvd.
Milpitas, California 95035

S. R. Mallinson
British Telecom Research Laboratories, Ipswich, England

Abstract

The techniques of silicon micromachining have been used to fabricate a miniature Fabry-Perot interferometer for use in the near infra-red spectral region. The device consists of two silicon wafers with deposited, highly reflective dielectric mirrors. The wafers are bonded together with a small gap between the mirrors, and sawn into individual devices. The wavelength tuning and parallelism control of the mirror elements are achieved electrostatically, by varying the voltage between control electrodes. The measured finesse of the structure exceeds 90 at a wavelength of 1.4 μm, resulting in a FWHM optical bandwidth of 3.1 nm. These devices are expected to find application as laser intercavity elements, wavelength demultiplexers in fiber optic telecommunications systems, and as sensors of pressure and acceleration.

Introduction

A Fabry-Perot interferometer (FPI) is an optical element consisting of two partially reflecting, parallel mirrors separated by a gap. The optical transmission characteristic of such an element consists of a series of very sharp transmission peaks when the gap equals multiples of a half wavelength of the incident light. These transmission peaks are caused by multiple reflections of the light in the cavity, and by using highly reflective mirrors, the response to small changes in gap can be very great. Even though two reflective mirrors are used, at the correct gap spacing, the transmission through the element approaches unity.

There are presently requirements for narrow-linewidth tunable filter components in optical communications systems.[1] A conventional grating monochromator can be used in such an application, but they tend to be large, expensive devices, which are difficult to tune electronically. The FPI offers the unique advantage of having a linewidth which can be matched to the system requirements by suitable choice of cavity spacing and finesse. Conventional FPI's, however, are difficult to manufacture due to the need to maintain near absolute parallelism between the two optical surfaces and the difficulty in mechanically varying the gap to tune the device. The micromachined FPI minimizes these difficulties.

Device Fabrication

The device, shown in Fig. 1, consists of two silicon pieces, bonded together at the wafer level, and sawn into individual devices. The individual devices are 13 mm x 15 mm and 0.6 mm thick. Both wafers have highly reflective, multi-layer dielectric mirrors deposited on the interior surfaces. These coatings have a reflectivity which ranges from 95% at 1.3 μm to 97.5% at 1.55 μm. Since silicon has a refractive index of about 3.5, anti-reflection coatings were deposited on the external surfaces to avoid substantial Fresnel reflection loss in the devices. Lightly doped silicon is highly transparent beyond 1.15 μm, which allows this device to operate.

One of the wafers has anisotropically etched moats outside the optical cavity area; the central regions thus being supported by 12-μm thick diaphragm suspensions. The thickness of the support can be adjusted to control the spring constant of the suspension, and thus set the voltage required to move the mirror. The other wafer has a set of metal electrodes and a spacer layer along with the dielectric mirror. The two wafers are bonded together to form an optical cavity with a nominal 3.5 μm gap, determined by the thickness of the spacer layer. The wafer is then sawn into individual die, mounted on a substrate, and wires bonded to pads connecting to the internal control electrodes.

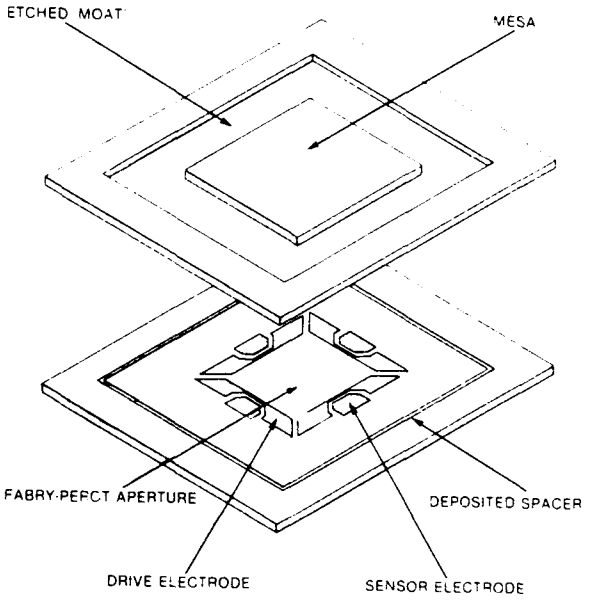

Fig. 1 Micromachined silicon Fabry-Perot Interferometer

The devices are controlled by the application of voltages across the drive electrodes and the electrically conducting suspended mesa. The electrostatic force thereby produced tends to draw the mesa towards the opposite surface, thus reducing the cavity spacing. This motion is balanced by the elastic restoring force of the etched diaphragm support. Four drive electrodes are provided on the mesa to allow control of not only the spacing of the cavity, but also the parallelism of the two mirrors, maximizing the finesse of the system. Additionally, four smaller electrodes are arranged to allow the spacing to be monitored capacitively and active feedback applied to the drive electrodes to maintain parallelism and environmental stability.[2]

TH0215-4/88/0000-0016

Theory

The transmission of a FPI is described by the Airy function:

$$I = \left(1 - \frac{A}{(1-R)}\right) \frac{1}{1 + \frac{4R \sin^2(kd\cos\theta)}{(1-R)^2}} \qquad (1)$$

where
A = mirror absorptance,
R = mirror reflectance,
d = cavity gap,
θ = angle of incidence of the beam, and
$k = 2\pi/\lambda$

The instrument finesse, F, is the ratio of the spacing of the transmission maxima, the free spectral range, to the FWHM linewidth. Defects are characterized by the defects finesse F_D which is related to the instrument finesse by:

$$\frac{1}{F^2} = \frac{1}{F_R^2} + \frac{1}{F_D^2}$$

where F_R is the reflection finesse given by:

$$F_R = \frac{\pi\sqrt{R}}{(1-R)}$$

It can be seen from eq. 1 that for kd equal to any multiple of π, the transmission for normal incidence is just:

$$T_{max} = \left(1 - \frac{A}{(1-R)}\right)$$

Thus for a dielectric mirror with A very small, the maximum transmission approaches unity.

Results

It is possible to observe the orientation of two surfaces of the device by using an infra-red source and TV camera. After fabrication, there is typically a misalignment of less than two fringes (Fig. 2a), corresponding to an angular misalignment on the order of 10^{-2} degrees. This result testifies to the excellent uniformity and stress-free nature of the suspension membrane after processing. By the application of appropriate bias voltages to the drive electrodes, the parallelism could be improved to better than 3×10^{-4} degrees (Fig. 2b). The relationship between the displacement of the mesa and the applied voltage is a quadratic:

$$d^2 - xd + (K V^2 A \varepsilon)/E = 0$$

where d is the mesa displacement, x the cavity spacing at rest, K a geometrical constant, V the voltage, A the area of the electrodes, ε the permittivity of free space, and E the modulus of elasticity of silicon.

As the voltage is increased, there is a proportional increase in displacement until a threshold is attained and the mesa moves, unrestrained, to its fullest extent. The region over which the mesa portion may be well controlled is approximately half the initial spacing. Hence, with these first devices with a gap of 3.5 μm, the mechanical tuning range is around 1.5 μm, attained

A

B

Fig. 2 Interferograms showing cavity parallelism a) at rest and b) with correction voltages applied

with a voltage of 18 V. Although the angular misalignment was sufficiently small to enable parallelism to be attained by the application of bias voltages to the drive electrodes, there was then insufficient mechanical tuning range to allow the optical passband to be tuned over a complete free spectral range. The initial gap will be widened on subsequent devices to allow increased tuning range.

The optical performance of the device was assessed by measuring the transmission response. White light was launched into a standard single-mode fiber attached to a proprietary beam collimation component. The silicon FPI was inserted into the beam and the transmitted light coupled into a second single-mode fiber connected to an optical spectrum analyzer. Fig. 3 shows the transmission peak with a FWHM linewidth of 3.1 nm at a wavelength of 1.43 μm. The cavity gap was calculated to be

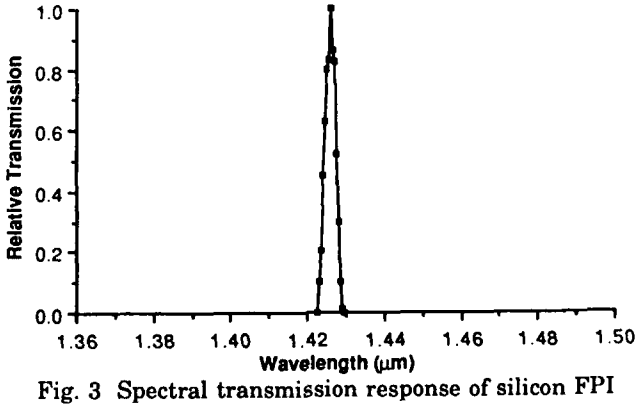

Fig. 3 Spectral transmission response of silicon FPI

3.58 μm, which yields a minimum etalon finesse of 93. The reflectivity at 1.43 μm was measured to be 0.974, yielding a reflection finesse of 119. The defect finesse, which is a measure of the ultimate attainable finesse, may be calculated to be 149. The insertion loss was measured to be 2.4 dB, of which 1 dB is accounted for by cavity defects; the remainder is attributed to antireflection coating imperfections and absorption.

Application as Sensors

These devices can be used in a number of ways as a sensor. Since the transmission of the device is a function of both the gap spacing and the wavelength, the device can be used as a sensor of either parameter. By varying the gap and monitoring the intensity, the device can be used as a monochrometer, within the free spectral range of the device. By maintaining the incident wavelength constant, the device can be used as a very sensitive position sensor, when the gap is near a transmission maxima. Fig. 4 shows the theoretical transmitted intensity and its derivative for a device with a reflection finesse of 150, for changes in gap, as opposed to wavelength, around a transmission maxima.

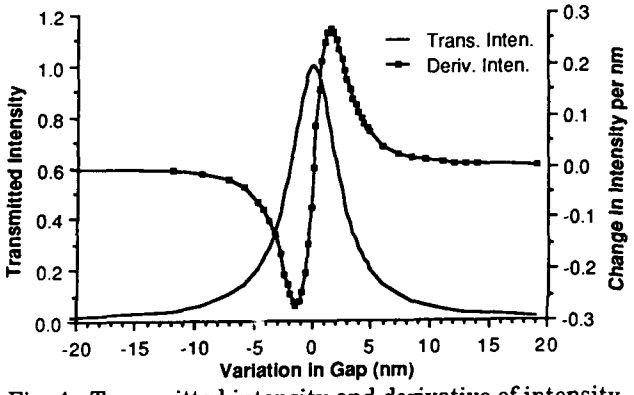

Fig. 4. Transmitted intensity and derivative of intensity with changes in gap about a transmission maxima for a Fabry-Perot Interferometer with reflection finesse of 150 operating at a wavelength of 1.5 μm.

The maximum slope of the transmission curve occurs at a transmitted intensity of about 0.75, where the slope is 0.04 nm per percent of intensity change. Thus, given the ability to detect a change in intensity of 0.1%, a change in gap of 0.004 nm can be detected. Similar performance has been reported for a confocal FPI, where a minimum sinusoidal displacement of about 2.5×10^{-3} nm was detected between 10 and 200 Hz.[3] These sensors are generally operated in a servo loop, where the gap is maintained such that the amplitude remains constant. A stable laser source is used so that the wavelength of the incident light is constant. The drive signal needed to maintain the gap is the output signal. The integrated drive electrodes in the micromachined structure make such operation very straightforward.

This position servo signal can be used to measure either differential pressure across the diaphragm support or acceleration of the center mass. Given the spring constant of the diaphragm support of the current device, a change in gap of 0.004 nm corresponds to a differential pressure of 1.5×10^{-8} PSI.

Conclusions

The use of silicon micromachining has resulted in a high performance Fabry-Perot interferometer. This fabrication technique allows the inclusion of electrodes to tune and adjust the parallelism, along with the ability to closely specify the initial gap of the device. The ability to batch fabricate these devices should result in a substantially less expensive device than is currently available. The measured finesse was sufficiently close to the reflection finesse to indicate that with higher-reflectivity coatings even better performance figures could be obtained. The devices have the significant benefits of being considerably smaller than other types of FPI and requiring low drive voltages. They will undoubtedly prove to be of use as wavelength selection components in optical fiber communication systems, and offer significant promise in use as sensors.

Acknolowledgments

We gratefully record the contributions of J. Knutti and S. Terry (ICS) and N. Vankoningsveld and R. Wesley (BT). The Director of Research at BTRL is thanked for permission to publish this paper.

References

1 Mallinson, S.R., "Wavelength-selective filters for single-mode fiber WDM systems using Fabry-Perot interferometers", *Appl. Opt.*, 1987, **26**, p. 430.

2 Hicks, T.R., Reay, N.K., and Atherton, P.D., "The application of capacitance micrometry to the control of Fabry-Perot etalons", *J. Phys. E.*, 1984, **17**, p. 49.

3 Jackson, D.A., Kersey, A.D., and Corke, M., Confocal Fabry-Perot Sensor, *Electronics Letters*, 4 March 1982, Vol. **18** No. 5, p. 227.

A TWIN-INTERFEROMETER FIBER-OPTIC READOUT FOR DIAPHRAGM PRESSURE TRANSDUCERS

Albert M. Young, James E. Goldsberry, Joseph H. Haritonidis,
Rosemary L. Smith, and Stephen D. Senturia
Massachusetts Institute of Technology
Rm 39-567
Cambridge, Massachusetts 02139

Abstract

A twin-interferometer fiber-optic readout scheme has been developed in order to monitor the deflection of pressure transducer diaphragms. This technique has a potential advantage at high temperatures, since the circuitry is kept at room temperature and is coupled to the sensor head via optical fibers. Only the diaphragm, optical fibers, and mounting hardware are exposed to the hostile environment. The interference scheme used here differs from conventional interferometry in that: 1) light is carried forward to the diaphragm and backwards to the photodetectors using a single fiber, and 2) the cleaved fiber end-face itself acts as the reference plane for the interference cavity. The cavity length is changed by deflection of a reflective diaphragm, thus changing the interference of the light propagating back to the detectors. A single interferometer cannot uniquely determine the direction of motion, but two such interferometers in parallel, i.e. the twin-interferometer, do provide the necessary information to measure both the magnitude and direction of deflection. Prototype sensor assemblies and detection circuitry have been developed and tested in an industrial setting. Limiting factors on sensor performance have been identified. This technique should also be applicable to other mechanical sensors in which deflections must be monitored.

Introduction

The deflection of a silicon diaphragm using either piezoresistive or capacitive readout is well established for pressure transducer applications. However, both readout schemes have temperature limitations. The goal of this work is to develop technology appropriate for optical readout of diaphragm deflection. Conventional fiber optic sensors usually monitor intensity changes [1,2] or interference due to changes in a sensing fiber relative to a reference fiber [3]. Other interference schemes involve the use of two Fabry-Perot resonators [4]. Optical techniques have potential advantages for high temperature applications, since only the diaphragm, optical fibers, and mounting hardware are exposed to the hostile environment; electronics and circuitry can all be located at room temperature.

Initial work in this regard was performed using bare laser beams [5]. Interference was achieved between a reference optical flat and a deformable micromachined silicon diaphragm. Laser light from a 5mW He-Ne source (633 nm) was brought in at an angle between 5 and 10 degrees from normal, and the interfered light was detected using a Motorola MFOD2202 phototransistor. Unfortunately, bare beams are difficult to work with since they require straight and unobstructed light paths. Optical fibers allow simpler remote positioning of the sensor head. Glass fiber with a silicone/teflon jacket is currently available which can withstand temperatures beyond 200 degrees Celsius. If the jacket is removed, the fiber may be able to withstand even higher temperatures. First attempts with fibers used two multimode fibers, one to bring the laser light to the diaphragm, and a second to carry the interfered light back to a photodetector. While coupling light into the first fiber was relatively simple, aligning the receiving fiber to gather the interfered light proved difficult. In addition, multimode fibers allow the propagation of unwanted higher order modes. It was then decided to use the single, single-mode fiber approach described below. Computer simulation has confirmed that the greatest sensitivity for an interferometer using the two-fiber approach can be achieved by merging the source and detection fibers into a single light path [6].

A single fiber interferometer can be constructed by using standard single-mode 50/50 fiber couplers as shown in Fig. 1 [5]. Light launched into one end of the fiber is split 50/50 at the coupler. If one of these ends is brought up to a reflective surface, reflections from this surface can interfere with reflections from the fiber-air interface and be transmitted back along the coupler fiber to a photodetector. The actual interference cavity is very localized; the fiber serves primarily to carry the correct intensity of light back to the detector. Although the single fiber interferometer can provide varying degrees of light intensity corresponding to movement of the diaphragm through interference fringes, the direction of movement cannot be uniquely determined. One solution to this problem is the twin-interferometer system, which measures both magnitude and direction of deflection of a transducer diaphragm.

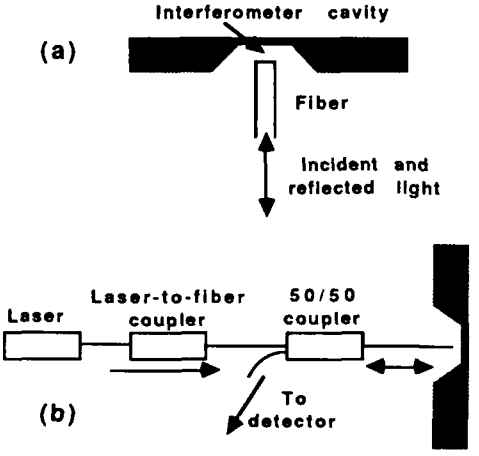

Fig. 1 Single fiber interferometer

a) Close-up of interferometer
b) Fiber-optic coupling arrangement

Adapted from [5]

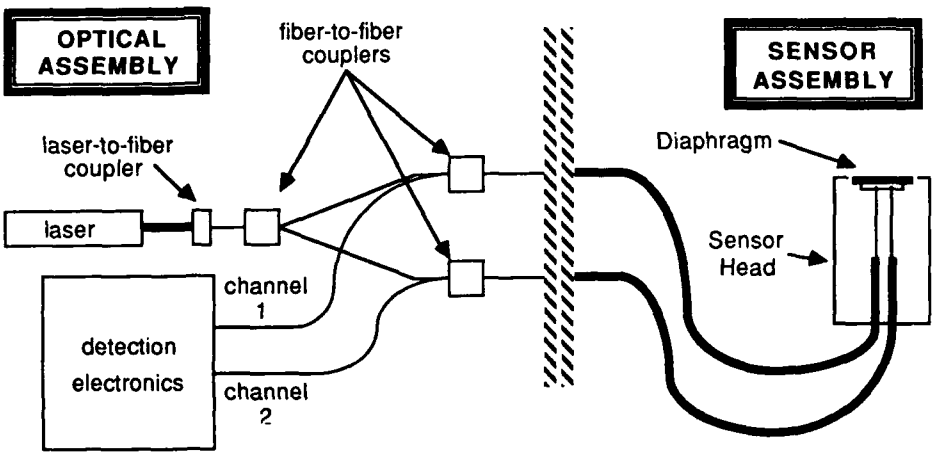

Fig. 2 Twin-interferometer system overview

Sensor Concept and System Design

Fig. 2 shows a system overview with the twin-interferometer scheme. Laser light is coupled into a single-mode fiber, where it is split 50/50 into two forward legs at the first fiber-to-fiber coupler. At this point, each of the two beams will be used in an independent interferometer, similar to the design shown in Fig. 1. Each leg has the laser light split again at a 50/50 coupler, with one forward leg travelling to the sensor head, and one reverse leg travelling to the photodetector and detection electronics. Each fiber end-face is cleaved perpendicular to the direction of light propagation so that it forms an independent interference cavity with the diaphragm. Reflections from the fiber end-face and the diaphragm surface interfere with each other, and propagate back along the fibers to a detection circuit, where the transducer response is analyzed. In general, because of slight length differences, the two cavities have different total path lengths; hence the two interference patterns are shifted in phase from one another. However, if the diaphragm is deflected by pressure, the cavity length changes identically for both interferometers. Each interferometer-output-versus-cavity-length curve can be described by its own Airy function, which may be approximated as a sinusoid for our values of reflectivity. Diaphragm deflection gives two phase-shifted signals, as shown schematically in Fig. 3. Plotting the output for channel 1 versus channel 2 should yield a closed loop Lissajous figure as illustrated in Fig. 4. A diaphragm

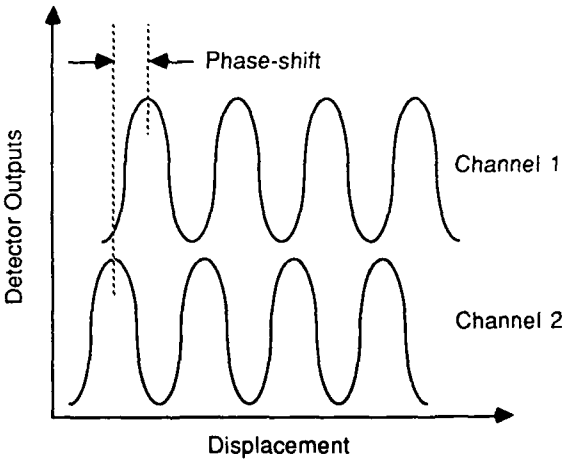

Fig. 3 Phase-shifted detector signals

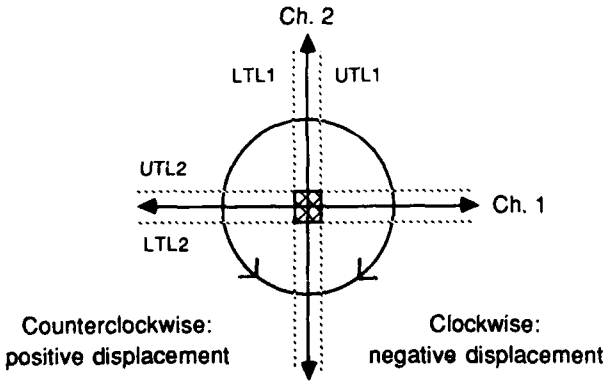

Fig. 4 Closed loop Lissajous curve

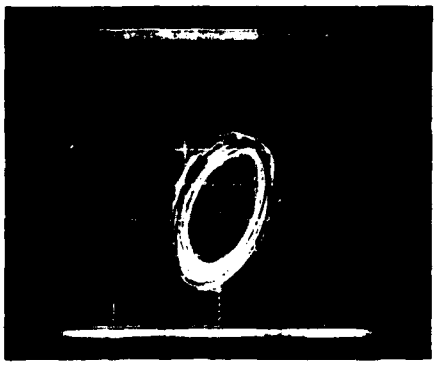

Fig. 5 Actual Lissajous curve

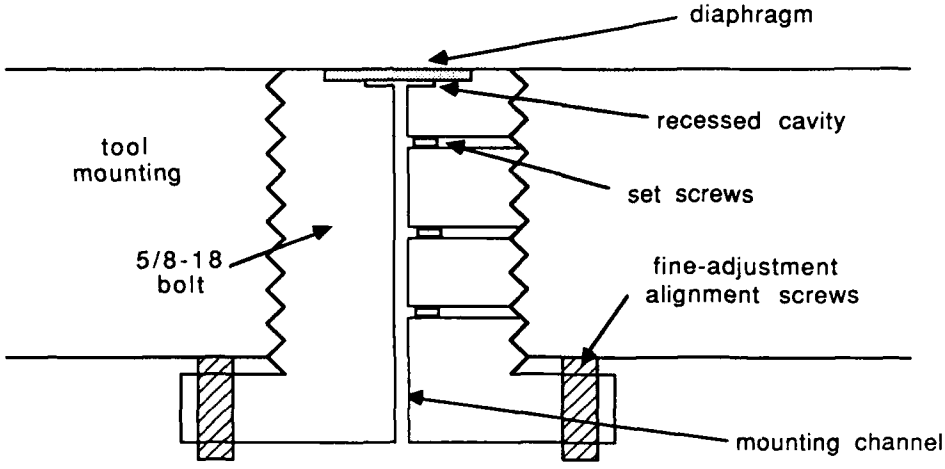

Fig. 6a Sensor head assembly

moving toward the end-faces will result in travel in one direction around the Lissajous curve, while a diaphragm moving away from the end-faces will result in movement in the other direction. A sample photograph of an experimental Lissajous curve is shown in Fig. 5. The channel 1 and channel 2 outputs have been shown thus far to illustrate the Lissajous concept. These outputs also serve as inputs to a fringe counting circuit which automatically counts down or up depending on whether the cavity is getting larger or smaller. A two bit binary description of the diaphragm displacement may be obtained by setting trigger levels on the Lissajous curve as shown in Fig. 4. As long as the curve remains outside the cross-hatched box defined by the upper (UTL) and lower (LTL) transition levels of each channel, the circuit will be able to correctly measure the magnitude and direction of displacement. This detection method has a resolution of one-eighth the wavelength of laser light (~80 nm).

Fabrication

Fabrication of silicon diaphragms was done using standard anisotropic etching techniques on double-side polished (100) wafers. Square diaphragms 2 mm on a side and 60 μm thick were fabricated in a temperature controlled potassium hydroxide (KOH) etching apparatus. Various alcohols were added to the solution to achieve more uniform etching. Isotropic polishing etches were used to smooth out the surface for reflective purposes. However, surface roughness continued to impair sensor operation. To circumvent this problem, diaphragms may be made from wafers with 60 μm of epitaxial silicon deposited on them. Using known anodic etch stop techniques, one can obtain very smooth surfaces of reflective silicon for deflection. This technique is presently under investigation. For this work, polished stainless steel diaphragms were used to demonstrate the interferometric technique.

A prototype sensor head was machined in a 5/8-18 bolt as shown in Fig. 6a. Since alignment of the sensor head with the top surface is critical for certain load transfer schemes (e.g. load transfer through an elastomer in composite manufacture tools), the threads were left loose and fine-adjustment alignment set screws were provided. A close-up of the fiber holder assembly is shown in Fig. 6b. The fibers were held in a piece of ceramic containing two 125 μm diameter holes, which matched the diameter of the glass cladding of the fiber. The ceramic was surrounded by a cylinder of hypodermic steel tubing for ruggedization. This steel tubing was passed through a mounting channel in the sensor head and was aligned normal to the diaphragm through the use of set screws.

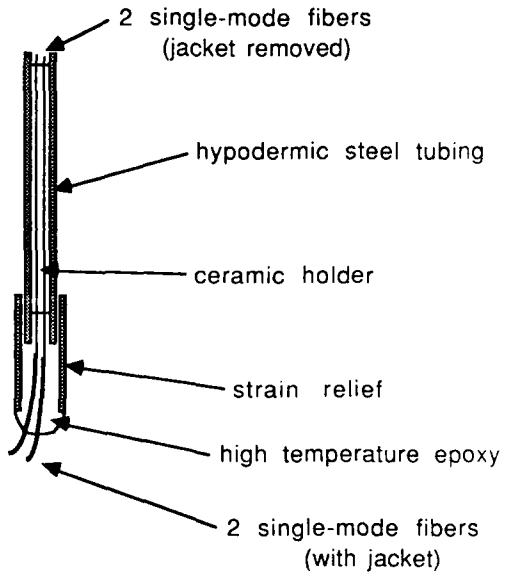

Fig. 6b Fiber holder assembly

Detection and Readout Circuit

To perform the task of decoding the optical signal, fringe counting and computer interface circuitry has been designed and constructed. This circuitry, shown functionally in Fig. 7, is used to amplify the input signals, remove noise, decode the results into up/down counts, and to send the digital information to a computer. The diaphragm displacement, measured in fringes, can then be correlated to a pressure reading in real time. First, the signals from the photodetectors are amplified and any DC offsets are removed. These amplified signals are fed to voltage comparators with adjustable transition levels. Noise

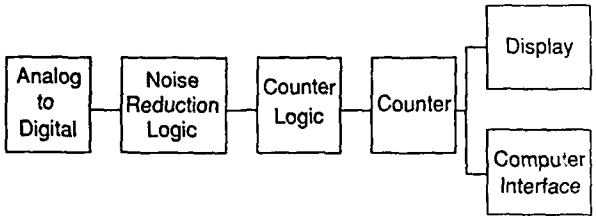

Fig. 7 Functional diagram of fringe counter

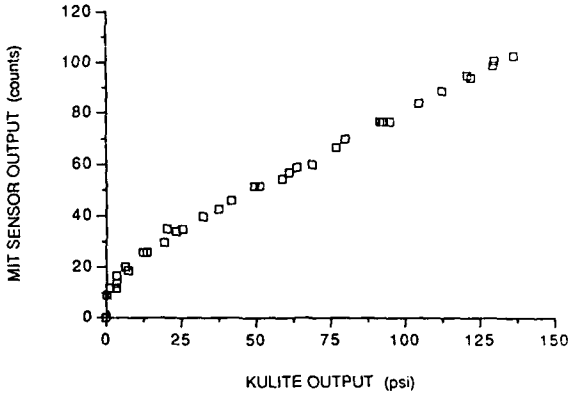

Fig. 8 Plot of fringe count versus applied load
Data is merged from three separate runs in a composite manufacture tool.

discrimination logic has been designed to allow the signal to drift repeatedly across any one of the transition levels without triggering the counter. The counter is only triggered when the signal has crossed both upper and lower transition levels. Combinational logic is used to determine counter trigger and counter direction, both of which depend on the relationship between the previous and present binary states of the system. This information is sent to on-board displays and to the digital I/O port of the interface unit, which is connected to an IBM PC/AT. Software performs data acquisition, analysis, and display routines. Sensor calibration data (fringes vs. pressure) is kept on disk.

Evaluation

Crosstalk between the two interferometers was not apparent. Unfortunately, severe diaphragm bending did tend to limit the operational range of this scheme. Diaphragm bending changes the difference between the lengths of the two interferometric cavities. If this difference is allowed to change by more than 0.32 microns (half a wavelength), then the combinational logic will be unable to properly detect the motion of the diaphragm. However, when the fibers are properly aligned, reasonable sensor operation is easily achieved. Temperature dependence tests have also been performed, where the sensor was mounted between the heated platens of a hydraulic press, and the fringe count versus applied load was studied as a function of temperature. These tests are still in progress; preliminary work with a single fiber interferometer show little temperature dependence.

The sensor was installed and tested in a composite manufacture tool at the Lockheed-California Composite Development Center. Measurements were taken in the actual tool, where the load is transferred through an elastomeric layer, which in turn deforms the stainless steel sensor diaphragm. Sensitivities of less than one percent of full scale were achieved over an operational range of 40 fringes (12.6 μm). A simultaneous in-tool comparison with a commercially available Kulite semiconductor sensor was made. Merged data from three separate test runs is shown in Fig. 8. The differences at low applied loads may be due to improper seating of the two pressure transducers on the test surface.

Conclusions

The twin-interferometer has been shown to be a viable technology for readout of diaphragm deflections. The interference of light is intrinsically insensitive to high temperature, and experimental results using a single interferometer indicate that thermal effects on the mechanical structure of the sensor should have little effect on the output. Since the interference cavity is highly localized, temperature effects on the fiber have little effect on the light intensity carried back to the detectors. The choice of diaphragm material is no longer restricted to silicon; any partially reflecting surface can serve as the transducer. This has been demonstrated using polished stainless steel diaphragms. Thus it has been shown that both the direction and magnitude of deflection of a diaphragm can be determined using a fiber- optic interferometric scheme. This technique should also be applicable to other mechanical sensors in which deflections must be monitored.

Acknowledgment

This work was supported in part by the Lockheed-California Company. Partial fellowship support from the 3M Sensor Fellowship (AY) and from a GEM Fellowship (JG) is gratefully acknowledged. Assistance in KOH etching from Lloyd D. Clark and Prof. David J. Edell is also greatly appreciated. Device fabrication was carried out in the Microsystems Technology Laboratories and the Turbulence Research Laboratory at MIT.

References

[1] B.E. Jones and G.S. Philp, "A fibre optic pressure sensor using reflective techniques," in *Proc. Int. Conf. on Optical Techniques in Process Control, The Hague, Neth., June 1983*, pp. 11-25.

[2] C. Lawson and V.J. Tekippe, "Fiber-optic diaphragm-curvature pressure transducer," *Opt. Lett.*, vol. 8, pp. 286-288, 1983.

[3] T.G. Giallorenzi, et. al., "Optical fiber sensor technology," *IEEE J. Quantum Electron.*, vol. QE-18, no. 4, pp. 626-665, Apr. 1982.

[4] M. Watanabe, M. Katagiri, and M. Hijikigawa, "Fiber optic digital force sensor based on double cavity configuration," *Transducers '87, Techn. Dig., Tokyo, June 1987*, pp. 208-211.

[5] D.J. Warkentin, J.H. Haritonidis, M. Mehregany, and S.D. Senturia, "A micromachined microphone with optical interference readout," *Transducers '87, Techn. Dig., Tokyo, June 1987*, pp. 291-294.

[6] M.W. Judy, "Sensitivity issues of an interferometric pressure sensor," Bachelor's Thesis, Department of Electrical Engineering, MIT, 1987

ACOUSTIC PLATE MODE DEVICES AS LIQUID PHASE SENSORS

A. J. Ricco, S. J. Martin, G. C. Frye, and T. M. Niemczyk

Sandia National Laboratories
Albuquerque, New Mexico 87185 USA

Abstract

Acoustic plate mode (APM) devices are sensitive to mass accumulation and removal from a solid surface immersed in a liquid, as well as solution viscosity, density, electrical conductivity, and dielectric coefficient. Operating in direct contact with liquid solution at 158 MHz, APM devices have been used to monitor electrodeposition, electroless deposition, and metal film corrosion. Calibration of a 0.19 mm thick ST-quartz APM sensor by vacuum deposition of silver yielded a detection limit of less than 1 ng/cm^2. Comparison of the frequency shift during Ag deposition to that obtained upon aqueous dissolution of the same Ag film demonstrates that the sensitivity to mass loading is not measurably altered by liquid contacting the device surface. Monitoring the propagation loss of the acoustic wave allows use of an APM device as a solid-state viscosity sensor, with the loss proportional to viscosity from 0 to 80 cP. Finally, acoustoelectric coupling between the APM and solution results in a velocity perturbation which imparts a sensitivity to the solution ionic conductivity and dielectric coefficient.

Introduction

Surface acoustic wave (SAW) devices have been studied in considerable detail as sensors of gaseous species [1-6] and to a lesser extent for the characterization of thin film properties [7,8]. The extremely high sensitivity of these devices to adsorbed surface mass - as little as 100 pg/cm^2 being detectable - results from the fact that the velocity of sound traveling through a SAW substrate can be monitored with parts per billion accuracy by utilizing the device as the frequency control element of an oscillator circuit. In addition to facilitating the development of new chemical sensors, extreme sensitivity to surface mass changes at a solid/liquid interface would be helpful in the study of many problems in fields such as electrochemistry, corrosion, and catalysis.

The large surface-normal component of displacement characteristic of Rayleigh waves (SAWs) efficiently couples acoustic energy from an oscillating device surface into a liquid contacting that surface. In general, this leads to prohibitively high attenuation of the wave [9]. Fortunately, the interdigitated electrode pattern typically used to launch and receive a SAW on a planar piezoelectric substrate can launch a number of other acoustic modes as well. In an ST-cut quartz substrate, a shear-horizontal (SH) acoustic plate mode (APM) propagates at 1.6 times the velocity of the Rayleigh mode [10]. The shear-horizontal nature of this mode means that it has negligible surface-normal displacement at the surface, with the result that transfer of acoustic energy from the device to the liquid is minimal. APM devices thus suffer considerably less attenuation (a few dB) than do SAW devices (tens of dB) in contact with liquids, yet still have sub-monolayer sensitivity to mass changes.

In this paper, we will describe the parameters affecting APM propagation and illustrate the utility of these devices for sensing mass changes at solid/liquid interfaces. Models for viscous coupling, mass loading, and acoustoelectric interactions will be outlined as well.

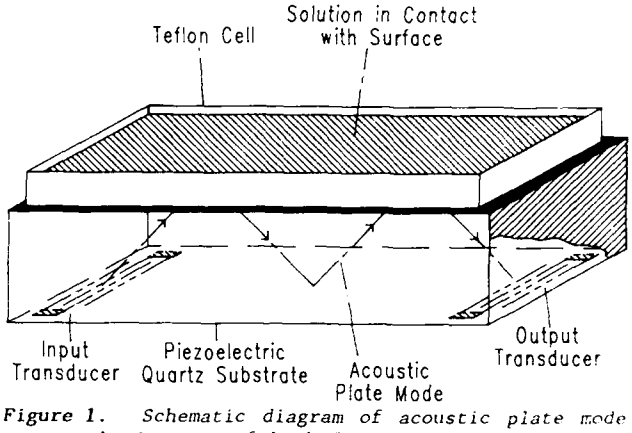

Figure 1. Schematic diagram of acoustic plate mode sensor showing use of back face of device for liquid sensing. Input and output transducers consist of 50 interdigitated electrodes on an ST-quartz substrate. The device is sensitive to the viscosity of liquids contacting the surface, solution electrical properties, and mass accumulated from solution.

Experimental Methods

Acoustic plate mode (APM) devices were designed at Sandia Labs and fabricated by Crystal Technologies, Inc., Palo Alto, CA. Devices have two interdigital transducers, each composed of fifty finger-pairs with 32 μm periodicity. Transducers are defined photolithographically from 200 nm thick Au on Cr metallization; finger length is 1.7 mm. Center-to-center separation between transducers is 7.36 mm. Devices were thinned to 0.19 mm by lapping and polishing in order to assist in the (frequency) resolution of one plate mode from the next, in addition to enhancing sensitivity to surface mass perturbations.

Thinned APM devices were mounted in a stainless-steel flatpack having a rectangular hole slightly larger than the path of the acoustic wave milled in its bottom surface. Using RTV (room temperature vulcanizing) silicone rubber, devices were sealed to the flatpack with the hole in the flatpack aligned with the wave-path on the back side of the substrate. Electrical connection was made between the transducer bonding pads and the flatpack leads by wire-bonding.

Devices were installed in a brass test case with the hole in the flatpack facing up. Electrical connections were made between the flatpack leads and impedance matching transformers located inside the brass test case. The transformers are connected to SMA jacks on the body of the case, and the jacks are connected by cable to the external circuitry. A teflon cell with internal dimensions 22 x 5.0 x 6.3 mm high (cell volume: 0.7 ml) was pressed against the side of the flatpack with the milled hole to contain solutions in contact with the back surface of the APM device.

An oscillator loop is formed by connecting the output transducer (*via* its transformer) of the APM device to the input of two cascaded wide-band amplifiers (HP 8447D); the output of the second amplifier is connected to a 158 MHz band-pass filter.

TH0215-4/88/0000-0023

The filter output is fed to two variable attenuators in series followed by a tunable phase shifter (Merrimac PSL-4-160B) and finally a 10 dB directional coupler. The main part of the signal from the coupler feeds the input transducer of the APM device, completing the loop; the coupled signal is fed to a frequency counter (HP 5384A), which is interfaced with an HP 9816 computer for data acquisition.

With sufficient external gain, the loop containing the APM device oscillates. Because the round-trip phase change in the loop must be a multiple of 2π to sustain oscillation, the phase shifter is adjusted until the frequency of oscillation matches the frequency of minimum loss for highest stability. The variable attenuators are then adjusted to give sufficient gain for stable oscillation, and several dB of excess gain are added to allow for increases in attenuation which may occur during an experiment.

Results and Discussion

The APM device, shown schematically in Figure 1, employs interdigital transducers to couple electrical energy into and out of the device substrate at radio frequencies. The transducers couple to a family of bulk acoustic waves which propagate at various angles to the surface; modes which are multiply reflected between the upper and lower crystal faces satisfy a transverse resonance condition. Multiple reflection of plate modes between the substrate faces means that the nature of the plate mode spectrum depends on substrate thickness.

We examined the APM propagating at 5050 m/s through ST-quartz; the 32 μm transducer periodicity results in an oscillation frequency of 158 MHz. Particle displacement for this mode is in the plane of the device surface, hence energy is coupled from the device to a contacting liquid *via* shear interactions. Because shear waves do not propagate efficiently through liquids, attenuation of the APM is minor.

APM devices interact with liquids and solids contacting either of the device surfaces in several ways. Viscous coupling between the wave and a liquid results in propagation loss dependent upon the viscosity and density of the contacting medium, as well as perturbations in wave velocity. Changes in the mass or mechanical properties of a thin film on the device surface perturb the wave velocity in a manner similar to that found for SAW devices. Solution electrical properties such as dielectric coefficient and conductivity affect wave propagation characteristics as well. Each of these perturbations will be discussed in turn.

Viscous Coupling [9]

To calculate the acoustic wave attenuation resulting from viscous coupling, both the velocity field in the liquid and the shear stress at the solid/liquid interface must be determined. The surface components of the APM generate a damped shear wave in the liquid which decays exponentially with distance from the surface. The decay length, a measure of the effective liquid thickness coupled to the oscillating surface of the sensor, is $\delta = \sqrt{2\eta/\rho\omega}$ where η and ρ are the liquid viscosity and density, respectively, and $\omega = 2\pi f_o = 10^9\ s^{-1}$ (f_o is the unperturbed oscillation frequency). For water, $\delta \approx 50$ nm. The loss L in signal level (in dB) at the receiving transducer liquid is given by [9]:

$$L = A\sqrt{\omega\rho\eta} \cdot F(\omega\tau) \qquad (1)$$

in which $F(\omega\tau) = \left[\dfrac{\sqrt{1+(\omega\tau)^2}+\omega\tau}{1+(\omega\tau)^2}\right]^{1/2}$ and A is a constant dependent on device configuration [9]. In many applications, the variation in viscosity is much greater than the variation in density; therefore, viscosity can be determined by measuring L. The function F, which results from modelling the liquid as a Maxwellian fluid, accounts for the effects of liquid relaxation; τ is the liquid shear relaxation time.

The shear behavior of a Maxwellian fluid becomes Newtonian (ideal) when $\omega\tau \ll 1$, in which case $F(\omega\tau) = 1$. When $\omega\tau \gg 1$, the fluid behaves as an amorphous solid with shear modulus μ, resulting in power loss saturation. Substituting the approximation $\tau = \eta/\mu$ [11] into Eq. 1 results in a saturation value for the power loss of $L_{sat} = A\sqrt{\mu\rho}$. This saturation sets an upper limit on the measurable viscosity.

To measure the viscous contribution to plate mode attenuation, the insertion loss between transducers was measured as liquids having viscosities between 0.3 and 1500 cP (centipoise) were placed in the cell. Figure 2 is a plot of the measured $L/\sqrt{\rho}$ as a function of low shear rate $\sqrt{\eta}$ values [12] for methanol, acetone, water, ethylene glycol, castor oil, and several water/glycerol mixtures. The change in propagation loss was measured at the frequency of maximum transmission near 158 MHz. Measurements were made at 23 C. Below $\eta \approx 50$ cP, $L/\sqrt{\rho}$ varies linearly with $\sqrt{\eta}$. Above 50 cP, molecular relaxation times in the liquids become longer than the wave period (6 ns) and loss begins to saturate. Complete saturation occurs by roughly 180 cP.

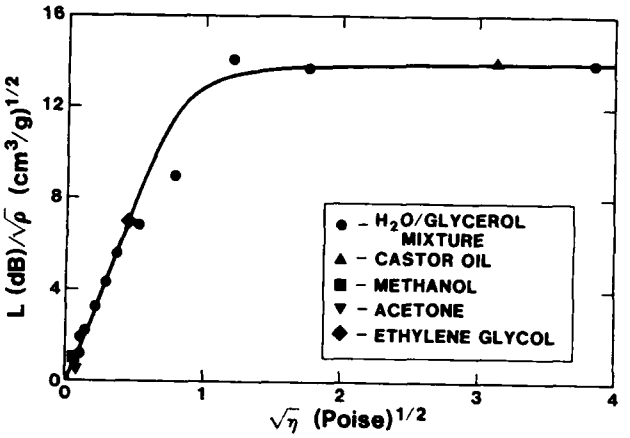

Figure 2. Relative power loss between transducers due to viscous damping of the acoustic wave. Saturation of loss occurs when the liquid relaxation time approaches the wave excitation period (6 ns). The solid line is calculated from Eq. 1.

Since the acoustic wave viscosity sensor samples a liquid thickness of approximately 50 nm, propagation loss depends critically on the nature of the solid/liquid interface. The necessity of wetting was demonstrated when one device failed to show any loss upon application of water to a dry surface. The addition of roughly 0.05% surfactant to the water resulted in the propagation loss expected for pure water.

Mass Loading [13,14]

To monitor APM wave velocity, the device of Figure 1 is utilized as the feedback element in an oscillator loop as described in the Experimental section. Perturbations in APM propagation velocity are proportional to the mass density (mass/area) of species accumulated on the surface. Fractional changes in the frequency of oscillation of the loop

are then directly proportional to the wave velocity,

$$\Delta f/f_o = \Delta v/v_o = -c_m \rho_s, \qquad (2)$$

in which v_o is the unperturbed plate mode velocity, c_m is a mass sensitivity constant, and ρ_s is the mass change per unit area deposited on (or removed from) the surface [14]. Eq. 2 holds when the wave velocity in any layer accumulating on the surface is much less than the velocity in the substrate; otherwise, changes in elastic properties influence the wave velocity as well. With the device operating at 158 MHz and the capability to resolve frequency changes of 1 Hz, fractional changes in the APM velocity are measured with parts per billion accuracy.

The electroless deposition of copper is of major commercial importance (e.g. in the fabrication of printed circuit boards) and was therefore chosen as a test process for the APM sensor. Pretreatment of the quartz substrate, necessary to catalyze the electroless deposition of copper, has been detailed elsewhere [13]. After treatment with a $SnCl_2$ solution, the substrate was exposed for 2 min to $PdCl_2$ to produce Pd nucleation sites for the Cu deposition. The response of the oscillation frequency of the APM device to the electroless deposition of Cu is shown in Figure 3. The electroless deposition solution is composed of 14 mM $CuSO_4$, 89 mM $KNaC_4H_4O_6$, 100 mM NaOH, and 0.37% HCHO. The APM deposition monitor reveals a short induction period, during which the rate of change in surface mass accelerates gradually, indicating slow initial Cu growth on the Pd nucleation sites [13]. The steady-state deposition rate is about 2.8 Å/s.

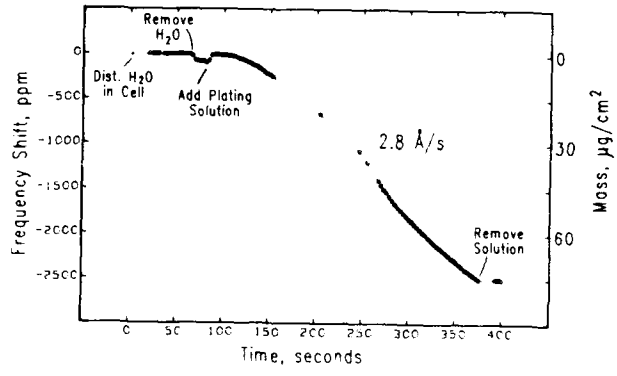

Figure 3. Frequency shift as a function of time during the electroless deposition of copper on a pretreated quartz APM device substrate. Formaldehyde reacts with Cu^{2+} to form Cu. Circles are data points, and the smooth line is drawn as a guide to the eye. Mass density is given on the right vertical axis.

The electroless deposition experiment was used to obtain a preliminary calibration of the APM device. By comparing the frequency shift with the thickness of the copper measured with a surface profilimeter (Dektak), it was found that an 800 Å-thick film of Cu electrolessly deposited on a 0.19 mm thick ST-quartz substrate resulted in a frequency shift of 2500 ppm. Assuming the Cu deposits with bulk density, the APM device has a nominal sensitivity of $c_m = 33$ cm²/g.

To obtain an additional measure of the mass sensitivity of the APM device, the APM test case and associated RF feedthroughs were adapted for use in a high vacuum system, allowing measurement of plate mode velocity shifts while vacuum depositing metal films onto the device surface. During the thermal evaporation of a silver film onto the substrate at a rate of 0.7 Å/sec, the frequency shift from the APM device was compared to the film thickness measured by a commercial (Inficon) quartz crystal microbalance (QCM); see Figure 4. Notably, the APM device shows significantly higher mass resolution than the QCM. The mass sensitivity measured was $c_m = 44$ cm²/g, in reasonable agreement with the electroless deposition results. This gives mass resolution of 0.7 ng/cm² (0.3% of a monolayer of Ag) for the 5 Hz stability of our APM system. For comparison, we estimate the minimum mass reliably measurable with the commercial QCM to be approximately 50 ng/cm².

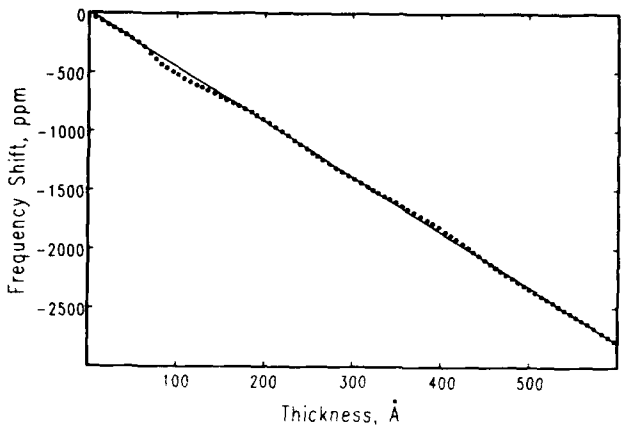

Figure 4. Frequency shift as a function of film thickness during the vacuum deposition of silver at 10^{-7} Torr.

To confirm that the sensitivity of the APM sensor is not appreciably altered by liquid contacting the device surface, we monitored the dissolution of the vacuum-evaporated silver film. Dilute nitric acid was gradually added to a cell containing water in direct contact with the silvered device surface, and the frequency shift was recorded during dissolution of the film. The measured mass sensitivity from this experiment was 40 cm²/g, within experimental uncertainty of the result obtained during the vacuum evaporation process.

Acoustoelectric Interactions [15]

APMs propagating through a piezoelectric crystal generate an evanescent RF electric field which extends into the adjacent liquid, coupling to nearby ions or dipoles (permanent or induced). This coupling causes ion and dipole motion, resulting in the storage and dissipation of electrical energy. Changes in stored electrical energy perturb the APM velocity, while dissipation leads to attenuation.

By modelling the APM device and adjacent ion-containing solution with an equivalent circuit, plate mode velocity and attenuation change can be related to solution conductivity σ and dielectric coefficient [15]:

$$\frac{\Delta v}{v_o} \simeq \frac{K^2}{2}\left(\frac{\epsilon_s + \epsilon_o}{\epsilon_s + \epsilon_\ell}\right)\frac{\sigma^2}{\sigma^2 + \omega^2(\epsilon_s + \epsilon_\ell)^2}$$

$$\frac{\alpha}{k} \simeq \frac{K^2}{2}\left(\frac{\epsilon_s + \epsilon_o}{\epsilon_s + \epsilon_\ell}\right)\frac{\omega\sigma(\epsilon_s + \epsilon_\ell)}{\sigma^2 + \omega^2(\epsilon_s + \epsilon_\ell)^2}. \qquad (3)$$

Here, K^2 is the electromechanical coupling coefficient of the substrate, α/k is attenuation per wavenumber, and ϵ_s, ϵ_ℓ, and ϵ_o are the dielectric coefficients of the substrate, the liquid, and free space, respectively.

The variation in APM propagation velocity as a function of solution conductivity is shown in Figure 5 for four solvents. Increasing the ionic conductivity from its initial value of 10^{-6} Ω^{-1}cm^{-1} initially has

little effect, but larger σ values cause rapid change in APM velocity. At higher conductivities, the electrical effect levels off. Data for KNO_3 and LiCl solutions in water are indistinguishable (Figure 5), ruling out specific ion effects. Attenuation of the APM due to ionic conductivity is too small to measure with precision using quartz APM devices.

The dielectric constant of the solvent significantly affects both the rate at which velocity changes with conductivity and the overall magnitude of the change. Lower dielectric constant solvents such as ethanol and methanol cause a more rapid velocity decrease with σ and a larger overall effect.

The solid lines in Figure 5 are velocity shifts calculated from Eq. 3 by fitting the value of K^2 and using low frequency values of the dielectric constant for each solvent [16]. The model works well for conductivities up to 0.1 $\Omega^{-1}cm^{-1}$, indicating that it reasonably accounts for both dipolar and ionic interactions. For greater values of conductivity, screening of the field from carrier redistribution should be taken into account, and salt concentrations become large enough to affect solution viscosity and dielectric coefficient.

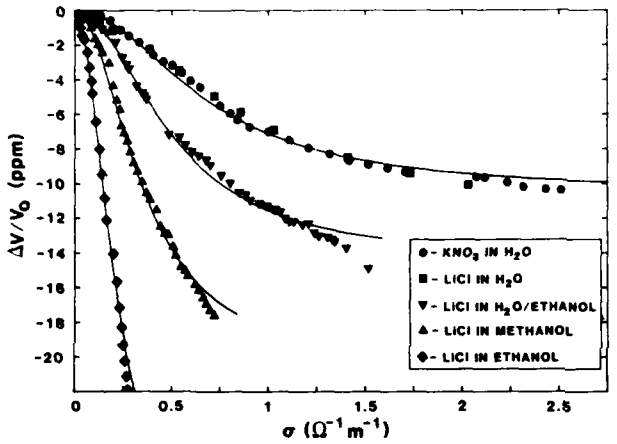

Figure 5. Perturbation in APM propagation velocity vs. ionic conductivity for ions in several different solvents (the H_2O/ethanol mixture is 44% ethanol by weight). Solid lines are velocity shifts calculated from Eq. 3.

Conclusions

Acoustic plate mode devices show considerable promise as sensors of liquid properties and solution species, and as probes of the solid/liquid interface. Their sensitivity to a variety of parameters including viscosity, dielectric coefficient, ionic conductivity, and changes in surface mass and mechanical properties will allow a variety of sensors to be constructed. At the same time, the relative magnitude of each of these effects must be considered at all times to properly interpret experimental results.

The experimentally determined mass sensitivity of the 158 MHz APM in 0.19 mm thick ST-quartz, 44 cm^2/g, is about one third of the 97 MHz SAW mass sensitivity, but nevertheless allows accurate measurement of fractional monolayer mass changes at the solid/solution interface. This work was supported by the US DOE under contract DE-AC04-76DP00789.

References

1. H. Wohltjen, "Mechanism of Operation and Design Considerations for Surface Acoustic Wave Device Vapor Sensors", Sensors and Actuators, 5, 307-25, 1984.

2. A. J. Ricco, S. J. Martin, and T. E. Zipperian, "Surface Acoustic Wave Gas Sensor Based on Film Conductivity Changes", Sensors and Actuators, 8, 319-333 (1985).

3. C. T. Chuang, R. M. White, and J. J. Bernstein, "A Thin-Membrane Surface Acoustic Wave Vapor-Sensing Device", IEEE Electron Device Lett., EDL-3, 145-48, 1982.

4. A. D'Amico, A. Palma, and E. Verona, "Surface Acoustic Wave Hydrogen Sensor", Sensors and Actuators, 3, 31-39, 1982.

5. A. Bryant, M. Poirier, G. Riley, D. L. Lee, and J. F. Vetelino, "Gas Detection using Surface Acoustic Wave Delay Lines", Sensors and Actuators, 4, 105-11, 1983.

6. A. Venema *et al.*, "Design Aspects of SAW Gas Sensors", Sensors and Actuators, 10, 47-64, 1986.

7. S. J. Martin and A. J. Ricco, "Measuring Thin Film Properties using SAW Devices: Diffusivity and Surface Area", Proc. IEEE Ultrasonics Symp., 1987, pp. 563-67.

8. H. Wohltjen and R. Dessy, "Surface Acoustic Wave Probe for Chemical Analysis. III. Thermochemical Polymer Analyzer", Anal. Chem., 51, 1470-75, 1979.

9. A. J. Ricco and S. J. Martin, "Acoustic Wave Viscosity Sensor", Appl. Phys. Lett., 50, 1474-76, 1987.

10. J. Hou and H. van de Vaart, "Mass Sensitivity of Plate Modes in Surface Acoustic Wave Devices and Their Potential as Chemical Sensors", Proc. IEEE Ultrasonics Symp., 1987, pp. 573-78.

11. A. J. Matheson, Molecular Acoustics, New York: John Wiley & Sons, 1971, pp. 82-83.

12. R. C. Weast, ed., CRC Handbook of Chemistry and Physics, 66th Edition, Boca Raton: Chemical Rubber Company Press, Inc., 1985, pp. D 221-269, F 38-42.

13. A. J. Ricco and S. J. Martin, "Acoustic Wave Electroless Deposition Monitor", Proc. 172nd Electrochem. Soc. Mtg., Vol. 87-13, 1988.

14. S. J. Martin and A. J. Ricco, "Sensing in Liquids Using Acoustic Plate Mode Devices", Proc. Int. Electron Devices Mtg., 1987, pp. 290-293.

15. S. J. Martin, T. M. Niemczyk, G. C. Frye, and A. J. Ricco, "Acoustoelectric Interactions of Plate Modes with Solutions", J. Appl. Phys., submitted for publication.

16. D. Dobos, Electrochemical Data, New York: Elsevier, 1975, p. 139; ref. 12, pp. E49-E52.

Silicon-Based Ultrasonic Lamb-Wave Multisensors

Stuart W. Wenzel and Richard M. White
Berkeley Sensor & Actuator Center, EECS Dept.,
University of California, Berkeley, CA 94720

ABSTRACT

We present initial experimental, analytical, and numerical evaluations of a new microsensor that employs ultrasonic Lamb waves propagating in a thin plate supported by a silicon die. Because it is sensitive to many measurands, the device could operate as a microphone, biosensor, chemical vapor or gas detector, scale, pressure sensor, densitometer, radiometer or thermometer. Lamb waves offer unique means for obtaining selective response, and permit sensitive operation in the low MHz frequency range in vacuum, in a gas, or while immersed in a liquid.

INTRODUCTION

The Lamb-wave sensor presented here is similar to ultrasonic oscillator sensors employing surface acoustic waves (SAWs) to measure pressure, acceleration, and chemical vapors and gases.[1,2] Major benefits over the SAW accrue from the use of Lamb waves, propagating in a plate whose thickness is small compared with the ultrasonic wavelength. Notable are the convenience of operating in the low MHz frequency range, and the possibility of operation while immersed in a liquid. Both are results of employing the low-velocity, flexural zeroth-order Lamb wave. Another benefit is the high sensitivity of the Lamb-wave device to changed mass per unit area of surface, a feature that can be employed in biological and chemical sensors. The thin plate also has a low heat capacity, and hence a rapid thermal response.

LAMB WAVE VELOCITY CHARACTERISTICS

Lamb waves are elastic waves that propagate in plates of finite thickness. These waves are divided into symmetric and antisymmetric modes to indicate the symmetry, about the median plane of the plate, of the particle displacements associated with the waves. In a plate whose thickness is much larger than the wavelength, the lowest-order symmetric and antisymmetric Lamb waves become very much like a SAW propagating on a semi-infinite medium. In very thin plates (i.e., plates whose thickness is much smaller than a wavelength) the lowest-order symmetric Lamb wave (usually labeled S_0) becomes dispersionless and its velocity becomes considerably larger than that of a SAW propagating on an identical material. In thin plates, the lowest antisymmetric mode, A_0, involves flexure and its wave velocity decreases monotonically to zero as the plate is made vanishingly thin.

Fig. 1 shows the computer-generated[3] phase velocity v_p of the S_0 and A_0 modes on a plate of silicon-nitride as a function of the plate thickness (d) normalized to the wavelength (λ). For reference we also included the SAW velocity on semi-infinite silicon-nitride (for which the thickness scale has no significance).

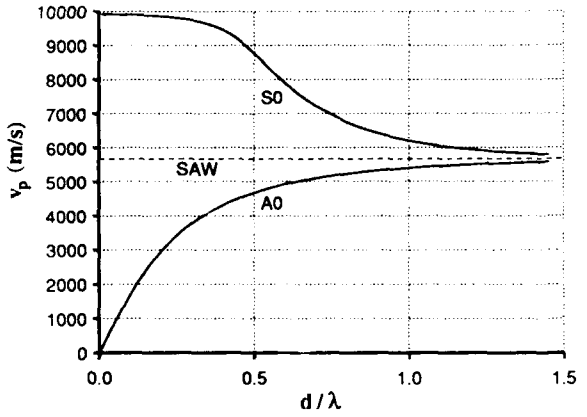

Fig. 1. Phase velocities on silicon-nitride of lowest-order symmetric (S_0) and antisymmetric (A_0) Lamb waves as a function of plate thickness normalized to wavelength. Also shown is the SAW velocity on semi-infinite nitride.

For Lamb waves propagating in thin, homogeneous, isotropic plates, the phase and group velocities of the lowest-order symmetric mode (v_{ps} and v_{gs}) and the lowest-order antisymmetric mode (v_{pa} and v_{ga}) are given by[4]

$$v_{ps} = \sqrt{\frac{E'}{\rho_p}} \qquad v_{gs} = v_{ps}, \text{ and} \tag{1}$$

$$v_{pa} = \sqrt{\omega d}\left(\frac{E'}{12\rho_p}\right)^{1/4} \qquad v_{ga} = 2v_{pa}. \tag{2}$$

Here, $E' = E/(1-\nu^2)$, E is Young's modulus, ν is Poisson's ratio, ρ_p is the plate density, and d is the plate thickness. Equations (1) and (2) were derived for plates with no external tension.

For the structures we have fabricated, tension in the plate affects the phase velocity of the A_0 flexural mode. We can include the effects of tension in solving the wave equation for an isotropic, homogeneous plate and obtain a modified expression for the phase velocity of the A_0 mode.[5] We launch waves with interdigital transducers so that the wavelength λ is known, and can take on discrete values $\lambda_n = P/n$, where P is the period of the transducers and n is an integer ($n = 1, 2, 3, \ldots$). (Note that n may be restricted to certain allowed values, obtained from spatial fourier analysis of the transducer. For example, if one uses transducers having equal finger widths and gaps between fingers, and further drives the transducers differentially with respect to a ground plane on the membrane, the voltages and displacements of adjacent fingers will be 180° out of phase. Consequently, n will be restricted to odd integers, $n = 1, 3, 5, \ldots$.) For these reasons we have found it most convenient to write this tension-modified equation for the A_0-mode phase velocity in the following form:

$$v_{pa_n} = \sqrt{\frac{1}{M}\left(T_x + \left[\frac{2\pi n}{P}\right]^2 \frac{E'}{12} d^3\right)}, \tag{3}$$

where T_x is the component of tension in the propagation direction per unit width perpendicular to this direction, and M is the mass per unit area of the membrane.

In the absence of tension ($T_x = 0$), (3) is equivalent to (2) as can be seen by substituting $\omega_n = 2\pi n v_{pa_n}/P$ for ω and $\rho_p = M/d$ in (2). For a very flexible material ($E' = 0$), (3) reduces to the phase velocity for flexural waves on an infinitely thin membrane,[6] $v_{pa_n} = \sqrt{T_x/M}$.

We can rewrite (3) in a more general form in order to apply it to composite membranes:

$$v_{pa_n} = \frac{2\pi n}{P}\sqrt{\frac{B_n}{M}}, \tag{4}$$

where

$$B_n = \left(\frac{P}{2\pi n}\right)^2 T_x + B_0 \tag{5}$$

is the effective bending stiffness of the plate including tension, and B_0 is the material stiffness contribution to this term ($B_0 = E'd^3/12$ for a homogeneous, isotropic plate).

The phase velocity of the A_0 mode also depends upon the loading effect of any fluid that contacts the membrane. (The above equations have not included these effects and are valid, strictly speaking, for operation in vacuum only). This loading is reactive (no attenuation due to radiated energy loss into the fluid) when $v_{pa_n} < v_f$ (v_f = sound velocity in the liquid), and dissipative (radiated energy and wave attenuation) for $v_{pa_n} > v_f$.[7] Using the radiation load method of Kurtze and Bolt,[8] we write equations governing the phase velocity for these two cases:

$$\frac{\alpha}{\beta}\left(\frac{\alpha^2}{\beta^4} - 1\right)\mu\sqrt{1-\beta^2} - 1 = 0 \qquad \text{for } v_{pa_n} < v_f, \text{ and} \tag{6}$$

$$\alpha^6 - \beta^4\alpha^4 + \beta^6/4\mu^2(1 - 1/\beta^2)^2 = 0 \qquad \text{for } v_{pa_n} > v_f. \tag{7}$$

In these equations,

$$\beta = v_{pa_n}/v_f \qquad \alpha = \omega_n/\omega_0 \qquad \omega_0 = v_f^{\,2}\sqrt{M/B_n} \qquad \mu = \omega_0 M/\rho_f v_f,$$

where ρ_f is the fluid density. Substituting $\omega_n = 2\pi n v_{pa_n}/P$ and rearranging, (6) becomes

$$\frac{2\pi n}{P}\left[\left[\frac{2\pi n}{P}\right]^2 \frac{B_n}{v_{pa_n}^{\,2}} - M\right]\sqrt{1 - \left(\frac{v_{pa_n}}{v_f}\right)^2} - \rho_f = 0 \qquad \text{for } v_{pa_n} < v_f, \tag{8}$$

TH0215-4/88/0000-0027 © 1988 IEEE

and (7) becomes

$$\left[\frac{2\pi n}{P}\right]^6 B_n^2 - \left[\frac{2\pi n}{P}\right]^4 M B_n v_{pa_n}^2 + \frac{\rho_f^2}{4\left[v_f^{-2} - v_{pa_n}^{-2}\right]^2} = 0 \qquad \text{for } v_{pa_n} > v_f \quad (9)$$

Therefore, the phase velocity of the A_0 mode is affected by both the density and the compressional wave velocity of the contacting fluid.

SENSOR OPERATION AND DEVICE FABRICATION

As with bulk and surface elastic waves, one may use Lamb waves for sensing by measuring the characteristics of passive delay lines, delay-line feedback oscillators, or individual transducers. The delay-line oscillator is of great interest to us because the output is a frequency which is proportional to the phase velocity, and can be measured easily on a counter to better that 1 ppm:[5]

$$f = \frac{v_p}{2\pi L}(2\pi N - \phi_E) \qquad (10)$$

Here, L is the acoustic path length, N is an integer, ϕ_E is the electronic phase shift of the amplifier, and v_p is the phase velocity of the mode being observed (e.g., v_{pa_1}, v_{pa_3} or v_{ps}). The delay-line acts as a bandpass filter to limit the integer N to one value, which is approximately equal to L/λ. For sensor operation the measurand should affect the phase velocity or transducer separation to cause a shift in oscillator frequency. Together with (10) equations (1), (4), (8) and (9) can be used to design a sensor which is sensitive to different physical quantities.

For example, using the A_0 mode, we could exploit the sensitivity to mass loading of a sorptive film on the membrane (changes in M in (4)) to make a chemical vapor sensor analogous to the SAW oscillator sensor. The A_0 mode velocity dependence on tension T_x could be used to design for sensitivity to force, acceleration or differential pressure in order to realize a scale, accelerometer, manometer or microphone. The dependence of this mode on fluid density could be used to implement a liquid densitometer or a gas pressure sensor. We considered the possible applications of this device more formally elsewhere.[5]

A typical oscillator design is shown in Fig. 2. It consists of a Lamb-wave delay line (plate and piezoelectric transducing film) and a feedback amplifier (A). The inset shows an expanded cross-sectional view of the membrane. Planning ultimately to integrate the delay line with the amplifier (and possibly more auxiliary circuitry), we formed the thin plate in a silicon wafer by depositing low-stress[9] LPCVD silicon nitride uniformly over a wafer and then etching away the silicon from beneath the nitride using ethylenediamine pyrocatechol and water. Following formation of the thin plate, we sputtered zinc oxide onto an evaporated aluminum ground plane, and then formed interdigitated transducing electrodes on top of the zinc oxide.

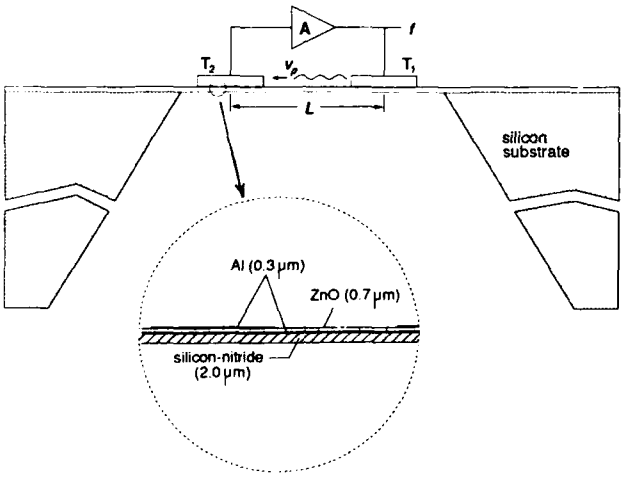

Fig. 2. Schematic cross-sectional view of experimental Lamb-wave delay-line oscillator (drawn to exaggerated vertical scale) showing transducers on the membrane and feedback amplifier. The inset shows an expanded view of the nitride membrane, aluminum ground plane, ZnO layer, and a transducer electrode.

The delay-line device on which most measurements were made consists of a $2\,\mu m$-thick silicon nitride plate, $0.3\,\mu m$-thick evaporated aluminum ground plane, $0.7\,\mu m$-thick ZnO, and $0.35\,\mu m$-thick aluminum interdigitated finger transducer electrodes. The transducers have $100\,\mu m$-period, $2.5\,mm$ apertures, 50 fingers on each of the two transducers (split finger design to reduce reflections[10]), and contact pads off the membrane. The distance between nearest edges of the transducers is $2.5\,mm$. The plate itself measures $3\,mm$ by $9\,mm$, and the ends are angled to reduce coherent end reflections.

The feedback amplifier used in the oscillator configuration of Fig. 2 consists of one or two LM733 differential video amplifiers. The device was driven untuned, and an amplifier gain of approximately 40 dB was necessary to sustain oscillation in the A_0 mode, $n = 1$. The oscillator frequency in this mode (measured directly on a frequency counter) was 4.67 MHz, and the short-term instability in still air was $\pm 1\,Hz$.

We measured the A_0-velocity of minimum insertion loss on the passive delay-line for $n = 1$, for comparison with computer results for zero tension. The measured value of v_{pa_1} is 474 m/s, compared to 422 m/s predicted with Nassar-Adler program. Using these values in (4) and (5) with $M = 11.34\times10^{-3}\,kg/m^2$ (found by summing the mass per unit area of the individual layers), the calculated tension T_x is 528 N/m. If we assume that this tension is generated by the $2\,\mu m$ nitride layer *alone*, then the tensile stress in the nitride would be $2.6\times10^8\,N/m^2$, which is reasonable for this nitride deposition process. The measured group velocity, 833 m/s, is 2% lower than the theoretical value we obtain by including tension effects, well within the experimental measurement error. Note that (2), which doesn't take tension into account, predicts that $v_{ga_1} = 2v_{pa_1} = 948\,m/s$, 14% above the measured value.

EXPERIMENTAL, ANALYTICAL AND NUMERICAL RESULTS

Fig. 3 shows the Lamb-wave oscillator sensor mounted in a test fixture that permits making coaxial connections to each set of transducing electrodes. With the device in this fixture, we performed various tests to show sensitivity to different measurands. These test results are all for the A_0 mode, $n = 1$.

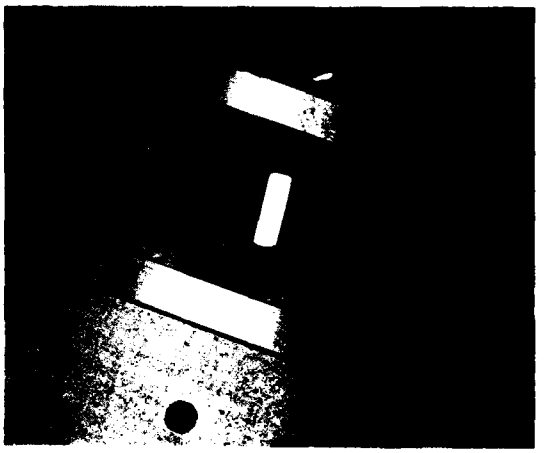

Fig. 3. View of device in test fixture, showing $3mm\times9mm$ membrane at center with the silicon-nitride layer facing upwards. Four coaxial feed-throughs connect, via gold bonding wires, the input and output interdigitated electrodes to external amplifiers.

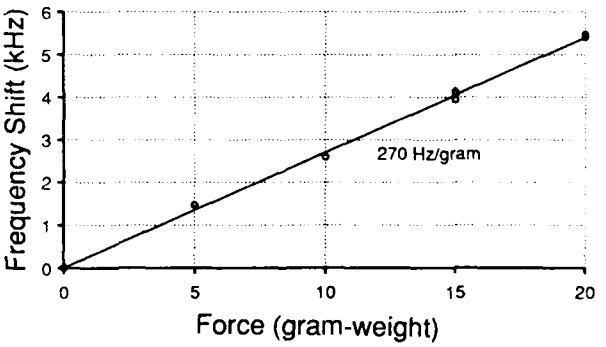

Fig. 4. Increase of membrane oscillator frequency as force is applied to the silicon surrounding the membrane at a point located approximately 3/8-inch to the left of the center of the membrane (as shown in Fig. 3).

Fig. 4 shows the upward frequency shift as a function of a force applied to the silicon die off the side of the membrane. This force causes the silicon chip to bend downward into the cavity in the fixture, increasing the tension on the membrane by increasing its length. Note the relatively linear dependence and the measured sensitivity, 270 *Hz/gram-weight*. We expect that greater sensitivity can be obtained by designing the chip and the mounting structure properly.

Loading one or both sides of the membrane with a fluid causes quite large velocity changes and oscillator frequency shifts. We loaded an operating sensor with different liquids and measured the frequency of minimum insertion loss. The results of this experiment for de-ionized water and methanol are listed and compared with expected values in Table I. The oscillator underwent similar changes in frequency when loaded with water. The frequency changes reported below are *much* larger than the transducer bandwidth, which in our device is only 2.6%. This is possible because the transducers, being located on the membrane itself, are loaded by the liquid and experience large shifts in their operating frequencies. This behavior permits these devices to have an unusually large dynamic range. We also found that contacting the membrane with water damped out modes for which $v_p > v_f$.

The theoretical values are obtained from (8) and (9). In order to solve these equations, we needed the value of B_1 for our multi-layer structure, which we solved for numerically using (9) with the known air-loaded phase velocity $v_{pa_1} = 473.7\ m/s$, and the density and sound velocity in air. This yielded $B_1 = 6.50\times10^{-7}\ Nm$, which we then used in (8) to solve for the liquid-loaded phase velocities, v_{pa_1}. As Table I shows, the agreement with theory is excellent.

Table I. A_0-mode frequency for fluid loading on one side of the composite membrane of Fig. 1. Relevant values are: Membrane: $M = 1.134\times10^{-2} kg/m^2$; $B_n = 6.50\times10^{-7}\ Nm$; $P = 100\times10^{-6}\ m$. Air: $\rho_f = 1.21\ kg/m^3$; $v_f = 343\ m/s$. De-ionized water: $\rho_f = 1\times10^3\ kg/m^3$; $v_f = 1480\ m/s$. Methanol: $\rho_f = 791\ kg/m^3$; $v_f = 1103\ m/s$. For air, the density was doubled to represent two-sided loading. From repeated measurements, we estimate standard deviations of experimental values to be $\pm 0.004\ MHz$ for air loading, and $\pm 0.008\ MHz$ for liquid loading.

Fluid	Lamb-wave frequency (*MHz*)	
	Experiment	Theory
Air	4.737	...
De-ionized water	3.035	3.043
Methanol	3.220	3.229

Equation (8) can be rearranged to show more intuitively the effects of reactive fluid loading:

$$v_{pa_n} = \frac{2\pi n}{P}\sqrt{\frac{B_n}{M + \rho_f P/2\pi n K}} \qquad (11)$$

where $K = \sqrt{1-(v_{pa_n}/v_f)^2}$. Comparing with (4), this shows that for $v_{pa_n} < v_f$ the effect of the fluid is to *mass load* the membrane by an amount equal to an evanescent skin-depth thickness ($P/2\pi nK$) of the fluid.

Fig. 5 shows the frequency shifts, calculated from (8), expected when this membrane oscillator is contacted on one side with a fluid whose density and velocity of sound vary incrementally from those of water. The separation of the curves shows that over a wide range, the device should be about twenty times more sensitive to changes of density that to changes of sound velocity.

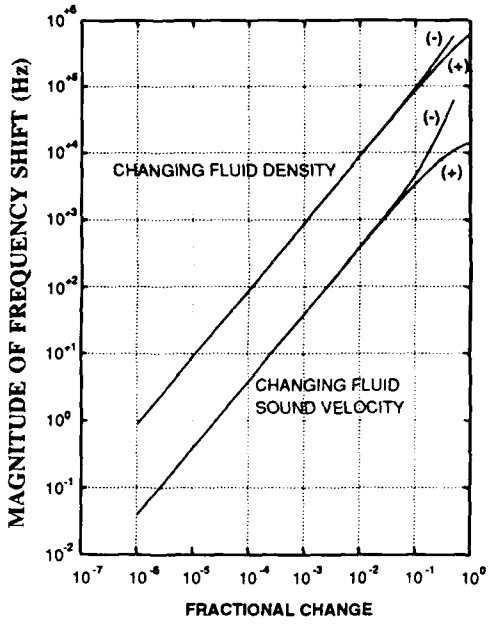

Fig. 5. Absolute values of calculated Lamb-wave oscillator frequency shifts as functions of fractional change of fluid density (with $c_0 = 1480\ m/s$) and fluid sound velocity (with $\rho = 1\times10^3\ kg/m^3$) in a fluid. Curves corresponding to an increase in ρ or c_0 are labeled (+), and those corresponding to a decrease in ρ or c_0 are labeled (-). The frequency decreases (negative shift) as ρ increases, and the frequency increases as c_0 increases.

Response to gas pressure can be realized in two ways. If the membrane is subjected to unequal pressures on its two sides, changes of membrane tension will cause an oscillator frequency change. If both sides of the membrane are subject to the same pressure, membrane tension will be constant but loading of the propagating Lamb wave will depend upon the gas density and therefore pressure.

Fig. 6 shows the oscillator response to varying *absolute* pressure of helium gas in which the sensor is immersed from a rough vacuum to 4 atmospheres. It is important to note that in this case there is *equal pressure on both sides of the membrane* and therefore the sensor can operate over a very large dynamic range without danger of breakage. The theoretical curve was calculated from (8) assuming that the response is due entirely to the density loading effect of the helium ($v_f = 984\ m/s$, $\rho_f = 0.163\ kg/m^3$ at 25°C).

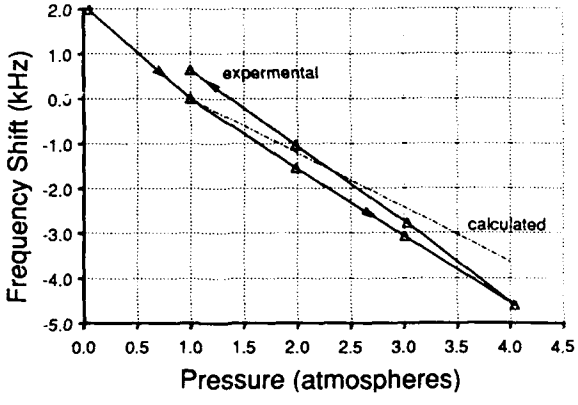

Fig. 6. Initial test of the oscillator response with the delay-line immersed in helium of varying pressure. Note that the pressure is the same on both sides of the membrane and was varied over a large range from a rough vacuum to approximately 4 atmospheres.

To simulate application of a differential pressure to the membrane, we loaded the membrane with a column of de-ionized water of variable height. As Fig. 7 shows, the variation of frequency with column height, and hence differential pressure, is linear, with a slope of 0.65 *Hz/microbar* (6.5 *Hz/Pa*). As the short-term instability of the water-loaded oscillator was about ±1 *Hz*, the minimum detectable pressure change would have been approximately 4.6 *microbars*, if we adopt the convention of taking the minimum as the level for which the signal-to-noise ratio equals three.

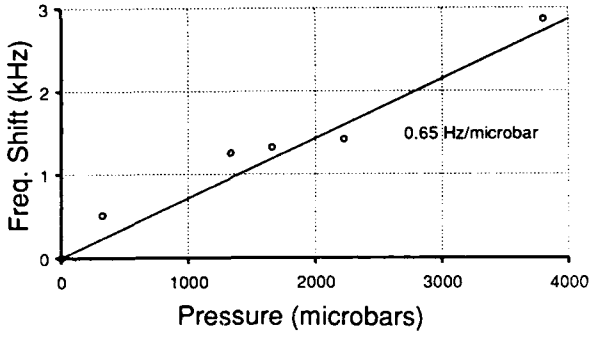

Fig. 7. Increase of membrane oscillator frequency upon application of differential pressure produced by a variable-height column of water above the membrane.

We have observed sensor response to radiation from a warm body. Fig. 8 shows the experimental frequency shift produced by allowing radiation from a nearly black body (hot plate coated with Nextel Velvet coating #101-C10 black) to be incident upon the silicon nitride membrane. The observed shift in the quiescent oscillator frequency (4.67 *MHz*, at ambient temperature, 24.5°C) is a linear function of the temperature rise of the black body above ambient over about a 30-degree range; the sensitivity is about −17 *Hz*/°C. As the black-body temperature increases further, the oscillator frequency decreases superlinearly, as Fig. 8 shows. This behavior can be understood qualitatively as resulting from a transition from a linear relationship -- valid for small temperature differences -- to a higher-power dependence valid for radiative heat transfer between surfaces at widely separated temperatures.

Because the membrane is quite thin, it equilibrates quickly. Experiments performed with a chopper between heater and sensor showed that oscillator output sidebands resulting from heater-induced frequency shifts were evident even when the radiation was chopped at 100 *Hz*.

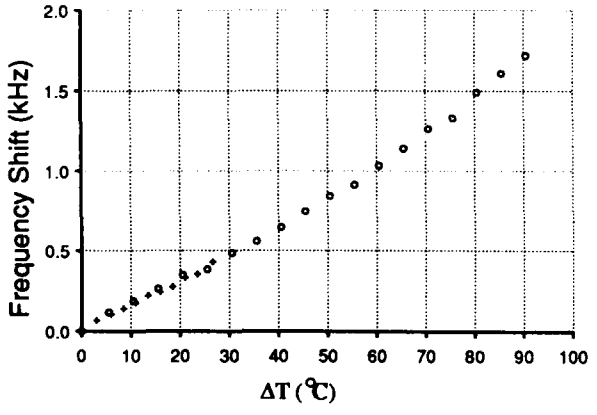

Fig. 8. Response of membrane oscillator to radiation from a nearby heated blackened plate. Ordinate: difference between plate temperature and ambient temperature (24.5°C). Abscissa: decrease of oscillator frequency from its initial value (4.67 *MHz*). Measurements were made on two different runs, the first over a 30-50°C range (+) and the second over a 30-120°C range (O).

CONCLUSIONS

We have described initial experimental, analytical, and numerical results on an ultrasonic oscillator sensor that employs Lamb waves propagating in a membrane whose thickness is a small fraction of a wavelength. We have shown that, for A_0 mode operation, this device responds to forces applied to the sensor die, differential pressure applied to the membrane, loading by a fluid on one or both its sides, and absorption of radiant energy. Analytical predictions and experimental results for liquid loading agree extremely well. Experimentally, we found that the device continues to oscillate while totally immersed; this ability, together with its calculated high sensitivity to the addition of small amounts of mass to the membrane, suggests its use for chemical and biological sensing. We also found agreement between experimental values of phase and group velocities and an analysis of the effect of intrinsic stress in the membrane, coupled with predictions obtained from a numerical analysis program.

The device is suited to use as a tool or testbed for studying certain chemical processes, such as etching of films deposited on the membrane, or exothermic or endothermic reactions in liquids that contact the sensor. Because the elastic interactions between a liquid and a low-velocity A_0 mode can be purely reactive, only an evanescent disturbance is excited in the liquid. Accordingly, it appears that only very small liquid volumes need be used.

We believe that many inexpensive, quasi-digital sensors can be based on this simple structure. Because of its sensitivity to many different measurands, for selective response it will be necessary to design the device properly for a given application, or to use one or more active and reference sensors together. It appears that information obtained from the different responses of the several propagating modes and operating wavelengths of the device can be used to obtain precise information about individual measurands.

ACKNOWLEDGEMENTS

We gratefully acknowledge contributions to this work made by Ken Hom, Leslie Field, Eun-Sok Kim and Richard Muller, and Roger Howe, all of Berkeley, together with Eric Adler of McGill University.

REFERENCES

1. See, *IEEE Transactions on Ultrasonics, Ferroelectrics and Frequency Control, Special Issue on Acoustic Sensors*, No. 2, March, 1987.
2. H. Wohltjen and R. Dessy, "Surface acoustic wave probe for chemical analysis. I. Introduction and instrument description; II. Gas chromatography detector; III. Thermomechanical polymer analyzer," *Anal. Chem.*, vol. 51, pp. 1458-1475, August, 1979.
3. A. A. Nassar and E. L. Adler, "Propagation and electromechanical coupling to plate modes in piezoelectric composite membranes," *Proc. IEEE Ultrasonics Symp.*, pp. 369-372, IEEE, Atlanta, GA, 1983.
4. I. A. Viktorov, *Rayleigh and Lamb Waves*, Plenum, New York, 1967.
5. Stuart W. Wenzel and Richard M. White, "Multisensor employing an ultrasonic Lamb-wave oscillator," *IEEE Transactions on Electon Devices, Special Issue on Microsensors and Microactuators*, June 1988 (to be published).
6. Lawrence E. Kinsler, Austin R. Frey, Alan B. Coppens, and James V. Sanders, *Fundamentals of Acoustics*, John Wiley & Sons, Inc., 1982.
7. R. D. Watkins et al., "The attenuation of Lamb waves in the presence of a fluid," *Ultrasonics*, vol. 20, pp. 257-264, November 1982.
8. G. Kurtze and R. H. Bolt, "On the interaction between plate bending waves and their radiation load," *Acustica*, vol. 9, pp. 238-242, 1959.
9. M. Sekimoto, H. Yoshihara, and T. Ohkubo, "Silicon nitride single-layer x-ray mask," *J. Vac. Sci. Technology*, vol. 21, pp. 1017-1021, Nov./Dec. 1982.
10. T. W. Bristol, "Analysis and design of surface acoustic wave transducers," *Proceedings of the IEE Specialist Seminar on Component Performance and Systems Applications of SAW Devices*, vol. 109, pp. 115-129, Aviemore, Scotland, 1973.

Theoretical Description of Gas/Film Interaction on SnO_x

Jay N. Zemel†
Department of Electrical Engineering
and
Center for Sensor Technologies
University of Pennsylvania
Philadelphia PA 19104-6390

Abstract

A simple depletion model based on the creation and destruction of Schottky oxygen vacancies near the gas-solid interface is shown to adequately account for the free carrier and mobility response of the SnO_x films reported by Chang and Hicks. Expressions for the relationship between the surface potential, bulk carrier concentration and the reducing gas concentration are derived using the standard semiconductor electrostatic surface model and first order kinetic equations for gas/solid interactions. The results obtained indicate that thin film gas sensors of the SnO_x variety behave more like a homogeneous system where free carriers dominate the response than as polycrystalline aggregates dominated by mobility variations arising from potential variations at the intergrain boundaries.

1. Introduction: Ever since the pioneering work of Seiyama et al.[1] and Taguchi[2] on SnO_2 gas sensors, there has been considerable interest in the mechanism of chemoresistance for these materials. Much of the work to date has employed fine grained calcined ceramic bodies. The mechanisms proposed to account for the behavior of these sensors has focussed on the possible roles of chemisorbed oxygen and intergrain barrier height modulation. This explanation followed the early work of Weisz[3] and Heiland[4] on other oxide materials. Recently, Chang and Hicks published data on Hall effect studies of gas sensitive SnO_x films at elevated temperatures in ordinary air both in the absence and presence of small concentrations of reducing and oxidizing gases[5]. These authors discussed their results qualitatively but did not develop formal relationships between the Hall constant and mobility, and the partial pressures of their reducing gas species, ethyl alcohol. The purpose of this paper is to consider these relationships and explore an oxygen vacancy model for interpreting these data. Such a model relies on variations in the electrical carrier concentration rather than mobility variations as the source of the gas sensitivity of SnO_x sputtered films.

A similar situation existed for photoconductivity in polycrystalline lead chalcogenide (PbS, PbSe, and PbTe) films. Slater argued that mobility variations induced by trapping of photo-injected carriers in the intergrain region induced the observed effects[6]. In SnO_x sensors, it is assumed thatchemisorbed oxygen plays the role of the trapped photo-induced carriers.The validity of the mobility model was settled when Woods demonstrated that Hall coefficient measurements did not support a mobility variation in lead sulfide[7]. He also showed that the Hall coefficient yields the average effective density of free carriers in polycrystalline films. It is for this reason that the data of Chang and Hicks are so relevant as a test of the corresponding mobility and carrier concentration models.

Almost all studies have used conductance measurements to provide insight into chemical reactions occurring both in the bulk of a single crystal and at its surface[8]. Heiland and coworkers demonstrated that the surface properties of binary compound semiconductors like ZnO and related II-VI compounds depend strongly on the kinetics of the gas-solid interactions[4]. Their studies, using Hall effect and resistivity measurements, clarified many of the fundamental aspects of the surface behavior of these materials by separating the influence of the chemical interactions on the mobility and the carrier concentration. By contrast, most recent studies of polycrystalline SnO_x films have focussed on their operational characteristics as sensors[9].

The model developed here focuses on the role of oxygen vacancies in the film grains. In that sense it differs from the generally accepted picture of oxygen interactions with a clean SnO_2 surfaces which emphasizes a chemisorptive process involving charge exchange[10]. Measurements on the the thermally programmed desorption of oxygen from poly- and micro-crystalline aggregates of SnO_2 indicate that oxygen is removed at relatively low temperatures. The low temperature desorbed oxygen is assumed to come from singly or doubly ionized chemisorbed species. There are no similar measurements on sputtered or evaporated films of SnO_x. While charge exchange-chemisorption of oxygen on SnO_x compounds is often asserted, there is no compelling evidence for this conclusion. The weight of experimental data argues that that the bulk free carriers in binary compounds such as SnO_2, or the closely related sputtered SnO_x films, arise from ionized donor impurities and/or oxygen vacancies. On the other hand, it has been suggested that surface defects and vacancies may be the determining factor in the chemiresistive behavior of binary semiconductor films, including those of SnO_x examined by Chang and Hicks[11,12]. The Chang-Hicks experimental data listed in Table I indicate that the films are strongly n-type. This behavior may arise from impurity donors and nuetral bulk oxygen Schottky defects, V_O^x. In removing the lattice oxygen, two electrons are released to the conduction band of the films.

The annealing behavior of sputtered SnO_x films has also been investigated by Demarne et al. supports the oxygen vacancy picture basic to this paper[13]. Kang et al. studied the displacement of the charge centroid in Pd-SnO_x-MIS couple at various oxygen partial pressures[14]. While a detailed analysis of this data in terms of our model has not been conducted, preliminary considerations suggest that the induced charge centroid's position would depend on the depletion layer strength and the applied electric field. The depletion layer characteristics in our model depends on the distribution of oxygen vacancies at the Pd-SnO_x interface. The decrease in oxygen vacancies at the higher oxygen partial pressures should increase the depletion layer strength and decrease the electron density that could be trapped, thereby accounting for the changes in the peak current and area under the curves.

The Schottky defect sites become negatively charged when occupied by oxygen drawn from the gas phase. If located in the surface, they will induce a surface depletion layer. A simple calculation indicates that a substantial amount of charge ($\approx 5\text{-}10\times10^{12}$ electrons/cm^2) could be withdrawn from the system by the occupation of the Schottky defects in just the first few monolayers of the film. Another way of stating this is that the pinning of the Fermi level in the surface region due to the creation of the Schottky defects would be removed. As a result, we will show that the electrostatics arising from the removal of the oxygen Schottky defects from the surface region is formally identical to a doubly charged chemisorbed *oxygen ion layer.*

2. Model: Assume that the electrical properties of the SnO_x films correspond to those of an average grain, see Figure 1. At the operational temperatures and oxygen partial pressures of the SnO_x device, the adsorbed concentration of reducing gas, H_2Pr, and its reaction products, H_2O and Pr, should be small . It is assumed that the uptake of oxygen gas follows a simple Langmuir process and that the residual oxygen Schottky defect density at the surface is so small that the space charge region is depleted.

The chemical reactions assumed to take place are illustrated in Figure 2. The procedure followed in measurements on SnO_x films is to use the "pure" air ambient gas environment as the reference state for the measurements. Chang and Hicks found that their films had a strong n type bulk conductivity and that a reducing gas increased the Hall carrier density substantially but had a fairly weak effect on the measured Hall mobility as indicated in Table 1. Since the "air" case is the reference state for these films, reducing gases are assumed to remove ionized lattice oxygen and inject electrons into the surface space charge region.

If the surface oxygen Schottky defect concentration/cm^2 is $[V_{O_s}^x]$ and the maximum number of oxygen surface sites is N_o, then the concentration of ionized oxygen sites on or at the surface is N_o-$[V_{O_s}^x]$. At flat band where $[V_{O_s}^x] = [V_O^x]$, the ionized oxygen site density will be N_o- $[V_O^x]$. The difference in the number of ionized oxygen surface sites, $[\Delta O_s^=]$, will be

TH0215-4/88/0000-0031 © 1988 IEEE

$$N_o - [V_O^x] - \{ N_o - [V_{O_s}^x] \} = [V_{O_s}^x] - [V_O^x] = -[\Delta O_s^{=}] \qquad 1)$$

This deficiency changes in the electrical properties of the SnO_x film. and $[\Delta O_s^{=}]$ can be written as a negative surface charge, ΔQ_s, in the form

$$\Delta Q_S = -2q[\Delta O_s^{=}] \qquad 2)$$

The effective carrier concentration of free carriers in a crystallite, n_{eff}, is then

$$n_{eff} = n^{\circ}_D - \frac{\alpha \Delta Q_s}{qW} \qquad 3)$$

where n°_D is the bulk carrier concentration and $\frac{\alpha}{W}$ is the ratio of surface area to bulk volume.

The reactions indicated in Figure 2 can now be used to derive the equilibrium relationships between the chemistry at the interface of the SnO_x and the electrical properties of the films.The simultaneous production of a surface oxygen atom and a Schottky defect is not included in this equation since this is likely to be much slower than the rate processes associated with the adsorption-desorption process of oxygen from the gas phase, even including the oxygen dissociation rates.

The adsorbed oxygen on the surface of the SnO_x, $[O_s]$, is assumed to be nuetral and is related to the oxygen partial pressure, $P_{O_2}^{(o)}$, by

$$[O_s] = \frac{k_1 N_o \sqrt{P_{O_2}^{(o)}}}{1 + k_1 N_o \sqrt{P_{O_2}^{(o)}}} \qquad 4)$$

The excess electronic surface charge density removed from the surface space charge region, i.e. measured with respect to flat band, is $[\Delta e_{sc}^{-(o)}]$. At flat band, $[\Delta O_s^{=(o)}]$ is zero and the surface oxygen concentration, $[O_s]$, will be negligible. The bulk electron density can be written as

$$n^{\circ}_D = (N_o - [V_O^x])\sqrt{N_o} \qquad 5)$$

Let $[\Delta e_{sc}^{-}]$ be the concentration of electrons injected into the space charge relative to an ambient air condition, $[H_2Pr_s]$ is the surface concentration of the reducing gas; $[Pr_s]$ is the surface concentration of the reaction product; and $[H_2O_s]$ is the surface concentration of water. From its definition,

$$[\Delta e_{sc}^{-}] = [\Delta O_s^{=(o)}] - [\Delta O_s^{=}] \qquad 6)$$

In the absence of reducing gases, Equation 5 yields

$$[\Delta O_s^{=(o)}][\Delta e_{sc}^{-(o)}]^2 = k_2[O_s] \qquad 7)$$

Because of the strong depletion in the space charge region, it is reasonable to assume that $2[\Delta e_{sc}^{-(o)}]$ will exactly equal $[\Delta O_s^{=}]$, which is another form of Equation 1. It can then be shown that

$$\Delta Q_S = q\left(\frac{N_o(\frac{4k_4k_2}{k_3k_1})\sqrt{P_{O_2}^{(o)}}}{1 + (\frac{k_1}{k_2N_o}\sqrt{P_{O_2}^{(o)}})} \right)^{\frac{1}{3}} \qquad 8)$$

2.1Reducing Gases Present in the Steady State: When reducing gases are present, surface lattice oxygen will be removed. It is straightforward to show that

$$\Delta Q_{(s)} \approx \Delta Q_{(s)}^{(o)} - 4q\sqrt{K\frac{P_{H_2Pr}}{P_{H_2O}P_{Pr}}} \qquad 9)$$

where it is assumed that $[H_2Pr_S]$, $[Pr_S]$, and $[H_2O_S]$ are linear functions of P_{H_2Pr}, P_{Pr} and P_{H_2O}, respectively, and K is a temperature dependent parameter. It is assumed that the partial pressure of oxygen is high enough to allow the surface of the SnO_x to be essentially oxygen saturated. These then are the basic equations for this analysis.

In the usual experimental configuration, the partial pressures of the reaction products is kept at a low level as a result of the flow of the gas over the sensor material. Assume that the concentrations of Pr and water vapor will not vary significantly as the reducing gas is varied. While the concentration of Pr in the ambient gas is essentially nill, there will always be a concentration within a diffusion length of the surface as a result of the reactions described in Figure 2. The square root dependence of the water vapor pressure in Equation 9) "squeezes" the response curves together at higher moisture pressures.

3. Carrier Concentration: The depletion of free carriers in the film is governed by the density of oxygen Schottky defects in the surface region. According to Equations 1) and 2), a reasonable first order approximation to the system response arises from the standard surface depletion model. The depletion layer chargemay be written as

$$\Delta Q_S = en^{\circ}_D L_{Depl} \qquad 10)$$

where L_{Depl} is the width of the depletion layer related to the surface band bending (see Figure 1b) by

$$L_{Depl}(T) = L_D(T)\sqrt{2(u_S(T) - 1)} \qquad 11)$$

The electrostatics on which these relations are based do not really apply here. Nevertheless, it is a simple way of getting estimates for the potential barrier height.

The effective carrier concentration for the average crystallite becomes

$$n_{eff}(T) = en^{\circ}_D\left(1 - \frac{\alpha L_{Depl}(T)}{W}\right) \qquad 12)$$

Since $n_{eff}(T)$ is obtained from the Hall data at different temperatures, and ΔQ_S is related to the concentration of reducing gases, en°_D and one other constant may be obtained from the data. Using Equations 3 and 9

$$n_{eff} = en^{\circ}_D - \frac{\alpha}{W}\Delta Q_S^{(o)} + \frac{4q\alpha}{W}\sqrt{K\frac{P_{H_2Pr}}{P_{H_2O}P_{Pr}}} \qquad 13)$$

The first two terms on the rhs of the above equation are the effective carrier concentration in the absence of a reducing gas partial pressure, i.e. the Hall carrier concentration in air.

$$n_{eff}^{(o)} = n_D^{\circ} - \frac{\alpha}{W}\Delta Q_S^{(o)} \qquad 14)$$

Using the following shorthand notation for Equation 13),

$$a(T) = \frac{4q\alpha}{W}\sqrt{\frac{K(T)}{P_{H_2O}P_{Pr}}},\ x = P_{H_2Pr},\ y_o = n^{(o)}_{eff},\ y = n_{eff}$$

then

$$y = y_o + a\sqrt{x} \qquad 15)$$

where x is measured in 10^3 ppm. In Table 1, the experimental data of Chang and Hicks for oxidizing and reducing ambient gas atmospheres are presented. The data in column (1) and (6) are for the device in air at two different temperatures, 167°C (440 K) and 230°C (503 K), respectively. The Hall carrier concentration, n_H, is initially defined to be equal to y_o. From Equation 15, the theoretical carrier concentrations corresponding to the reducing gas under ideal conditions, listed in columns 2 and 3, are

$y_o = y_o$ (column 1)
$y_1 = y_o + a$ (column 2)
$y_2 = y_o + \sqrt{2}a$ (column 3)

Let $\Delta y_i = y_i - y_o$ and $R_{ij} = \frac{\Delta y_i}{\Delta y_j}$. The theoretical value of $(R_{21})^2$ is 2 while the value obtained from the experimental data in columns 2 and 3 is 1.6. The discrepancy between the experimental and theoretical values suggests that the value of y_o is too large. It was pointed out by Chang and Hicks that a reducing gas was emitted from their sample holder which biased their results. If it is that is the case, there will be a residual term, δ, such that

$$y = y_o + a\sqrt{x+\delta} \qquad 16)$$

which then leads to the values listed in columns 6-8. Redefining $\Delta y_i = y_i - y_{air}$,

$$\delta = \frac{(2 - R_{21}^2)^2}{4R_{21}(2-R_{21})(R_{21} - 1)} \qquad 17)$$

δ, obtained from Equation 29 with the aid of observations conducted at the three different reducing gas pressures, range from 170 ppm equivalents of $H_2C_2H_3OH$ at 167°C to 270 ppm at 230°C with a probable error of ±50%. This error corresponds to an uncertainty in R_{21} of about 3%. For all intents and purposes, the partial pressure of the pyrolyzed gas vapor is constant over this temperature range. a(T) can be calculated from the various carrier concentrations and is found to be

$a(167°C) = (2.4\pm1.2)\times10^{18}/cm^3$
$a(230°C) = (6.1\pm3.0)\times10^{18}/cm^3$

Knowing what a(T) and δ are, $y_o(T)$ may be calculated from the measured values of $y_{air}(T)$.

$y_o(167°C) = (2.6\pm0.8)\times10^{18}/cm^3$
$y_o(230°C) = (7\pm2)\times10^{18}/cm^3$

These two values represent the effective carrier concentration in air in the absence of a reducing gas.

While the oxygen partial pressure of air is quite high, there is no *a priori* reason that the surface concentration of oxygen vacancy defects must be equal to the bulk vacancy density in the absence of a reducing gas. This will depend on the bulk diffusion coefficients of the oxygen vacancies. Furthermore, the quantity n^+_D may be limited by the donor impurities rather than the oxygen vacancies. As a result, there still may be a depletion layer at the surface of the average crystallite even in the absence of an observable concentration of reducing gas. If a very strongly oxidizing environment is created, e.g. by exposing the films to NO_x gas, the oxygen vacancies would be maximally suppressed and the bulk density of donor impurities would then be observable. If the values for the $y_o(T)$ are compared against the corresponding values in columns 5 and 10, two things are noted. First, the agreement between $y_o(167°C)$ and the value of n_H in column 5 is striking. The carrier concentration in column 5 corresponding to the strongest oxidation regime, i.e. the highest NO_x concentration for T = 167°C. While this is gratifying, the agreement between $y_o(230°C)$ and n_H in column 10 is poor. It is interesting that the carrier densities in columns 5 and 10 for both temperatures are empirically identical. In this strong oxidizing environment, the reduction in vacancy concentration may have allow the donor impurities to dominate the free carrier behavior at both temperatures. It is reasonable to expect that in the 230°C reducing atmosphere environment, the concentration of oxygen vacancies would be substantially greater than at lower temperatures and a larger value of y_o would result . A more systematic and rigorous set of the annealing experiments are needed to establish the vacancy behavior of the SnO_x films in a quantitative fashion

In any event, it is difficult to see how oxygen ion chemsorption models can adequately explain the extremely high densities of electrons in the presence of such a small density of H_2Pr and such a small density of electrons for an even smaller density of strong oxidant. Both results point toward a bulk-like process as the origin of these effects.

4. Mobility Models: The bulk carrier density cannot be less than the values given in columns 3 and 8. From y_o, the maximum height of the depletion layer barrier can be estimated from Equation 11. Assuming a cubic geometry for the crystallites, i.e., $\alpha = 6$ and that W lies in the 10-100nm range given by Chang and Hicks, The magnitude of the Schottky barrier can now be estimated.The extrinsic Debye length, L_D, defined by

$$L_D = \sqrt{\frac{\varepsilon\varepsilon_o K_B T}{q^2 n^+_D}} \qquad 18)$$

may be calculated using the vakues listed in Table 2. The barrier heights in air are found to range from 6.7 KT to 67 KT. Even a 6.7 KT barrier height is much larger than is permissible based on the observed mobility variations and

$$\mu_H = \mu^{(o)}_H e^{-u^{(o)}_s} \qquad 19)$$

The ratio of the Hall mobilities for $u_s(T) = 6.7\ K_BT$ would change by at least a factor of 800. However, the data in Table 1 shows that the largest ratio is only of the order of 3-4. We conclude that the intergrain-modulated mobility model does not account for the gas sensitivity of sputtered films of SnO_x.

Such mobility variation model as does occur can be more readily accounted for by the structure of the films themselves. The crystallite of the film are initially extremely small, have a high density of defects and the average size of the crystallites increase with increasing thickness. Since the estimated widths of the depletion region is of the order of 16-20nm, a distance that is 20% of the total thickness of the film, the zone at the surface with the largest crystallites is likely to have the highest mobility, i.e. depletion will confine the carriers to the lower mobility portion of the film at the substrate-film interface.

5. Conclusions: The significance of these theoretical results is that they point toward a carrier concentration modulation model for the sensitivity of thin film SnO_x gas sensors variety, i.e. mobility variations arising from potential variations at the intergrain boundaries do not play as strong a role in these films as they appear to play in the sintered bulk sensor materials. It is emphasized that the conclusions drawn here refer to sputtered films of rather uncertain composition and do not refer to the more clearly defined sintered materials that are more likely to be closer to pure SnO_2.

It also demonstrates that the type of measurements conducted by Chang and Hicks are essential for further development of both the devices and the physio-chemistry of these materials. More theoretical and experimental work on these films is needed, especially at higher temperatures. By combining galvanomagnetic measurements on SnO_x films that are better defined structurally in well characterized oxidizing and reducing gas atmospheres with more traditional surface analysis methods, it should be possible to obtain a better understanding of the mechanism of gas sensitivity in these materials.

6. Acknowledgements: The author would like to acknowledge the hospitality and support of the University of Neuchatel's Institute de Microtechnique and the FRSM during the period when this work was conducted. He would especially like to thank Dr. S. C. Chang

for reviewing the manuscript, Professor S. Roy Morrison for a valuable critique of the assumptions and both Professor N. deRooij and Dr. M. Ducloux for useful discussions.

† This work was performed while the author was a Visiting Professor at the University of Neuchatel's Institute de Microtechnique, Neuchatel, Switzerland

[1] T. Seiyama, A. Kato, K. Fujiiishi and M. Nagatani, Anal. Chem. **34**, 1502, (1962)

[2] N. Taguchi, Japan Patent 45-38200 (1962)

[3] P. B. Weisz, J. Chem. Phys., **20**, 1483, (1952), **21**, 1531, (1953)

[4] G. Heiland, Sensors and Actuators, **2**, 343, (1982). This review has extensive references to the earlier literature.

[5] S. C. Chang and D. B. Hicks, in "Fundamentals and Applications of Chemical Sensors", D. Schuetzle and R. Hammerle, Eds. American Chemical Society. Washington DC, 1986, p. 58

[6] J. C. Slater, Phys. Rev., **103**, 1631, (1956)

[7] J. F. Woods, Phys. Rev., **106**, 235, (1957)

[8] The most complete treatment of the relationship between the electrical and chemical properties of binary compounds is presented by F. A. Kroger in his well known monograph, "The Chemistry of Imperfect Crystals (3 Vols.), North Holland Publishing Co., Amsterdam, (1974)

[9] A number of papers may be found in the Technical Digest, 4th Int. Conf. on Sol. St. Sens. and Act. (Tokyo, IEE of Japan, 1987), Session A-9.

[10] M. Egashira, M. Nakashima and S. Kawasumi, in "Fundamentals and Applications of Chemical Sensors", D. Schuetzle and R. Hammerle, Eds. American Chemical Society, Washington DC, 1986, p. 71. Other references are given in this paper.

[11] M. Green, Sensors and Actuators, **1**, 379, (1981)

[12] J. N. Zemel in "Surface Physics of Phosphors and Semiconductors" edited by C. G. Scott and C. E. Reed, (Academic Press, New York, 1975) and specifically Figure 8.23 and related discussion on page 558.

[13] V. Demarne, A. Grisel and R. Sanjines,Technical Digest, 4th Int. Conf. on Sol. St. Sens. and Act. (Tokyo, IEE of Japan, 1987), p. 605

[14] W. P. Kang, J. F. Xu, B. Lalevic and T. L. Poteat, Technical Digest, 4th Int. Conf. on Sol. St. Sens. and Act. (Tokyo, IEE of Japan, 1987), p.610

Table I

T = 167°C

Ambient Gaseous Atmosphere	Air alone (1)	10^3ppm H_2Pr in Air (2)	$2x10^3$pp m H_2Pr in Air (3)	50ppm NO_x in Air (4)	100ppm NO_x in Air (5)
$n_H(10^{18}/cm^3)$	3.6	7.2	8.15	3.54	2.5
$\mu_H(cm^2/Vsec)$	3.14	4.9	5.5	2.0	1.54
Δy_i(exp)	N.A.	3.6	4.55	-.0.06	-1.1
Δy_i(theor,0)	0	a	$a\sqrt{2}$	N.A.	N.A.
Δy_i(theor,1)	$a\delta^O$	$a\sqrt{1+\delta}$	$a\sqrt{2+\delta}$	N.A.	N.A.

T = 230°C

Ambient Gaseous Atmosphere	Air Alone (6)	10^3ppm $H_2C_2H_3O$ in Air (7)	$2x10^3$pp m H_2Pr in Air (8)	50 ppm NO_x in Air (9)	100 ppm NO_x in Air (10)
$n_H(10^{18}/cm^3)$	10	20	22.3	2.4	1.25
$\mu_H(cm^2/Vsec)$	5.43	7	7.2	3	2.8
Δy_i(exp)	N.A.	10	12.3	-7.6	-8.75
Δy_i(theor,0)	0	a	$a\sqrt{2}$	N.A.	N.A.
Δy_i(theor,1)	$a\delta^O$	$a\sqrt{1+\delta}$	$a\sqrt{2+\delta}$	N.A.	N.A.

Table 2

Temperature; T	167°C (440 K)	230°C (503 K)
Bulk Concentration; n_b)*	$8.2x10^{18}/cm^3$	$24x10^{18}/cm^3$
Dielectric Constant; ε	12	12

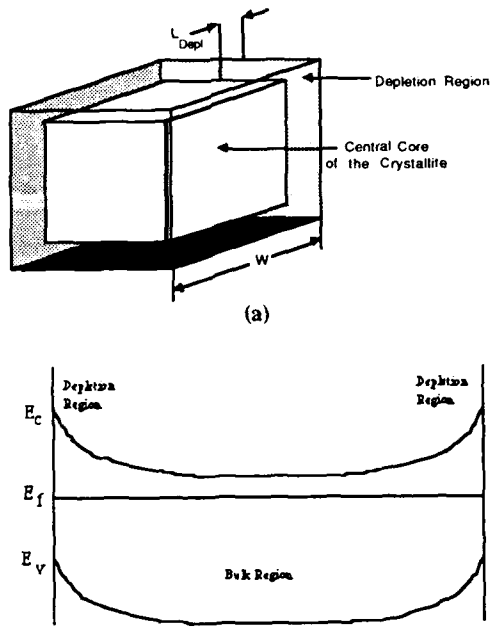

Figure 1: a) Schematic drawing of an average crystallite in the SnO_x film. It is assumed that all six sides of the cubic grain are accessible to oxygen coverage by diffusion. The surface to volume ratio in this case is 6/W. b) Band structure diagram showing the depletion layer, width = L_{Depl}, Fermi level, E_{fermi}, conduction band, E_C, and valence band, E_V. The width of the crystallite is W as in Figure 1a).

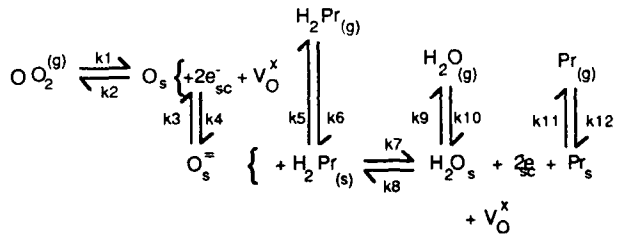

Figure 2: *Kinetic reactions governing the uptake of oxidizing and reducing gases at the surface of SnO_x films. The sub- or superscript, (g) refers to the gas phase, (s) to the external surface phase, sc to the space charge region, and (-) and (=) to singly and doubly negative charged species.*

A MONOLITHIC SILICON ACCELEROMETER WITH INTEGRAL AIR DAMPING AND OVERRANGE PROTECTION

Phillip W. Barth, Ph.D., Farzad Pourahmadi, Ph.D.
Robert Mayer, John Poydock, Kurt Petersen, Ph.D.

NovaSensor
1055 Mission Court
Fremont, CA 94539
415-490-9100

Abstract

Novel piezoresistive silicon accelerometers for full-scale accelerations on the order of 0.5G-100G have been designed, fabricated, and tested. These dual-beam cantilever devices incorporate silicon structures introduced at the wafer level for air damping and bi-directional overrange protection, resulting in a silicon/glass chip approximately 3.4 mm square and 1.5 mm thick, suitable for packaging in many configurations and for use in many applications. Critical damping and over-damping have been demonstrated with roll-off frequencies 500 Hz and above, and shock survival above 1000 G in all axes has been achieved. Cross-axis sensitivity is less than 2% for any axis. Device design was accomplished using finite element modelling (FEM) to assess sensitivity, temperature coefficients, resonance modes, cross-axis sensitivity, and overrange characteristics. Analytical modelling was used to "benchmark" the FEM predictions for simplest cases, and experimental results are in good agreement with FEM.

Introduction

Several market forces have pushed the development of low-cost batch-fabricated accelerometers over the past few years. Primary among these are automotive needs for crash sensors (for air bag deployment) and ride motion sensors (for active suspension components). Additional markets include military components (e.g., smart weapons) and aviation (e.g., rate-of-climb indicators). Accelerometer development efforts have pushed for medium performance (less than required for inertial navigation or gravitometers), reproducible characteristics, and low cost.

The primary obstacle to the development of such sensors has been the fragility of the fabricated devices: adequate sensitivity for low accelerations (0.5-1 G) has historically resulted in easy breakage of the sensor during and after fabrication. This breakage problem drives yield down and price up. The problem has been avoided in the accelerometer reported here by the introduction of mechanical overrange stops, batch-fabricated at the wafer level, into the silicon chip structure.

Overload Protection Considerations

Piezoresistive accelerometers generally place strain-sensing resistors at points of maximum stress on a bending beam attached to a "seismic mass," i.e. a mass which moves in relation to a supporting substrate under the influence of acceleration. While many beam arrangements are possible, most designs have used either a cantilever (in which the seismic mass is suspended along one edge)(e.g., [1]) or a doubly-fixed-beam (DFB) in which the mass is suspended from points along two opposing edges (e.g.[2]).

For a given seismic mass, and for a given width and thickness of the suspending beam, a cantilever displays at least eight times the sensitivity (beam stress per G) as a design with a doubly-fixed beam. This advantage offers the potential for low chip cost because a cantilever design of a given sensitivity can be fabricated in a smaller area.

However, basic cantilever designs are also less resistant to shock than DFB designs. Under overload accelerations a cantilever design continues to bend in the same way that it bends under normal accelerations. In this bending mode, stress is concentrated along one surface of the cantilever beam, and eventually the beam breaks (at a surface tensile stress of approximately 150,000 PSI). In contrast, a doubly-clamped design under overload can go into linear tension as well as bending stress, distributing the overload through the thickness of the beam, and so can support a greater overload than a cantilever design of equal sensitivity.

Cantilever designs thus require some additional overrange protection features if they are to compete with DFB designs and retain advantages in terms of small size. While such protection has been added during packaging in some previous designs [3-5], no previous accelerometer has been able to incorporate overrange stops directly into the sensor at the wafer level, before fabrication of the cantilever beams. The chip reported here contains such protection as illustrated in Figure 1.

The novel overrange protection in this chip is provided by a series of interdigitated tabs which extend over underlying shelves. A tab on the frame next to the seismic mass, and extending over a shelf on the seismic mass, prevents the mass from moving upward past a preset limit. Similarly, a tab on the seismic mass extending over a shelf on the supporting frame prevents the mass from moving downward past a preset limit. The tabs themselves are thin enough to be somewhat flexible, so that they don't shatter when they hit the stopping shelf.

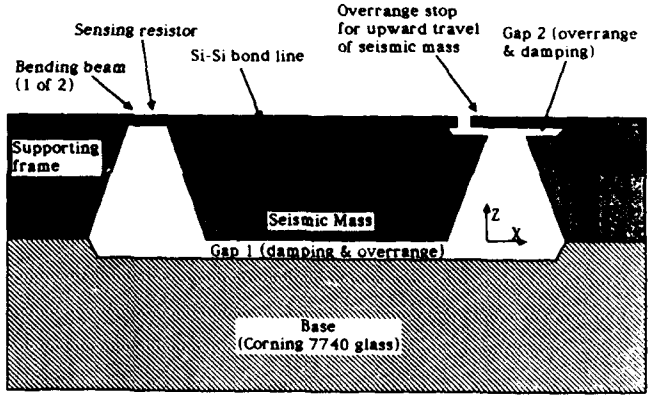

Figure 1. Schematic cross-section of dual-beam cantilever accelerometer.

TH0215-4/88/0000-0035

Overrange protection exists in all three axes. In the z-axis (perpendicular to the chip surface) protection is provided by the interlocking tabs described above.

In the x-axis (in the plane of the chip and parallel to the length of the beams), protection is provided by the strength of the beams themselves in linear tension and compression. The cross-sectional area of such beams is greater than it would be for a DFB design of equal sensitivity, so that overrange protection in the x-direction is greater.

In the y-axis (in the plane of the chip and perpendicular to the length of the beams), protection is provided by the great width of the cantilever beams in relation to their thickness, plus the wide separation of the beams, both of which provide great strength and stiffness in this direction (again greater than for a DFB design).

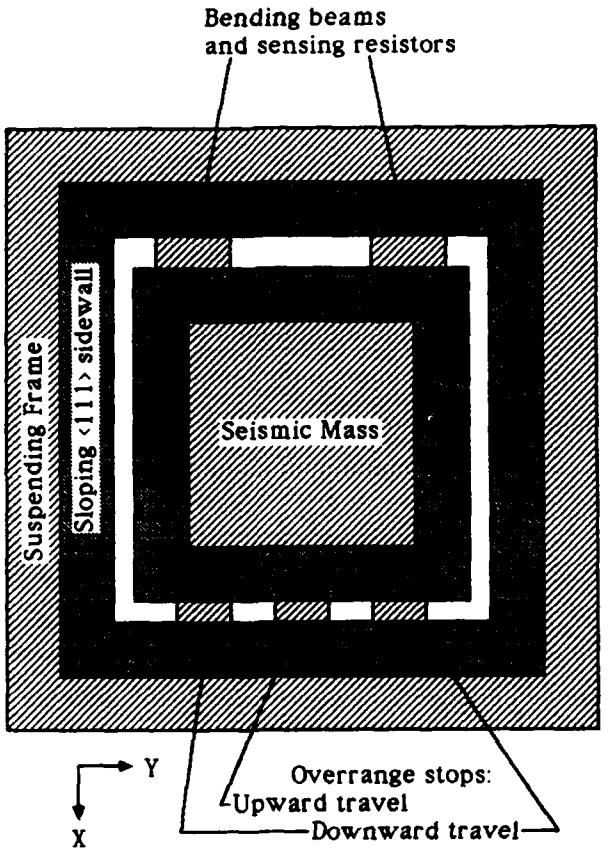

Figure 2. Schematic plan view of dual-beam cantilever accelerometer, viewed from the bottom.

Damping Considerations

All accelerometer designs include compromises among sensitivity, resonant frequency, and damping of undesirable resonances. Increased sensitivity generally results in lowered resonant frequency, and the lowest resonance limits the available measurement bandwidth. The sensitivity-bandwidth tradeoff is basic to any design (including the present design) in which the sensing element is placed directly on the bending beam, and can be avoided to some extent only by structures which remove the sensing element from the plane of the bending beam (e.g., [4,5]). The sensor reported here uses a fully active Wheatstone bridge to achieve the highest resonant frequency and highest sensitivity simultaneously possible.

Undamped accelerometers suffer serious measurement problems from oscillations occurring at resonance. (Undamped buildup of these oscillations can also lead to destruction of the device if no overrange protection is present.) To avoid measurement errors the oscillation must be damped to some extent; ideally, critical damping is preferred, which avoids oscillation while preserving signal amplitude to a frequency near the cutoff (-3dB) frequency, and results in a well-characterized phase lag at frequencies near cutoff.

Both liquid damping and gas damping are possible. Liquid damping suffers from several problems: reduction of sensitivity due to density of the liquid (which tends to buoy the seismic mass), viscosity variation with temperature, and costs associated with both the liquid material and the liquid filling procedure. Gas damping, in contrast, has minimal problems related to density and viscosity, and if the gas is air at atmospheric pressure it costs nothing. Air damping is thus the method of choice if it can be efficiently designed into the sensor structure.

The present sensor design achieves air damping by using controlled gaps in the chip structure (Figure 1). Beneath the seismic mass, Gap 1 between glass and silicon constitutes one air-damping area. Gap 2 between the overrange protection elements constitutes another such area. Gaps 1 and 2 can be set independently, as can the areas bounded by those gaps. The result is great freedom in designing the air-damping characteristics for the chip. For low-G-range devices the gaps can be fairly wide and can occupy minimal areas, while for high-G-range chips the gaps can be narrower and can occupy larger areas. Of course, there are also engineering tradeoffs involved between the overrange protection and the damping provided by the gap regions.

Chip Design Process

The design process for the cantilever accelerometer was set up to ensure maximum success of the first fabricated silicon and minimum effort devoted to redesign. Initial analytical models based on [1] were developed to rough out chip dimensions for the desired sensitivity ranges. Next, finite element models were developed and compared to the analytical models for simple cases. Then the finite element models (FEM) were used to predict quantities such as torsional resonances and cross-axis sensitivity which are difficult or impossible to model analytically. Finally, the FEM results were used as inputs to the mask design and the fabrication process design.

The ANSYS program from Swanson Associates was used for the FEM effort. Running on a MicroVAXII computer, this program predicted stress patterns on the cantilever beams (aiding in resistor placement), sensitivity (stress versus acceleration), first resonant frequency, higher order resonances (including off-axis resonances and torsional resonances), and overrange protection. Typical output plots from the analysis are shown in Figures 3 and 4. Figure 3 displays the fundamental bending mode of the chip at a resonant frequency of 839 Hz. Figure 4 displays the second resonance of the structure, a torsional mode at 68,575 Hz. The modelling makes it obvious that only the fundamental mode falls anywhere near the measurement bandwidth; the higher-order modes modes present no perceptible problems.

Fabrication

The fabrication process is designed for high yield and volume production at low cost. It incorporates NovaSensor's standard techniques of silicon fusion bonding [6], plasma etching, and programmed etch stopping. Batch processing techniques are used throughout, up to the point where devices are placed into individual packages.

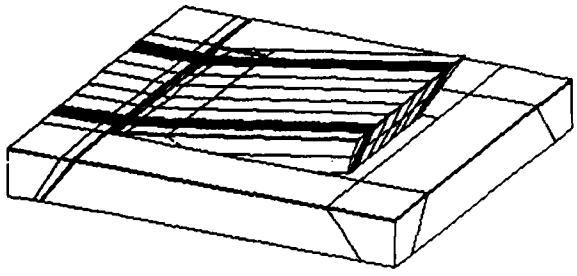

Figure 3. Finite element modelling results showing fundamental (bending) mode at 839 Hz.

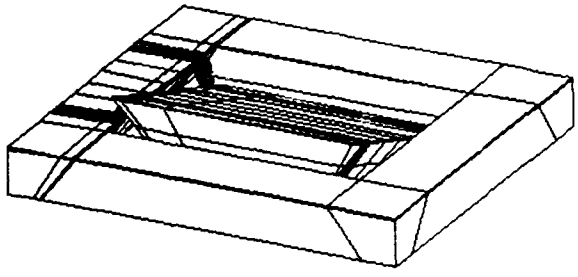

Figure 4. Finite element modelling results showing second (torsional) mode at 68,575 Hz.

The use of silicon fusion bonding permits great freedom in the fabrication process. For example, the cross section of Figure 1 illustrates a cavity (Gap 2) beneath the overrange stop tab; this cavity can be created by etching before two silicon wafers are laminated together.

The two-layer silicon structure shown in Figure 1 avoids placing any "capping" layer over the circuit side of the silicon chip as has been used in some previous designs (e.g. [1]). Because the top side of the chip is completely exposed, there are no contraints on the placement of metal lines, trim networks, and bonding pads on the chip surface. This freedom in the placement of interconncetions permits ease in creating design variations for specific applications, and also permits laser trimming of the chip as part of the packaging and calibration process after fabrication is complete.

The finished chip (without the glass base) is illustrated in the scanning electron micrograph of Figure 5. The central mass is surrounded by the supporting frame, and the two cantilever beams are evident near the far edge of the chip. The interdigitated fingers for overrange protection are present around three sides of the seismic mass, in contrast to the schematic illustration of Figure 2. The chip also contains a laser-trimmable resistor network for setting the offset voltage, plus extra resistors for temperature compensation of the output characteristic.

Chip Characterization

Chip size (3.4 mm square) and operational characteristics correspond closely to those of silicon piezoresistive pressure sensors, permitting packaging techniques, excitation voltages, calibration procedures, and temperature compensation methods to be compatible with those used for high-volume pressure sensor production. Devices have been packaged in TO5 and TO8 cans and on hybrid circuit boards.

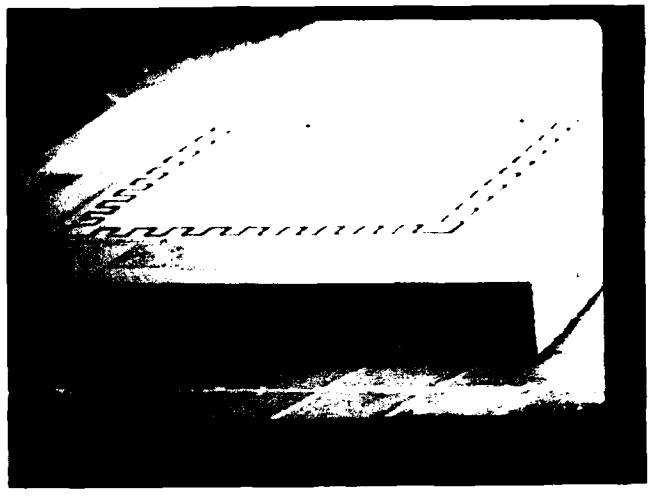

Figure 5. Scanning electron micrograph of a completed chip without glass base attached.

Typical characteristics for one chip configuration are as follows:

Bridge resistance	5000 Ohm
Sensitivity	10 mV/G at 5V excitation
-3dB frequency	500 Hz
Linearity	< 1% at 2G's
Cross-axis sensitivity	< 2% (any axis)
Overrange protection	> 1000G (any axis)

Summary

The cantilever accelerometer introduced here avoids many of the cost and performance limitations of prior designs. The basic cantilever structure provides high sensitivity for a given chip size. Overrange protection in all three axes is available as a basic property of the chip structure. Air damping is controllable by the use of adjustable gaps.

These advantages translate to small size, low cost, and good performance. The low cost constitutes an applications breakthrough which will permit penetration into new areas including automotive air-bag actuation, automotive active suspensions, motion detection in industrial process controls, military and aerospace components, and consumer and medical applications. The small size ensures that the device will be useful in many applications where space contraints are important.

Acknowledgements

We thank Lynn Roylance for providing us with a copy of her Ph.D. thesis at the inception of the design effort for this sensor. Her work on cantilever accelerometers was a great help in the development of the present sensor.

References

[1] Lynn Roylance, **A Miniature Integrated Circuit Accelerometer for Biomedical Applications**, Technical Report No. 4603-2, Integrated Circuits Laboratory, Stanford, CA 94305, November 1977.

[2] H. Sandmaier, et al, **A Silicon Based Micromechanical Accelerometer with Cross Acceleration Sensitivity Compensation**, Transducers '87: The 4th International Conference on Solid-State Sensors and Actuators, Digest of Technical Papers, ISBN 4-88686-010-9, pp 399-402, 1987.

[3] Masashi Nakamura, et al, **Novel Electrochemical Micro-Machining and it Application for Semiconductor Acceleration Sensor IC**, Transducers '87: The 4th International Conference on Solid-State Sensors and Actuators, Digest of Technical Papers, ISBN 4-88686-010-9, pp 112-115, 1987.

[4] Robert D. Sill, **Testing Techniques Involved with the Development of High Shock Acceleration Sensors**, Endevco Tech Paper TP284, Endevco, San Juan Capistrano, CA 92765.

[5] Howard C. Epstein, **Application of Piezoresistive Strain Gauges to Accelerometer Designs**, Endevco, San Juan Capistrano, CA 92765.

[6] Kurt E. Petersen, et al, **Silicon Fusion Bonding for Pressure Sensors**, these proceedings.

Nonplanar Silicon Strain Sensors

Robert W. Bower, Richard R. Spencer, and Derfu D. Lee*
Department of Electrical Engineering and Computer Science
* Department of Civil Engineering
University of California, Davis, CA 95616

ABSTRACT

Variations of conventional thin membrane strain sensors are described which use a series of anisotropic etches on (100) silicon to produce nonplanar structures. An example of a nonplanar structure is a pressure sensor diaphragm with a set of V-grooves etched along the periphery. A second example is given in which a relatively thick (100) oriented plate suspended by a set of relatively thin {111} oriented membranes along the periphery of the thick plate is described and analyzed. The fabrication procedures and analysis of strain characteristics of these examples are described.

INTRODUCTION

Standard (100) silicon pressure sensor diaphragms are usually produced using wet anisotropic etch techniques. These orientation dependent etches work well for forming rectangular diaphragms due to the four-fold symmetry of the (100) silicon and the steep angle of the {111} planes. The resulting diaphragms work well with passive piezoresistive bridge sensors, but are problematic with standard MOS devices built on (100) silicon because of the sensitivity of the piezoresistance coefficients in the inversion layer to electric fields perpendicular to the plane[1,2,3]. Recent work by us shows that using MOS devices in an active strain sensitive circuit provides greater sensitivity than standard piezoresistive techniques [4]. Inversion layers formed in {111} planes on silicon do not exhibit the electric field dependence in their piezoresistive coefficients that is found in inversion layers in the {100} and {110} planes. While {111} oriented MOS transistors have the desired piezoresistivity, it would be difficult to fabricate thinned membranes on (111) material. One solution to this problem, which combines the advantages of using (100) silicon and {111} oriented MOS devices, is to form the transistors in a V-groove on the surface of (100) silicon. These transistors are formed by etching {111} notches over the edges of the pressure diaphragm as shown in Figure 1. While the {111} MOS devices formed are not standard VMOS transistors [5], they are formed using standard process steps. This procedure clearly produces the desired {111} transistors while allowing standard anisotropic etching of the thin diaphragm in the (100) silicon. In addition to solving the MOS orientation problem, the V-groove notch focuses the strain near the apex of the V-groove on the diaphragm creating a strain magnification compared with a conventional thinned membrane pressure sensor. The strain magnification may prove useful whether active MOS or passive piezoresistive devices are used to sense the strain.

Conventional thinned membranes bend rather than deflecting as a rigid plate when subjected to a pressure differential [6]. While this nonplanar deflection is usable in a variety of sensors, it would certainly be desirable in applications such as a capacitive pressure sensors to translate a pressure differential into a linear change in capacitance. A structure is described which quite accurately translates pressure differential linearly into deflection of a rigid plate. This may be used to produce the desired linear change in capacitance with pressure differential. This suspended plate structure is shown in Figure 3. The fabrication and analysis of this device is described below. While this paper will focus on the two examples of nonplanar structures given above, variations on these ideas may be useful for a variety of pressure, strain, acceleration, and flow sensing devices [7,8].

V-GROOVE STRAIN ENHANCER

FABRICATION

The fabrication of these nonplanar structures follows relatively standard procedures of silicon process art and micromachining technique. The V-groove structure in Figure 1 is formed by conventional membrane thinning with an anisotropic etch from the backside of the wafer. This is followed by an anisotropic etch from the frontside of a set of V-grooves which are nominally aligned to cause the apex of the V to be directly over the edge of the thinned membrane. As mentioned in the discussion below, it would be best to have the apex nominally set just inside of the diaphragm edge in order to make the structure insensitive to small alignment errors.

FINITE ELEMENT SIMULATION RESULTS

Finite element simulations of the V-groove structure have been performed to determine the amount of strain magnification relative to a planar diaphragm and to determine the optimal location of the V-groove and how the strain varies with the depth of the groove. The simulations can be summarized with the aid of Figures 1 and 2. Figure 2 shows the strain in the {111} planes of the V-groove as a function of position. The position has been normalized so that different size V-grooves and V-grooves in different locations can be compared. The normalized position uses the apex of the groove as position zero and then normalizes all dimensions by dividing by the width of the groove so that all data fall within a range ±.5. The values for the strain at the discontinuities (the corners at ±.5 and the apex) are not reliable and so are not shown.

Figure 2 shows the strain for a 5 μm wide groove centered on the edge of the diaphragm as shown in Figure 1 along with strain for a 5 μm wide groove with the center shifted 10 μm inside the diaphragm edge and 10 μm outside the diaphragm edge. In addition, the strain is shown for a "deep" groove which has a width of 15 μm at the surface and is centered over the diaphragm edge. The strain in the {100} surface within ±2.5 μm of the diaphragm edge for a standard planar diaphragm is also shown for reference. All of the data are calculated for the center of a side of a square diaphragm 500 μm on a side and 20 μm thick.

The data clearly indicate that the strain near the apex is more than twice that in the surface of a planar diaphragm. The results also show that the strain is not a strong function of the position of the apex of the V-groove so long as it does not get outside of the diaphragm. In addition, the strain does not increase rapidly as the groove is made deeper. All in all, the structure does provide some strain magnification and also exposes the {111} planes necessary for reliable MOS strain sensing devices.

TH0215-4/88/0000-0039

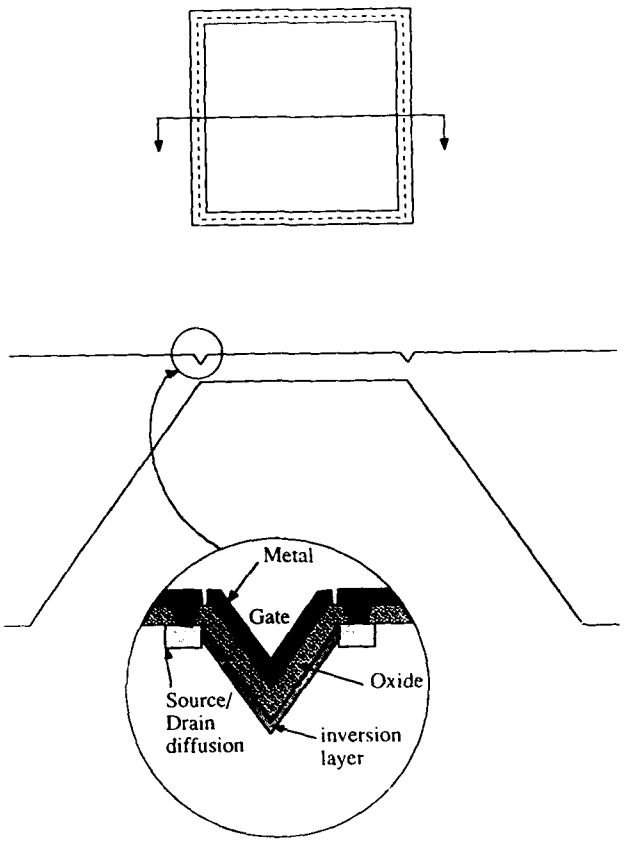

Figure 1 V-Groove pressure sensor showing a detail of how an MOS device could be fabricated in {111} planes using standard (100) silicon.

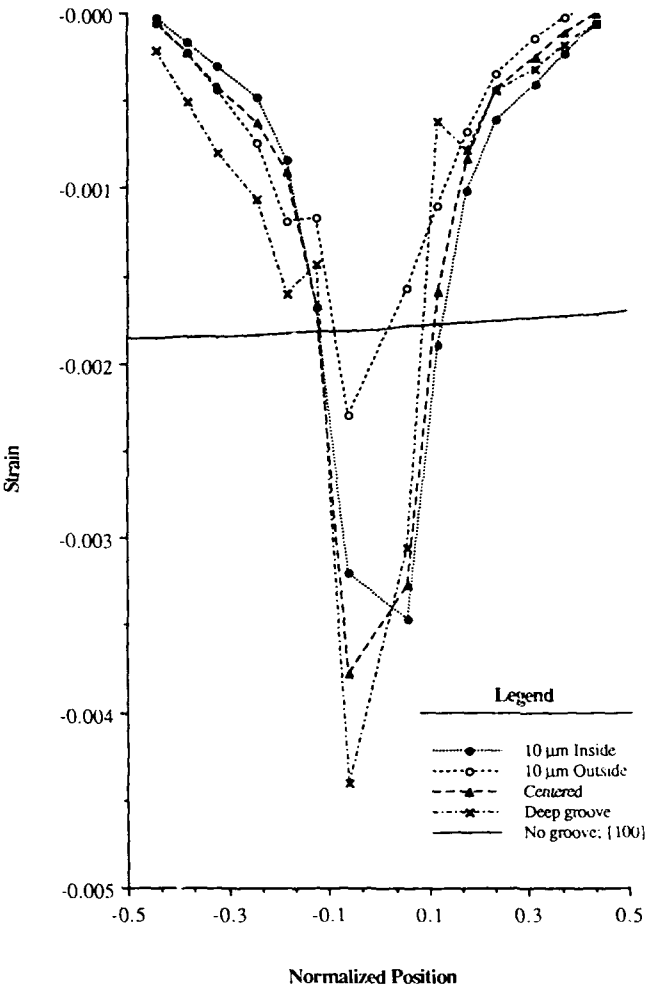

Figure 2 Strain versus normalized position for several different V-grooves and for the (100) surface of a standard planar diaphragm. The apex of the V-groove is at zero and the width is normalized to unity.

SUSPENDED PLATE STRUCTURE

FABRICATION

The structure illustrated in Figure 3 is also produced by a single anisotropic etch from the backside followed by a set of V-grooves etched from the frontside as in the V-groove strain enhancer; however, in the case of the suspended plate device the V-grooves are offset from the thinned layer produced by the backside etch and the grooves are generally much deeper than in the strain enhancer. In this structure the backside etch defines a relatively thick plate while the offset V-grooves establish the geometry of the {111} suspension membranes. Figure 3 highlights the geometrical factors which relate the dimension a and thickness h of the plate, and the offset b and width w of the V-groove to the thickness t and the effective length L of the {111} membrane. The thickness of the {111} membrane is easily seen to be given by

$$t = h\cos\phi + b\sin\phi \qquad (1)$$

where ϕ is the angle between the (111) and (100) planes which is 54.7°. The effective length of the membrane L, is given by

$$L = \left(\frac{w}{2}\right)\frac{1}{\cos\phi} + h\cos\phi - h\sin\phi \qquad (2)$$

It may not be obvious, but Equation 2 is valid for both positive and negative values of b. The effective length L, is generally restricted by the thickness of the wafer, which is usually about 300µm. In this case L is a small fraction of the side dimension of the plate a, which can easily range from 100 to 5,000 µm. Later, an analysis will show that the deflection of a plate constructed as described in Figure 3 would be very small for reasonable pressure differentials. Thus, while such a structure would produce the desirable planar deflection as a function of pressure change, the sensitivity would be very poor. This dilemma can be solved by modifying the structure so that the thickness of the supporting membrane is considerably less than would be possible when this dimension t is determined by the accuracy of the double-sided alignment. The fabrication of this structure proceeds as follows. After a standard backside etch a thin film is formed which will act as an etch stop to define the membrane thickness t, rather than having it depend on the alignment offset b. This can be accomplished in the silicon layer itself by forming a p-n junction along the {111} surfaces and etching the V-grooves in the top with a type-sensitive anisotropic etch such as Ethylenediamine Pyrocatechol. The membrane will then be formed with its thickness determined by the depth of the p-n junction along the {111} planes as shown in Figure 4. Alternatively, a silicon dioxide layer can be deposited or grown on the structure. In this case all of the silicon in the membrane region would be etched leaving a thin membrane of silicon dioxide defined by the {111} planes of the etched silicon. The elastic modulus of silicon dioxide is about 3 times smaller than

that of silicon while its yield strength is comparable, so even greater sensitivity may be realized with this solution [9]. A problem is anticipated for this alternative because the large compressive or tensile stress generally present in thin-film layers may cause the membrane to deform when the silicon is etched. Thus, this alternative is only valid if the internal stress of the thin-film layer can be reduced before etching.

ANALYSIS AND DISCUSSION OF THE SUSPENDED PLATE STRUCTURE

An approximate expression for the vertical displacement of the plate as a function of the total force on the structure can be made by assuming that all the force results in stress applied along the thin supporting membranes and that this stress causes only simple tension or compression of the membranes. In this case the vertical deflection ΔZ is given by:

$$\Delta Z = \left(\frac{F}{4at}\right)\frac{L}{E} \tag{3}$$

where F is the total force applied to the plate and diaphragm, and E is the elastic modulus for the thin membrane. In the case where the force F results from a pressure differential ΔP the expression

$$F = \Delta P\,(a + 2b + w)^2 \tag{4}$$

is approximately true. Table I depicts several solutions for various values of the parameters for this structure used in a pressure sensor application. Plate sizes of 100 and 5,000 μm are considered, with plate thickness of 50 and 100 μm. The offsets and widths of the V-groove were chosen to produce thin membrane lengths of about 100 μm. The offset was chosen to create a membrane thickness of about 10 μm for the alignment defined case, while the self-aligned cases were assumed to have a thickness of 0.3 μm. The pressure differentials and elastic moduli are given in pounds per square inch (PSI). Finally, the deflection of the plate is given in Angstroms. By choosing appropriate values of the plate parameters, with appropriate size and placement of the V-grooves it is possible to design a parallel plate capacitive pressure sensor for a wide range of full-scale pressures and dynamic ranges. This analysis shows that for the low pressure range the thickness of the {111} membranes should be determined by a self-aligned etch stop as shown in Figure 3. When this self-aligned etch stop technique is used very sensitive pressure sensors are possible.

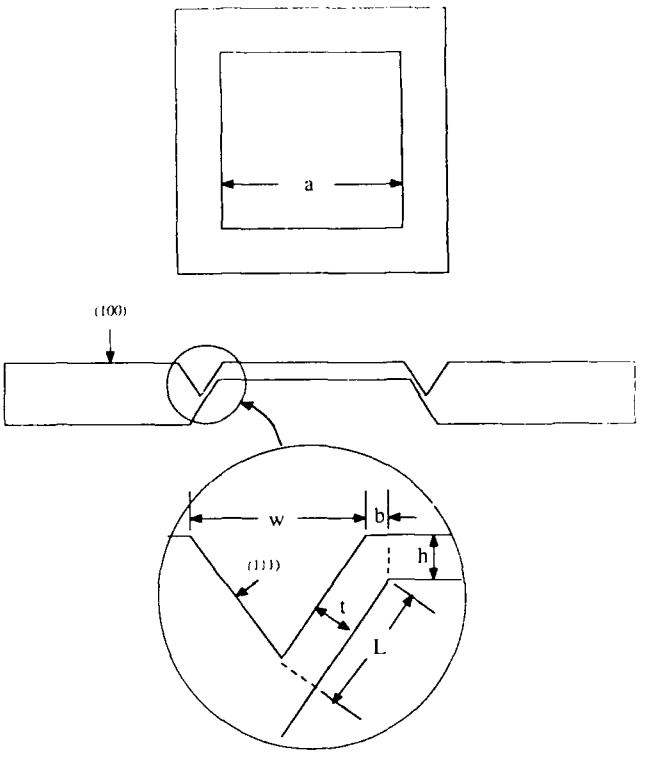

Figure 3 Suspended plate structure fabricated using an offset topside etch showing a detail of the dimensions of the supporting membrane.

CONCLUSIONS

In this work two examples of nonplanar strain sensors are described. Each of these is a variation of the standard thinned membrane pressure sensor. The first example uses a set of relatively small V-grooves nominally aligned over the edge of the thinned membrane to both locally increase the strain compared to a conventional sensor and to adapt the (100) sensor technology to the desired MOS devices formed on (111) surfaces. The strain was found by finite element analysis to be about a factor of two larger than in the conventional membrane sensor. The position and size of the V-groove was not found to be critical provided the groove was not placed outside of the thinned region of the membrane. In the second example a relatively thick plate was formed by a normal backside etch. In this case a set of relatively deep V-grooves were formed from the front side to produce a suspended plate structure. In this case the structure was designed to produce a rigid plate whose deflection was uniform. The structure not only produces a surface suitable for a parallel plate capacitive sensor but may be designed for a wide range of differential pressure conditions.

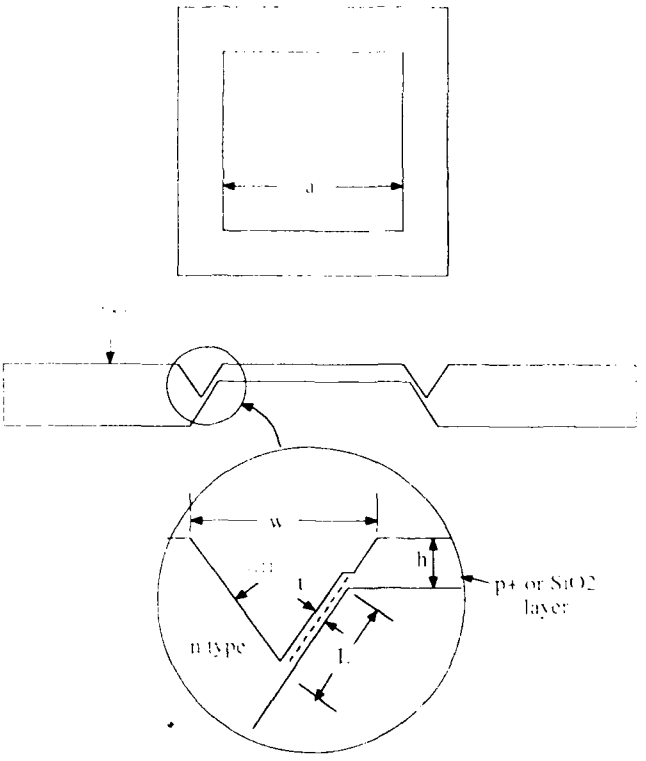

Figure 4 Suspended plate structure fabricated using a thin-film membrane.

ACKNOWLEDGEMENTS

This work was partially supported by NSF grant # ECS-8710320. The finite element simulations where performed using the 2D Linear Elasticity Finite element program written by Kyran Mish of UC Davis. The authors thank Prof. Leonard R. Herrmann for his help.

ΔZ (Å)	a (μm)	h (μm)	w (μm)	b (μm)	t (μm)	L (μm)	ΔP PSI	E PSI X10^7
485.9	5000	100	249	-59	10	100	100	3
496.6	100	50	178	-23	10	100	1000	3
488.0	5000	100	249	-58	0.3	100	3	3
585.3	1000	50	182	-29	0.3	100	15	3
423.4	5000	100	249	-58	0.3	100	1	1
507.8	1000	50	182	-29	0.3	100	5	1

Table 1 Plate displacement for various sets of dimensions and pressures. The first two rows are for the structure in Figure 3. The second two rows are for the thin membrane structure made using the p-n etch stop and the final two rows are for the thin membrane structure with SiO_2 as the thin film.

REFERENCES

[1] D. Colman, R. T. Bate, and J. P. Mize, "Mobility anisotropy and piezoresistance in silicon p-type inversion layers," *J. Applied Physics*, Vol. 39, No. 4, 1968, pg. 1923

[2] G. Dorda, "Effective mass change of electrons in silicon inversion layers observed by piezoresistance," *Applied Physics Letters*, Vol. 17, No. 9, 1970, pg. 406

[3] G. Dorda, "Piezoresistance in quantized conduction bands in silicon inversion layers," . *Applied Physics*, Vol. 42, No. 5, 1971, pg. 2053

[4] R.R. Spencer and R.W. Bower "PiezoMOS Strain Sensors," in preparation

[5] F.E. Holmes and C.A.T. Salama, "VMOS -- A new MOS integrated circuit technology," *Solid State Electron.*, Vol. 17, 1974, pg. 791

[6] Timoshenko and Woinowsky-Kreiger, "Theory of Plates and Shells", McGraw-Hill, 1959

[7] Robert W. Bower and Richard Spencer, Patent Disclosure.

[8] Robert W. Bower, Patent Disclosure.

[9] Kurt E. Peterson, "Silicon as a Mechanical Material", *Proceedings of the IEEE*, Vol. 70, No. 5, May 1982, pp 420-457

A CONSTANT-TEMPERATURE GAS FLOWMETER WITH A SILICON MICROMACHINED PACKAGE

C. H. Mastrangelo and R. S. Muller

Berkeley Sensor & Actuator Center
An NSF/University/Industry Research Center
Department of Electrical Engineering and Computer Science
and the Electronics Research Laboratory
University of California, Berkeley 94720

ABSTRACT

A micromachined flowmeter based on convective heat transfer from hot, heavily doped polycrystalline silicon bridges [1] has been designed, fabricated, packaged and tested. The flowmeter consists of two basic sensing units: one is exposed to the flow while the other acts as a reference. A silicon cap with a micromachined laminar-flow channel is placed on top of the sensor chip to confine the flow. The polysilicon bridge resistors operate at a constant temperature under the control of external circuits. An output signal voltage of 35 mV is obtained for air flow in the range of 0-100 sccm at an average device temperature of 250 °C. The applied heating power is 8 mW.

INTRODUCTION

The precise measurement of low flow rates (< 100 sccm) is essential in the semiconductor industry for furnace control and in medical and chemical applications for analytical gas chromatography equipment. Low flow rates inherently imply that the measurements are performed on very small control volumes of the fluid where rotameters become inaccurate. Miniature flow sensors are the most accurate flow devices for this range. The small control volume implies that the sensor should have a correspondingly small package, as was demonstrated by Petersen and Brown [2].

Although the feasibility of integrated-flow sensors has been experimentally proved, there has been little study about their flow-to-voltage transfer characteristics and even less about the design constraints and proper package design. In this paper, we describe the implementation of a microelectronic flowmeter based on a polysilicon bridge. The device is supported on a SiO_2 mesa to provide good thermal isolation while avoiding a thick isolation layer on the rest of the substrate. The two sensing units are enclosed under a micromachined silicon cap which provides a control volume for the flow (Fig. 1).

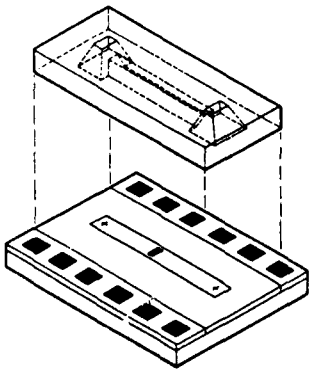

Figure 1 Schematic of the flowmeter assembly

FABRICATION

The sensor fabrication process starts with the deposition of a three-layer, low-pressure chemical-vapor-deposited (LPCVD) SiO_2 sandwich on a silicon substrate. The composite oxide layer consists of 1 μm of phosphosilicate glass (PSG) and 0.3 μm of undoped glass overlain with a further 2.2 μm of PSG. The top layer is etched with BHF to form a mesa. The thin layer of undoped glass acts as an etch stop. A 1 μm layer of *in-situ* phosphorus-doped polysilicon is deposited and patterned to form the sensors. The wafers are then annealed at 900 °C in a N_2 atmosphere for 30 minutes. After Al is sputtered on the samples and patterned, the wafers are covered with a 10 μm-thick layer of polyimide which will act as a gasket and as scratch protection. The bridges are then freed by etching away the oxide layer underneath the polysilicon patterns. After wafers are diced, each individual die is bonded to a DIP package and is covered with a micromachined silicon cap.

Each sensing unit (shown in Fig. 2) consists of two heavily doped polysilicon bridge resistors which act as the sensing elements and eight identical geometry reference resistors which are located near the bridges. All resistors are 270 μm long, 3 μm wide, and 1 μm thick. The bridges are elevated 3.5 μm above the substrate.

Figure 2 SEM photograph of the sensing unit

The silicon cap has two openings, a channel for the gas stream, and an isolated chamber for the reference device. The laminar-flow channel is 7 mm long, 1 mm wide and 300 μm deep. The cap process starts with a 0.7 μm wet oxidation of silicon wafers. The oxide layer is then patterned on one side with plasma etching. The channel and openings are cut when the wafers are subsequently etched using anisotropic ethylenediamine-pyrocatechol-water (EPW) etch [3]. Figure 3 shows both the sensor chip and the silicon cap.

TH0215-4/88/0000-0043

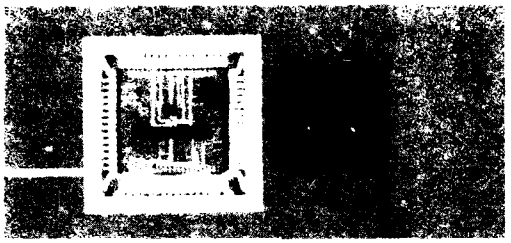

Figure 3 Flowmeter chip and micromachined silicon cap

DEVICE MODEL

The temperature profile, $u(x,t)$ for a heavily doped polysilicon-bridge resistor of width w, thickness z, gap s, and length l can be found by solving the heat equation

$$\frac{\partial^2 u}{\partial x^2} = \frac{1}{\alpha_p}\frac{\partial u}{\partial t} + \beta(u - T_a) + \gamma(u - T_s) - \delta(1 + \xi(u - T_o)) \quad (1)$$

with

$$\beta = \frac{H(c)}{\kappa_p}\left(\frac{1}{z} + \frac{2}{w}\right) + \frac{4\sigma_p T_a^3}{\kappa_p}\left(\frac{1}{w} + \frac{2}{z}\right)$$

$$\gamma = \left[\frac{\kappa_a}{\kappa_p}\right]\frac{1}{sz} + \frac{4\sigma_p T_s^3}{\kappa_p}\frac{1}{z}, \quad \delta = \frac{J^2\rho_o}{\kappa_p}$$

where α_p, κ_p, σ_p, ρ_o, and ξ are the thermal conductivity [4], thermal diffusivity, Stephan-Boltzmann constant, resistivity, and temperature coefficient of resistance (TCR) of polysilicon; T_s and T_a are the substrate and gas temperatures, and T_o is a reference temperature; κ_a is the thermal conductivity of the gas, and J is the current density. The parameter $H(c)$ is the heat-transfer coefficient which is a function of the gas velocity c.

The current-voltage characteristic is derived from the solutions for the temperature in Eq. (1) and the relationship

$$V_b = I R_b = I R_o [1 + \xi(\bar{u} - T_s)] \quad (2)$$

where $\bar{u}$ is the average temperature ($\bar{u} = \frac{1}{l}\int_0^l u(x)\,dx$) of the bridge. In steady state, for $T_a = T_s = T_o$

$$V_b = I R_o \left[1 + \frac{\xi\delta}{\varepsilon}\left(1 - \frac{\tanh\sqrt{\varepsilon}l/2}{\sqrt{\varepsilon}l/2}\right)\right] \quad (3)$$

where $\varepsilon = (\beta + \gamma - \delta\xi)$. The small-signal output voltage v can be obtained as a function of the small-signal variation of the Nusselt number Nu and the small-signal substrate temperature variation t_s from Eq. (2). Note that in this definition $Nu(c=0) = 0$.

$$v = V_c\, Nu(c) + G_s\, t_s \quad (4)$$

with

$$V_c = \frac{\kappa_a}{2(w+z)} I R_o \xi \frac{\partial \bar{u}}{\partial H} \quad (5)$$

$$G_s = I R_o \xi \frac{\partial \bar{u}}{\partial T_s} = I R_b \xi = V_b \xi .$$

The terms V_c and G_s are constants at a given operating point.

Sinusoidal small-signal analysis of Eq. (1) leads to the ac voltage and impedance parameters

$$V_c(j\omega) \approx \frac{V_c(0)}{\left(1 + j\frac{\omega}{p_o}\right)} \quad (6)$$

$$z(j\omega) \approx R_b + \frac{(r_b - R_b)}{\left(1 + j\frac{\omega}{p_o}\right)}$$

where z is the small-signal output impedance of the device; R_b and r_b are the large- and small-signal output resistance of the bridge. The bridge shows a one-pole characteristic with

$$p_o \approx \alpha_p\left(\varepsilon + \frac{\pi^2}{l^2}\right). \quad (7)$$

The parameter $\alpha_p = \frac{\kappa_p}{\rho_m C_p}$ where ρ_m and C_p are the density and specific heat of the film. Using ρ_m and C_p of single crystal silicon and the dimensions of our device, we find that the pole p_o occurs at roughly 3 kHz.

A theoretical heat-transfer calculation predicts that the small-signal Nusselt number is a function of the Peclet number Pe of the flow. The Peclet number $Pe = \frac{\bar{c}\,h}{\alpha_a}$ where $\bar{c}$ is the average velocity of the fluid, h is the height of the flow channel, and α_a is the thermal diffusivity of air. The Peclet number is a measure of mass-flow rate.

At very low Reynolds numbers associated with low-flow rates and for (channel height) $h >> s$ (gap under the bridge), Nu can be expanded in even powers of Pe

$$Nu(c) = Nu(Pe) = a_1 Pe^2 + a_2 Pe^4 + \cdots \quad (8)$$

Typical values of Pe for our device in air range from 0 to 50.

The transient response to a velocity step is determined by the pole p_o and the time-dependent small-signal Nusselt number. The exact time dependence of Nu is a function of the geometry of the channel in which the sensor is placed. For a two-dimensional channel of height h, Nu settles within a time τ_{sett} where

$$\tau_{sett} \leq \frac{h^2}{\alpha_a \pi^2}. \quad (9)$$

The upper bound on τ_{sett} is a direct result of the boundary conditions on the walls of the channel. For a channel with $h = 300$ μm filled with air, $\tau_{sett} \leq 440$ μs. An important conclusion is that τ_{sett} can be made small by decreasing h.

The parasitic substrate component of the output signal in Eq. (4) ($G_s\, t_s$) follows the temperature of the package which can be slowly varying because of the large substrate mass. To make a useful flowmeter, this signal must be canceled because it makes v dependent on room-temperature variations.

BIAS CIRCUIT

Each of the groups of bridges and 8 reference is connected in series, and driven by the external simplified bias circuit of Fig. 4. In Fig. 4, the two bridges comprise the resistor R_b, and the 8 reference resistors are represented by R_1. The operating point of the circuit is automatically adjusted such that a constant ratio is established between the resistance of the bridge and that of the reference resistor R_1

$$R_b = R_o[1 + \xi(\bar{u} - T_o)] = \frac{(1+\alpha)R_1 R_2}{R_3}[1 + \xi(T_s - T_o)] \quad (10)$$

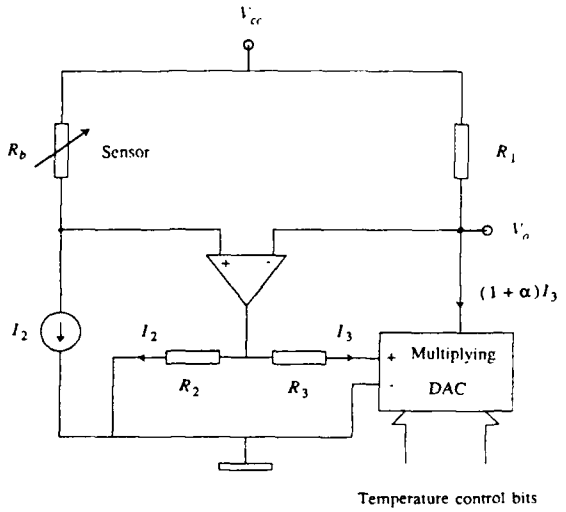

Figure 4 Simplified constant-temperature bias circuit

If $R_1 R_2 = R_o R_3$, Eq. (10) yields

$$\bar{u} = T_s + \frac{\alpha}{\xi} . \qquad (11)$$

From Eq. (11), we see that the average temperature of the bridge is directly proportional to the constant digital-analog converter (DAC) multiplying ratio α. The main advantage of this bias scheme is that the operating point of the bridges can be made independent of the power supply.

The circuit amplifies the convection signal $V_c\, Nu(c)$ with a gain

$$A \approx \frac{R_b}{r_b - R_b} . \qquad (12)$$

The outputs of the two biased sensing units are then subtracted to cancel any changes of v caused by variations of the substrate temperature t_s.

RESULTS AND DISCUSSION

The resistance of heavily doped polysilicon resistors has been measured as a function of substrate temperature from 25 up to 250 °C. We found that the resistance follows Eq. (2) with $\xi = 1.22\times10^{-3}$ °C^{-1}. Using this value in Fig. 5, we compare the measured *IV* characteristics of a sensor unit with those predicted by our model. The solid line represents the theoretical *IV* curve obtained from Eq. (3). The theory fits well to measured values for $\bar{u} \leq 200$ °C. At higher temperature, correction terms must be added to account for the strong temperature dependence of κ_a [5].

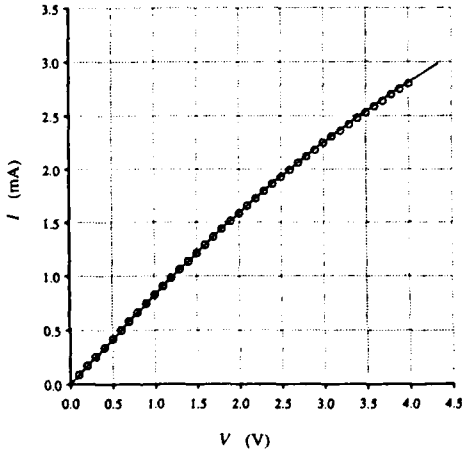

Figure 5 Bridge resistor *IV* characteristic

Figures 6(a) and 6(b) show measurements of magnitude and phase of the ac small-signal output impedance of the sensor as a function of frequency at $\bar{u}$ of 110 °C. The solid line represents the theoretical expression for $z(j\omega)$. Note that the pole occurs near 3 kHz as predicted by Eq. (7).

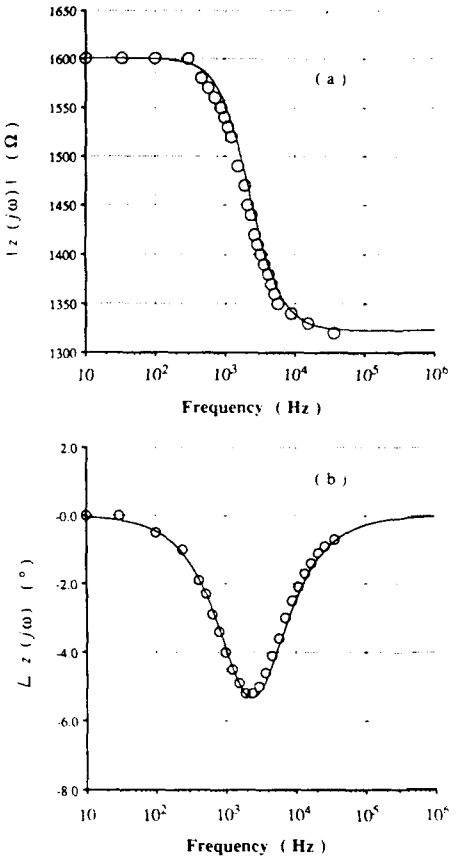

Figure 6 (a) Magnitude and (b) phase of the ac small-signal output impedance of bridge resistor

Figure 8 shows the response of the sensor to a pulsate flow generated with a piezoelectric valve driven by a pulse generator. The settling time of the voltage signal after a step in the pressure is approximately 25 ms consistent with the time constant of the gas velocity associated with the tube system.

Figure 7 shows the output voltage versus flow rate for the for the flowmeter. The rate was monitored with a rotameter (Gilmont F-9069) connected through 50 cm of 0.25-inch teflon tubing in series with the 10 cm of 0.125-inch tubing of the mounting hardware. The sensors were biased to achieve average bridge temperatures of 150, 190, and 250 °C (4 mW dissipation in the structure at 250 °C). Note that the small-signal output voltage follows a nearly quadratic curve at low flow rates. At higher rates, the signal seems to follow a linear relationship. We have observed that at very low rates (< 20 sccm) the output voltage fluctuates significantly.

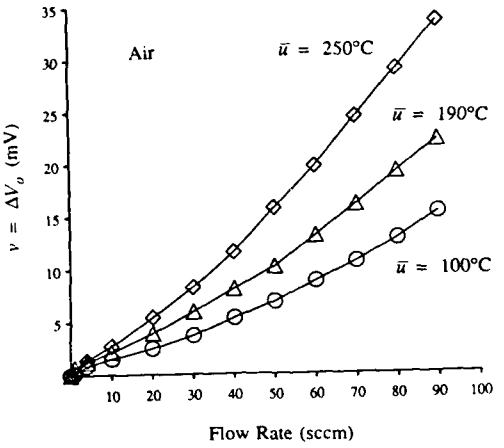

Figure 7 Small-signal output voltage as a function of flow rate

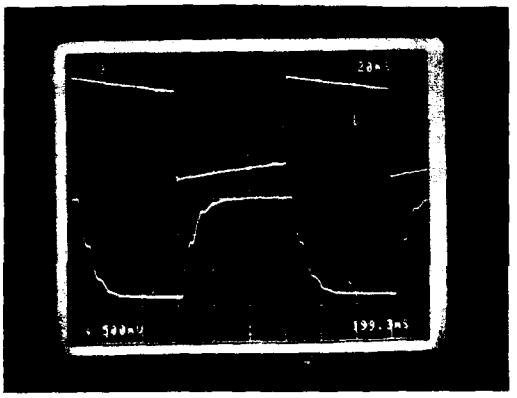

Figure 8 Response to a pulsate flow. The top signal dri·s the piezoelectric valve. The bottom signal is the response of the flowmeter.

Figure 9 shows the mounting hardware for the flowmeter chip. The gas is fed to the chip from the top by a drilled steel tube holder which also acts as a heat sink. A rubber gasket is placed at the interface between the tube holder and the silicon cap to prevent any leak.

Figure 9 Flowmeter mounting hardware

CONCLUSIONS

An integrated gas flowmeter implemented with polysilicon bridge resistors has been fabricated, packaged and tested. The flow sensors are enclosed in a micromachined channel etched separately on a silicon cap. This flow sensor is suitable for flow-rate measurements that require accuracy and fast response.

References

1. Y. C. Tai, R. S. Muller, and R. T. Howe, "Polysilicon bridges for anemometer applications," *Digest of Technical Papers, Int. Conf. on Solid-State Sensors and Actuators*, pp. 354-357, Philadelphia, June 4-7, 1985.
2. K. Petersen, J. Brown, and W. Renken, "High-precision, high-performance mass-flow sensor with integrated laminar flow micro-channels," *Proc. Int. Conf. Solid-State Sensors and Actuators 1985*, pp. 361-363.
3. K. E. Petersen, "Silicon as a mechanical material," *Proceedings of the IEEE*, vol. 70, pp. 420-457, May 1982.
4. Y. C. Tai, C. H. Mastrangelo, and R. S. Muller, "Thermal conductivity of heavily doped low-pressure chemical vapor deposited polycrystalline silicon films," *J. Appl. Phys.*, vol. 63, no. 5, pp. 1442-1447, March 1, 1988.
5. R. B. Bird, W. E. Stewart, and E. N. Lightfoot, *Transport Phenomena*, John Wiley & Sons, New York, 1960.

A Thermally Isolated Microstructure Suitable For Gas Sensing Applications

Michael A. Huff, Stephen D. Senturia, and Roger T. Howe*

Microsystems Technology Laboratory,
Dept. of Electrical Engineering and Computer Science,
Massachusetts Institute of Technology
Cambridge, Mass. 02139

Abstract

A thermally isolated microstructure for use in metal-oxide gas sensing applications was fabricated and tested. Using the techniques of bulk micromachining, a thin silicon membrane 5 μm thick was fabricated and then used as a structural support during subsequent device processing. The mechanical stability of the thin silicon membrane was found to be dependent on the compressive surface oxide thickness which induced membrane buckling. A study of the buckling criteria was examined in detail by performing etch-back experiments on a series of sequentially sized membranes and observing the transistion for buckling. A linear relationship between oxide thickness and membrane edge length squared was found. The device is fabricated over the membrane on the wafer surface and consists of a sandwich of LPCVD Si_3N_4, LPCVD poly-Si and LPCVD Si_3N_4. After device fabrication, the support membrane is etched away leaving the device completely isolated from the substrate. The power neccessary to maintain the released suspended plate temperature at 300 C was approximately 15 mW depending on the device design. We have measured a thermal time constant of approximately 2.0 msec depending also on the device design. The measured values of power consumption and thermal time constant are compared with a simple model.

Introduction

At temperatures of 200 to 350 C the conductivity of certain metal-oxides can be modulated by the presence of various oxidizing and reducing gases[1-3]. This material property has been exploited successfully for gas sensing applications using thick-film technology and more recently thin-film technology [4,5]. The elevated temperature, usually acheived through ohmic dissipation, is necessary to increase the metal-oxide sensitivity and response time [6]. It is desirable to localize the necessary heating to only the metal-oxide sense resistor in order to minimize power and to allow integration of nearby electronics. By using the techniques of bulk micromachining, improved thermal isolation can be obtained by placing the sense resistor on a silicon membrane [5,7,8].

This paper describes the fabrication process and testing of a thin-film microstructure which is suspended over a window etched completely through the silicon. Due to this thermal isolation, the power requirements for heating the structure are minimized. In addition, the heated structure has a very low thermal mass and this results in a rapid thermal repsonse. A device with a fast thermal response may have important applications in basic studies of desorption kinetics and in the realization of gas sensors with improved selectivity and sensitivity. In the technique of Thermally Programmed Desorption (TPD), the sample temperature is ramped in an ultra-high vacuum chamber and the variation in the resistance is monitored. It has been shown that sample resistance variations can be related to the desorption energy, desorption rate, and frequency factors for the species involved[9]. Rapid temperature ramping made possible by this device structure may yield additional information on the adsorbed species at atmospheric pressure.

*Present Address - Berkeley Sensors and Actuator Center, Dept. of Electrical Engineering and Computer Sciences, University of California, Berkeley, CA. 94720

Experimental

1. Fabrication

The process was designed to be as compatible as possible with the MIT baseline CMOS process. The device is fabricated on top of a thin p+ doped membrane made by conventional anisotropic silicon etching techniques (Figure 1). Once the device is complete a backside plasma etch removes the p+ doped silicon layer thereby releasing the structure and removing a significant heat conduction path (Figure 2).

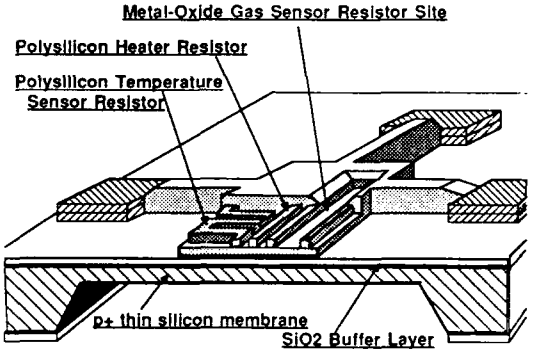

Figure 1 A drawing of the thermally isolated microstructure on the Suspended membrane before releasing. Important elements are identified.

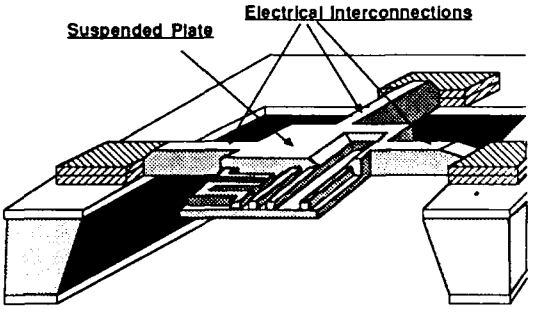

Figure 2 A drawing of the thermally isolated device after it has been completely released.

Starting with 4 inch (100) n-type silicon wafers, boron is diffused into the frontside to act as an etch stop. After backside oxide patterning, the wafers are anisotropically etched in a hydrazine hydrate solution at 120 C for approximately 4 hours. The resulting thin silicon membranes are approximately 5 μm thick. The oxide on the wafer surface is etched back to a thickness of less than 1000 Å to ensure an unbuckled membrane, as discussed below. A 1500 Å thick film of LPCVD silicon nitride is deposited

TH0215-4/88/0000-0047

and subsequently patterned and SF6 plasma etched to conform to the suspended plate structure. Next, a 5000 Å thick layer of undoped polysilicon is deposited by LPCVD. This film is patterned and plasma etched in a chlorine plasma resulting in the desired interconnect, heater resistor, and temperature sensing resistor pattern.

To maximize heater and temperature-sensor resistance relative to interconnect resistance while still minimizing the device size, a selective doping was performed on the patterned polysilicon. A thick layer (>1μm) of undoped LPCVD SiO_2 (LTO) is deposited and patterned to mask the heater and temperature sensing resistor area during the subsequent diffusion. A phosphorus diffusion is performed for 2 hours at 950 C to heavily dope the polysilicon interconnects. The resulting sheet resistance of these interconnects is less than 10 ohm/square. The wafer is then wet etched in buffered HF to remove the LTO diffusion mask. A 160 Kev phosphorus implant at a dose of 5×10^{15} atoms/cm^2 and subsequent anneal at 1100 C for 2 hours results in a sheet resistance of 1700 ohms/square for the heater and temperature-sensor resistors. The anneal also reduces the compressive residual stress in the polysilicon[10].

A 3000 Å-thick layer of LPCVD silicon nitride is deposited and patterned as before. This thickness of nitride is sufficient to compensate for the induced membrane buckling due to surface oxide compressive stress during the device release. Aluminum is DC sputtered onto the wafer, patterned and then sintered for ohmic contact to the pad regions, completing the fabrication process except for the supporting membrane removal.

For the initial fabrication run, individual chips are first separated by a dicing saw, and then released separately to overcome nonuniformities in the etcher. A parallel-plate plasma reactor is used to remove the silicon membrane by etching in a SF6 plasma from the backside. At an RF power of 160 Watts and a pressure of 100 mtorr in the etcher it takes about 10 minutes to completely remove the silicon. The initial thermal oxide is removed in buffered HF completing the device. Figure 3 shows an SEM of a functional device with dimensions.

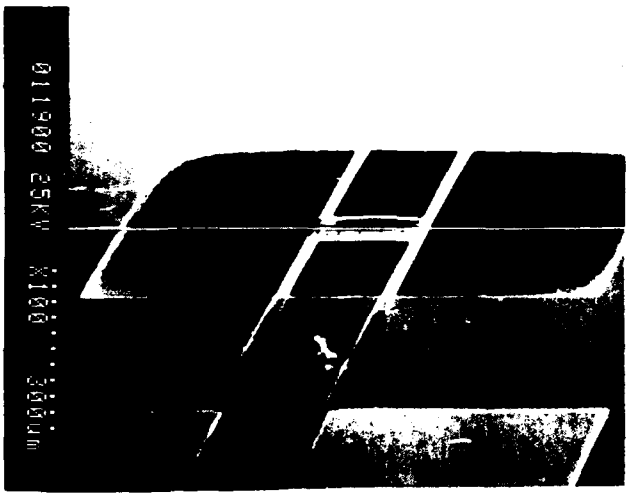

Figure 3 SEM of a functional device. The dimensions of the Suspended Plate are 220 μm by 150 μm. The supporting struts are 40 μm wide and 200 μm long as measured from the suspended plate to the substrate edge.

2. Membrane Buckling

Various materials issue had to be addresses during the fabrication of the device, the most important of which was the question of mechanical stability of the thin silicon membrane during device processing. A thin thermal oxide layer on the surface of the p+ membrane is required to act as an etch stop during the backside plasma etch, as shown in Figure 1[11]. Although it is well known that thermal oxide is under compressive stress[12], less is known about the stress in the heavily boron-doped membranes. The process requires that the suspended membrane not buckle at any point in the process, or else the microstructure will fracture. In order to investigate this phenomonon, we fabricated as array of oxide/p+ silicon square membranes of increasing sizes. By performing an etch-back of the oxide and observing the transition point for the onset of buckling (this point being defined as between two successively sized membranes, the larger of which is buckled and the smaller being unbuckled), we found a linear relationship between oxide thickness and the membrane edge length squared.

This relationship agrees with the theoretical analysis based on plate theory[13-15]. The critical load for buckling of a square plate is given by [15]:

$$P_{cr} = \frac{5.33\,\pi^2 D}{L^2}$$

where D is the flexural rigidity and L is the edge length. This result assumes that the load is applied along the plate's center and is uniform. The load on the membrane is given by:

$$P = \sigma_{ox} t_{ox} + \sigma_{si} t_{si}$$

where σ_{ox} is the oxide residual stress and t_{ox} is the oxide thickness and similarily for σ_{si} and t_{si}, where the si refers to silicon. Setting P_{cr} and P equal we expect to see a linear relationship between t_{ox} and L^{-2} if only t_{ox} is varied, where the slope is given by: $m = \frac{5.33\,D\,\pi^2}{\sigma_{ox}}$ and the vertical intercept by:

$$b = -\frac{\sigma_{si} t_{si}}{\sigma_{ox}}$$

In the above case, the oxide inducing the compressive stresses are not centrally loaded but are on the surface and therefore the membrane is asymmetrically loaded. Two problems arise, for a asymmetrically loaded plate: the plate will first bend, and then buckle [14,15], thus making the transistion for buckling somewhat arbitrary, and, second, the constant (i.e. 5.33) [14,15] in front of the relationship for the critical load will be different. In the above etchback test we defined buckling as the first visual evidence of four-fold buckling, as distinct from bending.

Figure 4 shows the results of the etch-back test where t_{ox} is plotted versus (membrane edge length)$^{-2}$. The horizontal lines correspond to the buckled-unbuckled transition point. Resolution in this initial experiment was limited due to the relative sizes between successive membranes. Therefore the slope and intercept cannot be defined with certainty. However, if the membranes are buckled with no oxide, as shown in Figure 4, then the intercept is clearly at a negative t_{ox}, and the membranes are compressive. If the intercept appears to cross at a positive t_{ox} value the sign of membrane residual stress is indeterminate, but can be resolved by examining thinner membranes as discussed below.

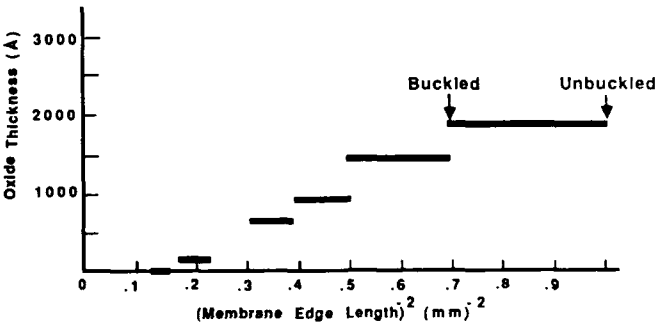

Figure 4 Curve showing the linear relationship between wafer surface oxide thickness and (membrane edge length)$^{-2}$. The horizontal lines represent the uncertainty in the experiment.

To investigate whether the stress in the p+ membranes may somehow be modified (made less compressive or even tensile) we performed the same etchback test on wafers that had been doped while the concentration of oxygen during the diffusion was at 4 %, 10%, 15%, 20% and 25%. The diffusions were performed for 6 hours and for 4 hours resulting in membrane thicknesses of 5.0 μm and 3.3 μm respectively. Additionally, to observe the effect of surface oxide growth temperature, this was also varied. Table I shows the condition of these membranes at the point of complete oxide removal. Note that even though the 5.0 μm membrane oxidized at 950 C is unbuckled at zero oxide, the thinner membrane at the same oxide condition is buckled. We therefore conclude that p+ membranes doped by a liquid source are under compressive residual stress.

An additional membrane buckling problem was that during the backside plasma etch, the once stable membrane would buckle since the silicon membrane mechanical support is being removed

TABLE I.

	Oxide Growth Temp C	950	950	1000	1050	1050	1100
	Membrane Thickness (μm)	3.3	5.0	5.0	5.0	3.3	3.3
Oxygen Conc. During Boron Diffusion	4%	B	UB	B	B	--	--
	10%	--	UB	--	B	--	--
	15%	B	UB	--	B	B	--
	20%	B	B	--	B	B	B
	25%	--	B	--	B	B	B

Key : B = Buckled Membrane and UB = Unbuckled Membrane

but the compressively stressed thermal oxide remains. Although not quantitatively investigated, we found that doubling the nitride thickness of the top layer was sufficient to compensate for the compressive-stress-induced buckling of the oxide during the backside plasma etch.

3. Thermal Model

The power consumption and the thermal time constant can be estimated using a simple one-dimensional lumped parameter thermal model based on elementary heat transfer theory[16,17]. Figure 5 shows the equivalent electrical circuit where R_{eq} is the parallel combination of the thermal resistances of the support struts and C_{eq} is the thermal capacitance of the structure. Convective heat transfer is neglected. The model elements can be calculated as:

$$\text{Thermal Capacitance} = C_{eq} = \sum_{i=0}^{n} r_i V_i C_{pi} ,$$

where: r_i is the density of the ith layer. Vi is the volume of the ith layer, and C_{pi} is thespecific heat of the ith layer.

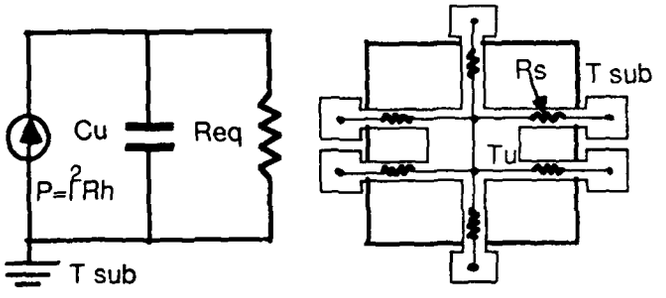

Figure 5 The thermal equivalent circuit for the device where, Cu is the thermal capacitance of the suspended plate and Req is the equivalent thermal resistance.

$$\text{Thermal Resistance of Support Strut} = R_s = \left(\sum_{i=0}^{n} K_i\left(\frac{A_i}{D}\right)\right)^{-1}$$

where: K_i is the thermal conductivity of the ith layer, A_i is the cross sectional area of the ith layer, and D is the length of the support strut. The temperature of the substrate, T_{sub}, is assumed to be a heat sink. The temperature of the heated microstructure equals T_u and is assumed uniform and the input power to the microstructure is $P = I^2R_h$, where R_h is the resistance of the heater resistor.

The power required to maintain a steady-state temperature T_u the microstructure can be found by:

$$T_u = T_{sub} + P\,R_{eq}$$

and the thermal time constant is found by:

$$\tau = R_{eq}\,C_u.$$

Approximate values for the above equivalent circuit elements can be calculated using literature values for the material constants and the device dimensions [18-20]. This was done for the four different devices having support struts length varying from 100 μm to 250 μm. Once values for the elements are found the power consumption and thermal time constant can be easily calculated. The results are shown in Table II.

TABLE II.

Strut Length (mm)	Power To Maintain 300 C (mW) Calculated	Measured	Thermal Time Constant (msec) Calculated	Measured
100	11.2	15.5	1.0	1.4
150	7.5	10.0	1.5	1.8
200	5.6	9.0	2.0	2.5
250	4.5	8.0	2.5	3.3

4. Device Testing Results

The current level for the onset of self-heating in the temperature sensing resistor was found to be less than the maximium current output of a Keithley Model 175 DMM and therefore the Keithley DMM could be used to calibrate the temperature sensing resistor.

Using a hot chuck capable of 350 C, the device was immersed in an isothermal medium consisting of Dupont 210H high temperature silicone oil in a container located on the chuck. The chuck was heated to some temperature, the temperature was allowed to stablize and the resistance was measured. The temperature of the oil was monitored via an Omega thermocouple. Resistance versus temperature curves were thereby generated for the temperature sensing resistors. See Figure 6.

The power consumption for maintaining a certain temperature was then measured for the device. Both voltage and the current were measured via a Keithley Model 175 DMM. Figure 7 shows the results of these power measurements.

The thermal time constant was measured by pulsing the device to some current known to heat the microstructure to 310 C. The current was suddenly turned off and the decay of the voltage on the temperature sensor was observed over time. The temperature sensor was biased in a bridge circuit at a current level far below the self-heating threshold. Figure 8 shows a photo of the pulse test. It should be noticed that the resistance response is nonlinear so that the voltage change shown in the photo is not linearly related to the temperature change. The thermal time constant is defined as the time for the temperature of the device to decay to 1/e of its original value.

Table II shows the measured power consumption and thermal time constant for the different devices of increasing support strut lengths. Better results can be obtained by more sophisiticated modelling[7].

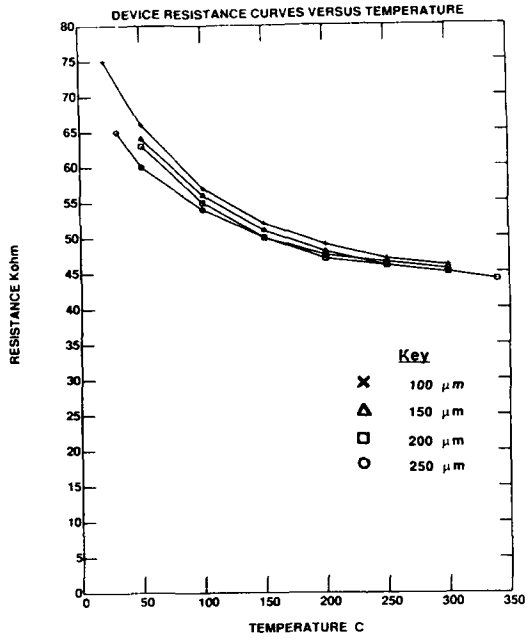

Figure 6 The measured resistance of the temperature sensor as a function of temperature. This data is used to calibrate the device. The lengths of the supporting struts are given for comparison.

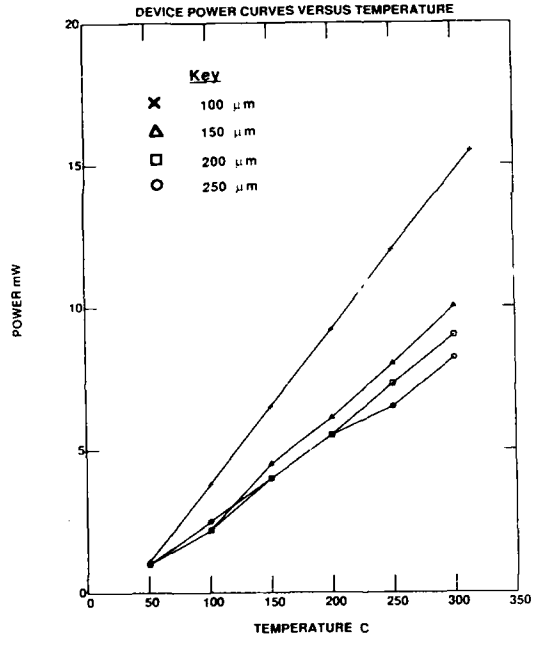

Figure 7 The measured steady-state power needed to maintain the temperature of the suspended plate as a function of temperature. The lengths of the supporting struts are given.

Summary

A thermally isoalted microstructure was successfully fabricated and tested. It offers lower power consumption and an extremely fast thermal response time and could be very useful in the applications of metal-oxide gas sensors.

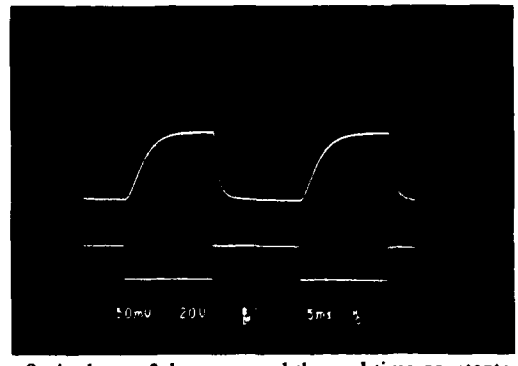

Figure 8 A photo of the measured thermal time constants. The upper curve is the response of the DC biased temperature sensor on the suspended plate. The positive going part of the pulse corresponds to cooling while the negative part corresponds to heating. The lower curve is the signal used to drive the heater resistor.

Acknowledgements

We wish to thank General Motors Research for their generous funding of this research project and in particular Dave Eddy and Scott Chang at GMR. Marty Schmidt at MIT is to be thanked for providing useful processing discussions. This work was done in the Integrated Circuits Laboratory and the Technology Research Laboratory both part of the MIT Microsystems Technology Laboratory. We are indebted to the MTL staff.

References

[1]S.C. Chang, D.B. Hicks, Fundamentals and Applications of Chemical Sensors, American Chemical Society, Washington D.C. 1986.
[2]H. Windischmann, P. Mark, Journ. Of Electrochem. Soc., Vol. 126, No.4, pp. 627.
[3]S.C. Chang, *IEEE Trans. Electron Devices, Vol. ED-26,* No.12, pp. 1875.
[4]S.C. Chang, A.L. Micheli, GM Research Report No. ET-358.
[5]S.C. Chang, D.B. Hicks, Tech Digest, IEEE Solid-State Sensors Worshop, Hilton Head S.C., June 2-5, 1986.
[6]G. Heiland, D. Kohl, Tech Digest, IEEE Solid-State Sensors Conf. 1985.
[7]S.B. Crary, Tech Digest, IEEE Solid-State Sensors Workshop, Hilton Head S.C.,June2-5, 1986.
[8]V. Demarne,A. Grisel,R. Sanjines, 4th International Conference On Solid-State Sensors and Actuators, Transducers '87, Tokyo Japan 1987.
[9]B. Fortin, et al., Thin Solid Films, 131 (1985)
[10]H.Guckel, R. Randazzo, D.W. Burns., J. App. Phys., 57 (5), 1985, pp. 1671.
[11]M. Allen, MIT Dept of Chem. Engr., S.M. Thesis, 1986.
[12]C. W. Wilmsen, et al., IEEE Trans. Electron Devices, ED-19, no.1, Jan 1972, pp.122.
[13]Gere and Timoshenko, Mechanics Of Materials, 2nd ED., PWS Engineering, Boston, 1984.
[14]Timoshenko, Theory of Plates and Shells, McGraw Hill, New York, 1940.
[15]Timoshenko, Theory of Elastic Stability, McGraw Hill, New York, 1936.
[16]Chapman, Heat Transfer, 3rd ed., Macmillan, New York, 1974.
[17]Holman, Heat Trausfer, 5th ed., McGraw Hill, New York, 1981.
[18]Muller and Kamins, Device Electronics for Integrated Circuits, Wiley, New York, 1977.
[19]Y.C. Tai, C.H. Mastrangelo, R.S. Muller, Tech Digest IEDM 87, Washington D.C. 1987
[20]*CRC Handbook of Physics and Chemistry* , CRC Press, 1985.

PROCESSING CONDITIONS FOR POLYSILICON FILMS WITH TENSILE STRAIN FOR LARGE ASPECT RATIO MICROSTRUCTURES

H. Guckel, D. W. Burns, H. A. C. Tilmans, C. C. G. Visser,* D. W. DeRoo,**
T. R. Christenson, P. J. Klomberg, J. J. Sniegowski and D. H. Jones

Wisconsin Center for Applied Microelectronics
Department of Electrical and Computer Engineering
University of Wisconsin
Madison, WI 53706

*Currently employed by DIMES, Delft, The Netherlands
**Currently employed by Delco Electronics Corp., Kokomo, Indiana

Abstract

The processing conditions to obtain high quality and repeatable polysilicon films are described. These include substrate preparation, the deposition procedure, reactor configuration and post deposition treatment. Examples of large aspect ratio microstructures are presented to illustrate the potential of polysilicon films that are in tension.

Introduction

Polysilicon has been used as a construction material in a variety of experimental micromechanical devices. All applications indicate that the built-in strain field is compressive and the morphology is variable. This causes at least two fundamental difficulties in mechanical applications: size restrictions of free-standing structures because of buckling, and morphology related variations in the mechanical properties e.g. tensile strength, Young's modulus and the Poisson ratio. In an accompanying paper,[1] we have indicated that a repeatable morphology is necessary when using polysilicon or any other thin film in the design of micromechanical devices. Therefore, a film for use in microstructural applications has the following properties:

a) repeatable i.e. controllable mechanical properties
b) controllable strain field
c) smooth, conformal surface with zero defects.

A high quality film with these properties has been obtained with fine grained polycrystalline silicon grown using Low Pressure Chemical Vapor Deposition (LPCVD) techniques. This paper describes the processing conditions necessary to accomplish this. The process consists of three main steps: 1) selection of starting material and surface preparation, 2) deposition, and 3) post deposition treatment.

Fine grained polysilicon films under moderate tension have been used to fabricate large aspect ratio microstructures such as long, thin beams and tuning forks for sensor applications and large area diaphragms for piezoresistive microphones and X-ray masks.

Selection of Starting Material and Surface Preparation

In microstructural applications at WCAM, it is of particular interest to deposit high quality films of polysilicon on three types of surfaces. These are:

1) single crystal silicon,
2) thermally grown silicon dioxide and
3) LPCVD silicon nitride.

As a basic starting material for our experiments, we used high quality single crystal silicon wafers. Ideally, initial substrate material must be free of any defects, contaminants or particulates. LPCVD polysilicon films are conformal and replicate substrate texture and debris. Surface contaminants and particulates acting as nucleation sites can cause accelerated growth of polysilicon grains leading to protrusions and nodules. Figure 1 shows an example of accelerated growth of poly due to handling the wafer with metal tweezers. Vacuum pickups are preferred to avoid any physical contact with the wafer surface. From depositions on the three surfaces mentioned above, we found that polysilicon deposited on freshly grown silicon dioxide is superior. High quality polysilicon films on silicon nitride are more difficult to achieve. Figure 2 shows a typical polysilicon film grown on nitride. The texture and irregularities of the nitride layer are being transferred to the polysilicon layer. Work on improving the quality of the nitride film is in progress.

TH0215-4/88/0000-0051

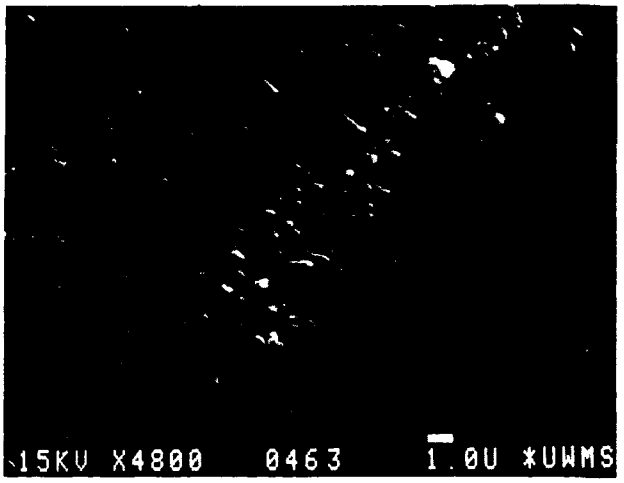

Figure 1. Defects in a polysilicon film caused by handling the wafer with metal tweezers.

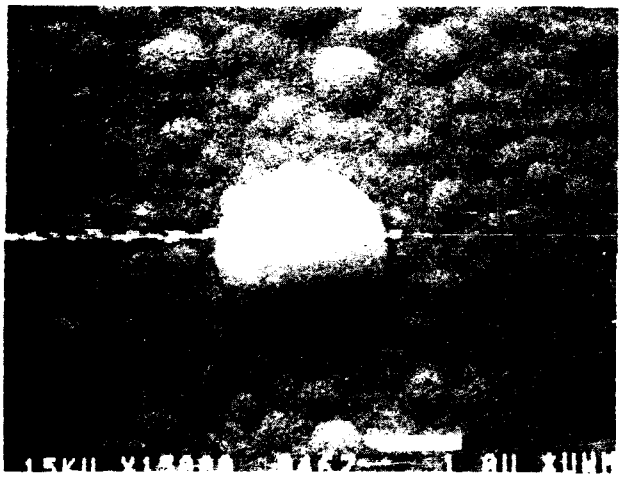

Figure 2. Protrusion (~1 μm high) in a 2 μm thick polysilicon film. The rough texture around the nodule finds its origin in the underlying silicon nitride film.

A good cleaning cycle is imperative to provide a surface having a low density of particulates and contaminants. An efficient cleaning cycle has been developed, which includes

a) ultrasonic cleaning in NH_4OH:H_2O_2:DI H_2O = 1:1:8 at room temperature to remove particulates,

b) hot sulfuric acid (180°C) to remove organic materials and oxidize the surface which is subsequently removed in dilute hydrofluoric acid (DI H_2O:HF = 50:1),

c) hot ammonia and peroxide solution (NH_4OH:H_2O_2:DI H_2O = 1:1:6 at 75-80°C) to further remove organics and certain metals,

d) final HF etch (50:1) to create a freshly etched surface prior to deposition.

Quenching, or dilution rinses are absolutely necessary after HF and ammonia steps to keep surface contamination and particulates down. All rinses have been done in ultrapure water. The WCAM DI water system consists of a reflux still, a titanium holding tank, a 5,000 MW continually rinsed cutoff filter and an all-Teflon distribution system. Water quality typically has zero plate count and measures 18.9 MΩ-cm at 21°C. Quartz and Teflon beakers and holders are used. Wafer transfers and final loading are done in class 100 or better clean room conditions.

Deposition

The polysilicon depositions are done in an LPCVD reactor. A schematic of the system used for this work is shown in Figure 3. It has been assembled from various available equipment with several custom-designed pieces. The LPCVD tube is a standard 110 mm O.D. x 105 mm I.D. quartz process tube, 70" long. The ends have no special treatment. The tube is installed in a Lindberg Omega 1 3-stack furnace. The front and rear doors are made from stainless steel, with a double O-ring seal and aluminum outer nuts. The doors are water cooled. The pump is a Leybold-Heraus D60AC mechanical two-stage pump, with appropriate traps and N_2 purge. Process pressure is monitored with a 1000 mTorr Baratron gauge and a Hastings thermocouple gauge.

Nitrogen is available for purging, venting and for throttling the pump. Nitrogen and silane are controlled with Tylan FC260 Mass Flow Controllers (MFC) and a Tylan Tymer 16 sequencer. Flow controllers are downstream from the shut-off valves. The range on the silane MFC is 0-100 sccm and 0-1000 sccm on the nitrogen MFC. The silane gas line can be evacuated directly to the pump. The silane lines are set up to allow slow and controlled application of silane at the beginning of the deposition cycle with no surges and for fast shutoff after deposition.

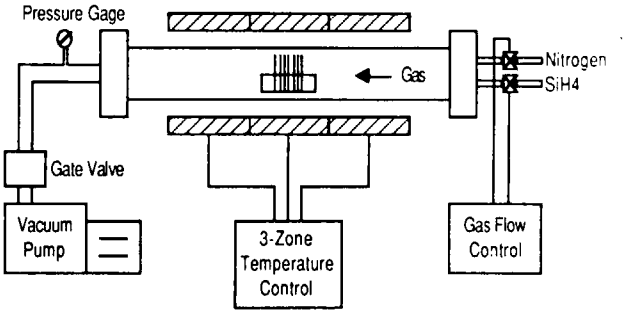

Figure 3. Schematic of the LPCVD reactor.

The reactor is normally pumped down, with modest nitrogen

purging to prevent backstreaming from the pump. Predepositions are required on the cradle and tube prior to deposition.

Wafers are placed concentric with the tube, facing the front of the system at a predetermined location. Two dummy wafers are placed in front of and behind the process wafers, with a 4 mm spacing between all wafers. The tube is pumped down and purged with nitrogen. All gas lines and the tube are purged, and checked for leaks, as excessive leak rates result in poor depositions. Surges in silane flow into the tube must be avoided. A controlled, slow application rate where the operating condition is reached in 20-30 seconds with little or no overshoot is necessary while the initial layers of polysilicon are being formed. To increase the deposition rate the silane flow rate must be raised in the same, controlled manner. Nitrogen can be injected at the pump inlet to raise the tube pressure, thereby increasing the deposition rate. After deposition, silane gas flows are reduced to zero as quickly as possible and nitrogen purging is completed before wafers are removed.

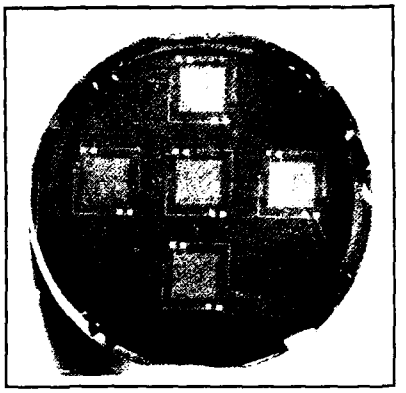

Figure 4. Piezoresistive microphones on a 3" silicon wafer. Polysilicon plates 1.0 cm x 1.0 cm with a thickness of 2.0 μm are decorated with boron implanted polysilicon piezoresistors. The resistors are passivated with a silicon nitride layer. The diaphragms are formed by etching the wafer in EDP^2 from the backside prior to metallization.

Post Deposition Treatment

As-deposited polysilicon films are under high compression. Anneal cycles are needed to achieve tensile strain in the films. Annealing takes place in a second quartz process tube. Wafers are placed in the tube at the deposition temperature (580°C) and are ramped to the the desired anneal temperatures. Intermediate anneal temperatures result in tensile films. Long, high temperature anneals result in increasingly lower strain fields. For more details, see Figure 2 in reference [1].

Applications of Tensile Polysilicon Films

Tensile polysilicon films allow the fabrication of large aspect ratio structures. Several structures have been fabricated in our lab. These include:

1) piezoresistive microphone (Figure 4)
2) large area diaphragms for X-ray mask blanks (Figure 5)
3) diaphragms perforated with holes (Figures 6a and 6b)
4) long thin beams and tuning forks (Figure 7).

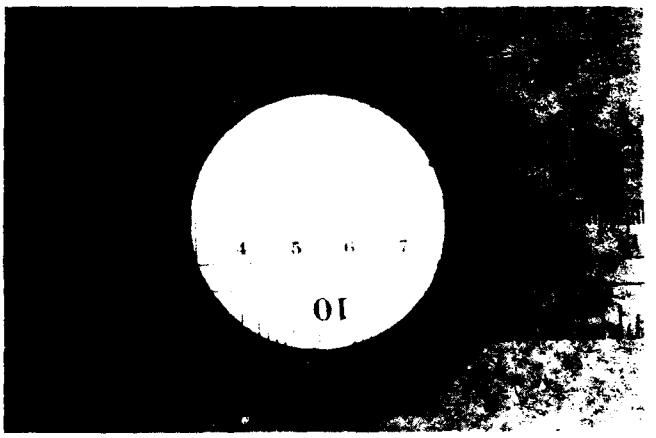

Figure 5. Large area polysilicon diaphragm in a 3" wafer. The diaphragm is 47 mm in diameter and 2 μm thick. It is formed by etching the substrate from the backside in EDP. The poly film is sandwiched between two layers of silicon nitride (each 2500Å thick) for protection against the etchant. The ruler is visible through the diaphragm which is light orange in color.

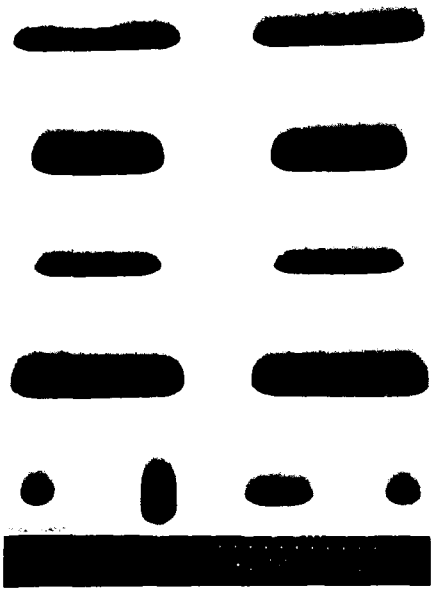

(a)

(b)

Figure 6. Perforated polysilicon diaphragms. Holes are etched into the polysilicon film in an RIE reactor with CF_4 gas using a sputtered chromium layer as an etch mask. Subsequently, the chromium is removed and a protective silicon nitride layer is deposited. The diaphragms are then formed by etching from the backside using EDP. The nitride is stripped in HF to produce the result shown in (a). The micrograph in (b) shows holes fabricated as in (a), that are "backfilled" with LPCVD nitride to reduce their size.

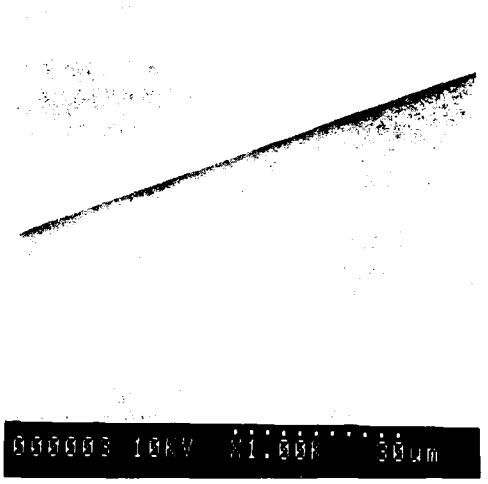

Figure 7. Doubly supported tuning fork. This structure is 520 μm long, 5 μm wide, 2 μm thick and is suspended 1.3 μm above the wafer surface. The slot is 400 μm long and 1 μm wide. Further processing is required to complete the device.

Discussion and Conclusions

An optimized process produces 2 μm thick films with low defect density and a smooth surface. Optical techniques show 8Å haze and less than 50 defects at 0.5 μm aperture per 3" wafer.[3]

Our experience with large aspect ratio devices exemplifies the importance of low defect densities, uniform properties and tensile strain fields. Defects in the films can cause fracturing of large diaphragms during formation. Patterning of sub-micron features may require hard contact printing necessitating nodule-free films to avoid mask damage and/or loss of resolution. Nonuniform properties can lead to local distortions which are not as apparent on smaller structures. Lack of a tensile strain field will result in mechanical instability, e.g. buckling of large plates.

References

[1] H. Guckel, D. W. Burns, H. A. C. Tilmans, D. W. DeRoo and C. R. Rutigliano, "Mechanical Properties of Fine Grained Polysilicon - The Repeatability Issue," 1988 Solid-State Sensor and Actuator Workshop, Hilton Head Is., SC, June 6-9, 1988.

[2] A. Reisman, M. Berkenblit, S. A. Chan, F. B. Kaufman, and D. C. Green, "The Controlled Etching of Silicon in Catalyzed Ethylenediamine-Pyrocatechol-Water Solutions," J. Electrochem. Soc., Vol. 126, No. 8, pp. 1406-1415, Aug. 1979.

[3] P. M. Zavracky, Kopin Corp., Taunton, MA, private communication, 1987.

AS-DEPOSITED LOW-STRAIN LPCVD POLYSILICON

L. S. Fan and R. S. Muller

Berkeley Sensor and Actuator Center
An NSF/Industry/University Cooperative Research Center
Department of Electrical Engineering and Computer Science
and the Electronics Research Laboratory
University of California, Berkeley CA 94720

Abstract

As-deposited polysilicon films with very low residual strain (lower than 5×10^{-5}) are obtained by a low-pressure, chemical-vapor-deposition (LPCVD) process. Straight polysilicon bridges 300 μm long, 1.2 μm thick, and 2 to 20 μm wide, have been made using this process. No buckling has been observed in any of the nearly one-thousand bridges of this type made in two separate process runs. In addition, no problems of sticking between the bridges and the substrate were encountered with these structures.

Introduction

Doped polysilicon films as deposited in conventional *IC* technology are typically under compressive stress in the -3×10^{-3} range [1,2]. This stress can easily cause mechanical microstructures such as bridges and diaphragms to buckle. The origin of this residual stress is uncertain. Thermal mismatch can account for about 10^{-4} strain; other mechanisms, possibly associated with grain-boundary effects, must be present to explain the order-of-magnitude larger residual strain. In principle, interstitial atoms, substitutional foreign atoms, dislocations and grain boundaries can all contribute to the strain field inside thin films. Compressive strain in polysilicon films can be reduced to the 10^{-4} range by high-temperature annealing [3]. This paper discusses a process which produces low-strain films without requiring a high-temperature annealing process.

As-deposited polysilicon films with very low residual strain (evidently lower than 5×10^{-5}) are obtained by an LPCVD process. Straight polysilicon bridges 300 μm long, 1.2 μm thick, and 2 to 20 μm wide, made using this process are shown in Figure 1. Roughly a thousand bridges of this type were made in two separate process runs and none of these were observed to buckle. In addition, no problems of sticking between the bridges and the substrate were encountered with these structures. According to theory presented by Guckel *et al* [3], a beam having these dimensions would buckle if the average strain in the polysilicon were larger than 5.3×10^{-5}

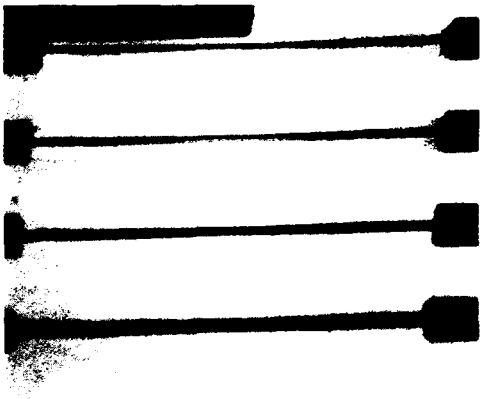

Figure 1 SEM photograph of four polysilicon bridges made with low-strain polysilicon. The bridges are 300 μm long, 1.2 μm thick, and 2, 5, 10, and 20 μm wide.

Deposition Process and Microstructure

The polysilicon films from which the beams were fabricated were deposited by pyrolyzing silane at 605°C on a phosphosilicate-glass (PSG) layer (8 wt. % P) in a hot-wall reactor. The PSG serves as a sacrificial layer to be subsequently etched away to free the bridge [4]. Typical deposition rates for this extremely low-strain polysilicon are 9 nm per minute at 320 mTorr. The 605°C deposition temperature is within the range of reported transition temperatures between amorphous and polycrystalline silicon [5]. Instead of an amorphous structure, the films are polycrystalline with a preferred [111] orientation normal to the substrate.

Evidence for the [111] orientational preference is seen in the x-ray diffraction scan of Figure 2. No peak is seen in the diffraction pattern corresponding to the [110] direction although [110] orientation dominates diffraction-scan patterns for polysilicon films deposited at 630°C, a temperature frequently employed for conventional *IC* processing. Peaks corresponding to orientations along the [311] and [100] directions, also plainly evident for 630°C polysilicon, are not seen in Figure 2. The [111] structure is temperature stable and the orientational preference appears to improve after annealing (900°C in N_2 for one hour) as shown in Figure 3.

TH0215-4/88/0000-0055

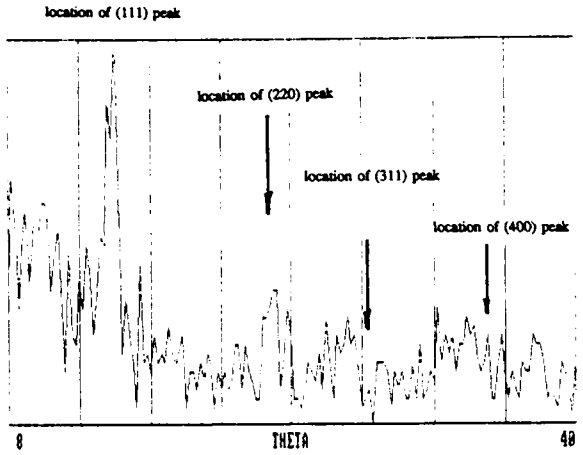

Figure 2 X-ray diffraction scan of an as-deposited polysilicon film (Cu-Kα source).

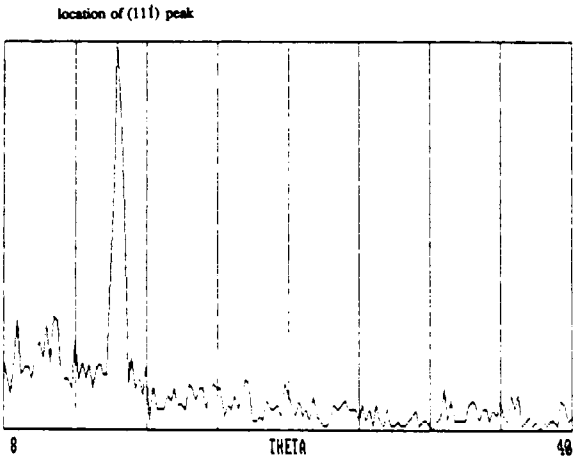

Figure 3 X-ray diffraction scan of the same film as used in the measurement of Figure 2 after N_2 annealing at 900°C for one hour.

Murarka and Retajczyk have shown that the incorporation of phosphorus is an important influence on the structure of polysilicon films [1]. Analysis of the dopant content in our low-strain films has shown the presence of phosphorus which may influence grain growth to a preferred (111) direction [6]. Spreading-resistance profiles on angle-lapped sections of a sample unannealed film are shown in Figure 4. Although there is no evidence of phosphorus diffusion into the silicon substrate in Figure 4, a retrograde profile is clearly visible in the polysilicon.

The phosphorus seems to play a role in the initial phases of grain growth. We have found that polysilicon deposited on undoped oxide at the same temperature is amorphous (by x-ray diffraction). However, phosphorus incorporation alone can not explain the low-strain in these films. We have also deposited polysilicon films at 625° C on PSG (8 wt.% P), and these (110) textured films show compressive strain in the -3×10^{-3} range as evidenced by buckled beams of 50 μm in length.

An experiment has been carried out to show that the phosphorus is incorporated in the polysilicon during its growth instead of diffused afterward. A PSG layer was deposited on top of a sample of the low-strain polysilicon and the wafer was then annealed in nitrogen at 600° C for three hours. No observable diffusion of phosphorus into the polysilicon from the overlying PSG was found by spreading-resistance profiling. This suggests that the phosphorus is incorporated during film deposition. The only possible sources for the phosphorus are out-diffused vapor from the PSG or doped polysilicon left on the furnace-tube wall. The furnace is used for deposition

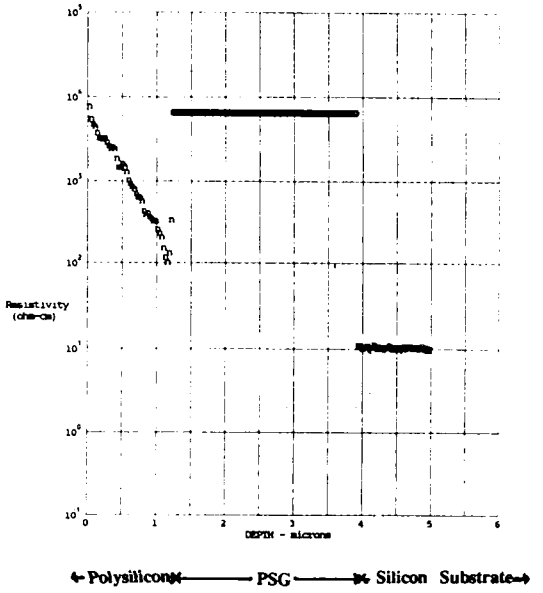

Figure 4 (a) Resistivity profile of an unannealed, angle-lapped polysilicon film (.0057 bevel angle).

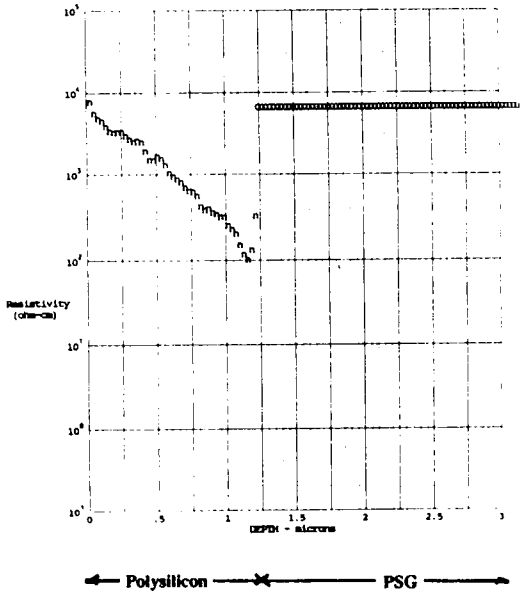

Figure 4 (b) Enlarged portion of the resistivity profile of Fig. 4(a) showing details of the phosphorus density in the polysilicon film (.0057 bevel angle).

of *in-situ* doped polysilicon as well as for undoped films. The second possibility has not been completely eliminated although pre-coating the tube wall with a layer of undoped polysilicon is carried out before deposition.

Mechanical Properties

Since the microstructure of this film is different from that of conventionally deposited (110) films, we can expect the Young's modulus to be different. For all classes of cubic crystals, Young's modulus E_Y can be expressed as a function of orientation

$$1/E_Y = s_{11} - 2\left[s_{11} - s_{12} - \frac{1}{2}s_{44}\right]\left(l^2_1 l^2_2 + l^2_2 l^2_3 + l^2_3 l^2_1\right) \quad [1]$$

where s represents elastic compliance, and l is the directional cosine of the orientation. For all orthogonal directions l within {111} planes, the value inside the second bracket of Eq. (1) is constant at 0.25. Therefore, the in-plane Young's modulus E_Y is a constant for crystallites oriented with {111} planes parallel to the substrate surface. Furthermore, the shear modulus G is also a constant for films under the conditions stated above.

$$G = \frac{1.5}{s_{11} - s_{12} + s_{44}} \quad [2]$$

If both the Young's modulus and the shear modulus are known, the Poisson's ratio (for isotropic materials) can be calculated.

$$\nu = \frac{E_Y}{2G} - 1 \quad [3]$$

The elastic properties of the film can be estimated from single-crystal elastic constants, given that the x-ray diffraction peak from {111} planes is the only strong peak observed normal to the substrate. For a [111]-oriented film, irrespective of the detailed distribution of crystallites in the lateral directions, the in-plane Young's modulus E_Y and the shear modulus G can be estimated using Eqs. (1) and (2). Any effects of grain boundaries are assumed negligible in this estimate. For silicon, the elastic compliances in Eqs (1) and (2) are $s_{11} = 0.768 \times 10^{-11}$ Pa^{-1}, $s_{12} = -0.214 \times 10^{-11}$ Pa^{-1}, and $s_{44} = 1.256 \times 10^{-11}$ Pa^{-1}.

Using Eqs. (1), (2), and (3), we find E_Y = 169 GPa, G = 67 GPa, and ν = 0.262.

In order to compare this low-strain polysilicon with conventionally processed material, fabrication runs were carried out to produce a series of micromechanical elements with both types of polysilicon. Figure 5 (low-strain polysilicon) and Figure 6 (conventionally deposited polysilicon) are Nomarski

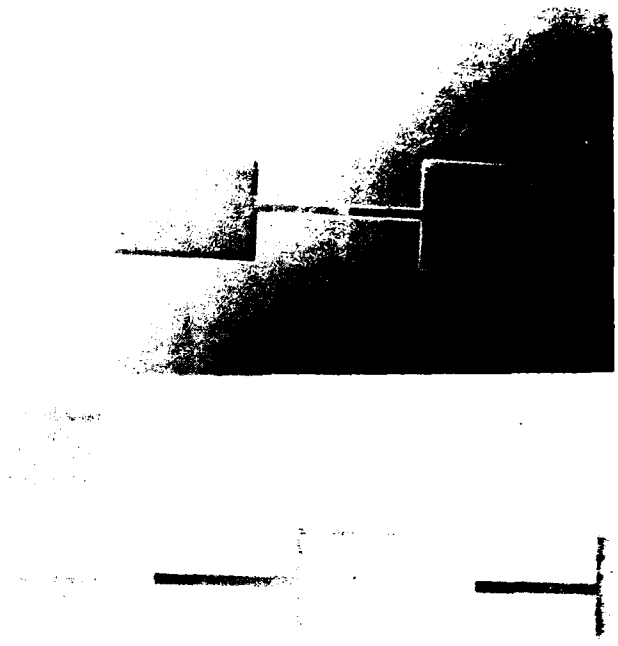

Figure 5 Nomarski phase-contrast images of beams made with low-strain polysilicon. The pedastals for these structures consist of 3 μm-thick PSG. The doubly supported beam has a 300 μm span and the cantilever is 260 μm long.

Figure 6 Micromechanical beams made using the same mask set as for the structures in Figure 5 with conventional *IC* polysilicon. The increased surface roughness of this polysilicon contrasts with the surface of the material in Figure 5.

phase-contrast images of two of the structures produced-- doubly supported and cantilever beams (300 and 260 μm in length, respectively). The beams were fabricated on a sacrificial layer of PSG 3 μm thick. If we compare the structures in the two pictures, the nearly uniform shading of Figure 5 gives evidence of the near planarity of the polysilicon surface in contrast to the darkened images of the polysilicon beams in Figure 6. The darkening is caused by the upward bending of the beams which makes them out of focus. By focusing adjustment of the microscope, we estimate that the cantilevers in Figure 6 are bent upward about 16 μm at their free ends. It is difficult to apply the same method to the beams in Figure 5 because there is so little apparent bending. They do, however, appear to be bent downward a very small amount (in the order of 1 μm). This slight bending downward may be the result of the observed retrograde phosphorus doping profile. Since phosphorus doping correlates with reduced compressive stress [1], stress near the PSG layer would be reduced below that at the surface, causing the cantilever beams to bend downward.

The average roughness of the low-strain films has been measured with a surface profilometer (Alpha Step 200) to be about 4.5nm. In contrast, the roughness of the conventional polysilicon is 8.5nm.

Conclusions

Low-strain polysilicon films can be produced by a silane deposition process without the necessity of high-temperature annealing. Films laid down using this process show a different preferred orientation and latent bending moment than those found in polysilicon produced in conventional *IC* depositions. Phosphorus is observed to be present in the films, although it is not intentionally used in the process. At this point, a clear cause-and-effect relationship between the phosphorus incorporation, selective [111] orientation, and low strain in the polycrystalline silicon films has not been established. Research is aimed at obtaining an understanding of these relationships through consideration of the role of interfacial stresses and the kinetics of initial crystallite nucleation is underway. Based only on the observed [111] orientation it is possible to make an estimate of the in-plane Young's modulus, shear modulus, and Poisson ratio. Although crystallite orientation is probably the dominant mechanism determining these parameters, other factors such as grain-boundary effects and imperfections can be expected to modify the estimated values in practice. Because no high-temperature annealing steps are required to produce these films, they can be applied advantageously to integrated systems of electronic devices and micromechanical structures.

Acknowledgements: We thank Professors George Johnson and Ping Ko for valuable discussion, Professor Rudy Wenk for assistance in x-ray diffraction, Katalin Voros, Bob Hamilton, Kim Chan and others on the staff of the Berkeley Microfabrication Laboratory for help in carrying out this research.

References

[1] S. P. Murarka and T. F. Retajczyk, Jr., "Effect of phosphorus doping on stress in silicon and polycrystalline silicon," *J. Appl. Phys. 54*, 2069-2072 (1983).

[2] M.S. Choi and E.W. Hearn," Stress effects in boron-implanted polysilicon films," *J. Electrochem. Soc.*, Vol. 131, pp.2443-2446 (1984)

[3] H. Guckel, D.W. Burns, C.R. Rutigliano, D.K. Showers and J. Uglow, "Fine grained polysilicon and its application to planar pressure transducers," *Transducers '87, 4th Int. Conf. on Solid-State Sensors and Actuators*, IEEE and Electrochem. Soc., Tokyo, Japan, 277-282, (June 1987).

[4] R.T. Howe and R.S. Muller, "Polycrystalline Silicon Micromechanical Beams," *1982 Spring Meeting of the Electrochemical Society,* Montreal, Canada, (May 9-14, 1982).

[5] T. I. Kamins, "Structure and properties of LPCVD silicon films," *J. Electrochem. Soc., 127*, 686-690 (1980).

[6] Y. Wada and S. Nishimatsu, " Grain growth mechanism of heavily phosphorus-implanted polycrystalline silicon," *J. Electrochem. Soc., 125,1499 (1978)*

[7] H.J. McSkimin and P. Andreatch, Jr., "Elastic moduli of silicon to hydrostatic pressure at 25.0°C and -195.8°C," *J. Appl. Phys.*, 35, 2161-2165 (1964).

SURFACE-MICROMACHINING PROCESSES FOR ELECTROSTATIC MICROACTUATOR FABRICATION

Theresa A. Lober and Roger T. Howe†

Microsystems Technology Laboratories
Dept. of Electrical Engineering and Computer Science
Massachusetts Institute of Technology
Cambridge, Massachusetts 02139

ABSTRACT

Surface-micromachining, the selective etching of multiple layers of deposited thin films, is essential for silicon microactuator fabrication. This paper presents a study of the etch characteristics of three forms of hydrofluoric acid, used as the micromachining etchant for fabricating a rotory variable-capacitance micromotor structure from polycrystalline silicon (poly-Si) thin films. Low pressure chemically vapor deposited SiO_2 (LPCVD LTO) is used to form the sacrificial layers and LPCVD Si_3N_4 is used as an electrical isolation layer for the micromachined structure. 7:1, NH_4F:HF buffered HF (BHF), 48 wt% concentrated hydrofluoric acid (LHF), and HF vapor in air (VHF) are evaluated at 20° C for etch rate and selectivity, and attack of four types of LPCVD poly-Si films: $POCl_3$-doped or undoped, with or without 1150° C annealing. Both BHF and VHF are found to damage $POCl_3$-doped poly-Si films, possibly by attack of grain boundaries. VHF is found to be effective for micromachining suspended structures since it avoids deformation of microstructures due to surface tension effects during drying after wet etching with LHF or BHF.

INTRODUCTION

Movable micromechanical parts, such as gears and turbines, have been fabricated recently from poly-Si thin films [1,2]. A means of applying forces to these movable structures is necessary if they are to perform useful mechanical work. Force-scaling calculations and materials compatibility with silicon technology argue for electrostatic actuation of micromechanical structures [3,4]. Of the various electrostatic motor configurations, the variable-capacitance type is attractive for an initial microfabrication study because it requires only conducting and insulating films [3].

Figure 1 illustrates the basic structure of the preliminary rotary, two-pole, three phase variable capacitance micromotor structure [3]. The sandwich of structural poly-Si and sacrificial LTO layers is shown schematically in Fig. 1(a) prior to the micromachining etch, while Fig 1(b) depicts the released structure. The segmented stator consists of overhanging poly-Si cantilevers which are dielectrically isolated from the silicon surface by a sandwich of LPCVD Si_3N_4 and thermal SiO_2. The poly-Si stator film is also used to fabricate a pin bearing to further confine the poly-Si rotor. In this preliminary structure, a torque can be applied to the rotor by sequential phasing of the voltage on the stator electrodes. The vertical electrostatic force attracting the rotor to the stator [3] may cause friction and electrical shorting of the stator pieces by conduction through the rotor.

This paper investigates surface-micromachining technology for fabricating the simple micromotor structure shown in Fig. 1. Characterization of this technology is critical, since the micromotor structural design is constrained by the etch rate and selectivity of the etchant used to release the microstructure by removing the sacrificial layers. The etch system must completely remove the oxide spacer films while leaving sufficient insulating Si_3N_4 and preserving the surface condition of the conducting, poly-Si structural layers. Additionally, the etching process should not produce residues or contribute to structural deformation through surface tension effects.

†Berkeley Sensor & Actuator Center, Dept. of Electrical Engineering and Computer Sciences. University of California, Berkeley, California 94720

Two types of wafers are fabricated for this study. The first contains complete micromotor structures and singly and doubly-supported poly-Si beams. The second type contains only patterned micromotor rotors from a single poly-Si layer deposited on various films on the substrate. Four poly-Si process conditions are evaluated: undoped, unannealed and annealed; and doped, unannealed and annealed. Three micromachining etchants are compared in this study to release the poly-Si structures: 48 wt% hydrofluoric acid (LHF), 7:1, NH_4F: HF buffered HF (BHF), and HF vapor in air (VHF). Relative etch rates of unpatterned LTO layers, LTO spacer layers, and the LPCVD Si_3N_4 insulating layer are measured by releasing the microstructures fabricated on the first set of sample wafers with the three HF etchants. Structural attack of LPCVD poly-Si films is evaluated as a function of process conditions and underlying films by exposing the second group of sample structures to the three HF etchants. Together, these experiments are utilized to determine the potential of poly-Si to act as both an electronic and structural material for micromachined structures.

FABRICATION PROCESS

The process sequence for fabrication of the preliminary micromotor structure and the first set of wafer samples, with the exception of the final micromachining etch, is a subset of the MIT Baseline CMOS process [5]. Compatibility with this IC process constrains the film deposition conditions, thicknesses, and doping levels of the microstructures. Silicon wafers (n-type, 2 ohm-cm resistivity) of <100> orientation are first oxidized to grow a 400 Å-thick thermal stress-relief SiO_2 layer. This is followed by a 1500 Å-thick LPCVD silicon nitride film, deposited by reacting dichlorosilane and ammonia at 800° C and a pressure of 400 mT. The first LTO spacer layer, 0.5 µm-thick, is then deposited at 400° C and 250 mT with a reaction of silane and oxygen. Silane is reacted at 250 mT and 625° C to deposit the first LPCVD polysilicon structural layer, 5000 Å-thick, on the LTO spacer. This polysilicon film is phosphorus-doped during a 60 minute, 925° C diffusion cycle using a $POCl_3$ liquid diffusion source in a nitrogen ambient. Rotor structures are then patterned and anisotropically etched in the polysilicon film using a CCl_4 plasma. The second LPCVD LTO spacer, 1 µm-thick, is deposited on these patterned structures, and trenches are patterned and plasma etched through both LTO layers to expose the nitride-coated substrate. A final poly-Si film, either 0.5 or 1 µm-thick, is then deposited and doped

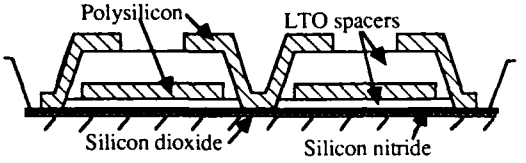

Figure 1(a). Sandwich of films creating the micromotor

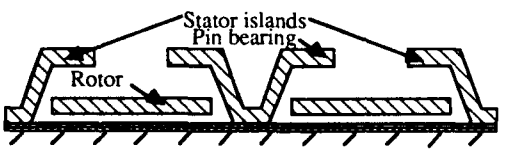

Figure 1(b). Released micromotor structure

during a second $POCl_3$ diffusion cycle. This second poly-Si layer is patterned and plasma etched to define the 1 μm-thick micromotor pin bearing and stator islands, as well as 0.5 μm-thick singly and doubly-supported micro-beams. Finally, the sandwich of patterned LTO and poly-Si films is annealed in a nitrogen ambient at 1150° C for 20 minutes to reduce residual stress in the polysilicon films. The completed set of wafers is split into three groups; each group to be released by one of the HF etchants.

The second set of test structures, utilized to characterize the attack of thin poly-Si films by HF the micromachining etchants, is fabricated using a subset of the first process sequence. Micromotor rotor patterns are plasma etched in 5000Å-thick poly-Si films for four film process conditions: undoped, unannealed and annealed; and doped, unannealed and annealed. Each type of film is deposited on the following materials:

1)1 μm-thick, 1.8 wt% $POCL_3$-doped thermal oxide;
2)1 μm-thick LTO;
3)1500 Å-thick silicon nitride;
4)1000 Å-thick undoped thermal oxide;
5)lightly doped single crystal silicon.

As with the micromotor wafers, the second set of test wafers is split into three groups for exposure to the three micromachining etchants. Wafers to be etched in BHF or LHF are placed into a 1000 ml teflon beaker containing the etch bath. After etching, wafers are rinsed first in deionized (DI) water for 5 minutes, then in methanol for 2 minutes, and then dried in air under a chemical hood. Wafers to be etched with VHF are suspended 1 cm above the surface of 1000 ml of LHF in an air flow of 28 l/min. No rinsing or drying of VHF-released samples is required; however, removal of nonvolatile etch products may require a DI water rinse.

EXPERIMENTAL RESULTS

Timed etches are completed on the micromotor sample wafers and the singly and doubly-supported beams to determine HF, BHF, and VHF etch rates for unpatterned LTO and Si_3N_4, and LTO spacer layers under 5000Å-thick polysilicon films. The etch front, and thus the etch rate, of spacer layers under 5000 Å-thick poly-Si structures can be visually monitored, since polysilicon is transparent at that thickness. Table I tabulates the measured etch rates, which indicate that VHF provides the highest etch selectivity, ≈ 90:1, between undercutting LTO spacer layers and unpatterned silicon nitride.

Etchant \ Material	Silicon nitride	Unpatterned LTO	LTO spacer
BHF	7 - 12 Å/min	700 Å/min	570 Å/min
LHF	140-175Å/min	10500 Å/min	7800 Å/min
VHF	85-125Å/min	15000 Å/min	8400 Å/min

Table I. Etch rates of the three micromachining etchants

Timed etches using the three HF etchants are also completed with the second set of wafers, containing the poly-Si rotor structures, after which the samples are inspected for attack of the poly-Si films by each etch system. Three distinct phenomena are observed: *i)* LHF does not noticeably attack poly-Si films, regardless of doping and annealing history or the underlying film; *ii)* BHF and VHF attack $POCl_3$-doped, 5000 Å-thick poly-Si films to a degree dependent on anncaling condition and underlying materials; and *iii)* undoped poly-Si films, unannealed or annealed, are not attacked by any of the etchants. By "attack," is meant nonuniform, isolated etching completely through the poly-Si film, appearing to occur at grain boundaries. The SEM in Fig. 2(a) illustrates this condition on a doped and annealed poly-Si rotor, deposited on LTO, which was exposed to VHF for 15 minutes. Figure 2(b) depicts the same film after VHF exposure for 30 minutes.

Table II compares the degree of poly-Si attack by BHF and VHF for each of the five layers used as the underlying material for the poly-Si films, as listed above. The greatest degree of attack occurs to annealed films deposited on $POCl_3$-doped oxide, while no noticeable attack occurs to films

Figure 2(a). Poly-Si film attack after 15 min VHF exposure

Figure 2(b). Poly-Si film attack after 30 min VHF exposure

deposited on single crystal silicon or undoped thermal oxide. Attack of poly-Si films deposited on LTO is worse than for films deposited on Si_3N_4, and annealed films are more susceptible to the nonuniform etch than unannealed films. These observations suggest that the poly-Si attack mechanism is dependent on grain configuration and size, which is determined by the material underlying the poly-Si layer and the temperature of the poly-Si deposition.

Underlying material	Doped unannealed	Doped annealed
Silicon	—	—
1000 Å thermal oxide	—	—
1500 Å silicon nitride	+	+
1 μm LTO	+++	++++
1 μm doped thermal oxide	++++	+++++

Table II. Attack of poly-Si for different underlying layers

The following reaction models describe the etching of silicon dioxide and silicon nitride, respectively, when water is present as a catalyst:

$$SiO_2 + 4HF + 2H_2O \rightarrow SiF_4 + 4H_2O \quad (a)$$

$$3H_2O + 2Si_3N_4 + 18HF \rightarrow 3SiF_4 + 8NH_3 + 3SiOF_2. \quad (b)$$

These models describe both liquid and vapor etching of the films. Products of the silicon dioxide etch are volatile; they are removed by either the liquid solution of BHF and LHF or the air flow of VHF. The silicates ($SiOF_2$) produced by the silicon nitride etch are removed by liquid etch solutions, but not by the VHF air flow; thus, vapor etching of silicon nitride results in the deposition of a uniform layer of silicate "dust" on the nitride surface. Fig. 3 illustrates this dust in the field regions of the SEM, showing a poly-Si film on a nitride surface. This dust appears to mask the nitride from oxidation, thus slowing its etch rate below that for LHF, as shown in Table I [6]. The dust particles are removed by DI rinsing of the etched samples, but not by air flow.

Figure 3. Silicate dust from VHF-etched nitride

U. of VHF rather than either of the liquid etchants to release suspended structures appears to eliminate possible structural deformations due to surface tension effects during drying of the microstructures. Comparison of the LHF-etched cantilever beams shown in Fig. 4(a), ranging in length from 100-250 µm , and the same VHF-etched geometries in Fig. 4(b) suggests that the removal of liquid etch and rinse solutions from under suspended structures may cause deflections unattributable to built-in bending moments, and may produce surface conditions causing the suspended structures to stick to the substrate. During the vapor etch of unsupported structures, however, insufficient air flow may permit condensation under and around the releasing structure. Figure 5 illustrates this condition with a VHF-released poly-Si rotor which is stuck to the silicon substrate by the condensed liquid at its periphery.

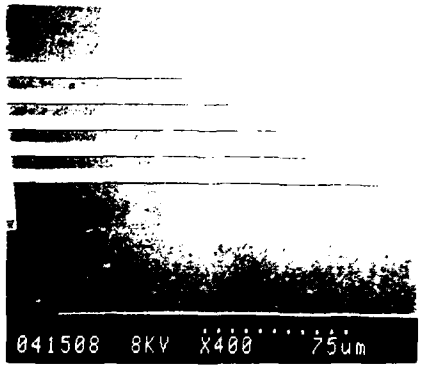

Figure 4(a). 100-250 µm-long LHF-released cantilevers

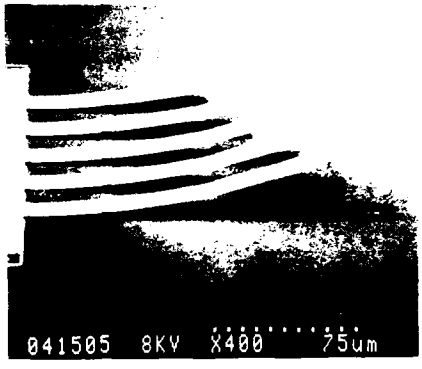

Figure 4(b). 100-250 µm-long VHF-released cantilevers

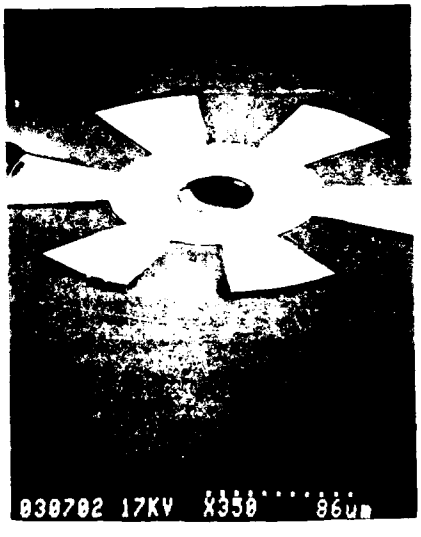

Figure 5. VHF-released poly-Si rotor

CONCLUSIONS

The selectivity of all three etchants between LTO and Si_3N_4 is found to be insufficient to release the preliminary micromotor structure while preserving the Si_3N_4 dielectric isolation under the stator anchors. In addition, BHF and VHF attack the $POCl_3$ doped poly-Si motor components. The SEM shown in Fig. 6 of a micromotor structure released in LHF indicates that the rotor and stator structures are completely released and that the nitride and oxide films have been removed from the field areas. Although VHF release avoids surface tension-related structural deflections, it produces an accumulation of silicate dust within the micromotor periphery which is difficult to remove without a liquid rinse.

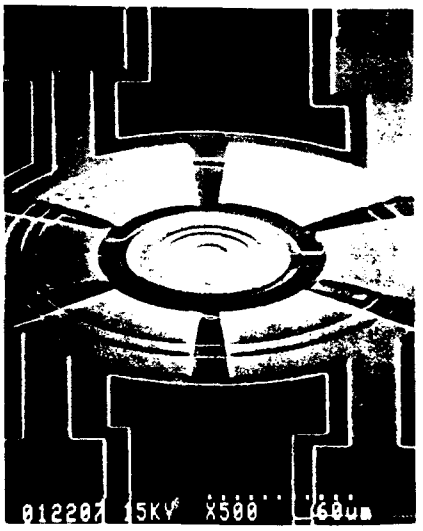

Figure 6. Poly-Si micromotor structure released with LHF

Given its attack by BHF and VHF, $POCl_3$ doped and 1150° C annealed poly-Si films are not attractive for micromachining applications. Heavy doping of the film is done in the preliminary fabrication sequence to achieve high conductivity for charge induction in the rotor structure, while high temperature annealing is completed to reduce built-in stresses of the micromachined structures. Thus, additional research is needed to develop poly-Si process conditions and micromachining etch systems for microactuator fabrication. For undoped, unannealed poly-Si films, VHF provides an attractive technique for releasing suspended micromachined structures while avoiding structural deflection due to liquid-induced surface tension effects.

ACKNOWLEDGEMENTS

The authors would like to acknowledge Prof. Rosemary L. Smith for initially suggesting the use of vapor HF as a micromachining etchant, and Prof. Stephen D. Senturia for many helpful technical discussions and a critical reading of the manuscript. This work was supported in part by the Power Electronic Collegium of the MIT Laboratory for Electromagnetic and Electronic Systems, and by the National Science Foundation, under contract ECS-8614328. Fabrication of all test structures was completed in the MIT Integrated Circuits Laboratory of the Microsystems Technology Laboratories. The authors thank Paul Maciel, Joe Walsh, and Mike Schroth for process development assistance.

REFERENCES

[1]L.S. Fan, Y.C. Tai, and R.S. Muller, "Pin joints, gears, springs, cranks, and other novel micromechanical structures," in Technical digest, International Conference on Solid-State Sensors and Actuators, Tokyo, Japan, pp. 849 - 852, 1987.

[2]K.J. Gabriel, W.S.N. Trimmer, and M. Mehregany, "Micro gears and turbines etched from silicon," in Technical digest, International Conference on Solid-State Sensors and Actuators, Tokyo, Japan, pp. 853 - 856, 1987.

[3]S.F. Bart, T.A. Lober, R.T. Howe, J.H. Lang, and M.F. Schlect, "Design considerations for microfabricated electric actuators," Sensors and Actuators , at press.

[4]W.S.N. Trimmer and K.J. Gabriel, "Design considerations for a practical electrostatic micro-motor," Sensors and Actuators, 11, vol. 11, pp. 189 - 206, 1987.

[5]P.K. Tedrow and C.G. Sodini, "The MIT twin-well CMOS process," Microsystems Technology Laboratories Report, 1988.

[6]T.A. Lober, "A microfabricated electrostatic motor design and process," MIT EECS Dept., S.M. Thesis, 1988.

GNAT ROBOTS: A LOW-INTELLIGENCE, LOW-COST APPROACH

A. M. Flynn

MIT Artificial Intelligence Laboratory
545 Technology Square
Cambridge, MA 02139

Abstract

Mobile robots today are not very intelligent, mostly due to limitations in sensing and perception. Worse than that, this low level of sophistication is very expensive. In order to make automation technology more generally useful, we propose not only to continue trying to build increasingly intelligent robots, but to also produce a line of robots which freeze the intelligence at a level which we can attain today and build cheap, mass-producible machines. The idea is that while a technology costing $80,000 for a certain level of sophistication may not be desirable, that same level of intelligence may be useful at twenty-five cents. Scaling down to integrate sensors, brains, actuators and power supplies on a single piece of silicon holds the promise of developing mass-producible, low-cost robots. Consequently however, we have to rethink how to accomplish useful tasks with low-intelligence machines.

1. Introduction

The state of the art of intelligent mobile robots is not very high. Expectations and science fiction point to wonderful contraptions, but the reality is that most mobile robots are large, expensive, klunky, rather dumb machines. The problem isn't so much with the task of writing sophisticated planning or control systems, but rather that Artificial Intelligence has run up against the hard realities of building sensing and perception systems. Either perception systems must get much better, or the whole organization of how to use sensed information to accomplish useful tasks must be rethought.

In the MIT Mobile Robot Project, we're pursuing two avenues to advance the state of the art in building intelligent, useful machines. The first is to focus on intelligence by creating *autonomous creatures* which are forced to exist in unstructured, dynamically changing environments. The second is to try to make machines more generally useful and available to people by freezing the level of intelligence we can attain now and making that technology *cheaper*. This paper focuses on that second path as shown in figure 1.

Mobile robots today are very expensive and hardly worth the investment for the level of sophistication delivered. One cause of the expense is that these machines are large and have a multitude of components from many different vendors. Although sensors and electronics have gotten less expensive and smaller over the past few years, motor and battery technology has seen no such advances. For mobile robots which are used primarily as autonomous sensors, such as sentries, guards or explorers, the extra weight and size due to large motors and batteries serves no useful purpose. Oftentimes a mobile robot will be the size of a truck, but will be guided by only a small amount of silicon - a 68000 chip and a CCD array perhaps.

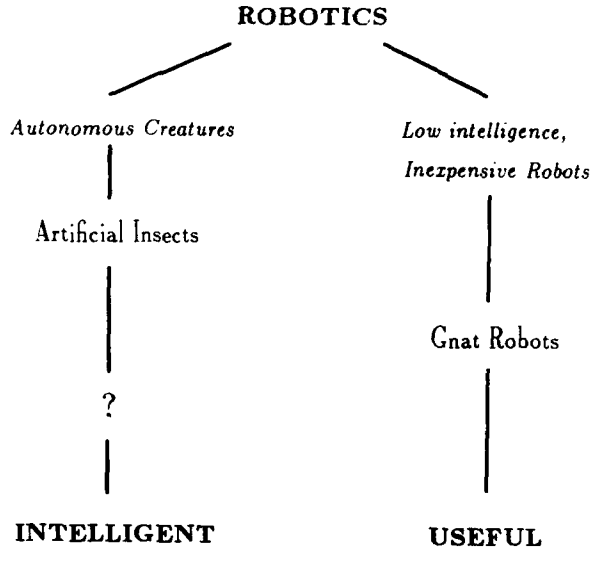

Figure 1. In an effort to produce intelligent useful robots, we've been pursuing two paths. By developing *autonomous creatures*, which are forced to exist in unstructured, dynamically changing environments, we hope to understand the mechanisms involved in building intelligence. At the same time, we feel that one way to make robots more generally useful, is to freeze the level of intelligence we can attain now and develop low-cost, mass-producible robots.

By shrinking motors and power supplies to the same scale as the more interesting parts of a mobile robot, the sensors and control systems, to create gnat-sized autonomous robots, we would not only reduce the size and cost of robots, but also open up new application areas. Now that actuators are beginning to be etched on chips [Bart, Lober, Howe, Lang and Schlecht 1987], [Trimmer and Gabriel 1987], it raises the possibility of integrating all components of a robotic system into silicon: sensors, electronics, actuators and power sources. By shrinking to this scale, we can take advantage of VLSI manufacturing technology to en-

This report describes research done at the Artificial Intelligence Laboratory of the Massachusetts Institute of Technology. Support for the research is provided in part by the University Research Initiative under Office of Naval Research contract N00014-86-K-0685, in part by a grant from the Systems Development Foundation, and in part by the Advanced Research Projects Agency under Office of Naval Research contract N00014-85-K-0124.

TH0215-4/88/0000-0063 © 1988 IEEE

Figure 2. The MIT Mobot Line presently consists of four mobile robots, all exhibiting various levels of "insect level" intelligence implemented through subsumption architectures.

able mass-production. Lowering costs is the driving function behind this proposal. The idea has an analogy with the introduction of the first eight bit microprocessor. Although simple and at not first considered useful, due to their low cost they've been enhanced and have found their way into many new applications. Similarly, by scaling down robotic technology to the chip level in order to reduce costs, we can introduce the technology to the general public and let it grow from there.

1.1 Intelligent Behavior

If the machine is cheap enough, it may be worthwhile to apply robotic technology to perform useful tasks even with the level of sophistication available now. The traditional approach to designing an intelligence architecture has been to think in terms of a hierarchical decomposition in which a global map of the environment is built by "fusing" data from various sensors. A centralized planner would then use that representation for directing robot actions. However a different approach has recently been proposed [Brooks 1986], which calls for distributed control, "sensor fission" and reactive instead of centralized planning. The idea is to use a network of processing modules which implement layers of behavior. Simple layers are built first which create complete control systems from sensed input to actuator output. Higher layers are then added on top and subsume lower levels when triggered. In this way, intelligence is built up incrementally, granting robustness to the system, because, should higher levels break, lower levels keep on working. The beauty of this approach, termed the ***subsumption architecture***, is that the computation being performed in each module is actually very simple and can be compiled down to a small number of gates. Figure 2 shows four robots which exhibit various forms of "insect level" intelligence: wandering, avoiding, looking for and collecting interesting objects, etc. Experiments with the subsumption architecture have shown that when the intelligence architecture is organized well and the computation is understood, the implementation can be made small. The two cars in the foreground of figure 2 use only single-chip PALs for brains, yet can exhibit avoid, wander and follow behaviors [Connell 1987]. We feel that this approach then is appropriate for control systems for integrated robots.

1.2 The Perception Problem: Measurement vs. Environmental Awareness

One of the biggest problems in developing intelligent mobile machines is adequately perceiving surroundings which may be new or changing, or may have uncontrolled light sources or be full of hazardous conditions. Mobile robots are demanding consumers of sensors and require that the sensors provide more than just measurement information. Complements of sensors are required to turn signals into useful symbols representing important information for environmental awareness. The capability, which is natural to humans, is deceivingly hard to instill in a robot, because a robot cannot simply sense, but has to manipulate the data and close the loop to react meaningfully.

Robotics is about building complete systems and there are two approaches to organizing the way sensor data is handled. On the one hand, the data from separate sensors can be calibrated against each another and fused into a common representation of the environment. A different approach, termed ***sensor fission***, builds no central view of the world, but instead uses separate sensors to trigger distinct behaviors. [Connell 1988] gives an account of a mobile robot arm which relies soley on this approach to collect soda cans. This method of handling the data makes the computational requirements for the task far simpler than with the sensor fusion approach. Consequently, sensor fission is a more viable alternative for gnat robots.

2. Gnat Robots

With these new approaches to designing intelligence and using sensor data, onboard computational requirements for mobile robots can be kept quite low. Now with micro actuators beginning to emerge, we can envision scaling down an entire system. The possibility of creating single chip robots dramatically changes our thinking about mobile robots. Not only would entirely new fields of application open up, but the mass production capability available from integrated circuit fabrication technology holds the promise that someday such robots could be made very cheaply.

Is it feasible? Certainly control logic and microsensors are amenable to such scaling; if power consumption is kept to a minimum, highly efficient solar cells might be usable. But could any type of micromotor develop enough power to locomote a small robot? [Flynn 1987] has taken an look at these questions and has shown that the available power from such micromotors is roughly equivalent to that needed to drive a small vehicle. By combining such motors with microsensors, a compiled-down version of our subsumption architecture, and miniature power supplies, we can imagine gnat-sized microrobotic systems on a chip at a fraction of the cost of traditional robots, with none of the problems associated with maintenance and spare parts.

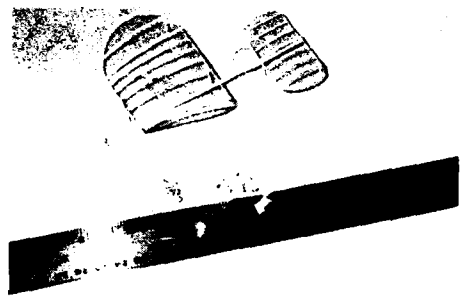

Figure 3. One of the smallest, lightest airplanes ever produced is about five inches long and weighs $80mg$, including a $50mg$ rubber band - Mark Drela.

Having such robots would change the way we think about robotics and open up new areas of application. Possibilities span from autonomous fishing lures to eavesdroppers to inspectors for spacecraft. With low cost and small size, we can begin to envision *massive parallelism*; using millions of small simple robots to perform tasks that might otherwise be done with one large, expensive, complex robot. In addition, we also begin to view our robots as *disposable*. They can be cheap enough that they are thrown away when they have finished their mission or are broken, and we do not have to worry about retrieving them from hazardous or hard to reach places.

To actually build a gnat robot, a research plan is needed that takes the project step by step, from technology that can be produced now to the end goal of what should be developed. Having a clear picture of that goal clarifies what problems should be addressed and in what order.

There are two major guiding considerations here. To create a gnat robot we need to minimize power consumption and save space on chip.

We have a few strategies for design that will enable us to implement these guidelines. First, a gnat robot should rely entirely on passive sensing in order to keep down power consumption. Active sensors, such as those used on our present robots, emit energy to the environment. These types of sensors therefore require significant amounts of power. Although passive sensors usually do not give the information desired directly, we hope to trade off computation for power consumption. Development of better algorithms can keep computational depth shallow and make this feasible (see [Brooks, Flynn and Marill 1987] for an example). A second strategy, one which aids in conserving real estate, is to be clever with sensor design so that one sensor can sense more than one environmental phenomenon. Third, using actuators also as sensors reduces chip size even further. Fourth, we will have to use the most efficient power transmission system possible so that power savings from other strategies are not wiped out.

A plan for the design of a first prototype is detailed in [Flynn 1987] and shows that micromotors can provide power equivalent to that of a rubber band for propelling a small $80mg$ airplane [Drela 1987], shown in figure 3. A research plan is proposed to target the first prototype of a gnat robot to be a single piece of silicon, incorporating sensing, guidance and control systems, which is attached to a macroscopic aerofoil. This example of a small airplane is proposed because it can be the simplest possible system; few actuators are needed and we do not need to worry about micro-aerodynamics and the associated problems of flight in the regime of low Reynold's numbers. This is not giving up on self-propelled gnat robots but is merely good engineering use of abstraction in order to isolate hard problems.

3. A Research Plan

In order to create such a single-chip microrobot for this application it is necessary to pinpoint what problems need to be solved. We can then develop a realistic research plan which best focuses our efforts and expertise to address these issues step by step. Foremost among the difficult problems involved is the development of micromotors, micro power transmission systems and some means of attaching micromotors to macro linkages. We need more knowledge about the aerodynamics of low-speed, small scale flight. Passive sensing, intelligent control systems integrated down to chip level, and small lightweight power sources are other major hurdles. We feel that our most immediate contribution can be in the areas of passive sensing and control systems and it is in these areas where we are focusing our upcoming projects [Flynn and Brooks 1988].

3.1 Micro Robotic Airplane

Figure 4 shows a plan, working backwards from gnat robots, that depict a series of projects that are succeedingly simpler and focus our research on specific areas of technology that are needed. [Flynn 1987] proposes building a miniature airplane. Basically, the suggestion is to put together an entire robotic system on a chip and then mount that chip on an airfoil which requires only one actuator for power and one actuator for control. What pieces would have to be developed to realize this? A passive sensing system would have to be built so that the airplane would not crash. A control system would have to be laid out on an integrated circuit to turn the sensed data into appropriate actuator commands. Micromotors would have to be built. Complex, highly efficient solar cells would have to be produced. Some type of transmission system would have to be conceived to couple the micromotors to a macro propeller or rudder.

The hardest problems here are probably the micromotors and solar cells. However, we feel we have a good angle of attack on the sensing and control issues. Our aim therefore is to concentrate on developing the technologies in these areas, and to hope for outside progress in micromotors and solar cells. Advances in micromotors and solar cells will be brought about by those with more expertise. Our strategy then is to take one more step back and aim towards a project that isolates the problems where we feel we can make a contribution.

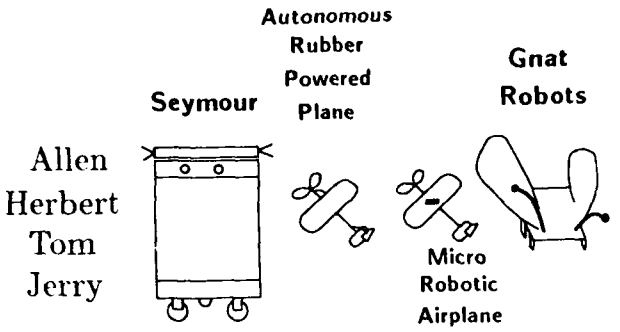

Figure 4. The research plan for pushing towards Gnat Robots involves a series of projects to develop the appropriate technology. One step back from Gnat Robots is to first place a micro-robotic system on a macroscopic aerofoil. A more easily attainable project still, would be to automate a rubber powered airplane, focusing on microsensors and control systems. Prototyping and algorithm evaluation for those technologies can be carried out in yet an even earlier project - producing board-level systems for a passive-sensor-only robot, Seymour.

5.2 Autonomous Rubber Band Powered Airplane

Consequently, a more immediate stepping stone would be to take the same lightweight airplane and leave the rubber band on to power it. This would give roughly six minutes of flight. Automating that airplane for that time interval would still be quite remarkable.

We will work on building a miniature vision system that provides input to a compiled down subsumption architecture. This sensing and control system will give the airplane the ability to fly around, avoiding obstacles, turning left or right as appropriate. The hand wound rubber band can remain, in order to provide power. Control of the rudder could be performed by a small nitinol actuator [Walker 1987] or possibly even a scaled down piezoelectric actuator. Recently, we've developed a $4g$ airplane with a nitinol actuator for the rudder which is powered through radiowaves [Lau 1988].

5.3 Seymour

For the most part however, we intend focus on creating the sensors and control systems for gnat robots. We've recently begun a new project with emphasis in these two areas. This new robot, Seymour, will specifically be targeted at developing the passive sensors that would someday be appropriate for gnat robots. We are going to constrain ourselves, artificially, to these low power devices in order to see how much sensory information we can extract and how intelligent a robot we can build, based on passive sensors.

The constraint of using passive sensors is a tough one. One can acquire direct information and acquire it much more easily by using active sensors such as light stripers, infrared proximity sensors or sonar sensors. We are hoping however, that by using clever algorithms for passive sensors such as CCD cameras or pyroelectric sensors, we can trade off power consumption for computation, as we can do computation with low-power CMOS microprocessors. We recently developed computationally shallow, real-time algorithms using CCD cameras for obstacle avoidance [Brooks, Flynn and Marill 1987] and for object tracking and following [Horswill and Brooks 1988].

4. Conclusion

Integration of an entire robotic system onto a single piece of silicon is the appropriate avenue for future robotics research. By integrating propulsion systems, sensors and intelligent control, mass production and low cost can be achieved, enabling robotics to become much more widely available and useful. With the advent of micro sensors and micro actuators along with new approaches for intelligence architectures and sensor integration schemes, gnat robots become feasible. They won't appear tomorrow, but we've outlined our research plan for pushing on a few of the problem areas where we feel we can make the most contribution, namely perception and control.

References

[Bart, Lober, Howe, Lang and Schlecht 1988] "Design Considerations for Microfabricated Electric Actuators", S.F. Bart, T.A. Lober, R.T. Howe, J.H. Lang and M.F. Schlecht. To appear in *Sensors and Actuators*.

[Brooks 1986] "A Robust Layered Control System for a Mobile Robot", Rodney A. Brooks, *IEEE Journal of Robotics and Automation*, RA-2, April, 14-23.

[Brooks, Flynn and Marill 1987] "Self Calibration of Motion and Stereo Vision for Mobile Robot Navigation", Rodney A. Brooks, A. M. Flynn and Thomas Marill, *MIT AI Lab Memo AIM-984*, August.

[Connell 1987] "Creature Design with the Subsumption Architecture", Jonathan H. Connell, *Proceedings IJCAI-87, Milan, Italy*, August.

[Connell 1988] "A Behavior-Based Arm Controller, Jonathan H. Connell. Submitted to *AAAI-88*.

[Drela 1987] Prof. Mark Drela, MIT Aeronautics and Astronautics Department. Personal communication.

[Flynn 1987] "Gnat Robots (And How They Will Change Robotics)", A. M. Flynn, *Proceedings Micro Robots and Teleoperators Workshop, Hyannis, MA*, November.

[Flynn and Brooks 1988] "MIT Mobile Robots - What's Next?", A. M. Flynn and R. A. Brooks, *Proceedings of the IEEE Robotics and Automation Conference, Philadelphia, PA*, April.

[Horswill and Brooks 1988] "Situated Vision in a Dynamic World: Chasing Objects, Ian D. Horswill and Rodney A. Brooks. Submitted to *AAAI-88*.

[Lau 1988] T. C. Lau. Forthcoming Bachelor's Thesis, MIT May

[Trimmer and Gabriel 1987] "Design Considerations for a Practical Electrostatic Micro Motor", W.S.N. Trimmer and K.J. Gabriel, *Sensors and Actuators*, 11(2):189-206.

[Walker 1987] "A Small Rotary Actuator Based on Torsionally Strained SMA", James A. Walker, *Micro Robots and Teleoperators Workshop, Hyannis, MA*, November.

INTEGRATED RELATIVE HUMIDITY SENSOR

S. V. Silverthorne
C. W. Watson
R. D. Baxter

Leeds & Northrup Company
A Unit of General Signal
Sumneytown Pike
North Wales, PA 19454

Abstract

An integrated relative humidity sensor has been designed and fabricated. The integrated sensor combines a capacitive relative humidity sensor with CMOS measurement circuitry on the same silicon chip.

Switched capacitor techniques are employed to compare the humidity dependent value of the polymer dielectric sensing capacitor C_x with two fixed SiO_2 reference capacitors, C_o and C_{ref}. These two reference capacitors set the gain and offset of the output according to the expression:

$$V_{out} = V_{ref} \left[\frac{C_x - C_o}{C_{ref}}\right] .$$

The design, implemented in 5 μm metal-gate CMOS on a .055" x .200" chip, results in a dc voltage output which varies linearly with relative humidity over the range 0-100%RH. For the design parameters presently empolyed, the sensitivity of the device is about 30mV/percent RH at an applied bias of 5V, corresponding to a capacitance change ΔC_x of 0.034pF/percent RH.

Design, fabrication and performance details are presented.

Introduction

Capacitive humidity sensors which exploit changes in the dielectric constant of polymer films upon absorption of water vapor are gaining increasing attention for the measurement and control of relative humidity. A number of RH sensors, employing various electrode configurations and polymer dielectrics have been described in recent literature (1-5). Although all of the devices offer various combinations of the "most-desired properties" (e.g., high performance, low cost, small size, fast response and interchangeability) they generally do not address the problem of interfacing the sensor to existing instrumentation and/or control loops in a simple, cost effective manner.

The sensor described in this paper combines a polymer-based capacitive humidity sensor on the same chip with CMOS electronics. The resulting three-lead integrated sensor provides a dc output voltage which varies linearly with relative humidity. Thus, the sensor is readily adapted to conventional 4-20 ma control loops. Further, its low power consumption (~1mW at 5V) makes it useful for battery operation and the dc output eliminates the need for shielded cable and special connectors in applications requiring the sensor to be located remote from auxiliary electronics.

Device Structure

The basic device consists of a humidity sensitive capacitor C_x, two SiO_2 reference capacitors C_o and C_{ref}, and CMOS measurement circuitry combined onto a single Si chip as illustrated in Figure 1.

Capacitor Structure

The polymer based sensing capacitor is a simple parallel plate structure consisting of an ~1μm thick polymer layer sandwiched between a boron diffused P^+ lower electrode plate and a porous metal upper electrode plate.

The reference capacitors are of a similar structure except that they employ SiO_2 as the dielectric and the upper electrode plate is non-porous. The P^+ lower plates for both the sensing and reference capacitors are formed as part of the normal CMOS process sequence. Al was used for the C_o, C_{ref} metallization and a thin Pt film was used as the porous C_x electrode.

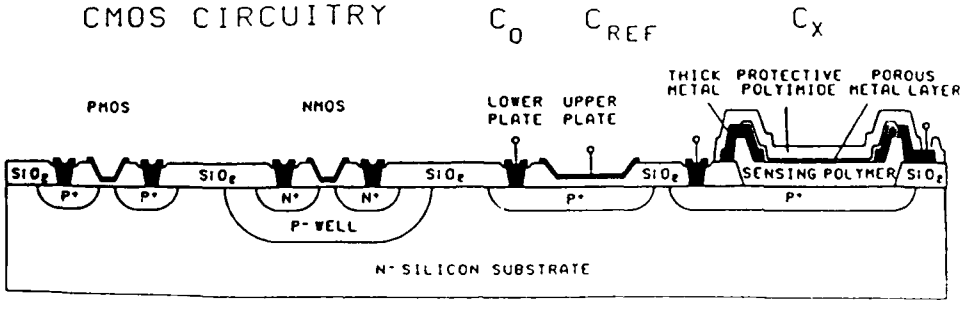

Figure 1: Device Structure showing the Conventional CMOS Structures, the Reference Capacitor Structure for C_o and C_{ref} and the Sensing Capacitor Structure

Measuring Circuitry

Figure 2 illustrates the switched capacitor measuring circuit which consists of three stages: Charge Balance, Comparator, and Integrator.

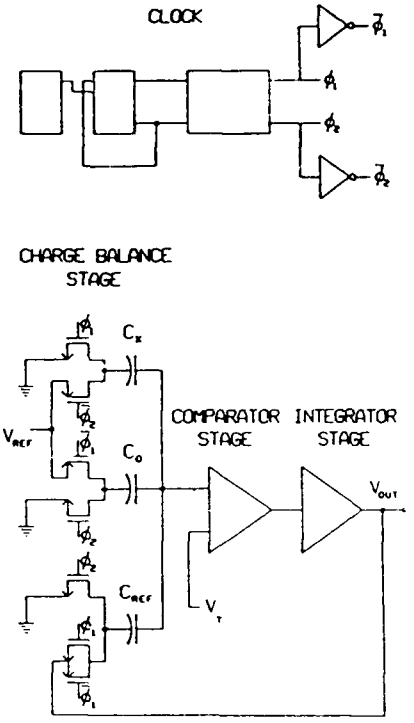

Figure 2: Sensor Circuit

The first or Charge Balance stage consists of the sensing capacitor, Cx and the two reference capacitors, C_o and C_{ref}. One plate of each of the capacitors is connected to the input of the succeeding comparator stage. The other plates of the capacitors are connected to the appropriate voltage by CMOS switches during the two phases of circuit operation. An on-board clock generates a two-phase clock signal that drives the switches for the capacitors, the comparator, and the integrator.

Figure 3(a) shows the condition of the Charge Balance stage during the first or set-up phase of circuit operations when ϕ_1 is high. The input to the comparator is clamped to its self biasing trigger voltage, V_t. The sum of the changes appearing on C_x, C_o and C_{ref} is:

$$Q_1 = C_x(-V_t) + C_o(V_{ref} - V_t) + C_{ref}(V_{out} - V_t) \quad (1)$$

where V_{ref} is the power supply voltage. V_{out} is the output voltage of the sensor which is fed back as shown in Figure 2.

Figure 3(b) shows the condition of the Charge Balance stage during the second or measuring phase of circuit operation when ϕ_2 is high. The input to the Comparator is allowed to float to a voltage, V_{sum}. The total charge, Q_2, is now given by:

$$Q_2 = C_x(V_{ref} - V_{sum}) + C_o(-V_{sum}) + C_{ref}(-V_{sum}). \quad (2)$$

Because the input to the Comparator is allowed to float during the second phase, we can assume that the total charge is conserved so that:

$$Q_1 = Q_2$$

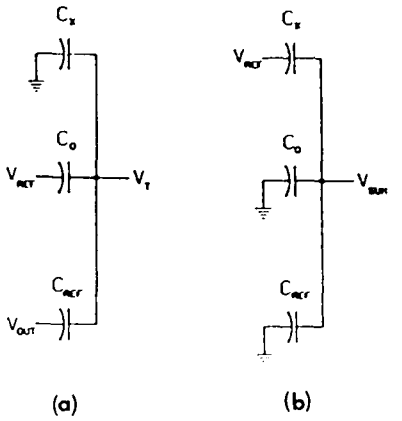

Fig. 3: Condition of the Charge Balance Stage During (a) Phase 1 and (b) Phase 2 of Circuit Operation

Equating equations (1) and (2) and solving for V_{sum} yields the equation:

$$V_{sum} = V_t + \frac{(C_x - C_o)\,V_{ref}}{(C_x + C_o + C_{ref})} - \frac{(C_{ref})\,V_{out}}{(C_x + C_o + C_{ref})}. \quad (4)$$

The basic function of the two succeeding stages, the Comparator and Integrator is to adjust V_{out}, the output voltage of the device so that:

$$V_{sum} = V_t. \quad (5)$$

When this occurs, consideration of equation (4) shows that the output voltage V_{out}, becomes:

$$V_{out} = \frac{(C_x - C_o)\,V_{ref}}{C_{ref}} \quad (6)$$

Thus, the output voltage of the device varies linearly with C_x. Selection of the reference capacitors, C_o and C_{ref}, and the power supply voltage, V_{ref}, sets the gain, $\frac{V_{ref}}{C_{ref}}$ and the offset, $\frac{V_{ref}\,(C_o)}{C_{ref}}$.

If the dielectric in the sensing capacitor has a permittivity, ε, which varies linearly with abmient relative humidity, then ε is given by:

$$\varepsilon = \varepsilon_d(1 + \alpha RH) \quad (7)$$

where α is a constant and ε_d is the permittivity of the dielectric when the ambient relative humidity is 0. The response of the sensor is then:

$$V_{out} = \frac{[C_{xd} - C_o + (\Delta C_x)RH]V_{ref}}{C_{ref}} = \left[\frac{C_{xd}[1+\alpha RH]}{C_{ref}} - \frac{C_o}{C_{ref}}\right]V_{ref} \quad (8)$$

where $C_{xd} = \frac{(\varepsilon_d)A}{t}$, $\Delta C_x = \frac{(\alpha\varepsilon_d)A}{t}$, A is the area of the sensing capacitor and t is the thickness of the dielectric.

Design Parameters

The principal parameters to be specified are the span $S = V_{out}(100\%RH) - V_{out}(0\%RH)$ and offset voltage, $V_o \equiv V_{out}(0\%\ RH)$. For a desired span, equation 8 yields:

$$\frac{C_{xd}}{C_{ref}} = \frac{S}{100\alpha V_{ref}} \quad (9)$$

while for a desired offset,

$$\frac{C_o}{C_{ref}} = \frac{C_{xd}}{C_{ref}} - \frac{V_o}{V_{ref}} = \frac{S}{100\alpha V_{ref}} - \frac{V_o}{V_{ref}}. \quad (10)$$

Substituting the target values S = 3V, V_o = 0.8V and the value α = .00372 characteristic of the polymer employed, the nominal design values for the capacitance ratio are determined to be $\frac{C_{xd}}{C_{ref}} = 1.613$, $\frac{C_o}{C_{ref}} = 1.453$. By fixing the geometry of one of the capacitors, the rest are determined from the required ratios.

Fabrication

Sensor fabrication was implemented using a 10 mask p-well CMOS technology as shown in Table 1. The first 6 masks provide the basic CMOS circuitry. Masks 7 through 10 accomplish the addition of the sensing capacitor C_x and patterning of the polyimide protection layer over the completed wafer.

Table I

PHOTOMASK SEQUENCE FOR SENSOR FABRICATION

Photomask Level	Function
1	Define P^- Wells
2	Define N^+ Regions
3	Define P^+ Regions
4	Define Gates
5	Define Contacts
6	Pattern First Metal
7	Define Sensing Polymer
8	Define Second Metal
9	Define Upper Plate
10	Define Polyimide Cover

After wafer level testing and dicing, chips were mounted on TO5 headers as shown in Figure 4. A thermistor was incorporated into the package to facilitate temperature compensation. During final packaging, either slotted caps or caps containing a sintered filter were employed to permit exposure of the sensor to the atmosphere.

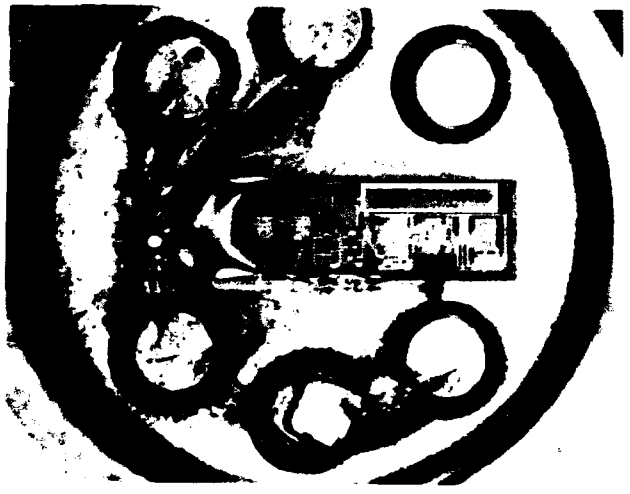

Fig. 4: Packaged sensor

Results and Discussion:

Packaged sensors were characterized for linearity, response time, repeatability, and long term stability at high humidity. Most sensors were characterized at fixed humidity points using thermostatted salt baths. Dry N_2 was used for the 0% RH point.

Typical values of output voltage versus relative humidity for four sensors are plotted in Figure 5. Note that all devices exhibit good linearity over the entire humidity range at room temperature. The solid lines in Figure 5 represent theoretical curves calculated from Equation 8 with $\frac{C_o}{C_{ref}} = 1.456$ and $\alpha = 0.00377$.

The good agreement with experimental data indicates that C_o/C_{ref} and α are in fact constant and that any differences among the various devices arise primarily through run-to-run variations in polymer thickness. These thickness variations appear in Equation 8 as variations in the ratio $\frac{C_{xd}}{C_{ref}}$.

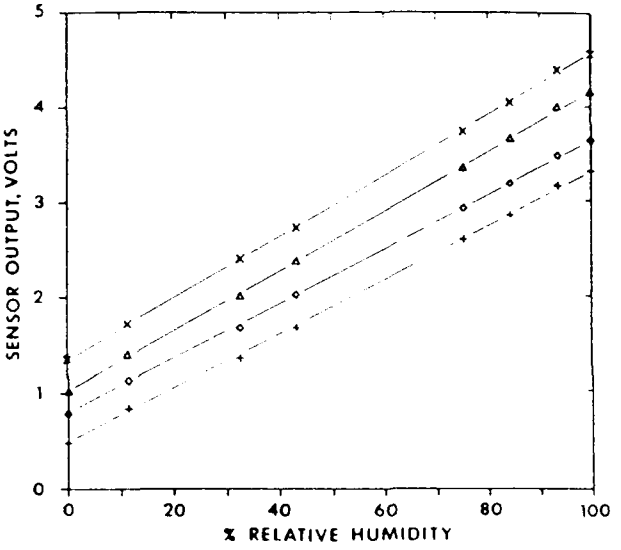

Fig. 5 : Output Voltage as a Function of Relative Humidity for Four Sensors

This has important implications for device calibrations since from Equation 10, the span S and offset V_o are related by the expression

$S = 100\alpha(V_o + \frac{C_o}{C_{ref}})$. With both α and C_o/C_{ref} constants, it is possible to design a circuit which simultaneously adjusts S and V_o thereby providing for a true single point calibration.

Further illustration of the utility of this approach is presented in Table II which compares the measured and calculated values of S for a given V_o. The difference between calculated and measured span is expressed both in terms of span error (in volts) and the corresponding calibration error in percent RH. Note that for the worst case, the error is less than 3% over the 0-100% RH range.

Table II

PREDICTED SINGLE POINT CALIBRATION ERROR

Device	Output in Volts 1	2	3	4
Measured V_o	0.470	0.783	1.020	1.349
Measured Span	2.853	2.868	3.152	3.214
Calculated Span	2.915	3.033	3.123	3.247
Delta Span	-0.062	-0.165	0.029	-0.033
Calibration ± %RH	1.1	2.9	0.5	-0.5

Calibration data for a single sensor are presented for both increasing and decreasing RH in Table III. The data indicate a maximum deviation of less than 2 RH including effects of hysteresis and repeatability. Short term repeatability during humidity cycling was measured on 30 sensors during 34 humidity cycles between 0 and 75 RH. After 34 cycles, the average deviation in V_o was 3 mV or about 0.1 RH. The average deviation in a V_{out} at 75 RH after 34 cycles was 9.8mV or about 0.3 RH. Further, the maximum deviation observed for any of the 30 sensors amounted to only 9 mV (0.3 RH) at RH 0 and 56 mV (1.9 RH) at 75 RH.

Table III

CALIBRATION TEST DATA AT 25°C

RH Bath	Indicated RH	Deviation RH
53.20	51.79	-1.41
75.30	73.88	-1.42
93.60	92.39	-1.21
75.30	75.60	.30
53.20	53.60	.40
32.80	32.06	-.74
6.40	6.82	.42
32.80	31.47	-1.33

Figure 4 presents the results of long term operation at 75 relative humidity. The figure contains results for two sensors. Initially one sensor was in a [illegible] while the other was in a [illegible] area in the same oven. Then, after two months for the test, the sensors were placed in the [illegible] that over the approximately six-month test period, the typical drift at 75% RH was only about [illegible] that the rather more abrupt changes in offset are attributed to the devices subjecting [illegible] the large time associated with temperature changes in the oven. Several artifacts are evident with the test system. For example, the approximately [illegible] which occurred about four months into the test was associated with the malfunction of a fan [illegible] the air in the test oven. Temperature changes affect the [illegible] way. First, the equilibrium relative humidity of saturated salt solutions is temperature dependent. Second, nonequilibrium changes in relative humidity occur upon rapid temperature change, and third, the sensor itself has a temperature sensitive response. The latter can be described in terms of a humidity dependent component and a humidity independent component as follows: Error(RH) (-.036 -.003)/°C. At 93.6 RH, the sensor error is 0.32 RH per degree C, and the equilibrium relative humidity of the saturated salt changes by about 0.22 RH per degree C. It seems likely, then, that many of the abrupt changes are to be identified with nonequilibrium effects which typically result in RH change of about 3 per degree C.

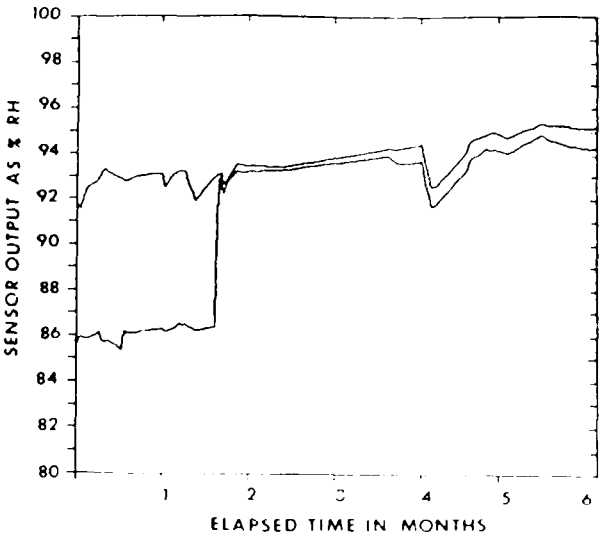

Fig. 4 Sensor Stability at High Humidity

The sensor is presently being used in two commercially available products. One of these is a battery powered pocket RH pen, rated at +3 accuracy over the range 10-90 RH and 10-30°C. The other is a two-wire 4-20 mA transmitter, also rated at +3 but over the range 0-90 RH and 15-50°C.

Summary and Conclusions

An integrated capacitive humidity sensor combining a polymer based sensing capacitor and CMOS measurement circuitry on the same .055 x .200" chip has been developed. The device produces a linear dc output voltage in response to humidity changes with a sensitivity of 30 mV percent RH at 5V applied bias. The device offers accuracy, repeatability, and stability characteristic of discrete capacitive RH sensors but with the additional advantage of battery powered [illegible] insensitivity to lead length, ease of [illegible], and compatibility with existing [illegible] processes.

2. M.Colgan and J.A.Schuetz, An IC Compatible Polymer Humidity Sensor, Proceedings of the International Conference on Solid State Sensors and Actuators, pp 217-220, 1986.

3. M. Hijikigawa, T.Sugihara T.Tanaka and M.Watanabe, "Micro-chip FET Humidity sensor with a Long Term Stability," ibid pp 221-224.

4. T. Sashida and Y.Sakaino, "An Interchangeable Humidity Sensor for an Industrial Hygrometer," Proceedings of the 1985 International Symposium on Moisture and Humidity, pp 525-534, 1985.

5. W.A.Clayton, P.J.Freud and R.D.Baxter, "Contamination Resistant Capacitive Humidity Sensor," ibid pp 535-544.

CMOS Magnetic Sensor Arrays

James J. Clark
Division of Applied Sciences
Harvard University
Cambridge, MA 02138

Abstract

We describe the design of a monolithic 64 by 64 element array of magnetic sensors, implemented in a standard 3 micron CMOS process. The individual magnetic field sensors are split drain MAGFETS. A split drain MAGFET is a field effect transistor that has one source, one gate, and two drains. When current is flowing in the FET in the absence of a magnetic field both drains receive an equal current. If a magnetic field is present, with a component perpendicular to the direction of current flow, the current flow is deflected towards one drain and away from the other, resulting in a current differential between the two drains. The current differential is proportional to the applied magnetic field component perpendicular to the current flow in the MAGFETs.

The MAGFETs in the array are scanned in a raster scan fashion, by allowing current to flow through all elements in a given row, while all other rows are turned off. While a row is selected, the differential current output of the sensing elements in the row are amplified by a current mirror which also converts the current differential to a voltage. These voltages (one for each column) are multiplexed onto a common output bus that is connected to a buffer stage which provides additional amplification and lowers the output impedance.

This array has been implemented in 3 micron CMOS, through the MOSIS facility. We present experimental results as to its sensitivity.

1 Introduction

The utility of MOS technology for implementing sensing devices has long been known [1,5]. MOSFET based devices are currently being fabricated to measure quantities as varied as chemical activity [1] and magnetic field strengths [6]. Although much effort has been expended in developing sensors, proportionally less effort has been directed to the task in making integrated arrays of these sensors. This paper describes the development of an integrated magnetic field sensor array. Such an array has many applications, the most obvious being field mapping, for example in determining the fringing fields in an electric motor. Novel applications also exist such as the compliant tactile sensor developed by the author [4], which uses the magnetic field sensor array to measure the deformation of a membrane to which small magnetic dipoles are attached.

2 Split Drain Magnetic Field Sensors

The basic sensing element of the magnetic field sensor array is a device known as a split drain magnetic field sensitive MOSFET, or MAGFET for short. This device is a MOSFET, that has two drains, as shown in figure 1. In operation the MAGFET is biased on so that current flows strongly through the transistor. In the absence of a magnetic field the currents flowing through the two drains of the MOSFET are equal. However, when there is a magnetic field with a non zero component, B_z, perpendicular to the plane of the sensor, the carriers (electrons or holes) flowing in the transistor are deflected, due to the Lorentz force. As the carriers are deflected by this force, an electric field is built up due to the separation of charge. The force on the carriers due to this field will counteract the force due to the magnetic field. Hence an equilibrium will be attained at a certain displacement of the charge carriers. This charge carrier deflection results in an imbalance in the current flowing through the two drains of the MAGFET. This imbalance is a function of both B_z and the geometry of the split drain. If the split drain consists of two equally sized sections, the currents through the two sections are of the form $I_1 = \frac{I}{2} + \Delta I$ and $I_2 = \frac{I}{2} - \Delta I$, where ΔI is a function of B_z [5]. This current differential can be converted to a voltage and amplified by a current mirror acting as a transresistance amplifier as shown in figure 2. The gate of the MAGFET is connected to one of its drains ensuring operation in the saturation region. Note that this drain is connected to the diode connected transistor of the current mirror and thus the voltage at this drain is held virtually constant. Ideally the gate of the MAGFET should be connected to ground, but in practice doing this results in a larger sized cell because of the need to bring in a ground wire.

This research was supported in part by the Office of Naval Research under grant N0014-84-K0504 and the Joint Services Electronics Program.

The combination of the split drain MOSFET and the current mirror is equivalent to the input stage of an operational amplifier. The sensitivity of this arrangement can be much higher than a circuit utilizing the Hall voltage. A device similar to this has been built and tested by Popovic and Baltes [6]. They claim sensitivities on the order of 1 Volt per Tesla. Their circuit uses complementary split drain MAGFETS, whereas our design uses only a single MAGFET in conjunction with a current mirror. The reason we use the single ended design is to make the sensor as compact as possible. In addition to requiring two transistors in each sensor cell having complementary FETS in a sensing cell requires that both well and substrate contacts be present, and that there be extra space between the P and N channels FETS to minimize the probability of latchup.

3 Design of the Sensor Array

We have designed and laid out a 64 by 64 element array of such split drain transistors in an integrated circuit for fabrication in a 3 micron CMOS process. This circuit has fabricated through MOSIS, which is a service run by the Information Sciences Institute of the University of Southern California for DARPA, that acts as an interface between university IC designers and industrial fabrication facilities. Each of the split drain transistor sensing elements on the chip is 100 microns square. The size of the entire array is 7.9 by 9.2 mm. The chip is shown in figure 3a. A microphoto of one of the split drain MAGFETs is shown in figure 3b.

The array is scanned in a raster scan fashion by the circuit shown in schematic form in figure 4. Shift registers along the left hand side of the circuit shift a single "turn-on" bit which allows current to flow through all of the split drain devices in a single row. As the scan proceeds, successive rows are turned on. Only one row at a time is one. Shift registers along the bottom shift a single "select" bit which selects the output of one column at a time. All the split drain devices in a given column share a single current mirror transresistance amplifier located at the bottom of the column. Since only one row is on at a time, these current mirrors have current flowing through them from one split drain device only. The row shift register is shifted only when a complete column scan has been finished. The column shift register is shifted by an external clock signal. The output of the selected current mirror is amplified and buffered before it is sent to an analog output pad. The shift registers are initialized by a reset pulse. The amount of current that passes through the split drain devices is controlled by a bias voltage which is switched in when a row is selected. This bias is used to adjust the offset voltage of the current mirror to be roughly half of the supply voltage in order that the buffer amplifier operates in its linear, high gain region. The sensitivity of the split drain devices are also affected by the bias voltage.

4 Experimental Properties of the Sensor Array

We have measured a number of properties of the 4096 element sensor array chip that we have fabricated. The power dissipation of the chip is 12.5 milliwatts with a 5 volt power supply. The sensitivity of the magnetic sensors to changes in magnetic fields is illustrated in figures 5 and 6. The graph in figure 5 shows the relationship between the sensor output and the magnetic field at the sensor. The B_z - V_o characteristic of the sensor is seen to be quite linear over most of the range. Figure 6 shows the output of a single sensing element as a function of the lateral position of a rare earth bar magnet, with

IH0215-4/88/0000-0072 © 1988 IEEE

a surface field of 2KGauss and dimensions 15mm X 9mm X 4mm, when the height of the bar magnet above the sensing plane is kept constant (at 5 mm). This graph indicates the spatial sensitivity of the sensing array. In obtaining this plot the bar magnet was aligned so that the north-south axis was parallel to the sensor plane. The lateral resolution of the sensing array is hidden somewhat in the above graph since the bar magnet has a thickness of about 4mm and acts as a distributed source.

The maximum practical clock speed of the fabricated arrays has been found to be about 500Khs. This works out to a frame rate of about 125 frames/sec (500,000 pixels/sec / 4096 pixels/frame). We are looking at ways in which faster scan rates can be obtained in future array designs.

The current mirrors which amplify the current differential of the split drain MAGFETS have been found to be quite sensitive to process induced variations in their dimensions. As a result we observed some nonuniformity in the offset voltage between the transresistance amplifiers in each columns of the array. This non-uniformity can be compensated for to some extent with a post-processing stage once the array output has been digitized. A new design is currently being fabricated which will solve this problem, albeit at the cost of some loss in speed. In the new design, only a single transresistance amplifier is used and instead of multiplexing the outputs of transresistance amplifiers in each column to an output bus, we multiplex the differential current lines for each column on to a differential bus which is then connected to a single transresistance amplifier. This eliminates the column to column non-uniform offset problem since only one transresistance amplifier isused, but slows down the circuit since we have effectively doubled the capacitance on the differential current busses attached to the split drain magfets.

5 Acknowledgments

I would like to acknowledge the support provided by the Joint Services Electronics Program, through grant N00014-84-K-0465. I would also like to thank R. Brockett for providing the facilities and encouragement for the development of the magnetic sensor array. D. Friedman helped out in many ways on this project, for which I am grateful.

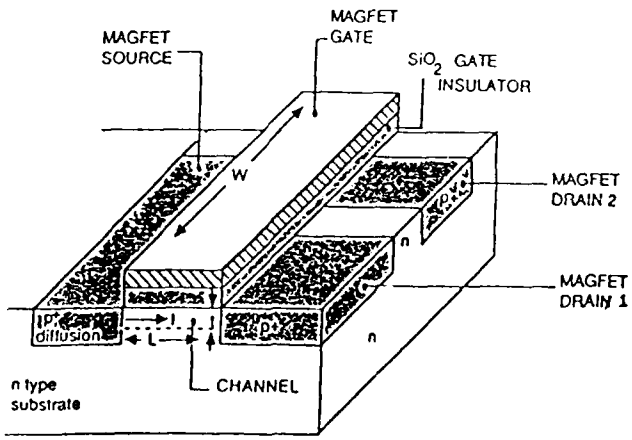

Figure 1. A split drain magnetic field sensitive MOSFET

References

[1] Bergveld, P., "The impact of MOSFET-based sensors.", Sensors and Actuators, Vol. 8, pp 109-127, 1985

[2] Brockett, R.W., "Robotic hand with rheological surfaces"., Proceedings of the 1985 IEEE Conference on Robotics and Automation, pp 942-947

[3] Clark, J.J., "Circuit Techniques for Sensor Design", presented at the 2nd IEEE Conference on Synthetic Microstructures in Biological Research, Airlie VA., March 1988, to be published in IEEE Electron Devices Special Issue on Synthetic Microstuctures.

[4] Clark, J.J. "A magnetic field based compliance matching sensor for high resolution, high compliance tactile sensing.", Proceedings of the 1988 IEEE Conference on Robotics and Automation, Philadelphia, April 1988

[5] Fry, P.W., and Hoey, S.J., "A silicon magnetic field transducer of high sensitivity.", IEEE Transactions on Electron Devices, Vol. 16, pp 35-39, 1969

[6] Popovic, R.S., and Baltes, H.P., "A CMOS magnetic field sensor.", IEEE Journal of Solid State Circuits, Vol. 18, No. 4, pp 426-428, 1983

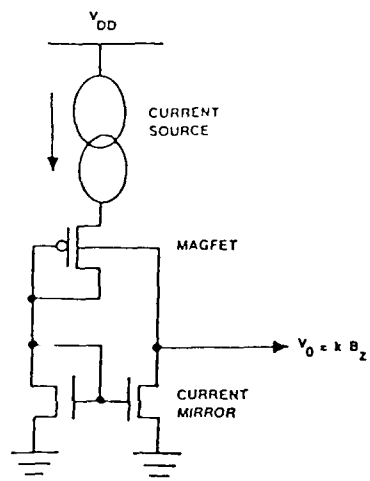

Figure 2. Amplification of the split drain MAGFET current

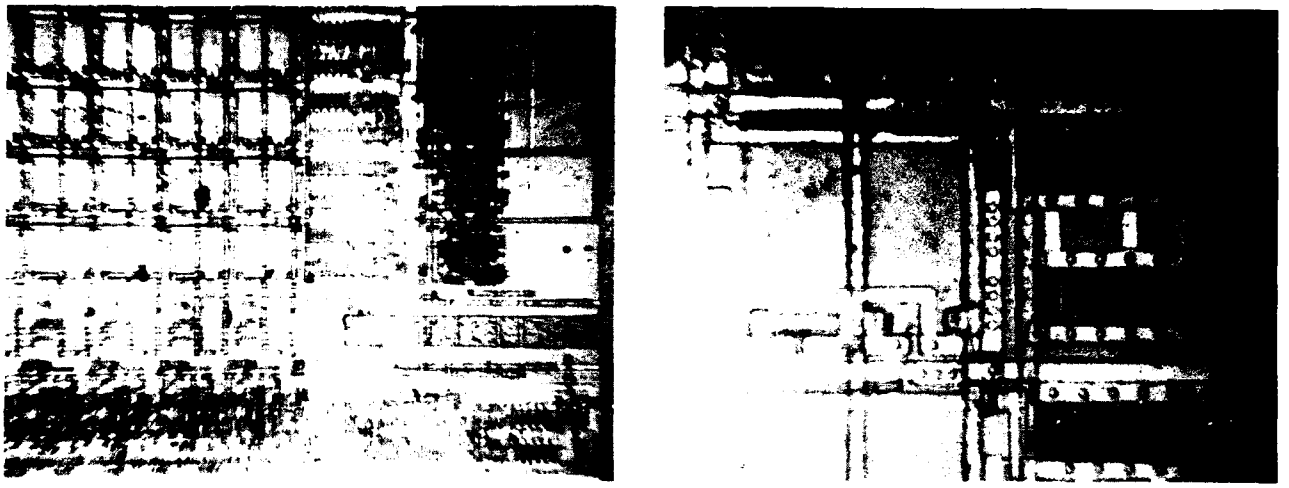

Figure 3. a) A portion of the magnetic field sensor array chip. b) Detail of the split drain MAGFET as fabricated.

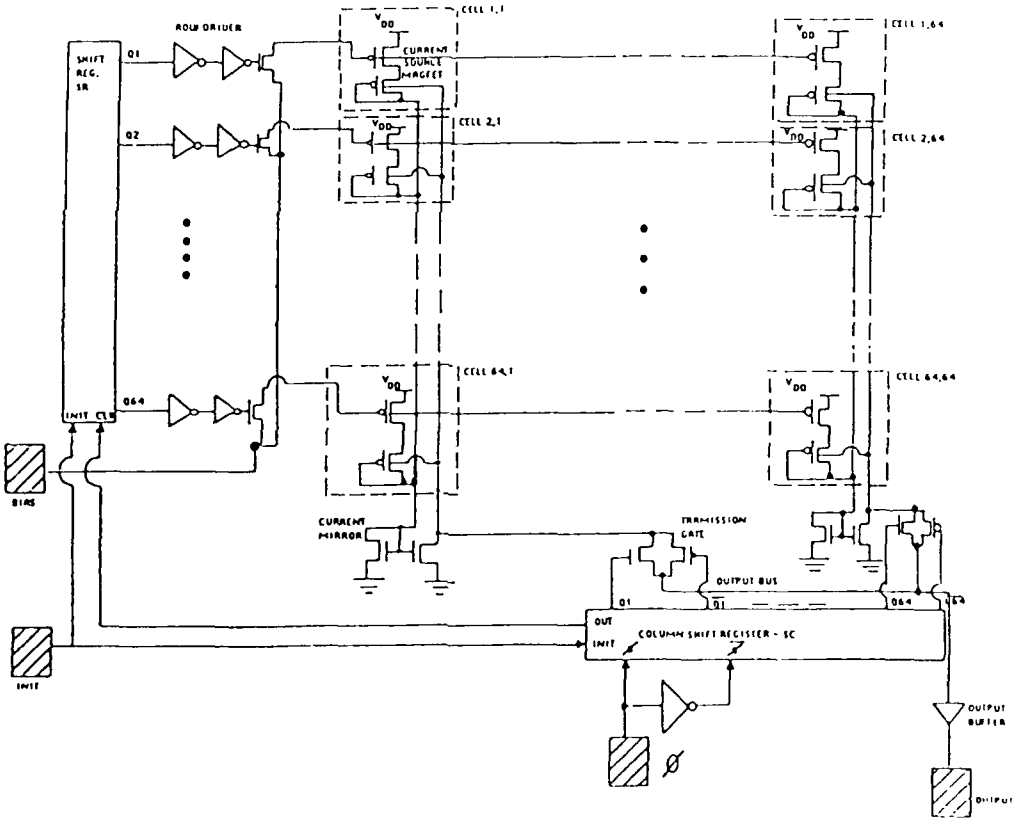

Figure 4. The circuitry of the sensor array.

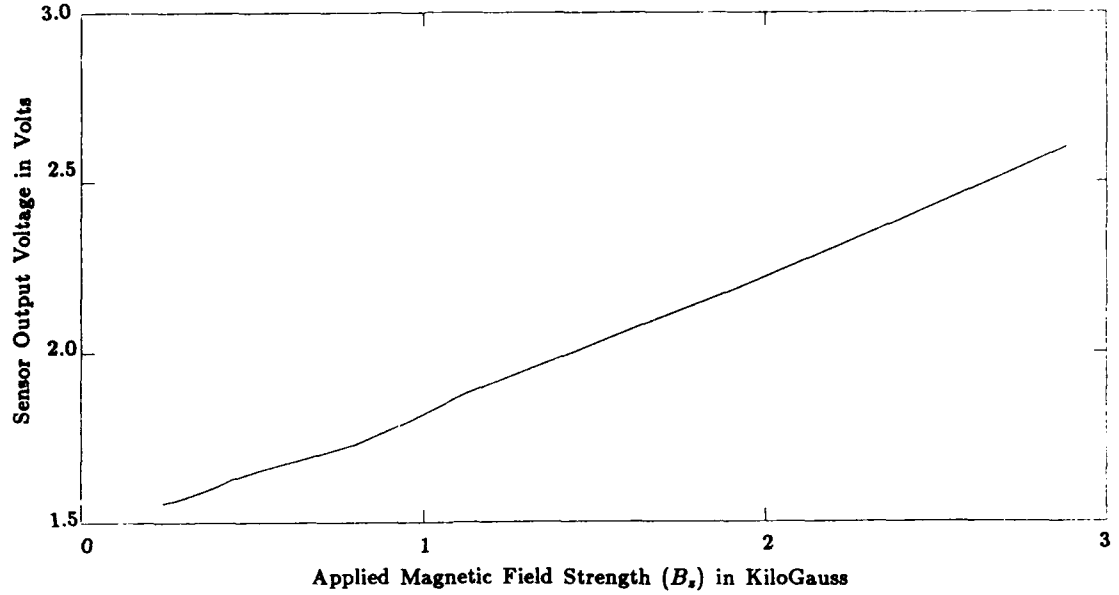

Figure 5. The output of a sensing element (after buffering) as a function of the applied magnetic field strength.

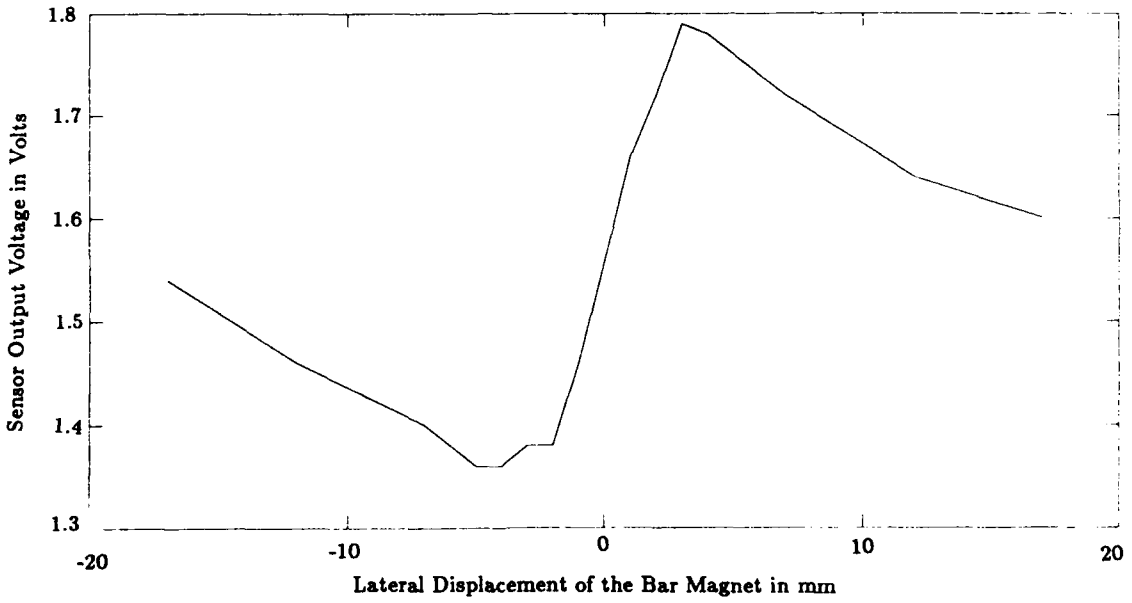

Figure 6. The output of a sensing element as a function of the lateral displacement of a bar magnet located above the sensor array.

AN ARCHITECTURE AND INTERFACE FOR VLSI SENSORS

N. Najafi, K. W. Clayton, W. Baer, K. Najafi, and K. D. Wise

Center for Integrated Sensors and Circuits
University of Michigan
Ann Arbor, Michigan 48109-2122

ABSTRACT

A VLSI sensor interface has been designed for use in bus-organized sensor-driven process control systems where high accuracy and high reliability are important. The interface permits 12-bit digital sensor data to be communicated to the host processor over a bidirectional parallel data bus which includes parity checking. The sensor can be self-testing and employs digital compensation of cross-parameter sensitivities. The interface has been implemented using discrete commercial components and has been designed in monolithic form in 3μm single-metal double-poly CMOS technology. The chip has a die area of 10.8mm x 8.5mm before compaction and has a simulated power dissipation of 75mW. The on-chip microprocessor operates at 4MHz and the 12-bit ADC has a conversion time of 14μSec.

INTRODUCTION

As integrated transducers are combined with increasing amounts of on-chip or in-module circuitry, where to partition the electronic system and how much electronics to include with the "sensor" become major issues. Integrated sensors, and particularly those associated with automated manufacturing and process equipment control, are likely to evolve into smart peripherals, and the definition of appropriate sensor interface standards is currently the subject of at least three national committees. For process control applications, high accuracy and high reliability are important goals, suggesting the use of substantial amounts of on-chip circuitry. More and more sensors are also being implemented as multi-transducer arrays, requiring input as well as output data for their operation. For example, thermally-based flow devices require heater control as well as temperature readout, and more advanced devices require that the heater be externally adjustable. This implies a bidirectional sensor interface capable of enhanced control; however, there are no agreed-on standards, feature lists, or architectures at the present time for the high-end integrated sensors which will be needed for the 1990s and beyond.

This paper reports initial results from a research program which has a number of long-term goals, including 1) the development of improved architectures for integrated sensing systems, 2) understanding the implications of using increased amounts of on-chip electronics on sensors, 3) the development of standards for the sensor-system interface, 4) the development of high-performance, modular, generic interface circuits for use on sensors, and 5) the study of the barriers associated with sensor performance at the 12-bit level. The work is intended to address the problems associated with the development of a generic process controller for the 1990s and involves a number of fundamental issues in system partitioning, controller architecture, sensor function, and sensor testing/compensation. It is hoped that the work will serve to initiate discussions which will lead to the development of standards for sensors and their associated control systems.

This paper describes a possible organization for high-end sensors and associated interface protocols. The interface described is addressable, programmable, self-testing, compatible with a bidirectional digital sensor bus, and offers 12-bit accuracy using internally-stored compensation coefficients. The design is sufficiently flexible to allow upward-compatible sensor designs to be inserted in existing equipment without reprogramming the host system and will accommodate differing sensor features. Thus, it should be possible within this organization to automatically upgrade machine performance in the field while preserving the ability of the sensor manufacturer to provide innovative and unique product features.

SYSTEM ORGANIZATION

Figure 1 shows a block diagram of the overall sensor-driven control system. A host computer, acting as system controller, interfaces with up to 256 nodes over a standardized bidirectional digital bus. Each node can contain a number of sensors and/or actuators. It is expected that each actuator will effectively be in a system feedback loop with one or more sensors. The sensors represent the critical element in the control loop since overall system operation depends on their accuracy. If they are not accurate and reliable, then no matter how sophisticated the controller is, the machine will not perform adequately. Thus, it is expected that the use of sensors which cannot be tested from the host controller will become increasingly unacceptable as automated control systems evolve into the 1990s.

Figure 2 shows the bus developed for communication between the nodes and the host. This Michigan Parallel Standard (MPS) bus contains 16 lines, including eight bidirectional data lines (D0-D7), a parity line, four control lines (HHS, NBR, NHS, and NAL) for synchronizing message transfers, and three power lines. For the discrete implementation of this interface, ±12V supplies have been used, while the monolithic design uses ±5V supplies. Message transfer is initiated by the host when it addresses a specific node to request or transfer data. The first (address) byte is decoded by all nodes on application of HHS. The addressed node acknowledges by pulsing NHS high and sets NBR high, locking out other nodes for subsequent bus data. Subsequent message bytes are entered and acknowledged using HHS and NHS, respectively, as

TH0215-4/88/0000-0076

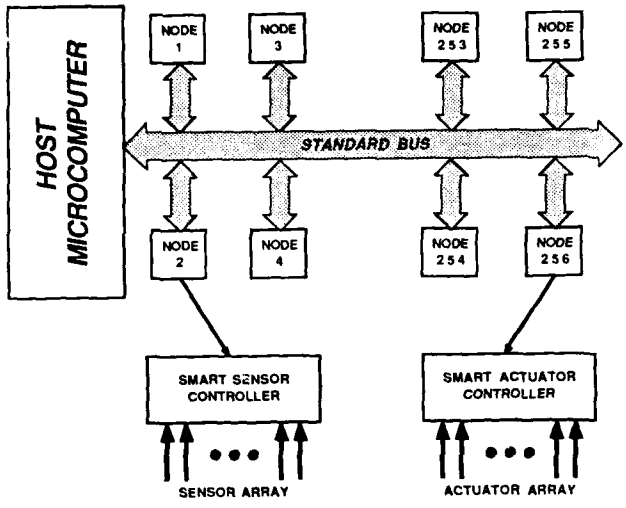

Fig. 1: Block diagram of a sensor-driven control system

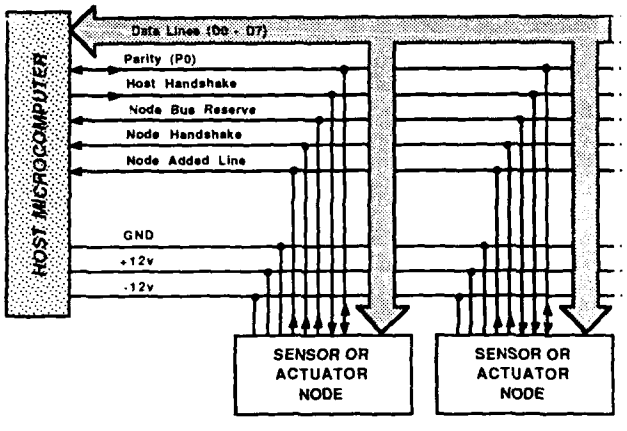

Fig. 2: The Michigan Parallel Bus (MPS) and its message transfer diagrams.

indicated in Fig. 2. Messages are of variable length, with the bus released as NBR drops low. The NAL line can be used as a system interrupt in the event of situations requiring immediate action by the host or can be used to signal the insertion of a new sensor in the event of a replacement or addition to the system.

Figure 3 shows a block diagram of a sensing node for this "fifth-generation" sensor design. An array of transducer outputs are amplified, multiplexed, and converted to digital data under the control of a microprocessor-based microcontroller, which interfaces to the external sensor bus through a communication interface. The PROM contains the node address as well as information as to the sensor compensation techniques and interface protocols. Thus, upon insertion in the host system, the node can deliver to the host information as to its features, the compensation techniques employed, and the compensation coefficients. This PROM is encoded at the time of sensor test and allows digital "trims" to be substituted for the traditional analog laser trims long associated with cross-parameter compensation and offset/slope control. Amplifier offsets and gains are set via this PROM as well and are internally compensated so that the analog signals remain in-range for the analog-to-digital converter (ADC). Actual precision compensation (e.g., for temperature) is performed by the host system, where much greater processing power is assumed. This organization attempts to implement as many system features associated with high accuracy and reliability as possible while maintaining the sensor electronics at a moderate level of complexity. It is possible that sixth-generation sensors will eventually do all compensation on-chip, thus simplifying the host system; however, if suitable standards can be developed for both the hardware and the software interface to the sensors, the use of data compensation in the host via standard modules should not present a serious

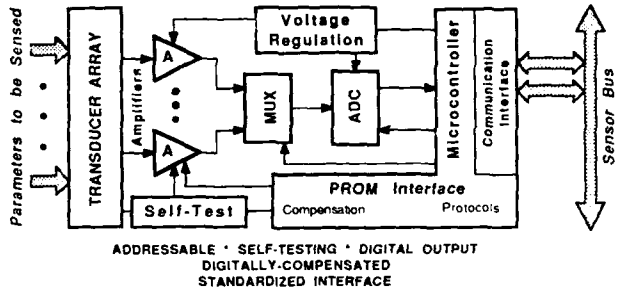

Fig. 3: Block diagram of a VLSI fifth-generation integrated sensor

problem. In the event of a parity error, the host requests retransmission, and in the event of repeated errors, the node can be tested by the host and a particular sensor, or an entire node, can be removed from service. The goal is to be able to detect sensor drift prior to catestrophic failure, however, so that timely replacements can be made and equipment downtime can be avoided.

The sensors are sampled sequentially by the microcontroller so that their most recent values are always present in RAM; hence, the external host system is not required to wait for data conversion by the node, and sensor reads appear much like memory accesses.

DISCRETE SYSTEM IMPLEMENTATION

The above system organization has been implemented in discrete form using an IBM PC/XT as host. The sensor node was implemented on an Augat URG1 wirewrap panel and requires 22 commercial components. The microcontroller was realized using a National NSC-800 microprocessor. This present system is configured to measure reference pressure, chamber/unknown pressure, and temperature, and can be used as an automated sensor characterization system. The system noise level currently corresponds to

about 11 bits, with temperature automatically controlled from -70°C to +205°C and pressure controlled from vacuum to 2000 Torr. Figure 4 shows representative signals on the system bus during a message transfer from a node to the host. System speed here is set by the host.

Figure 5 shows an example of digital compensation of the sensor data using PROM-based compensation coefficients. The commercial piezoresistive pressure sensor used for this example was measured from 50 Torr to 1000 Torr at over 2000 points. The uncompensated pressure nonlinearity over this range had a maximum of about 0.6 percent. Based on this data, compensation coefficients were automatically generated using a statistical analysis program for a fifth-order polynomial to convert the measured pressure response into true pressure. The compensated nonlinearity is reduced to less than 0.1 percent. Similar results appear possible for the compensation of temperature effects. Thus, it appears feasible to considerably enhance the performance of sensors using digital compensation (and its ability to handle nonlinear effects). Sensor stability then becomes a major concern and focus in the realization of high-accuracy devices. It is not yet known whether polynomial compensation can be used to reduce the required accuracy in the data converter so that the entire signal path can be handled using PROM-based compensation. If it can be, then substantial savings in testing and die area may be possible.

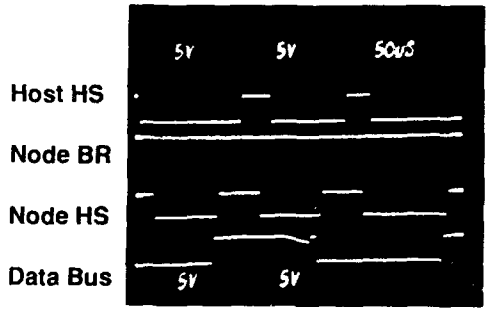

Fig. 4: Representative signals on the MPS system bus during a message transfer from a node to the host.

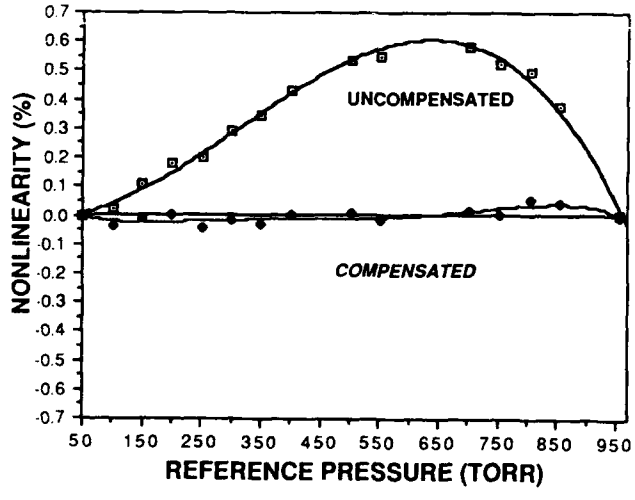

Fig. 5: Digital compensation of pressure nonlinearity for a commercial piezoresistive pressure sensor at 21.5°C.

MONOLITHIC INTERFACE IMPLEMENTATION

Figure 6 shows a representation of the interface in more highly integrated form. The transducer array is implemented on one chip, which includes front-end circuitry and initial signal amplification. The sensor interface is realized as a single monolithic chip and interfaces with a commercial PROM such as a 2716. While in a practical (ca. 1994) application, the system might appear as a single monolithic chip (after all of the associated circuitry is optimized), at the present time a hybrid implementation appears more realistic using an off-chip PROM. Splitting the analog and digital portions of the interface chip into a hybrid might also be done for the near term.

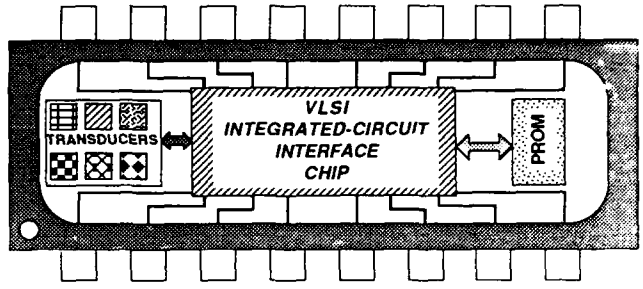

Fig. 6: A high-end hybrid (modular) integrated sensor for semiconductor process control.

Figure 7 shows a block diagram of the sensor interface chip as designed in monolithic form. The chip is realized in 3µm single-metal double-poly CMOS technology. Up to seven voltage-level sensor outputs are amplified and digitized under the control of a custom microprocessor. The chip also accepts eight digital (event) inputs as well as one pulse-rate (FM) sensor output. A 256-bit RAM stores the digitized sensor data, while a ROM stores the program code for the processor. The communication interface can be configured for either the MPS bus or for a serial bus; all other circuitry is independent of the bus configuration used. The processor employs a 12-bit internal bus, consistent with handling sensor data at the 12-bit level.

The microprocessor executes up to sixteen different commands from the host and implements 22 different instructions internally. All transducers can be read on command or only a single transducer can be interrogated. Compensation data can also be readout or self-test can be initiated on command. In addition, an 8-bit register can be loaded from the host for the control of internal flags or on-chip actuators.

Figure 8 summarizes the layout area of the chip in 3µm CMOS. The microprocessor and communication interface are custom implementations, while the amplifier and ADC were realized with the aid of a silicon compiler. Substantial compaction of the layout is thought to be possible as circuits are further optimized, and this optimization will be performed prior to initial integration of the interface. The present overall chip size is 10.3mm x 8.5mm. The use of a 2µm double-metal double-poly process would also be expected to decrease this die area by about 50%. As

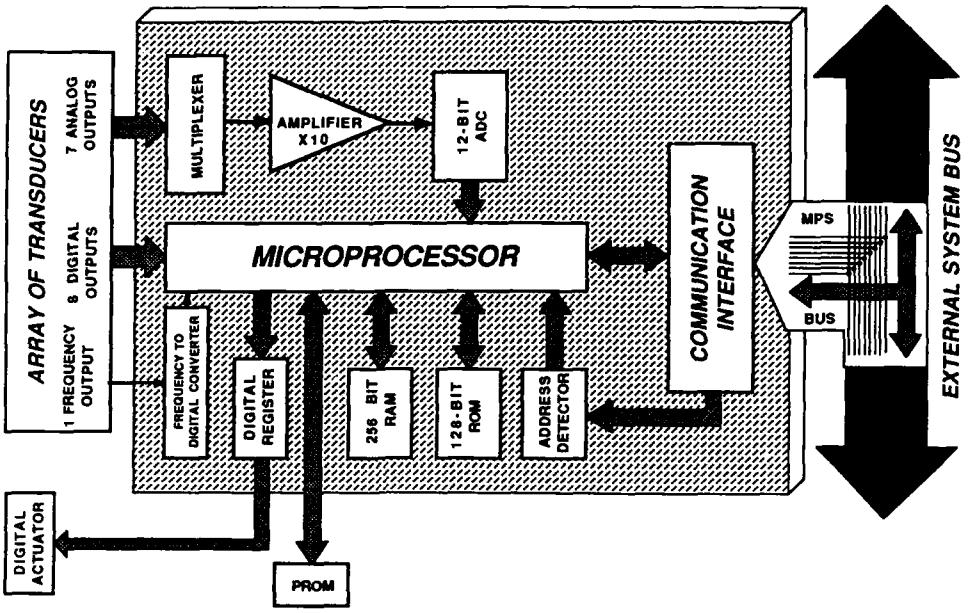

Fig. 7: Block diagram of the integrated sensor/actuator interface chip.

noted in Fig. 9, the simulated power dissipation for the entire chip is 75mW. The amplifier has an open loop gain of 87dB, an output swing from -4.8V to +4.3V, a bandwidth of 2.3MHz, and a closed-loop gain of 20dB. The common-mode and power-supply rejection ratios are -71dB and -80dB, respectively. The analog-to-digital converter has a conversion time of 13.5μSec at 12 bits.

While the die area associated with the full monolithic implementation of the sensor interface is relatively large by present standards, by the early 1990s it will not appear so formidible as further feature size reductions, technology improvements, and circuit refinements reduce the die size and the associated chip cost. It appears likely that such interfaces will be viewed as increasingly attractive and practical for process control systems over the next few years as efforts continue to achieve higher accuracy and improved system reliability. While substantial challenges lie ahead in generic controller design, sensor testing, circuit development, and fundamental transducer design, it is hoped that this work will be useful as a starting point in the development of high-end sensors for process equipment control and perhaps for other applications as well.

ACKNOWLEDGMENTS

The authors would like to acknowledge the support of the Semiconductor Research Corporation for this work under Contract 87-MP-085. Mr. T. Huang contributed substantially to the layout of the monolithic sensor interface while S. Cho and J. Cowles assisted in the development of the process technology and in the design of the analog portions of the interface circuitry.

Microprocessor	5.6x6.1mm^2
ALU	1.2x2.6mm^2
Data Path	3.7x1.8mm^2
Control Unit	2.3x2.3mm^2
Analog-to-Digital Converter	4.2x4.7mm^2
Communication Interface	1.8x2.1mm^2
Frequency-to-Digital Converter	1.2x1.1mm^2
RAM	1.3x1.1mm^2
ROM	0.8x0.3mm^2
Operational Amplifier	0.8x0.3mm^2
Address Detector	0.6x0.4mm^2
Multiplexer	0.4x0.4mm^2

Figure 8: Layout areas for individual circuit blocks of the interface chip

Active Area*	10.3x8.5mm^2
Power Dissipation	~75mW
Supply Voltage	±5V
Technology	3μm Single-Metal, Double-Poly CMOS
Amplifier Gain	20dB
ADC Conversion Time	13.5μsec, 12-Bits
Microprocessor Clock	4MHz (Simulated @ 2,4,8 MHz)
RAM Size	256 Bits
FIFO Size	144 Bits (18x8)

*Compaction and optimization of circuit blocks will reduce the area in future designs considerably.

Fig. 9: Characteristics of the integrated interface chip.

Fiber Optic Data Bus for Solid State Sensors

Jim Lenz, Paul Bjork, Kyuri Fujiwara

Honeywell Systems & Research Center
3660 Technology Drive
Minneapolis, MN 55418

Fiber optic busses and fiber optics sensors offer the potential for EMI immune systems. While numerous laboratories are working to develop fiber optic sensors, few can presently compete with the performance, size, and cost of existing solid state sensors. This paper describes a sensor system which is immune to EMI by combining the advantages of a fiber optic data bus with existing solid state sensors.

Introduction

Electromagnetic interference (EMI) is becoming an ever increasing concern for systems designers and operators. The reports of automobiles stalling at specific locations, machines activating independent of a trigger, and non-repeatable computer upsets are pointing toward EMI as the source of these mysteries. As more powerful radio towers are erected and as more factory and vehicle instrumentation is being specified, a systems EMI immunity is becoming more difficult to test and certify.

Systems designers are looking to fiber optics for a guarantee in EMI immunity. A first approach for may be to utilize optical fibers for data links between shielded boxes as well as fiber optic sensors. Fiber optics has been proven for communications but has yet to demonstrate cost effective sensors.

The system designer might next approach the EMI issue by utilizing battery powered sensors with optical fiber data links. However battery life will always raise questions on system reliability and ease of maintenance.

A third approach for the system designer which offers EMI immunity is described in this paper. It combines the optoelectronics technology for EMI immunity with the low power solid state electronics and sensors technology available today.

System Design

The system design consists of four parts: an optical source, a single optical fiber link, a low power electronic transducer, and the sensor readout. A layout of these four parts is shown in Figure 1. A single multimode optical fiber is connected between the optical control readout end and the transducer. The fiber serves two purposes: it transmits optical energy to the transducer and provides a control/data link between the readout and the transducer.

A block diagram of the critical issues in designing an optically powered sensor is shown in Figure 2. There are four critical functions: delivering optical energy to the sensor end, converting the optical energy to electrical energy at a sufficient voltage, low power sensors and electronics, and a transmit scheme for sending sensor data to the control end. The major driver in assessing the critical issues for a specific implementation of an optically powered sensor is the available electrical power at the sensor end. Even with the best optical components only a few milliwatts of electrical power are available. Synchronous control between the sensor and control end and effectively duty cycling the sensor electronics are necessary for maximum energy efficiency.

Another important aspect of this approach to fiber optic sensors is the wide variability, adaptability, and availability of low power digital electronics and solid state sensors. This makes it possible to maximize the energy conversion efficiency as well as minimize the power consumption at the transducer end. Power is needed for the sensing transducer, the associated electronics (i.e. A/D, control logic, etc.), and generating the return data light pulses. Designing transducers to operate at microwatt power levels with 12-bit accuracy and linearity requires careful design and attention to efficiency issues. Complicating this problem are the low impedance and low signal level characteristics of typical electrical transducers.

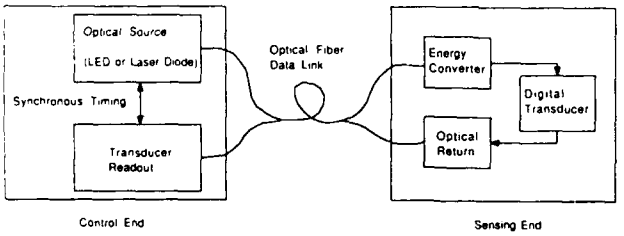

Figure 1. Design layout for Optically Powered Sensors.

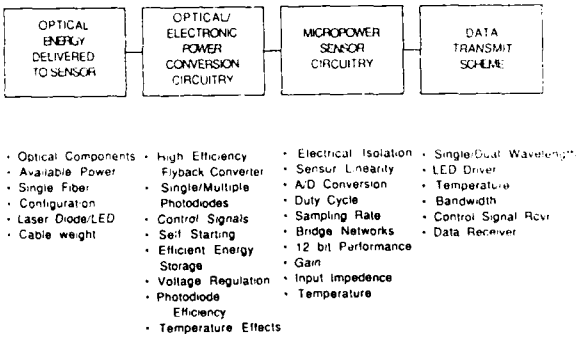

Figure 2. Critical issues in Optically Powered Sensor Design.

Hardware Design

In implementing an optically powered sensor there are four basic configurations, as shown in Figure 3. The choices are in the type of light source at the control end and the number of strands in the fiber cable. With the single fiber design, a single photodiode with a step-up transformer is used to produce the necessary voltage level at the sensor end. With the multiple fiber cable each power transmitting fiber connects an LED to a photodiode. The photodiodes form a series array for generating the proper voltage level. The single fiber cable configuration has the advantage of utilizing standard connectors whereas the multiple fiber cable has the advantage of not requiring an optical coupler. The source selection tradeoff between multiple LED and a laser diode is driven by the cost of the laser diode and its reliability over the systems environmental requirements. The use of a laser diode with multiple fiber energy conversion offers no advantages over the other three configurations. We have fabricated and reported [1] a breadboard based on this configuration. This design requires a star coupler at some point in the optical path. Our findings indicate star couplers to be optically inefficient. Also, they do not allow for highy efficient dual wavelength operation.

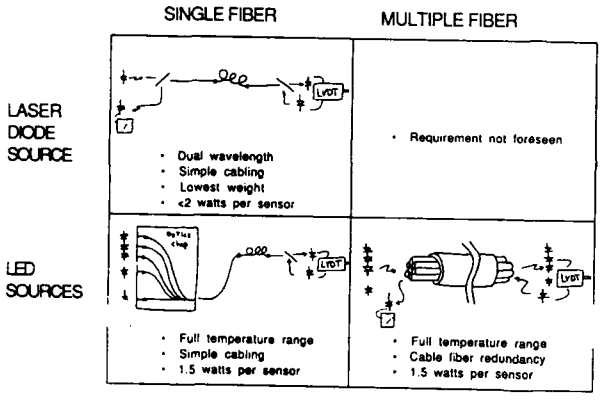

Figure 3. Optically Powered Sensors configuration matrix.

A breadboard based on a laser diode optical source, a single fiber cable, and dual wavelength operation (i.e. laser-840 nm, return LED-1300 nm) is shown in Figure 4. Optical to electrical energy conversion data for the single photodiode/step up transformer converter is shown in Figure 5. This breadboard demonstrates five functions: a temperature sensor, a current sensor, two position sensors, and a LVDT displacement sensor. A micropower 8-bit A/D converter digitizes the sensor's signal and serially shifts the bits to the return LED through a pulse driver circuit. The sample rate of the A/D is controlled from the control end and varys form 1 to 100 hertz.

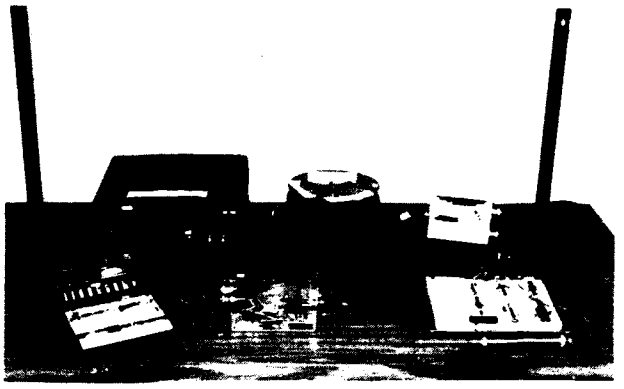

Figure 4. Laser diode, single fiber experimental configuration

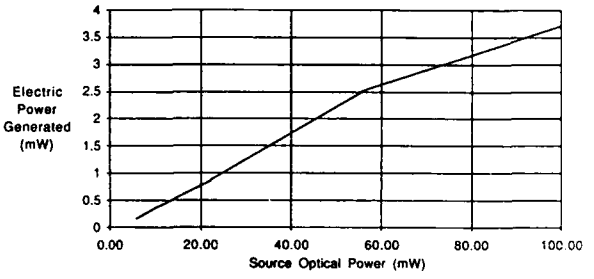

Figure 5. Optical to electric energy conversion for single photodiode configuration.

The key to single fiber operation is the standardized synchronization protocol for power supply and communication between the control end and the remote sensor. The communication process is initiated by a polling operation at the interface module. Logic in each of several sensors on the network is wired to respond to a unique signal or a address on the incoming optical power. This signal may be a particular combination of pulses or a particular frequency or repetition rate of pulses. All the advantages of low power CMOS digital circuitry are available for address coding and decoding.

When the sensor is triggered in this way, the sensor A/D converter is activated and the 8-bit result is sent back to the interface module one bit at a time between a set of 25 short optical source pulses, which now are interpreted as synchronization pulses. Since the sensor LED transmits the only optical power on the network between synchronization pulses, signal to noise ratio at the interface module is maximized. Figure 6 is a timing diagram of the process. Information from the last sensor addressed is sent bit by bit between synchronization clock pulses. Laser retroreflections into the detector are easily masked out using this synchronization scheme.

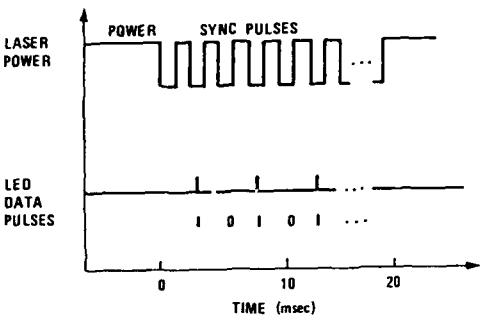

Figure 6. Data link communication protocol.

The Micro Switch and Optoelectronics Division of Honeywell are producing a proximity switch based on another configuration of this optically powered data link design. Their production prototype, pictured in Figure 7, is based on six LED sources and a multiple fiber cable. Special connectors incorporating the six LED's and single receiving photodiode for the control end and the six photodiodes and single transmitting LED at the sensor end are being fabricated for this wide temperature range, high reliability design. Data on energy conversion at the sensor end for a series of photodiodes is shown in Figure 8.

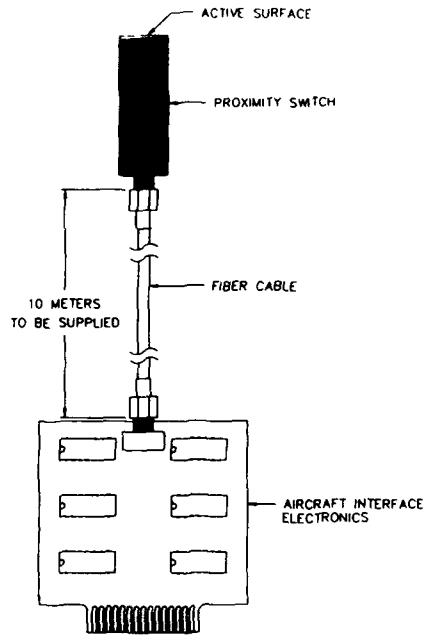

Figure 7. LED, multiple fiber production prototype.

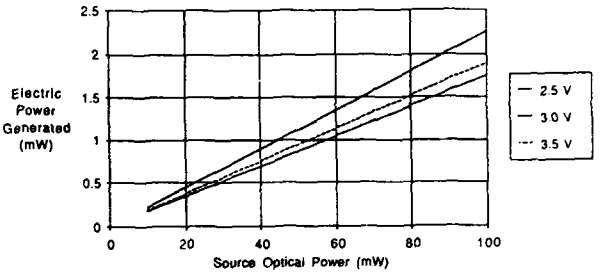

Figure 8. Optical to electric energy conversion for multiple photodiode configuration.

Data

Data from five different sensing functions are shown in Figure 9. Five sensor responses are plotted. Each shows the digital output recieved at the control end versus the input to the sensor. The data obtained with our optically powered sensor breadboard has better than ±1 LSB error. The dominant error in linearity and repeatability is in the sensor and A/D electronics.

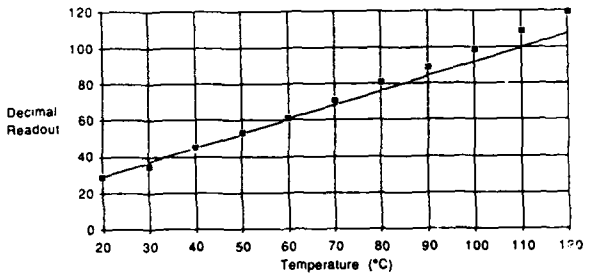

Figure 9a. Temperature sensor using type J thermocouple.

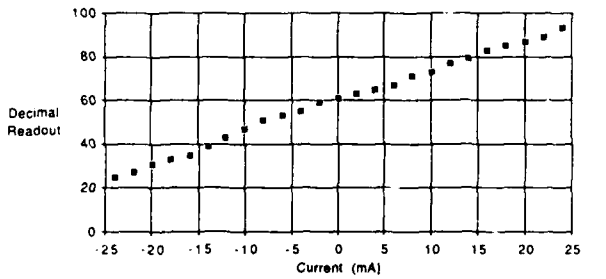

Figure 9b. Current sensor using permalloy magnetic sensor.

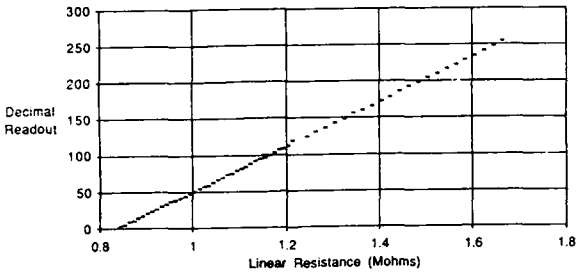

Figure 9c. Position sensor using potentiometer.

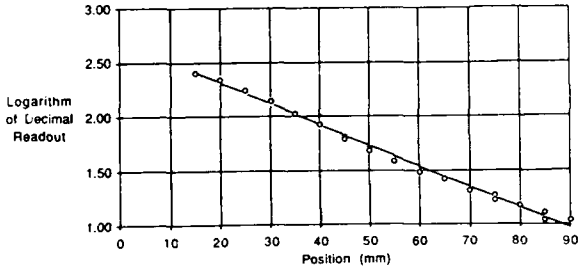

Figure 9d. Position sensor using magnetic sensor.

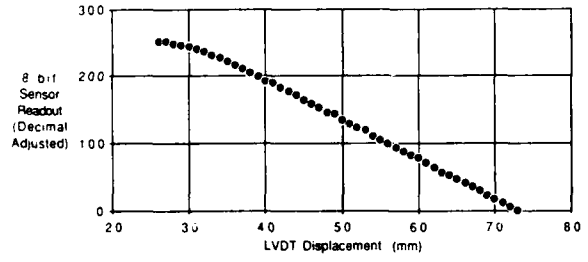

Figure 9e. Displacement sensor using LVDT.

Summary

The optically powered sensors concept requires low power sensors and electronics. Through the use of solid state sensors, linear, repeatable sensors are readily attainable because of the ability to precisely fabricate each sensor and incorporate first stage readout electronics directly with the sensor. These electronics can also provide EMI protection to the sensor. Environmental compensation circuitry can also be added which reduces calibration complexity when multiplexing several sensors.

This concept for an EMI hardened sensor system offers greater flexibility over passive fiber optic sensors. By optimizing the electrical design, through the wide variety of standardized circuits, this concept allows for using a relatively inexpensive optical design based on standard optical components. Also power consumption can be traded off with added functions at the transducer end. With low power electronics the options to address individual sensors, multiplex between sensors, change the sensor sample rate, and set threshold alarms are relatively simple compared to performing these functions with an optical scheme.

References

1. "Optically Powered Sensors", P. Bjork, J. Lenz, K. Fujiwara, Optical Fiber Sensors Conference, New Orleans, January 1988.

CALIBRATED MEASUREMENTS OF ELASTIC LIMIT, MODULUS, AND THE RESIDUAL STRESS OF THIN FILMS USING MICROMACHINED SUSPENDED STRUCTURES

Fariborz Maseeh, Martin A. Schmidt, Mark G. Allen, and Stephen D. Senturia
MIT Microsystems Technology Laboratories, Cambridge, MA

Abstract

Quantitative determination of material properties such as the Young's modulus (E), Poisson's ratio (ν), residual stress (σ_o), and elastic limit of polymer films used in electronics and microsensors devices is essential. This paper reports on the calibration of the suspended square membrane method using both finite element methods (FEM) and comparison with conventional tensile tests. We also report on the use of suspended circular membranes to measure the elastic limit of thin films.

Introduction

Most microelectronic devices and sensors are fabricated using thin film deposition or diffusion. The films are often under residual stresses developed in the fabrication process. A number of different techniques have been employed for determining mechanical properties of thin films. Techniques such as beam buckling are used for measuring thin films under compressive stress [1], while released structures[2], and membrane deflection under applied pressure [3,4] have been employed to measure the properties of thin films under tensile residual stress. Wafer curvature methods can be used to measure average stress of both tensile and compressive thin films [6].

In this work we have used the membrane technique to measure the mechanical properties of polyimide thin films under residual tensile stress. A polyimide square membrane is microfabricated by spin depositing polyimide on a p^+ doped square silicon diaphragm. The p^+ diaphragm is fabricated by patterning the backside of the wafer and anisotropically etching the undoped silicon and stoping on the p^+ diffused layer. This layer is removed as the last step by dry etching, releasing a square polyimide membrane supported by the silicon wafer. The state of stress is maintained by the silicon support.

The residual stress and Young's modulus of thin films under tensile stress can be determined by fitting the pressure vs deflection data of the square membrane with a suitable model. The simplest approach is an approximate analytical model based on membrane mechanics. The center deflection d under applied pressure p of a square membrane of size 2a and thickness t with in-plane residual stress σ_o can be shown from membrane mechanics to be of the form [4]:

$$p = c_1 (t \sigma_o / a^2) d + c_2 (E t / a^4) d^3 \qquad (1)$$

where E is the Young's modulus, c_1 is a constant (3.0 in the membrane model) and c_2 depends weakly on Poisson's ratio (assumed to be 0.25 throughout the work, for which c_2 is 1.8 in the membrane model).

Equation (1) is used to extract σ_o and E by fitting to the experimental pressure vs deflection results. In the original work, the constants c_1 and c_2 were evaluated by an energy minimization technique using an approximate functional form for the deflected shape of the membrane. This paper reports several approaches to confirm the results obtained from equation (1). Finite element methods (FEM) were used to fit the p vs d data independently, from which we both confirmed the functional form of Eqn.(1) and calibrated the constants c_1 and c_2. Young's modulus was independently measured by direct tensile testing of microfabricated thin polyimide strips from which the modulus values were compared against Eqn.(1) and FEM results. Circular membranes, for which superior analytical models exist, were microfabricated and from the p vs d of such membranes, σ_o and E were evaluated. Finally, from the circular membranes we could detect the elastic limit properties such as the yield stress and strain.

Calibration of Membrane Equation

The finite element methods were utilized to fit the pressure vs center deflection data from the square polyimide membranes of different sizes. Fig.1 shows the FEM iterative procedure used to evaluate the stress and modulus. Three different membranes were chosen for which the p vs d data was available. Each membrane was modeled using nonlinear FEM. The input required specification of the geometry, boundary conditions, material properties, and applied loads. Each membrane was discretized with 64 4-noded shell elements. All boundaries were fixed. The residual stress was introduced artificially into the FEM model by using a thermoelastic material law and inducing a negative differential temperature. Nonlinear analysis based on large displacements and small strains were used in the solution. Convergence was achieved using full Newton iteration with line search in each run.

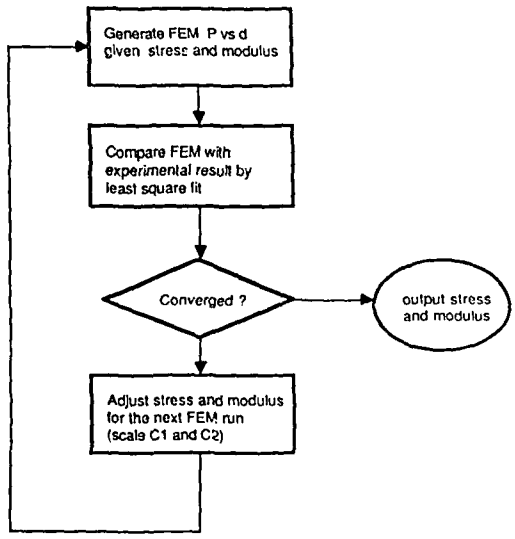

Fig.1

Iterative finite element approach to obtain residual stress and modulus

TH0215-4/88/0000-0084 © 1988 IEEE

The FEM output gives the deflection contour over the entire membrane as well as stresses over each element. The stresses were used for detecting the correctness in modeling. The center deflection vs the applied pressure from each run was of interest for comparison with the experimental data.

To investigate the integrity of Eqn.(1) as a tool to measure the residual stress and Young's modulus, we examined this equation both functionally and quantitatively. The results showed that the functional dependence of Eqn.(1) on geometry, on σ_0, and on E was correct. Furthermore, as shown by the results in Table 1, the FEM results agreed with Eq.1 to within 6% in residual stress and 10% in modulus, confirming the values of c_1 and c_2 to those levels of accuracy

Side (mm)	Thick (μ)	FEM Stress	Eq.(1) Stress	FEM/Eq.(1) Stress ratio	FEM Modulus	Eq.(1) Modulus	FEM/Eq.(1) Modulus ratio
4	10	28.25	30.0	1.067	2430	2600	1.070
8	8.5	37.60	39.8	1.058	2900	3200	1.103
10	7.0	28.71	30.0	1.045	2900	3200	1.100

Table 1

FEM vs Eq.(1) results for residual stress (MPa), and Young's modulus(MPa) using data from three square membranes of BTDA-MPDA/ODA. The two ratio columns indicate the agreement between c_1 and c_2 for the two models.

Direct Tensile Test

The goal of this measurement was to independently and directly measure the Young's modulus and to study the stress vs strain behavior of different polyimide chemistries. Two different polyimide types, namely, BTDA-MPDA/ODA and PMDA-ODA, were used in sample fabrication. Thin polyimide strips of 24 mm x 12 mm with different thicknesses were micromachined. The fabrication process follows the released structure fabrication procedure of Ref.[1] except that the diaphragms were anisotropically etched using KOH instead of hydrazine. Fig.2 shows the Instron specimen fabrication sequence. Polyimide was spin deposited on a 1 inch x 1 inch p^+ doped diaphragm, aluminum was evaporated on polyimide and patterned to the specimen shape as shown in Figs.2a,b. This forms an etch mask for the polyimide which is removed by dry etching. The aluminum layer is then removed by wet etching, and finally, the back side membrane is removed, releasing the specimen as shown in Fig.2d. Before loading this specimen in the Instron, two sections of the wafer are removed along four pre-etched scribe lines (in the back), as shown in Fig.2e, releasing the stress. The remaining silicon acts as supports for the grips of the Instron. Care was required during sample fabrication to avoid any edge cracks during handling. An Instron Model 1123 was utilized for the test with a crosshead speed of 0.5 mm/min.

Fig.3 shows stress vs strain curve for high viscosity BTDA-MPDA/ODA polyimide with thickness 14 μm. The specimen was loaded to 11 N (65 MPa) and unloaded. The unloading curve followed the loading curve closely except for a small offset which is believed to be due to backlash of reverse gears of the machine. The sample was reloaded and the loading curve followed the first one closely, as shown, up to 11 N, and then the sample was unloaded, and the unloading curve followed the loading curve again with the same offset. The sample was then loaded to the break point. The slope of

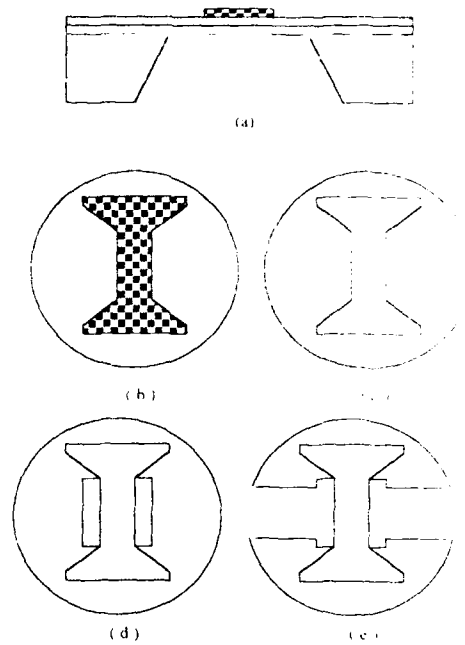

Fig.2

Fabrication of Instron specimen; a) p^+ diaphragm with polyimide and patterned aluminum; b) top view of patterned aluminum etch mask; c) polyimide specimen after dry etch and aluminum removal; d) backside silicon diaphragm removed. dashed lines are the etched scribe lines in backside; e) sections of silicon removed along scribe lines, yielding specimen ready for the Instron test

the final loading curve was the same as the slope of the previous curves for this specimen. One would conclude that BTDA-MPDA/ODA has linear elastic brittle type behavior and the use of one E value in the analysis is sufficient. However, we will show below that, in fact, this type polymer does exhibit yield behavior prior to fracture. The Young's modulus and the strain at break for this specimen were measured to be 3040 MPa and 2.8% respectively. The E value agrees well with the membrane results for standard type BTDA-MPDA/ODA.

Fig.4 is the Instron test results for standard PMDA-ODA polyimide type sample 6.5 μm in thickness. The sample was loaded to 7 N and unloaded (solid line). The unloading curve was significantly different from the loading curve. Plastic deformation is evident as the unloading curve crossed the strain axis at an offset. The sample was reloaded and unloaded (dotted line), and again, an offset was observed on the strain axis. The loading and unloading was repeated one more time (not shown, but identical to dotted line), and finally the sample was loaded to the break point (dashed line) which occured at 8.7 N (112 MPa). The Young's modulus and strain at break were measured to be 2700 MPa and 15.6% for this sample.

The direct tensile test is a useful measurement technique for understanding the behavior of thin films. The information obtained from this test will help analytical modeling of structures involving polymer thin films in general. This is evident from the comparison of the two polyimide types where in one (BTDA-MPDA/ODA) a single value for E is sufficient in the analytical model since the material shows linear elastic behavior up to the break point, while in the other

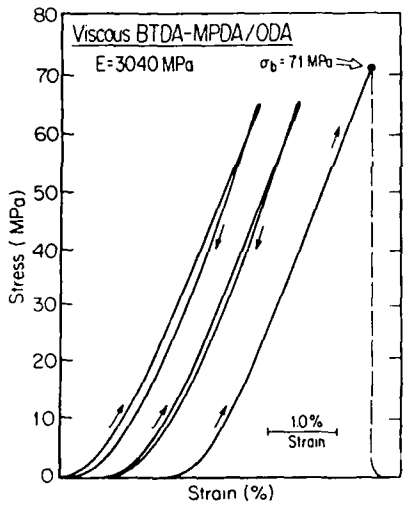

Fig.3

Stress vs strain results for BTDA-MPDA/ODA; two load cycles and final loading to break. Successive load cycles are displaced horizantally for clarity. The strain at break was 2.8%.

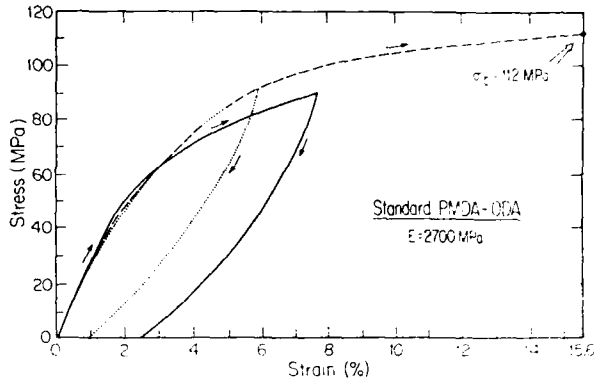

Fig.4

Stress vs strain results for PMDA-ODA; three load cycles and final loading to break :
solid line = first load/unload;
dotted line = second and third load/unload;
dashed line = loading to break

(PMDA-ODA) the stress-strain relation is nonlinear in which a single E cannot be assumed in the analysis after the proportional limit point.

On the other hand, because the Instron specimens are under uniform uniaxial stress, the yield and ultimate strength properties measured by this method can be dominated by edge cracks and other processing imperfections. In the following section, we present an alternative approach which is more effective for studying the yield properties of thin films.

Elastic Limit Properties

The elastic limit of thin polyimide films was measured by investigating plastic deformation of circular membranes under applied pressure. Circular membranes lack stress concentration points present in the square membranes. Furthermore, the fabrication procedure is free from sharp edges eliminating the presence of microscopic edge defects which are difficult to avoid in the Instron specimen fabrication. It was then possible to directly measure the yield point using the circular membranes in a controled experiment.

One inch diameter membranes of standard BTDA-MPDA/ODA type polyimide were fabricated and loaded to their elastic limit. The fabrication process consists of spin depositing polyimide on a silicon wafer, adhering a prefabricated circular ring to the polyimide side, and wet etching the silicon. The ring supports the released membrane, maintaining the state of stress in the polyimide film. The circular membrane fabricated as above is then mounted to another substrate for our standard pressure vs deflection measurements. From the p vs d results measured before the yield point, we obtained the stress and modulus to be 28 MPa and 3300 MPa respectively. These values were consistent with the results obtained from the previous methods. The load was then increased until plastic deformation was initiated and then the load was kept constant. The plastic deformation started at the center of the loaded sample, where the stresses are the highest and gradually moved outwards. Using the pressure at yield and the measured deformation, the yield stress and strain were determined.

Fig.5 shows the measured p vs d results for a 1 inch circular membrane. The yield stress and strain was measured to be 130 MPa and 3% respectively. The measured yield strain of the circular membrane is higher than the break strain of the same chemistry polyimide from the Instron measurement (2.8%), implying the circular membrane technique's superiority (due to its symmetry) in studying the material behavior in the post-elastic range.

Fig. 6 shows the plastically deformed sample after the applied pressure was removed. The domed shape region is the plastically deformed region which initiated from the center of the membrane and propagated radially outward. The flat region is the unyielded region, which is still under residual stress.

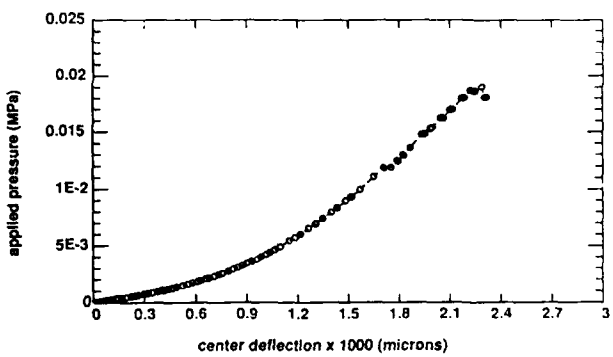

Fig.5

Pressure vs deflection results for a BTDA-MPDA/ODA circular membrane

Conclusion

A number of consistent measurement techniques have been employed to determine the mechanical propeties of thin polyimide films. The techniques can be adapted to other thin films from which microfabricated specimens can be made. The Instron test results provided useful information about the material behavior including Young's modulus whereas the membranes were used to determine quantitative values for residual stress and elastic modulus. Finally the axisymmetric state of circular membranes under pressure were utilized effectively in determining the elastic limit of thin polymer films.

Acknowledgements

This work was sponsored in part by Digital Equipment Corporation. The authors gratefully aknowledge Dr. P.J. McGonigal of DuPont Marshall Laboratory for his assistance with the Instron measurements; and Mr. G. G. Shahidi, J. Carter, and Prof. H. I. Smith of the Submicron Structures Laboratory at MIT for their valuble comments and assistance in developing the process for fabricating the circular membranes. Microfabrication was carried out in the Microsystems Technology Laboratory, and in the Microelectronics Laboratory of the MIT Center for Material Science and Engineering, which is supported in part by the National Science Foundation under Contract No. DMR-84-18718.

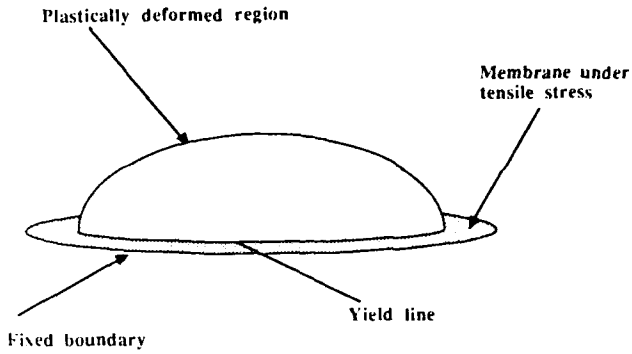

Fig.6

BTDA-MPDA/ODA circular membrane under plastic deformation; domed region is under permanent deformation, and the flat region under residual stress

References

[1]. H. Guckel, T. Randazzo, and D. W. Burns, "A simple technique for the determination of mechanical strain in thin films with application to polysilicon", J. Appl. Phys., 57, 1671-1675, 1985.

[2]. M. Mehregany, R. T. Howe, and S. D. Senturia, "Novel microstructures for the in situ measurement of mechanical properties of thin films", J. Appl. Phys. 62 , 3579-3584, 1987.

[3]. E. I. Bromley, J. N. Randall, D. C. Flanders and R. W. Mountain, "A technique for the determination of stress in thin films", J. Vac. Sci. Tech., 1, 1364-1366,1983.

[4]. M. G. Allen, M. Mehregany, R. T. Howe, and S. D. Senturia, "Microfabricated structures for the in situ measurement of residual stress, Young's modulus, and ultimate strain of thin films", Appl. Phys. Lett., 51, 241-243,1987.

[5]. S. D. Senturia, "Microfabricated structures for the measurement of mechanical properties and adhesion of thin films", Proc. Transducers '87,Tokyo, June 87, pp. 11-16.

[6]. D. S. Campbell, Handbook of Thin Films Technology, McGraw Hill Co., New York, 1970; ch.12.

FRACTURE STRAIN OF LPCVD POLYSILICON

Y. C. Tai and R. S. Muller

Berkeley Sensor and Actuator Center
An NSF/Industry/University Cooperative Research Center
Department of Electrical Engineering and Computer Sciences
and the Electronics Research Laboratory
University of California, Berkeley CA 94720

ABSTRACT

A new polysilicon bridge-slider structure (Fig. 1), in which one end of the bridge is fixed and the other is connected to a plate sliding in two flanged guideways, is designed and fabricated to study the strain at fracture of LPCVD polysilicon. In the experiments, a mechanical probe is used to push against the plate end, compressing and forcing the bridge to buckle until it breaks. The distance that the plate needs to be pushed to break the bridge is recorded. Nonlinear beam theory is then used to interpret the results of these axially-loaded-bridge experiments. The measured average fracture strain of as-deposited LPCVD polysilicon is 1.72%. High-temperature annealing of the bridge-sliders at 1000 °C for one hour decreases the average fracture strain to 0.93%.

INTRODUCTION

Polysilicon has been demonstrated to have useful applications for sensors and actuators. Moreover, complex polysilicon micromechanisms have been shown to be feasible [1,2] using pin joints, gears, springs, and cranks. As a result, new devices like micro-motors and micro optical shutters are becoming possible. Proper design of these structures is hindered, however, by the lack of precise knowledge of the mechanical properties of polysilicon. Of these parameters, strain at fracture is particularly important.

For single-crystal silicon, Eisner [3] reported a maximum fracture strain of 2.03% measured on whiskers about one micrometer in diameter under tension. Pearson, Read, and Feldmann [4] reported a maximum fracture strain of 2.6% for silicon whiskers both grown from vapor and cut from bulk silicon. Moreover, it is found that below 600 °C there is little or no plastic flow in silicon whiskers about 20 μm in diameter before fracture.

It is expected that polysilicon will also behave linear-elastically before fracture at room temperature because grain boundaries in polysilicon can greatly block dislocation motion [6] and make the polysilicon more like an ideal brittle material. Based on this assumption, Fan, Tai, and Muller [5] reported preliminary experiments which determined an experimental fracture strain of polysilicon to be 1.7% using a spiral-spring-restrained pin-joint structure. However, such a spring-restrained pin-joint structure is not optimal for the fracture experiment. Moreover, it is generally accepted that a statistical method should be used to study the fracture strength in brittle materials [6].

We report here a systematic method to study the fracture strain of polysilicon. We introduce a new, easily implemented method using a bridge-slider structure to avoid the difficulties of handling small samples as reported in the silicon whisker experiments [3,4]. The bridge-slider structure is specially designed and processed to improve experimental accuracy.

BRIDGE-SLIDER STRUCTURE

Figure 1 shows an SEM photograph of the newly designed bridge-slider structure. The right end of the free-standing bridge, shown in Fig. 1, is anchored to the silicon substrate, while the left end is connected to a sliding plate guided by two flanges. The outer edges of the slider flanges are sawtooth shaped with a tooth pitch of 4 μm to provide scales for locating the end of the slider. This sawtooth feature greatly simplifies our experiments. Figure 2 shows a cross section of the slider to demonstrate its translational freedom of motion. Clearly, the slider, made of second-layer polysilicon, is fully separated from the restraining elements that are made of first-layer polysilicon. The flanges one of which is circled in Fig. 2 allow the slider only to slide in and out of the plane of Fig. 2.

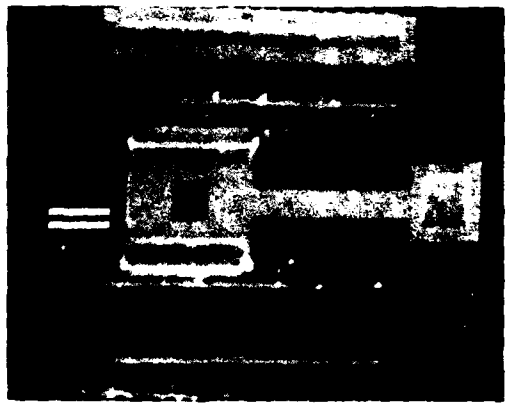

Figure 1 A bridge-slider structure. The bridge-slider is made of second-layer polysilicon. Integrated sawtooth scales are defined at the outer side of flanges. The marker is 30 μm in length.

THC215-4/88/0000-0088 © 1988 IEEE

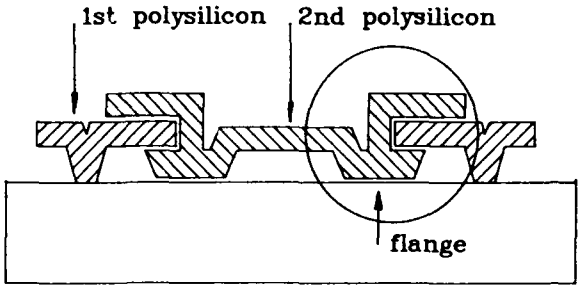

Figure 2 Cross section of the flanged plate slider. The plate can move freely in and out of the paper.

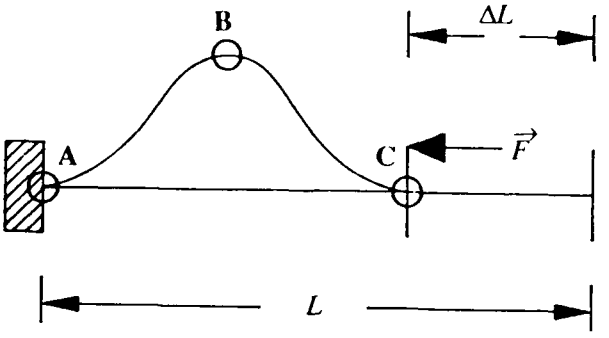

Figure 3 Side view of a buckled beam. The beam is straight before loading. Points A, B, and C have the maximum bending moment and therefore are the expected locations of fracture.

This bridge-slider structure is fabricated using five masks in a sacrificial layer technique. Fabrication starts by coating the four-inch wafers with 1.5-μm-thick low-pressure-chemical-vapor-deposited (LPCVD) phosphosilicate glass (PSG). Mask 1 is used to open anchor windows for the first-layer polysilicon. The first-layer LPCVD polysilicon is then deposited and patterned using mask 2. Polysilicon is patterned in a CCl_4 plasma by reactive-ion-etching (RIE) to provide anisotropic etching. Mask 3 is used to open the flange windows with a time-controlled PSG etch in 5:1 buffered hydrofloric acid (BHF). This step creates a 1.5 μm-long undercut of the first-layer-polysilicon restraining element which forms the flanges. A LPCVD silicon-nitride sacrificial layer is then deposited to coat all the exposed surfaces including the flange undercuts. This silicon-nitride layer is 200 nm thick and, therefore, determines the gap between the two polysilicon layers. Mask 4 opens the anchor windows for the bridges. The second-layer polysilicon is then deposited and patterned using mask 5. The last step which frees the structures in concentrated HF (49%) takes several hours. For unannealed polysilicon structures, the highest temperature in the fabrication process is 650 °C which occurs during deposition of the phosphorus-doped polysilicon films. Annealed samples are treated at 1000 °C for one hour before the final etching.

Figure 4 SEM picture of strained bridge-sliders. When sufficiently strained, the bridges retain their buckled shapes. The lengths of the bridges are 4, 3, and 2 mm, respectively, from top to bottom of the picture.

EXPERIMENTAL PROCEDURE

Figure 3 demonstrates the fracture experiment. By pushing the slider with a mechanical probe, an initially straight bridge can be buckled until it fractures. Pushing is done under an optical microscope and the whole procedure is video-taped to provide a record. Since the edges of the flanges are shaped with sawtooth scales, the maximum distance ΔL that the slider can be pushed is easily measured. Figure 4 shows some pre-pushed and buckled bridge-sliders to demonstrate the experiment. The bridges retain their buckled shapes in Fig. 4 because they are jammed in the slider under such high strain. Figure 5 also shows a pre-buckled bridge to demonstrate the clamped boundary conditions used in our theory. Once ΔL is measured, a nonlinear beam-bending theory is used to interpret the strain in the beam.

Figure 5 SEM picture of a strained bridge-slider. The buckled shape is a result of clamped boundary conditions.

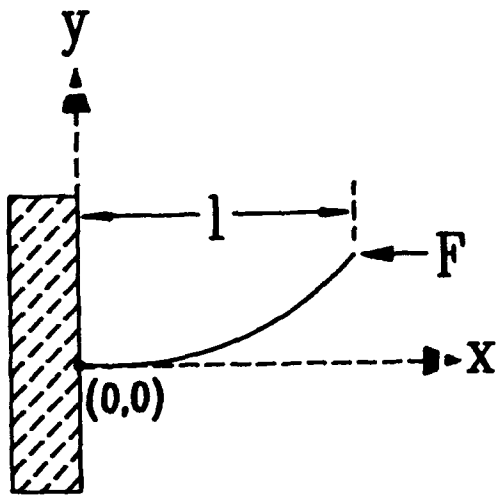

Figure 6 Side view of an axially loaded cantilever.

THEORY

Because the bridge bending is symmetric (Fig. 3), only one quarter of the structure needs to be analyzed. Figure 6 shows the bending of a cantilever beam due to a horizontal force. The analysis starts with the bending equation [7]

$$\frac{1}{r(x,y)} = \frac{M(x,y)}{E_Y I} \tag{1}$$

where the $r(x,y)$ is the curvature, $M(x,y)$ is the bending moment, E_Y is Young's modulus, and I is the moment of inertia. In the case of a rectangular cross section, $I = \frac{wt^3}{12}$. Here, w is the beam width and t is the beam thickness. Eq. (1) can be rewritten as

$$-\frac{y''}{(1+y'^2)^{3/2}} = \frac{F[y(l)-y]}{E_Y I} \tag{2}$$

where l is the projection length of the beam on the x-axis and $y(l)$ is the beam-end deflection (which will be solved for later). The boundary conditions on Eq. (2) are $y'(0)=0$ and $y''(l)=0$. The solution for $y(l)$, obtained by solving Eq. (2), is [8]

$$y(l) = \frac{pL}{2K(p)} \tag{3}$$

and intermediate solutions for for l and F are

$$l = \frac{L-\Delta L}{4} = \frac{L}{4}\left[\frac{2E(p)}{K(p)} - 1\right] \tag{4}$$

$$F = 16E_Y I \frac{K^2(p)}{L^2} \tag{5}$$

where L is the total length of the bridge and $p = \frac{y(l)}{2}\sqrt{\frac{F}{E_Y I}}$ is defined to simplify the derivation. The quantities $K(p)$ and $E(p)$ are complete elliptic integrals of the first and second kind, respectively. These two functions are defined by

$$K(p) = \int_0^{\pi/2} (1-p^2\sin\phi)^{-1/2} d\phi \tag{6}$$

$$E(p) = \int_0^{\pi/2} (1-p^2\sin\phi)^{1/2} d\phi \tag{7}$$

For a given value of p, both $K(p)$ and $E(p)$ can be obtained from mathematical tables. The parameter p can be obtained using Eq. (4) since ΔL is measured and p is the only unknown in Eq. (4). Knowing p, one can calculate the force F from Eq. (5) and $y(l)$ from Eq. (3).

Once F and $y(l)$ have been calculated, the maximum strain can also be determined. The maximum strain (which occurs at the clamped end) is [7]

$$\varepsilon_{\pm max} = \pm\frac{M(0,0)t}{2E_Y I} - \frac{F}{wtE_Y}$$

$$= \pm 4pK(p)\frac{t}{L} - \frac{4}{3}K^2(p)\left(\frac{t}{L}\right)^2 \tag{8}$$

where the + sign stands for tension and the − sign for compression. Since we have used one-dimensional beam theory, strain is independent of beam width w. As shown in Fig. 6, the lower half of the polysilicon beam is in tension and the upper part is in compression. In fact, the difference in magnitude between compressive and tensile strains is twice the last term in Eq. (8). This term represents compressive strain caused by horizontal force. It is relatively small compared to the bending strain due to its $(\frac{t}{L})^2$ dependence. Moreover, in brittle materials, tensile stress is usually regarded as the most significant cause of fracture [6]. Therefore, we consider only the maximum tensile strain which is

$$\varepsilon_{+max} = 4pK(p)\frac{t}{L} - \frac{4}{3}K^2(p)\left(\frac{t}{L}\right)^2 \tag{9}$$

Figure 7 shows the results of theoretical calculations of ε_{+max} using Eq. (9) for bridge lengths L = 100, 200, 300, and 400 μm and thickness 1.27 μm. Using Fig. 7, one can convert the experimental ΔL into fracture strain. For example, one finds ΔL to be 41 μm for a bridge that is 200 μm long. This value of ΔL can be used with Fig. 7 to find the corresponding fracture strain which is 1.88%.

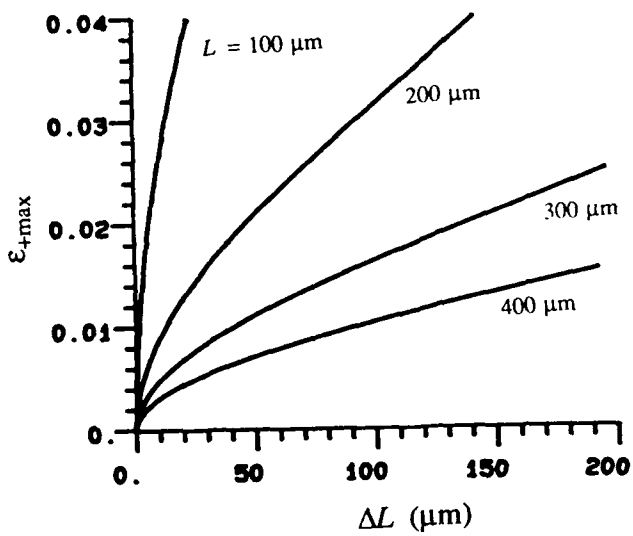

Figure 7 Theoretical calculations of $\varepsilon_{+max}(\Delta L)$ from Eqs. (4) and (9). Thickness of the bridges is 1.27 μm.

Since the cantilever beam is only one quarter of the full bridge, the maximum strain occurs at the center and the two ends of the bridge as pointed out in Fig. 3. Therefore, the theory predicts that fracture should happen at those three points, as is observed experimentally.

RESULTS

In brittle materials, fracture occurs when a crack can propagate in the material. Cracks can originate from defects in solids such as impurity inclusions and segregations, and grain boundaries. The probability that these defects will cause fracture depends heavily on their spatial extent, shape, and orientation, which are statistically distributed Therefore, the study of polysilicon fracture should be done statistically. To facilitate this, we present statistical results obtained from our experiments.

Table 1 lists ΔL and ε_{+max} deduced from the theory presented for both the unannealed and annealed bridge sliders. The highest processing temperature for the unannealed polysilicon is 650 °C. Annealing is carried out at 1000 °C.

For the unannealed bridge-sliders, the average fracture strain is 1.72% with a 95% confidence interval bounded by 1.63% and 1.81%. The variance is 0.217%. For the annealed bridge-sliders, the average fracture strain is 0.93% and the 95% confidence interval is (0.89%, 0.97%) with a variance of 0.1%.

Two important results emerge from this study. One is that the annealed bridge-sliders have a much smaller average fracture strain than do the unannealed samples (0.93% versus 1.72%). The second result is that unannealed bridges show larger scatter of the fracture strain in terms of both confidence interval and variance. Our experiments have shown that high-temperature annealing has, therefore, decreased both the magnitude and distribution of the fracture strain of polysilicon.

REFERENCE

[1] L. S. Fan, Y. C. Tai and R. S. Muller, "Pin joints, gears, springs, cranks, and other novel micromechanical structures," *Transducers'87*, 4th Intl. Conf. on Solid-State Sensors and Actuators, Tokyo, Japan (June 3-5, 1987), pp. 849-852.

[2] K. J. Gabriel, W. S. N. Trimmer, and M. Mehregany, "Micro gears and turbines etched from silicon," *Transducers'87*, 4th Intl. Conf. on Solid-State Sensors and Actuators, Tokyo, Japan (June 3-5, 1987), pp. 853-856.

[3] R. L. Eisner, "Tensile tests on silicon whiskers," *Acta Metallurgica, Vol.* **3**, 1955, pp.414-415.

[4] G. L. Pearson, W. T. Read Jr, and W. L. Feldmann, "Deformation and fracture of small silicon crystals," *Acta Metallurgica, Vol.* **5**, April, 1955, pp.181-191.

[5] L. S. Fan, Y. C. Tai, and R. S. Muller, "Integrated movable micromechanical structures for sensors and actuators," *IEEE Trans. ED*, (to appear June, 1988).

[6] A. de S. Jayatilaka, "Fracture of engineering brittle materials," London, Applied Science Publishers LTD, 1979.

[7] S. Timoshenko and D. H. Young, "Elements of strength of materials," Princeton, N.J., D. Van Nostrand Co., 1968.

[8] R. Frisch-Fay, "Flexible bars," Washington, Butterworth Inc., 1962.

Table 1 Experimental fracture strain of polysilicon

Size	Unannealed		Annealed	
L/w/t	ΔL (μm)	ε_{+max}(%)	ΔL (μm)	ε_{+max}(%)
100/2/1.27	5,7	1.80,2.14	x	x
100/6/1.27	8	2.29	x	x
100/10/1.27	x	x	x	x
100/20/1.27	x	x	x	x
200/2/1.27	41	1.88	10,16	0.90,1.14
200/6/1.27	36,40	1.75,1.86	11,15	0.94,1.11
200/10/1.27	27,29,33,37	1.51,1.56,1.67,1.78	10,11	0.90,0.94
200/20/1.27	29,31,35,37,41	1.56,1.62,1.73,1.78,1.88	9,10	0.85,0.90
300/2/1.27	124	1.87	35,36	0.93,0.94
300/6/1.27	75,100	1.40,1.65	30,45	0.86,1.06
300/10/1.27	77,95,97	1.42,1.60,1.62	38,38	0.97,0.97
300/20/1.27	85	1.50	23,27	0.75,0.81
400/2/1.27	x	x	90,94	0.99,1.01
400/6/1.27	x	x	74,84	0.89,0.95
400/10/1.27	x	x	79,84	0.92,0.95
400/20/1.27	x	x	53,60	0.75,0.80

CHARACTERIZATION OF THE MECHANISMS PRODUCING BENDING MOMENTS IN POLYSILICON MICRO-CANTILEVER BEAMS BY INTERFEROMETRIC DEFLECTION MEASUREMENTS

Theresa A. Lober, Jiahua Huang, Martin A. Schmidt, and Stephen D. Senturia

Microsystems Technology Laboratories
Massachusetts Institute of Technology
Cambridge, Massachusetts 02139

ABSTRACT

Polysilicon micro-cantilever beams and doubly-supported beams are fabricated and conditioned with phosphorus doping and high temperature anneal cycles to assess the effects of process history and geometry on polysilicon microstructure rigidity. Using a Linnik interferometer, deflection trends for series of beams are measured and compared for several process conditions. Two bending moments can induce beam deflection: the first due to the beam boundary support, and the second due to stress nonuniformity through the beam thickness. A comparison of polysilicon microstructure deflection behavior for doping and annealing conditions is presented and discussed.

INTRODUCTION

Surface-micromachining techniques have been employed to create a polysilicon microbridge vapor sensor and planar pressure transducer [1, 2]. Successful fabrication of these suspended microstructures critically depends on the ability to reliably and routinely deposit low pressure chemically vapor deposited (LPCVD) polysilicon films with known physical properties. In particular, the stressed condition of polysilicon films presents design limitations for the development of microstructures since film warpage determines the maximum free standing lateral dimensions of a suspended microstructure. Guckel used measurements of doubly-supported polysilicon beam deflection as a function of geometry to determine the residual strain of thin polysilicon films for a given film condition [3]. Howe compared the buckling length of polysilicon cantilever beams with different process conditions to characterize the stress of thin polysilicon films for these conditions [4]. Together, these techniques provide an in situ method for determining the combined effects of geometry and process history on the structural rigidity of suspended microstructures. This study utilizes measurement of both cantilever beam deflection and doubly-supported beam buckling to distinguish the origins of polysilicon film warpage for differing film conditions and geometry.

EXPERIMENTAL

The polysilicon micro-beams are fabricated using surface-micromachining techniques on <100> oriented, 4-inch, 2 Ω-cm, n-type silicon wafers. A 0.8 μm-thick, undoped, sacrificial oxide layer is deposited on the wafers using a 400° C LPCVD cycle with a deposition rate of 125 Å/min. Trenches are patterned and dry-etched in the oxide layer to expose the underlying silicon surface. Pure silane is reacted at 250 mT and 625° C to deposit LPCVD polysilicon films ranging in thickness from 0.25 - 1 μm with a deposition rate of 100 Å/min. Half of the samples are phosphorus doped during a 60 minute diffusion cycle at 925° C using a $POCl_3$ liquid diffusion source. The samples are then patterned and anisotropically dry-etched using CCl_4 to form cantilevers and doubly-supported beams. Half of the doped and undoped samples then are annealed in a nitrogen ambient at 1150° C for 20 minutes. The suspended structures are released using 48 wt% hydrofluoric acid to undercut the oxide spacer layer, and are dried under a chemical hood after being rinsed in deionized water and methanol. Some undoped structures are released using the vapors of evaporating 48 wt% hydrofluoric acid to remove the oxide film, requiring no final rinse or dry cycle [5].

Once dried, the beams are inspected for vertical deflections using a Linnik interferometer attached to the 100X objective of an optical microscope. When viewed through the interferometric objective, cantilever and doubly-supported beams like those of Figs. 1 and 2 display interference fringes generated by the passage of coherent light through the interferometer's lenses onto the suspended structures. As shown in Figs. 3 and 4, the interference fringe patterns follow the deflection profile of the structures. Spacing of the straight fringes in the field regions of Figs. 3 and 4 corresponds to the half-wavelength of the coherent light used - the 5240 Å sodium yellow line. This distance provides coordinates for calibrating the vertical beam deflections. A measure of the angle, θ, defined by the curvature of the fringe profile between a beam boundary support and the edge of a cantilever or the center of a doubly-supported beam determines the vertical beam deflection, δ, as

$$\frac{\delta}{L} = \mathrm{Tan}\theta \, \frac{\lambda}{2D} \, , \qquad (1)$$

where L is the suspension length, λ is the illuminating light's wavelength, and D is the separation between two undeflected fringes. With the ability to resolve 1/10 of a fringe spacing, accuracy of the vertical deflection measurements is 250 Å.

Deflections are measured for series of cantilever beams and doubly-supported beams for each of four polysilicon film conditions: undoped, unannealed and annealed; and doped, unannealed and annealed. The cantilever beams range in length from 10 - 70 μm with 2 μm increments in length, and are 15 μm-wide, while the bridges range from 10 - 100 μm in length with 5 μm length increments, and are 15 μm-wide. All cantilever samples are 0.5 μm-thick, while for each polysilicon condition, doubly-supported beams are fabricated of 0.25, 0.5, 0.75, and 1 μm-thick films. Samples used for the two annealed conditions are inspected before and after the annealing cycles; comparison of the pre-anneal and post-anneal structural profiles indicates that no pre-release deflection of any structures occurs due to "softening" of the oxide spacer layer during the anneal cycle.

TH0215-4/88/0000-0092

Figure 1. Released polysilicon cantilever beams

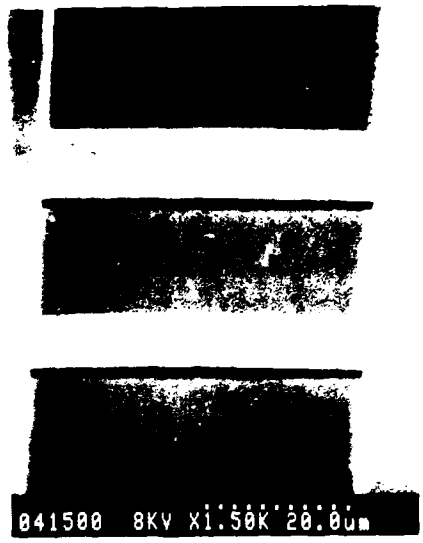

Figure 2. Released polysilicon doubly-supported beams

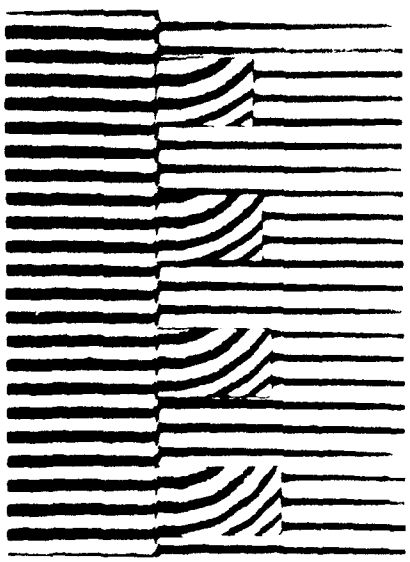

Figure 3. Interference pattern of beams in Fig. 1

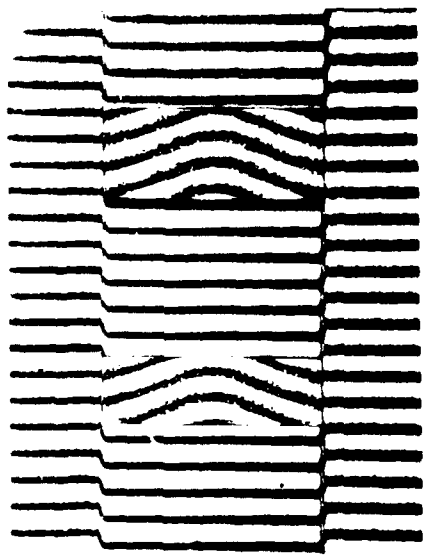

Figure 4. Interference pattern of beams in Fig. 2

RESULTS

Singly Supported Beams

Deflection trends for the undoped cantilever samples, etched with liquid HF (LHF) or vapor HF (VHF), are shown in Fig. 5 as a function of length. For the cantilevers released with the liquid etchant, deflections are upward for short beams, but the beams deflect downward and become stuck to the substrate at all lengths greater than 30 - 32 μm. This large deflection and sticking may be due to surface tension effects from the liquid etch and rinse baths and surface conditions of the suspended structures and the substrate. Deflections of the VHF-released samples match those of the LHF-released samples for short beam lengths, but never change direction to bend downward and touch the substrate. This indicates that the downward deflections of longer LHF-released beams are not caused by built-in bending moments but rather by the etch technique, so that deflections of beams less than 30 μm-long adequately characterize deflection trends due to built-in bending moments. Deflections of VHF-released beams longer than 50 μm are also upward, but too large to accurately measure with the interferometer.

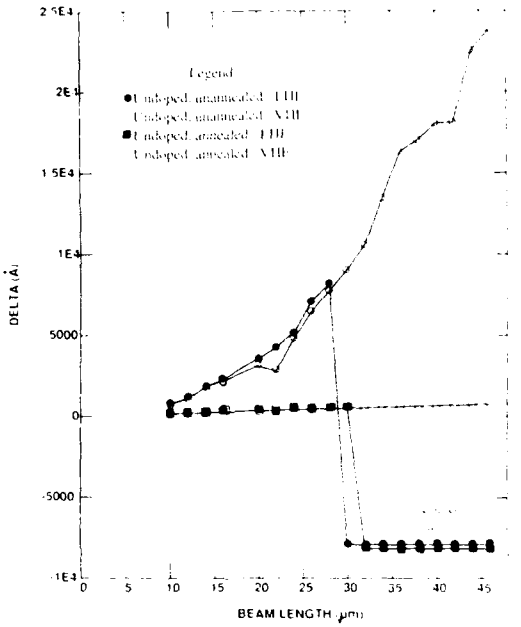

Figure 5. Deflection, δ, as a function of length for undoped cantilever beams etched with LHF or VHF

Two bending moments can induce cantilever deflection, as shown in Fig. 6. The first is due to the clamped step-up boundary, and causes a deflection linearly dependent on the cantilever length, L. The second is due to stress nonuniformity through the beam thickness, and causes a deflection that depends quadratically on L. Since the effects are additive [6], the combined effect of both moments is of the form

$$\delta \propto K_1 L + K_2 L^2 \qquad (2)$$

Thus, a plot of δ/L versus L should be a straight line, with an intercept at K_1 reflecting the boundary bending moment, and a slope K_2 reflecting the stress nonuniformity.

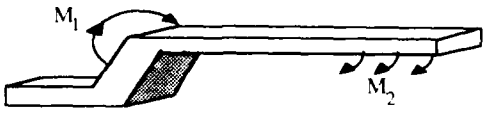

Figure 6. Built-in bending moments of cantilever beams

Figure 7 illustrates the dependence of δ/L on L, the cantilever length, for the four polysilicon beam film conditions, all released with LHF. Trends for the undoped cantilevers, unannealed and annealed, with either positive or zero slope, respectively, indicate upward beam deflection, while the negatively sloped trends of the two doped cantilever conditions indicate deflections downward. The y-axis intercept of the four trends represents K_1 in the model above, and the slope of each line indicates K_2, confirming that the observed deflection behavior agrees with the model.

Deflections of the undoped, unannealed samples indicate a large boundary moment and stress nonuniformity, while the undoped, but annealed samples exhibit a much smaller boundary moment and negligible stress nonuniformity. This demonstrates that the 1150° C annealing cycle effectively reduces both the bending moment due to the step-up boundary and the intrinsic stress nonuniformity through the film thickness. Deflection data

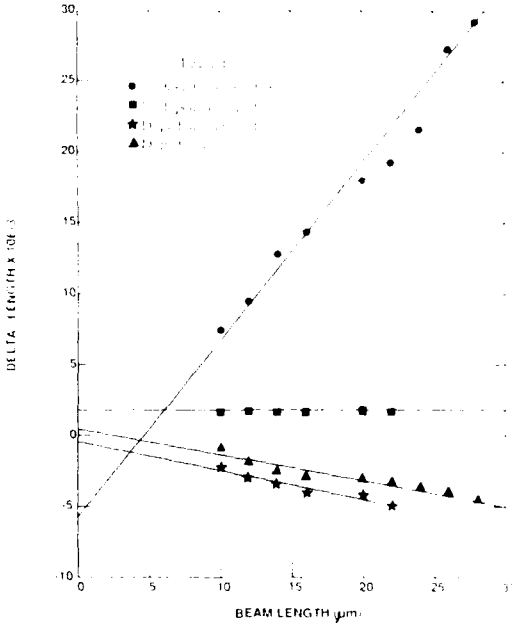

Figure 7. δ/L as a function of length, L, for polysilicon cantilever beams with four process conditions: undoped, unannealed and annealed; and doped, unannealed and annealed

from samples for both doped conditions exhibit identical slopes, characteristic of a stress nonuniformity due to the doping profile through the films, and similar boundary bending moments. While all undoped beams deflect upward, the doped beams deflect downward, indicating that doped and undoped polysilicon films are in opposing states of stress nonuniformity. The similarity of the unannealed and annealed, doped beam deflections suggests that the grain structure of $POCl_3$-doped films is in a stable state of equilibrium after the doping cycle; the annealing cycle does not effectively alter this state.

Doubly-Supported Beams

Buckling lengths for the four doubly-supported beam conditions are shown in Fig. 8 as a function of polysilicon film thickness. At lengths less than the buckling length, L_c, the beams deflect upward, while at lengths greater than L_c the beams deflect downward. For the undoped beams, those conditioned with an anneal cycle exhibit a longer buckling length than those without the cycle, demonstrating that the anneal cycle has produced a more structurally rigid beam. L_c is constant for doped beams, regardless of their annealing condition, suggesting, like the cantilever deflections, that $POCl_3$-doped polysilicon films are in a stable equilibrium state. The increase in buckling lengths for thin beams beyond that predicted by the thicker beams may be explained by a simple model that accounts for compliance of the step-up beam supports. This model will be reported separately.

If compliance of the beam support is ignored, a good approximation for the residual strain level, ε_p, of the 1 μm-thick beams at the buckling length is estimated by Euler buckling theory [6] for each process condition as

$$\varepsilon_p = \frac{\pi^2 t_p^2}{3 L_c^2} \ , \qquad (3)$$

where t_p is the polysilicon film thickness, and L_c is the beam buckling length for each of the polysilicon process conditions. Based on Eq. (3), undoped, unannealed films exhibit the highest residual strain, 1.27×10^{-3}, while doped and annealed films exhibit 0.41×10^{-3}, the least residual strain. These values agree well with those previously

reported by Guckel [3], to indicate that high temperature doping and annealing cycles significantly reduce the residual strain of intrinsic polysilicon films, producing longer unbuckled beams than intrinsic films.

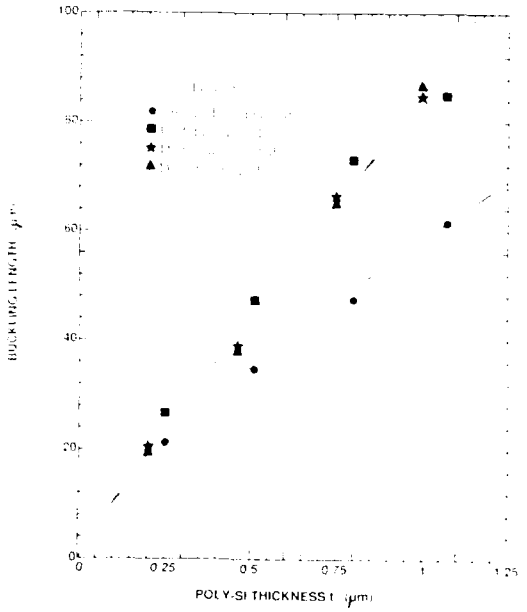

Figure 8 Buckling length as a function of film thickness for polysilicon doubly-supported beams with four process conditions: undoped, unannealed and annealed; and doped, unannealed and annealed

CONCLUSIONS

This study demonstrates that both end-effects and stress nonuniformity contribute to the deflections of suspended, surface-micromachined, polysilicon structures. High temperature annealing of the polysilicon film significantly decreases both the boundary bending moment and the intrinsic stress nonuniformity of the structures, thus increasing structural rigidity. Doping of the films also decreases these bending moments, but introduces an opposing stress nonuniformity possibly due to the doping profile through the film thickness, inducing further beam deflection. Calculation of the residual strain of doubly-supported beams at their buckling length demonstrates that the residual strain of intrinsic polysilicon is significantly reduced by high temperature phosphorus-doping and annealing cycles, providing the ability to fabricate larger suspended polysilicon microstructures.

ACKNOWLEDGEMENTS

The authors are indebted to Prof. H.I. Smith, James Carter, and Yao-Ching Ku for providing access to and assistance with the Linnik interferometer. Prof. R.L. Smith is thanked for first suggesting to use vapor HF as a release etchant. This work was sponsored in part by the National Science Foundation, under contract ECS-8614328 and by the DARPA CAF project, under contract 87-SP-080. Support of the 3M Sensor Fellowship (MAS) is gratefully acknowledged. All fabrication was carried out in the MIT Integrated Circuits Laboratory of the Microsystems Technology Laboratories.

REFERENCES

[1] H. Guckel and D. W. Burns, "Planar processed polysilicon sealed cavities for pressure transducer arrays," in Technical Digest IEEE IEDM, p. 233, 1984.

[2] R.T. Howe and R.S. Muller, "Resonant-microbridge vapor sensor," IEEE Trans. on Electron Devices, vol. ED-22, pp. 499 - 506, 1986.

[3] H. Guckel, T. Randazzo and D. W. Burns, "A simple technique for the determination of mechanical strain in thin films with application to polysilicon," J. Appl. Phys., 57(5), pp. 1671 - 1675, March 1985.

[4] R.T. Howe and R.S. Muller, "Stress in polycrystalline and amorphous silicon thin films," J. Appl. Phys., 54, pp. 4674 - 4675, August 1983.

[5] T.A. Lober and R.T. Howe, "Surface micromachining processes for electrostatic microactuator fabrication," this conference.

[6] J.M. Gere and S.P. Timoshenko, Mechanics of Materials, Belmont, CA: Wadsworth, Inc., 1984.

MECHANICAL PROPERTIES OF FINE GRAINED POLYSILICON THE REPEATABILITY ISSUE

H. Guckel, D. W. Burns, H. A. C. Tilmans, D. W. DeRoo,* and C. R. Rutigliano**

Wisconsin Center for Applied Microelectronics
Department of Electrical and Computer Engineering
University of Wisconsin
Madison, Wisconsin 53706

*Currently employed by Delco Electronics Corp., Kokomo, Indiana
**Currently employed by BIT, Inc., Beaverton, Oregon

Abstract

Calculation and measurements of Young's modulus, Poisson's ratio, shear modulus and internal strain for fine grained polysilicon as a function of processing conditions are presented. Calculations are based on appropriate averaging of single crystal silicon properties, taking into account the film morphology. Experimental data are taken from strain diagnostic and resonant beam structures. It is found that polysilicon films can be in tension and that the intrinsic quality factor is approaching 75,000.

Introduction

Polycrystalline silicon is an important material in micromechanical integrated sensors and microstructures.[1-3] It has been used extensively to study feasibility of experimental structures. Proper design of these structures requires knowledge of the material properties such as Young's modulus, Poisson's ratio, internal stress and tensile strength. An understanding of the sensitivity of the device performance on the mechanical properties determines the tolerances allowed on these properties. For example, the pressure sensitivity of the planar processed pressure transducer[4] varies with Young's modulus. A 1.0% increase in Young's modulus decreases the pressure sensitivity by 1.0%, keeping all other parameters fixed. Fabrication of repeatable devices is only possible if full control over the mechanical properties of the materials being used has been accomplished.

This paper deals with the role of morphology changes on the mechanical properties of polysilicon and the measurement of these properties using thin film microstructures.

Theoretical Calculation of Mechanical Properties

The mechanical properties of polysilicon films can be calculated from the properties of single crystal silicon taking into account the effect of the film morphology. In single crystal material, Young's modulus, the Poisson ratio and the shear modulus are calculated using the compliance coefficients and appropriate tensor transformations.[5,6] Calculations of the properties for polycrystalline material requires averaging over the various grain orientations and distribution. A texture function $G(\phi,\theta)$ is defined to mathematically describe the film morphology.[4] Young's modulus for polysilicon is calculated from the following integral,

$$\langle E \rangle = (1/4\pi)\int\int G(\phi,\theta)(1/s_{33}')\,d\phi\,d\theta \qquad (1)$$

where ϕ and θ are the Eulerian angles for coordinate transformations, s_{33}' is the effective compliance coefficient in the x_3' direction for single crystal material and integration is performed over all possible crystal orientations. The effect of grain boundaries is neglected in this formulation. This is valid for cases where the volume fraction of the grain boundaries is small.[4] A varying texture function can lead to as much as a 30% variation in Young's modulus for single crystal or polycrystalline silicon. The other properties are computed by similar but more complex techniques.

Young's modulus, the Poisson ratio and the shear modulus are calculated for polysilicon using equation (1) and values are given in Table 1. The stiffness coefficients for silicon (c_{11}, c_{12} and c_{44}) have been measured by McSkimin and Andreatch.[7] The transformation of stiffness coefficients to compliance coefficients

0002-4/88/0000-0096

can be found in reference [5]. Estimated temperature coefficients of these properties are calculated from the temperature dependence of the stiffness coefficients.[8] Also, the texture function for randomly oriented single crystal grains, i.e. $G(\phi,\theta) = 1$, is used. Texture functions other than unity can be derived from X-Ray diffraction data.[9]

Table 1. Calculated Values and Temperature Coefficients for Young's Modulus E, Poisson's Ratio υ, Shear Modulus G and Bulk Modulus B for Randomly Oriented Polysilicon Films.

Property	Value	TC (ppm/°C)
E	1.61E11 Pa	-74.5
v	0.226	+25.7
G	0.659E11 Pa	-78.5
B	0.978E11 Pa	-53.2

In order to make polysilicon films with reproducible mechanical properties, it is essential to control the texture function, or in other words, the film morphology. Similar comments apply to other polycrystalline materials, such as metals.

Experiments

After achieving a controllable process (see accompanying paper,[10] this digest), measurement techniques can be applied to extract the material properties. Strain diagnostics including doubly supported beams, cantilevered beams and ring and beam structures have been used to measure compressive as well as tensile strain fields. Resonant beam structures have been used to extract Young's modulus and the strain field.[11]

Strain Diagnostics

Doubly supported beams used to measure compressive strain fields based on buckling and cantilevered beams for observing strain nonuniformities have been published elsewhere.[12] Ring and beam structures are used to measure tensile strain fields.[13] A beam is suspended between two points on a ring as shown in Figure 1. The ring is attached to the substrate at two diametrically opposite points. A tensile strain field in the film results in a compressive load on the cross beam. Large geometries become unstable, resulting in buckling of the beam, which is readily seen under a phase contrast microscope. Observation of the critical geometry leads to a determination of the value of the strain field. Detailed mathematical analysis will be published at a later date.

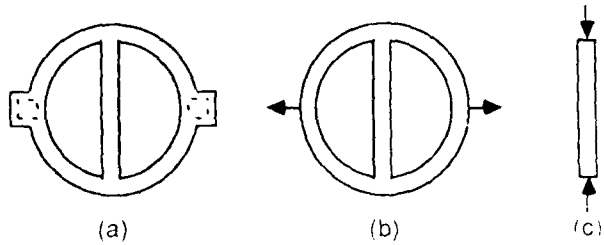

Figure 1. Ring and beam diagnostic structure.
(a) Top view.
(b) Free-body diagram of the ring for a film in tension.
(c) Free-body diagram of the cross beam for a film in tension.

In applying this structure to LPCVD polysilicon films,[10] it was discovered that films deposited at 580°C and annealed under nitrogen at higher temperatures resulted in a tensile strain field.[14] This was surprising since all previous work indicated compressive strain fields. The effect of the anneal cycles on the strain field is shown in Figure 2. As-deposited fine grained polysilicon films are under high compression. Annealing at moderate temperatures results in high tensile strain, and annealing at high temperatures results in nearly zero-strain. Thus, polysilicon films with compressive, tensile, and zero strain fields have been made.

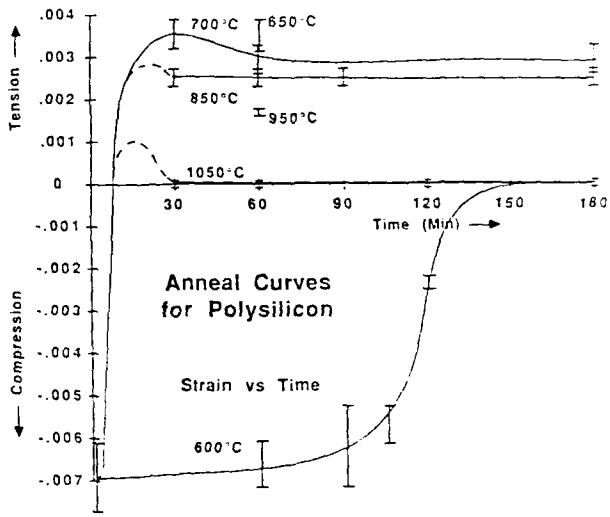

Figure 2. Internal strain for LPCVD polysilicon films deposited on oxidized silicon substrates as a function of post-deposition anneal time and temperature. These films were deposited using the pyrolysis of 100% silane at a temperature of 580°C and a pressure of 300 mTorr.[10]

Resonating Beam Structures

Polysilicon films in tension allow the fabrication of long (> 300 μm) beams which can be used to extract mechanical properties of fine grained polysilicon. Vibrating cantilevered beams have been

used to determine Young's modulus of thin films.[15] Doubly supported clamped-clamped beams can be used to extract both Young's modulus and the internal strain field by measuring the resonant frequencies.

The resonant frequency of a doubly supported beam with a rectangular cross section is a function of Young's modulus E, length L, thickness h, mass density ρ and internal strain field ε_o. The differential equation of motion for the deflection profile w as a function of distance x along the beam and time t is[16]

$$EI\partial^4w/\partial x^4 - \varepsilon_o EA\partial^2w/\partial x^2 = -\rho A\partial^2w/\partial t^2 \qquad (2)$$

where I is the moment of inertia and A is the cross sectional area. The resonant frequency of a clamped-clamped beam can be obtained by numerically solving the eigenvalue equation of this differential equation. However, this approach is not convenient in extracting values for E and ε_o from the resonant frequency. An approximate analytical solution is more suitable and can be obtained using Rayleigh's method.[17] The fundamental resonant frequency, ω, can then be expressed by Rayleigh's quotient,

$$\omega^2 = [\int EI(d^2W/dx^2)^2dx + \varepsilon_o EA\int(dW/dx)^2dx]/\int\rho AW^2dx \quad (3)$$

where W is the exact eigenfunction of the first mode and integration is performed over the entire length of the beam. By choosing an appropriate approximate eigenfunction denoted by W_R, an approximate expression for the resonant frequency can be obtained. A good choice for $W_R(x)$ is

$$W_R(x) = Cx^2(x-L)^2 \qquad (4)$$

where C is a constant. This is the deflection profile of a clamped-clamped beam subjected to a uniformly distributed lateral load. Substitution of (4) into (3) gives the following expression for the approximate resonant frequency ω_R,

$$\omega_R^2 = [504EI/(L^4\rho A)]*[1 + \varepsilon_o AL^2/(42I)] \qquad (5)$$

Comparison with the exact solution from equation (2) gives an error less than 2.5% for the structures used.

Sets of two polysilicon beams, 400 μm and 1000 μm long, 160 μm wide and 2.1 μm thick were used to obtain values for E and ε_o. Electrostatic excitation and optical techniques using reflected laser light were used for detection.[11,15] Measurements were performed at low pressures to achieve high Q values. The results are: E = (1.75 ± 0.21) x 10^{11} Pa and ε_o = +0.021% ± 0.002% for a 2 hour anneal at 1000°C and +0.0084% ± 0.0009% for a 3 hour anneal at 1050°C. The Q factor was determined as a function of pressure by measuring the logarithmic decrement.[17] Extrapolation to zero absolute pressure gives a value of the intrinsic Q for fine grained polysilicon of 74,900. Results can be found in Figure 3.

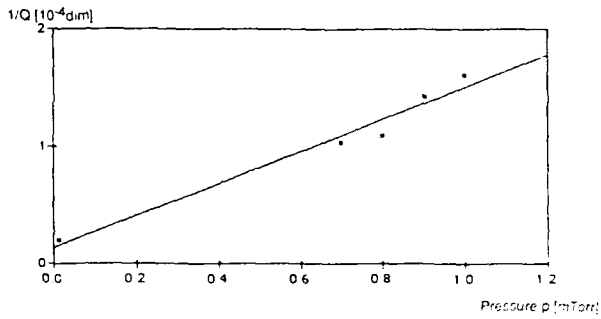

Figure 3. 1/Q vs. pressure for a 1000 μm long beam. The inverse of the intercept with the vertical axis gives the intrinsic quality factor.

Discussion and Conclusions

The calculated value of Young's modulus for polysilicon from published data on single crystal silicon, employing a unity texture function, was found to lie within the range of values obtained from resonant beam experiments. Similar results are expected for the Poisson ratio and the shear modulus, but these properties have not been experimentally determined. More work is needed on the resonant beam technique to achieve higher accuracy and to build more confidence in the measured values of Young's modulus and the internal strain. This can be done by using beams with varying lengths and performing the experiments over a wider range of anneal temperatures and times. Linear regression can then be used with the approximate analytical expression for the resonant frequency given by equation (5). Further improvements can be made using the Rayleigh-Ritz method which employs additional terms in the eigenfunction of the first mode. Work on this is currently in progress.

Fine grained polycrystalline silicon has revealed remarkably good mechanical properties for use in micromechanical devices. Tensile strain fields allow the fabrication of mechanically stable microstructures such as long beams and large area plates which are not feasible with compressive strain fields. Furthermore, resonant structures using polysilicon films with intrinsic Q values (74,900) approaching that of quartz (77,000)[18] become very attractive. The tensile strength of the polysilicon films has been observed to be

quite high; values on the order of 1.0 GPa (150,000 psi) have been estimated from deflections in excess of 300 μm of 0.6 x 0.6 cm^2 square polysilicon plates with a thickness of 2.0 μm.

We have shown that the mechanical properties of polysilicon films can be measured and/or calculated which allows the intelligent design of micromechanical devices.

References

[1] E. Obermeier, "Polysilicon Layers Lead to a New Generation of Pressure Sensors," in Proceedings Transducers '85, pp. 430-433.

[2] R. T. Howe and R. S. Muller, "Resonant-Microbridge Vapor Sensor," IEEE Trans. Electron Devices, Vol ED-33, No. 4, pp. 499-506, Apr. 1986,

[3] H. Guckel and D. W. Burns, C. R. Rutigliano, D. K. Showers and J. Uglow, "Fine Grained Polysilicon and its Application to Planar Pressure Transducers," in Proceedings Transducers '87, pp. 287-282.

[4] D. W. Burns, "Micromechanical Integrated Sensors and the Planar Processed Pressure Transducer," Ph.D. dissertation, University of Wisconsin, Madison, WI, May 1988.

[5] W. P. Mason, Crystal Physics of Interaction Processes. New York: Academic Press, 1966.

[6] J. J. Wortman and R. A. Evans, "Young's Modulus, Shear Modulus, and Poisson's Ratio in Silicon and Germanium," J. Appl. Phys., Vol. 36, No. 1, pp. 153-156, Jan. 1965.

[7] H. J. McSkimin and P. Andreatch, Jr., "Elastic Moduli of Silicon vs. Hydrostatic Pressure at 25°C and -195.8°C," J. Appl. Phys., Vol. 35, No. 7, pp. 2161-2165, July 1964.

[8] H. J. McSkimin, W. L. Bond, E. Beuhler and G. K. Teal, "Measurement of the Elastic Constants of Silicon Single Crytals and their Thermal Coefficients," Phys. Rev., Ser. 2, Vol. 83, No. 5, p. 1080, Sept. 1, 1951.

[9] T. I. Kamins, M. M. Mandurah and K. C. Saraswat, "Structure and Stability of Low Pressure Chemically Vapor-Deposited Silicon Films," J. Electrochem. Soc., Vol. 125, No. 6, pp. 927-932, June 1978.

[10] H. Guckel, D. W. Burns, H. A. C. Tilmans, C. C. G. Visser, D. W. DeRoo, T. R. Christenson, P. J. Klomberg, J. J. Sniegowski and D. H. Jones, "Processing Conditions for Polysilicon Films with Tensile Strain for Large Aspect Ratio Microstructures," 1988 Solid-State Sensor and Actuator Workshop, Hilton Head Is., June 6-9, 1988.

[11] D. W. DeRoo, "Determination of Young's Modulus of Polysilicon Using Resonant Micromechanical Beams," Master's report, ECE Dept., University of Wisconsin, Madison, WI, Jan. 1988.

[12] H. Guckel, T. Randazzo and D. W. Burns, "A Simple Technique for the Determination of Mechanical Strain in Thin Films with Applications to Polysilicon," J. Appl. Physics, Vol. 57, No. 5, pp. 1671-1675, 1 March 1985.

[13] C. R. Rutigliano, "Diagnostic Structures for the Determination of Tensile Strain Fields in Thin Films," Master's report, ECE Dept., University of Wisconsin, Madison, WI, May 1987.

[14] H. Guckel, D. W. Burns, C. C. G. Visser, H. A. C. Tilmans and D. W. DeRoo, "Fine Grained Polysilicon Films with Built-In Tensile Strain," submitted to the IEEE Trans. Electron Devices, June 1988.

[15] K. E. Petersen and C. R. Guarnieri, "Young's Modulus Measurement of Thin Films Using Micromechanics," J. Appl. Phys., Vol. 50, No. 11, pp. 6761-6766, Nov. 1979.

[16] D. J. Gorham, Free Vibration Analysis of Beams and Shafts. New York: John Wiley & Sons, 1975.

[17] W. F. Thomson, Theory of Mechanical Vibrations. Englewood Cliffs, NJ: Prentice-Hall, Inc., 1981.

[18] B. Hok and K. Gustafsson, "Vibration Analysis of Micromechanical Elements," Sensors and Actuators, Vol. 8, pp. 235-243, 1985.

Reoxidized Nitrided Oxides as Gate Dielectrics for High Temperature Integrated Sensor MOS Devices

by:
Wei-Tsun Shiau and Fred L. Terry, Jr.
Solid State Electronics Laboratory, Department of Electrical Engineering and Computer Science, University of Michigan,
Ann Arbor, MI 48109-2122

Abstract

It is well known that bias-temperature stressing of MOS devices produces increased interface state densities and insulator fixed charges, thus limiting the high temperature applications of these devices. Nitrided oxides have previously been reported to offer increased resistance to interface state generation and insulator charge buildup in ionizing radiation, but are known to suffer from problems which include a low field bias temperature instability. We will report that reoxidized nitrided oxides can offer increased resistance to both bias-temperature stress-induced interface state generation and insulator charge buildup compared with the original oxides.

I. Introduction

Insulated gate field effect transistors, particularly when used in CMOS circuits, are promising candidates for high temperature applications such as automotive and aircraft engine sensors and controls, oil well logging instrumentation, and nuclear power plant instrumentation. However, it is well known that extended operation of MOS devices under even low gate field conditions at elevated temperatures (>100°C) leads to generation of interface states and insulator trapped charges [1,2] which adversely effect the operation of the transistors and eventually lead to circuit failures. Furthermore, it is also well known that negative gate biases lead to more rapid positive insulator charge buildup and interface state generation in oxides.

Nitrided oxides (thermally grown SiO_2 films which are annealed in NH_3) have previously been reported to offer increased resistance to interface state generation and insulator charge buildup in ionizing radiation environments [3]. They have also been shown to offer resistance to interface state generation in high electric field stress. However, nitrided oxides are also known to suffer from significant electron trapping in the insulator [4], and from a low-field bias-temperature instability [5] which would seem to make them poor candidates as high temperature gate dielectrics. Reoxidation of the nitrided oxide films has previously been shown to improve the electron trapping problem in nitrided oxides without reducing the resistance to high field generation of interface states [6]; therefore, we have made an initial investigation of reoxidized nitrided oxides as high temperature gate insulators.

We will show that reoxidized nitrided oxides can offer both increased resistance to generation of interface states and insulator charge buildup due to bias-temperature stress for gate fields from 1-4 MV/cm and temperatures from 100-300°C. We have also found preliminary indications that nitrided oxided may offer increased resistance to accelerated destructive breakdown at high temperatures.

II. Experimental Methods

The fabrication of the MOS capacitors used in this study is described below. Phosphorous-doped (~$1X10^{15}$ cm^{-3}), (100) orientation Si wafers were heavily backside doped with phosphorous to insure good ohmic contacts, cleaned using the RCA-type cleaning solutions, and oxidized at 1000°C in dry O_2 to a thickness of 365Å.

All oxidations were followed by a 1 hour N_2 anneal at 1000°C. Some samples were then nitrided at 1000°C for 1 hour in NH_3 at 1 atmosphere and were then annealed at 1000°C in N_2. Some of the nitrided oxides were reoxidized in dry O_2 at 1000°C for times of either 1/2, 1, 2, or 4 hours. For these conditions, the oxidation resistance of the nitrided oxide is lost after approximately 5 hours of reoxidation. The wafers were then metallized with pure Al using a planar magnetron sputtering system and patterned to form MOS capacitors. A low temperature oxide layer was then deposited, followed by a second Al deposition. The second layer of Al was then patterned to form guard rings around the capacitors, and contacts to the capacitors were opened through the deposited oxide. The backsides of the wafers were stripped of residual films, metallized with Al, and the wafers were sintered at 455°C for 20 minutes in forming gas to complete fabrication.

The devices were characterized using standard high frequency and quasistatic capacitance voltage measurements. Interface state densities were computed using the Berglund quasistatic technique. Stress-induced insulator charge buildup was characterized using the shifts in the midgap voltages extracted from the measured HFCV data, using the assumption that the total charge in interface states will be minimized when the Fermi level is at midgap. Devices were subjected to constant-voltage bias-temperature stress using a wafer prober with a hot chuck. Stress voltages were scaled to achieve approximate insulator electric fields from 1 to 4 MV/cm.

III. Results and Discussion

The results of negative gate bias stress results for midgap interface state densities and midgap voltage shifts are summarized in figures 1-6. Following a negative gate bias stress, the interface state distribution for the oxide shows a weak peak in the lower half of the bandgap but a generally U-shaped distribution. The nitrided oxide and reoxidized nitrided oxides D_{it} distributions are also U-shaped with no observable peaks. Since there is no strong structure in the shape of the D_{it} distributions, we have plotted only the midgap values.

Several trends are clear from this data. First, as has been observed by many other researchers, the oxide suffers from significant buildup of interface states and positive insulator charge as the stress temperature, electric field, or time is increased. Second, the nitrided oxide, as we might have expected from prior work, shows significant suppression of bias-temperature induced interface states, but suffers from significant positive charge buildup in the insulator. This positive charge increase is presumably related to the bias-temperature instability previously observed by others [5]. The most striking result that emerges from these results is the suppression of both interface state generation and insulator charge buildup in the reoxidized nitrided oxide films. For clarity we have shown only data from the 1/2 hour and 4 hour reoxidation conditions, but the data from the intermediate reoxidation conditions lie in between those of the two extreme conditions.

Figure 2 shows slightly higher values for the midgap interface state density for some of the reoxidized nitrided oxide conditions vs the oxide. Our data shows minor lateral nonuniformity problems after stress which may account for this effect. Nevertheless, it is clear that there is a substantial difference in the interface state densities between oxide and the reoxidized nitrided oxides for the more severe stress temperatures.

Our results from positive gate bias-temperature stress experiments are less extensive due to destructive breakdown problems but generally show the same trends. These tests did confirm, however, that the rates of positive charge buildup and interface state generation were lower under positive bias than negative for all three types of films, and that the basic trends were the same under positive bias. Qualitatively, the nitrided oxide and reoxidized nitrided oxides seem to be more resistant to early destructive failure than the oxide. This result is consistent with the observations of improvements in breakdown voltage distributions for thin oxides following nitridation. Further work will be required to confirm if our qualitative impressions are correct.

The processing time and temperature conditions which we have used in this work are clearly not desirable for VLSI MOSFET processes. They do, however, demonstrate substantial promise for development of a high temperature gate insulator process. We are currently investigating less severe time-temperature combinations for the nitridation/reoxidation processing.

Acknowledgments

We would like to thank the Digital Integrated Circuits Group of MIT Lincoln Laboratory for providing the samples used in this work. We would also like to thank Greg Dunn for useful discussions. This work was supported by grants from the Ford Motor Company Scientific Research Laboratories and the Ford Fund.

References

1. B.E. Deal, M. Sklar, A.S. Grove, and E.H. Snow, *J.Electrochem.Soc.*,**114**,p.266, 1967.
2. G. Haller, M. Knoll, D. Braunig, F. Wulf, and W.R. Fahrner, *J. Appl. Phys.*, **56**, p 1844, 1984.
3. F. L. Terry, Jr., R. J. Aucoin, M. L. Naiman, and S. D. Senturia, *IEEE Electon Dev. Lett.*, **4**, p. 191, 1983.
4. S.T. Chang, N.M. Johnson, and S.A. Lyon, *Appl. Phys. Lett.*, **44**, p. 316, 1984.
5. C.T. Chang, F.C. Tseng, C.Y. Chang, and M.K. Lee, *J. Electrochem. Soc.*, **131**, p. 875, 1984.
6. S.K. Lai, J Lee, and V.K. Dham, *IEEE IEDM Tech. Dig., p. 190, 1983.*

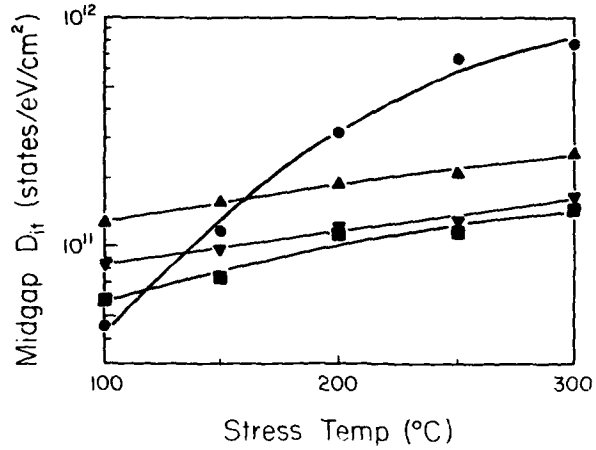

Figure 1. Midgap interface state densities vs stress temperature for a -4 MV/cm, 15 minute stress for (●) oxide, (▲) nitrided oxide, (▼) 1/2 hour reoxidation, and (■) 4 hour reoxidation.

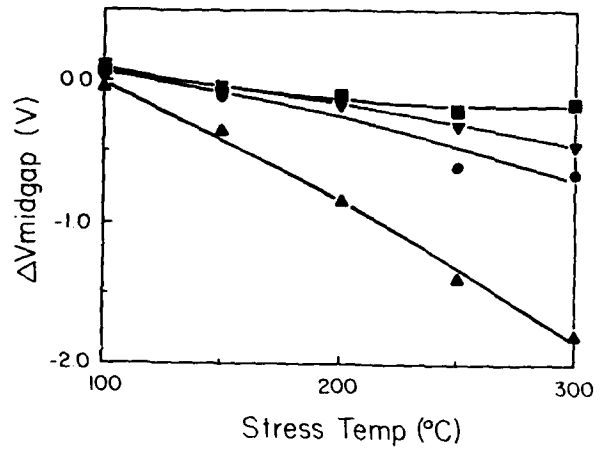

Figure 2. Midgap voltage change vs stress temperature for a -4 MV/cm, 15 minute stress for (●) oxide, (▲) nitrided oxide, (▼) 1/2 hour reoxidation, and (■) 4 hour reoxidation.

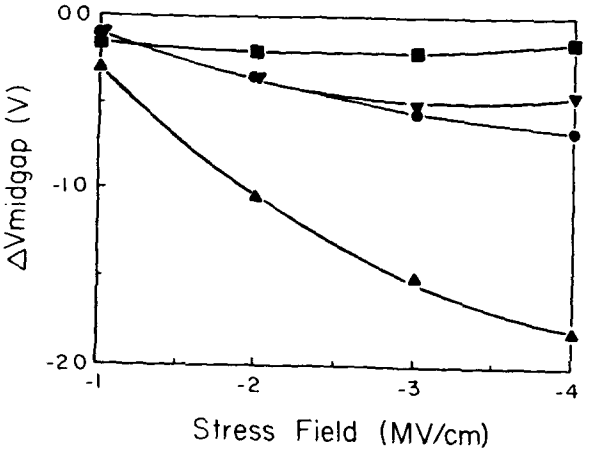

Figure 3. Midgap interface state densities vs stress field for a 300°C, 15 minute stress for (●) oxide, (▲) nitrided oxide, (▼) 1/2 hour reoxidation, and (■) 4 hour reoxidation.

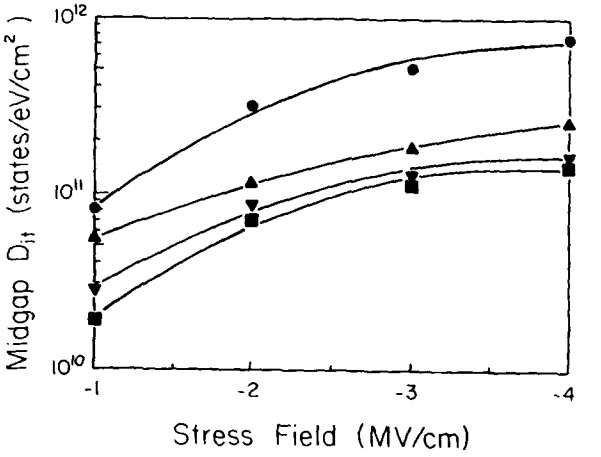

Figure 4. Midgap voltage change vs stress field for a 300°C, 15 minute stress for (●) oxide, (▲) nitrided oxide, (▼) 1/2 hour reoxidation, and (■) 4 hour reoxidation.

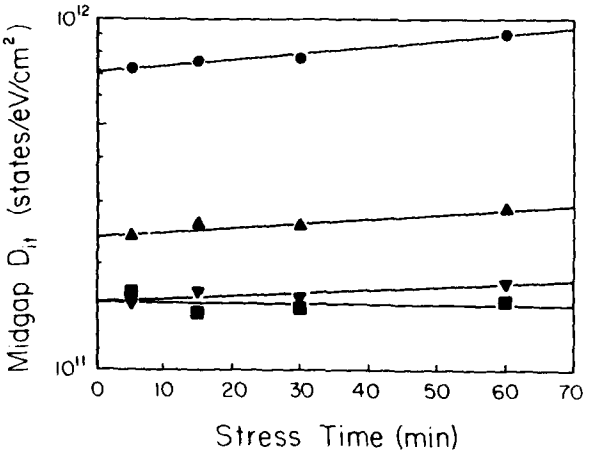

Figure 5. Midgap interface state densities vs stress time for a 300°C, -4 MV/cm stress for (●) oxide, (▲) nitrided oxide, (▼) 1/2 hour reoxidation, and (■) 4 hour reoxidation.

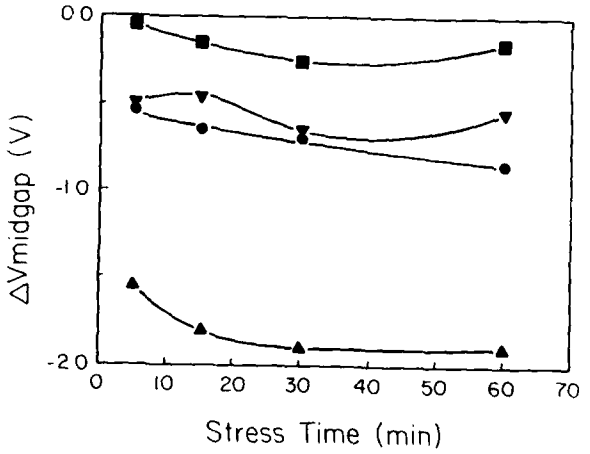

Figure 6. Midgap voltage change vs stress field for a 300°C, -4 MV/cm stress for (●) oxide, (▲) nitrided oxide, (▼) 1/2 hour reoxidation, and (■) 4 hour reoxidation.

MESA STRUCTURE FORMATION USING POTASSIUM HYDROXIDE AND ETHYLENE DIAMINE BASED ETCHANTS

Shih-Chia Chang and David B. Hicks
Electrical and Electronics Engineering Department
General Motors Research Laboratories
Warren, Michigan 48090-9055

Abstract

A comparative study was done between ethylene diamine-pyrocatechol (EDP) and potassium hydroxide (KOH) etching systems for micromachining mesas in (100)-oriented silicon wafers. A "street" corner compensation scheme was used to fabricate a perfect mesa, using KOH as the etchant. This perfect mesa structure is attributed to the relative etch rates of KOH for the three major crystal planes which are, in decreasing order, $R_{110} > R_{100} > R_{111}$. The etch rate ratios of R_{110} / R_{100} estimated from this experiment are $2^{-1/2}$ and $\geq 2^{1/2}$ for EDP and KOH, respectively.

Introduction

Recently, Buser, et al., disclosed a new masking technique which is capable of producing "perfect" mesa structures in (100)-orientated silicon [1]. In their experiment, properly scaled compensation streets, oriented along the <100> directions, were attached to the four corners of the square which defines the top surface of the mesa. The four sides of the square were aligned with respect to the <110> directions. The etchant used was 41w/o KOH in water. They attributed the unique etching characteristics of KOH to the equal etch rate of the equivalent <100> directions.

In our experiment, a comparative study was done between EDP and KOH etching systems for micromachining mesa structures in (100)-oriented silicon. Distinct differences in etching characteristics were observed between the two systems and, based upon these results, we conclude that the model presented by Buser, et al., is inaccurate.

In this paper, a plausible model is presented which explains the diverse etching characteristics of EDP and KOH.

Experiment

For this experiment, (100)-oriented wafers were prepared by growing thermal silicon dioxide (SiO_2), patterning the oxide using the mask layout shown in Fig. 1, and finally, etching the mesa structures in the orientation-dependent etchant. The 120 μm-wide compensation streets were defined photolithographically and were aligned with respect to the <100> directions. The etchants used were an ethylene diamine-pyrocatechol (EDP) commercial etchant and a 41 w/o potassium hydroxide (KOH) solution. Both etchants were placed in water-cooled reflux systems so as to minimize changes in concentration due to water loss. The solution temperatures were kept at 105°C and 82°C for EDP and KOH, respectively.

Results and Discussion

Figures 2a and 2b are SEM photographs of the partially etched mesa structures in EDP and in KOH, respectively. In both cases, the masking oxide layer has been removed. The most striking difference between the two etched features is in their cross sections: The street etched in EDP is triangular -- or trapezoidal if the etch time is shorter -- whereas the KOH sample is rectangular. The reason for the different etch features is illustrated in Figures 2c (for EDP) and 2d (for KOH) and is explained as follows.

The relative etch rates in EDP for the major crystal planes are, in descending order, $R_{100} > R_{110} > R_{111}$, while for KOH they are $R_{110} > R_{100} > R_{111}$ [2,3]. In the EDP etch case, the (110) plane is developed due to the fact that $R_{100} = R_{001}$ [i.e., the horizontal (100) etch rate is equal to the vertical (001) etch rate] and $R_{100} > R_{110}$. When the two {110} planes meet, convex corners are formed. Because of the gradual exposure and etching - from top to bottom - of the mesa corners, a perfect mesa can not be generated as shown in Fig. 3a. For KOH, the (110) plane cannot be preserved due to the fact that the etch rate in the <110> direction is greater than the etch rate in both the <100> and <001> directions. Furthermore, the perfect rectangular cross section of the etched feature implies that the etch rate of KOH in the <110> direction should be greater than or equal to $2^{1/2}$ times the etch rate in the <100> direction, i.e., $R_{110} \geq 2^{1/2} R_{100}$. This is consistent with the result of $R_{110} = 2 R_{100}$ reported by Kendall [2]. The rectangularly-shaped compensation streets are etched simultaneously at the top and bottom, which preserve the mesa characteristic and allows for the formation of a perfect mesa, as shown in Fig. 3b.

Conclusion

Perfect mesa structures can be fabricated in (100) silicon by using the street corner compensation scheme proposed by Buser, et al, with KOH as the etchant. This is attributed to the fact that the etch rate of KOH in the <110> direction is at least $2^{1/2}$ times faster than in the <100> direction and that the etch rate in the <111> direction is, in turn much slower than both of these.

In the case of EDP, perfect mesas are not obtainable using the street corner compensation mask because of the etch rate in the <100> and <110> directions bearing the relationship $R_{100} = 2^{1/2} R_{110}$ as verified by our experimental results.

References

1. R. Buser, B. Stauffer and N. F. de Rooij, "Realization of a Mesa Array in (001) Oriented Silicon Wafers for Tactile Sensing Applications," The Electrochemical Society, Fall Meeting, San Diego, CA, Oct. 1986 Extended Abstract, 86, 879 (1986).

2. K. E. Bean, "Anisotropic Etching of Silicon," IEEE Trans. Electron Devices, ED-25, 1185(1978).

3. J. B. Price, "Anisotropic Etching of Silicon with KOH-H_2O-Isopropyl Alcohol," ECS Semiconductor Silicon, p.339(1973).

TH0215-4/88/0000-0102

4. D. L. Kendall and G. R. de Guel, "Orientations of the Third Kind: The Coming of Age of (110) Silicon," Micromachining Micropackaging of Transducers. Ed. C. D. Fung, P. W. Cheung, W. H. Ko and D. G. Fleming, p. 107 (1985).

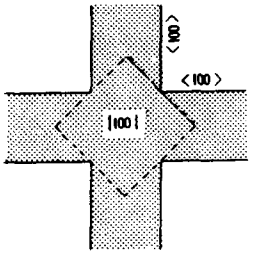

Fig. 1 Mask layout. The compensation streets are aligned in the <100> directions. The width of the street is 120 μm.

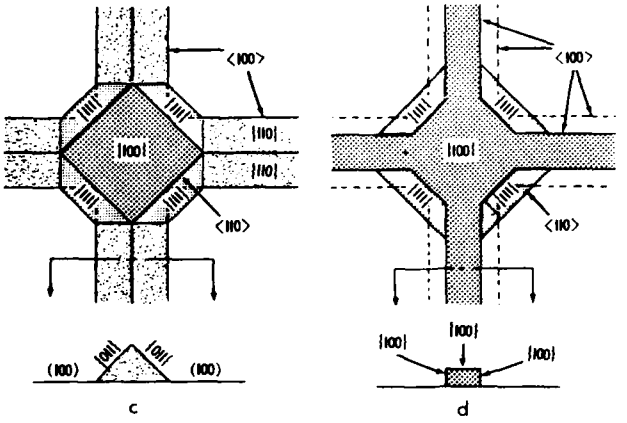

Fig. 2 (a) An SEM photograph of a silicon feature etched in EDP for 45 minutes. Note the triangular cross section of the street; (b) The same feature etched in KOH for 30 minutes. Note the rectangular cross section of the street; (c) and (d) are illustrations of the different etching characteristics between EDP and KOH respectively.

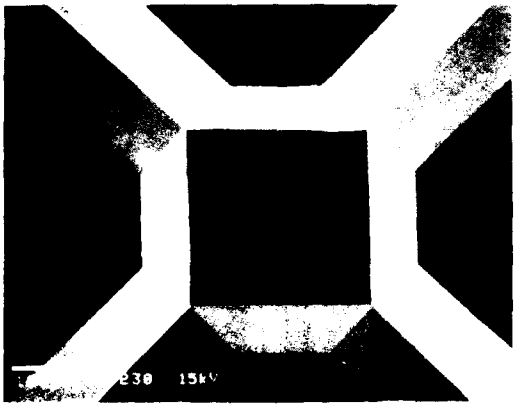

a

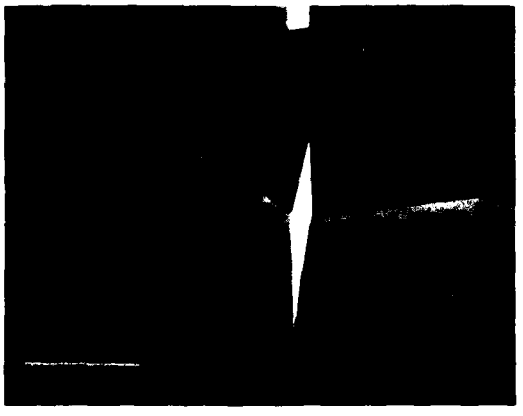

b

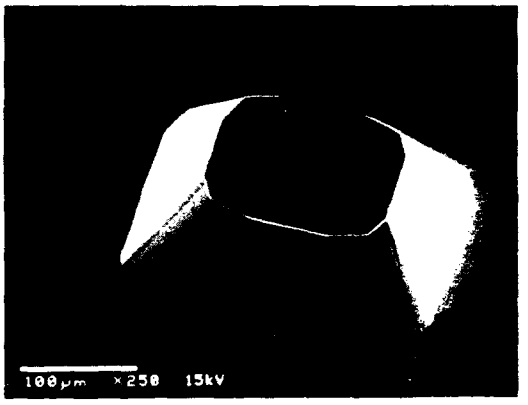

a

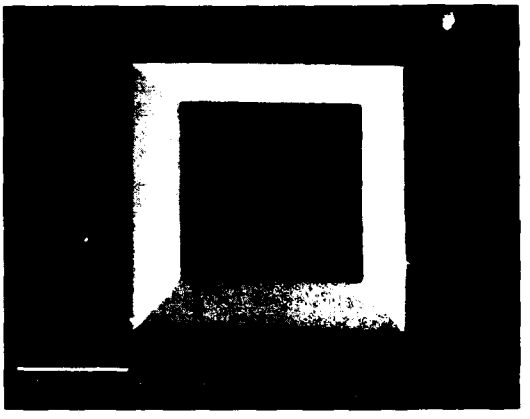

b

Fig. 3 SEM photographs of silicon mesa structures generated by (a) EDP and (b) KOH.

NOISE CORRELATIONS IN MAGNETIC FIELD SENSITIVE TRANSISTORS

Henry P. Baltes, Arokia Nathan*, and Davide R. Briglio
Department of Electrical Engineering, The University of Alberta
Edmonton, Alberta, Canada T6G 2G7
*LSI Logic Corp., MS J-201, 3115 Alfred Street, S. Clara 95054

Abstract

Measurement results of low frequency ($1/f$) noise in dual- collector magnetotransistors are presented and compared with corresponding data of dual-drain MAGFET's. Evaluation of the cross spectral density as well as the correlation coefficient shows a strong positive correlation of the noise voltages of the two collectors. A corresponding evaluation from the drain noise voltage spectra of the MAGFET counterpart is in striking contrast, exhibiting a strong negative correlation.

INTRODUCTION

The noise intrinsic to magnetic field sensitive transistors is a fundamental physical effect (indeterministic in nature) that ultimately limits the field resolution, B_{min}. In particular, at low frequency operation, the $1/f$ noise can impose major restrictions on the application range of such devices. It is unlike extrinsic noise (such as device offset) which can be minimised by careful selection of design, fabrication, and operating conditions.

In this paper, we present measurements of noise voltage power spectral density (PSD) on various dual collector magnetotransistors (MT's) fabricated in CMOS and bipolar technologies which are sensitive to magnetic fields parallel to the chip surface. The PSD of the differential signal is at least 100 times smaller than the single ended counterpart. The correlation coefficient is approximately unity and seems to be independent of the fabrication process. In dual-drain MAGFET's, the noise voltage PSD is about 4 times as large as that of the single ended output. A strong negative correlation in drain noise voltages is observed.

DEVICE DESCRIPTION

The cross sections of the CMOS and bipolar MT's used are shown in Figs. 1 and 2 respectively. Details of device fabrication are given in [1]. The bipolar MT has a pair of 8 μm × 8 μm Hall probes, symmetrically placed between the emitter and base contacts, which were utilised for previous device analysis [2]. We assume that the effect of these probes (which were left unactivated in the course of our noise measurements), on the collector noise voltage PSD's is negligible. The MT's of the two technologies (Figs. 1 and 2) differ in magnetic characteristics (such as output sensitivity to B), but the zero magnetic field electrical characteristics are almost identical. The MAGFET (Fig. 3) is fabricated using 5 μm standard CMOS technology and is sensitive to magnetic fields perpendicular to the chip surface (see [3]). Measurements for $|B| \leq 0.5$ T performed for the devices discussed, indicate that the noise is not explicitly a function of magnetic field [1]. We define the sensitivity of the device to the magnetic field as $S = \Delta I(B) / [(I_1 + I_2)B]$ where $\Delta I(B) = (I_1 - I_2)$, denotes the collector current imbalance in the case of the MT's and drain current imbalance for the case of the MAGFET's and $(I_1 + I_2)$ denotes the respective collector and drain currents.

RESULTS AND DISCUSSION

In Figs. 4 and 5, we illustrate measurements of noise spectra of the single-ended and differential collector noise voltages for MT's fabricated in both CMOS (Fig. 4) and bipolar (Fig. 5) technologies. The individual collectors of the respective MT's have identical spectra, $S_{11}(\omega) = S_{22}(\omega)$ and they all follow an approximate $1/f$ spectrum. From inspection of Figs. 4 and 5, we learn that for frequencies, 1 Hz $\leq f \leq$ 100 kHz, and for both fabrication technologies, the differential PSD is much smaller than the single ended PSD, viz., $S_D(\omega) \leq 10^{-4} S_{11}(\omega)$. Based on the formulations shown in [1], we calculate $\rho = Re[S_{12}(\omega)]/S_{11}(\omega) \approx 1.00$ which indicates a strong positive correlation between the collector noise voltages. Similarly, on assumption that the noise voltage follows a Gaussian probability distribution, we find from oscilloscope measurements (see [4]) that the mean square differential noise voltage is an order of magnitude smaller than the single ended counterpart, $\langle v^2_{nd} \rangle \leq 0.1 \langle v^2_{n1} \rangle$. The correlation coefficient $\gamma = 1 - (\langle v^2_{nd} \rangle / 2 \langle v^2_{n1} \rangle)$, which is obtained by virtue of the exhibited property $\langle v^2_{n1} \rangle = \langle v^2_{n2} \rangle$, turns out to be $0.95 \leq \gamma \leq 1.00$.

These results are in striking contrast to the case of the dual-drain MAGFET, where the differential spectral densities are *larger* than the single ended ones [$S_D(\omega) \sim 4S_{11}(\omega)$] and a *negative* correlation of $\rho \approx -0.9$ is found [3].

Based on the measured results of noise voltage PSD's shown, we evaluated the signal-to-noise ratio (SNR) for the CMOS MT for both differential and single ended measurement modes for the same operating conditions as in Fig. 4. At 1 kHz, the rms differential collector noise voltage is approximately 10 nV/√Hz, yielding a SNR of 4×10^9 √Hz/T, consequently $B_{min} \approx 25$ nT for $\Delta f = 1$ Hz. In the case of the single ended collector, the SNR is four orders of magnitude lower than the differential operation, and $B_{min} \approx 14$ μT for $\Delta f = 1$ Hz. A performance comparison of the CMOS MT and the MAGFET is shown in Table 1. The MT operated in differential mode is far superior to the MAGFET in terms of resolution requirements.

An intuitive interpretation of the observed phenomena maybe as follows. In the case of the bipolar MT, the device

TH0215-4/88/0000-0104

noise current is governed by events localised at the emitter base junction vicinity. This manifests itself as fluctuations in the emitter injected current, equally felt by both collectors. For the MAGFET, fluctuations in the drain current are due to noise sources distributed throughout the conducting channel, while effects of the noise mechanisms at the source are minimal. The carriers at the vicinity of the channel pinch-off undergo the partition effect, i.e. they land on one drain or the other. Consequently the fluctuation at one drain is complemented by a fluctuation in the opposite sense at the other drain.

REFERENCES

[1] A. Nathan, H. P. Baltes, D. R. Briglio, and M. Doan, "Noise correlation in dual-collector magnetotransistors," *IEEE Trans. Electron Devices*, submitted.

[2] A. Nathan, K. Maenaka, W. Allegretto, H. P. Baltes, and T. Nakamura, "The Hall effect in magnetotransistors," *IEEE Trans. Electron Devices*, submitted.

[3] D. R. Briglio, *Characterisation of CMOS Magnetic Field Sensors*, M.Sc. Thesis, University of Alberta, Edmonton, Canada, 1984.

[4] Y. Netzer, "The design of low-noise amplifiers," *Proc. IEEE*, vol. 69, No. 6, pp. 728-741, 1981.

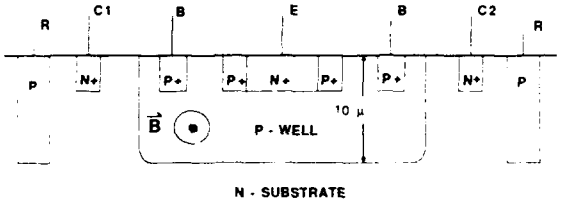

Fig. 1. Dual-collector CMOS MT.

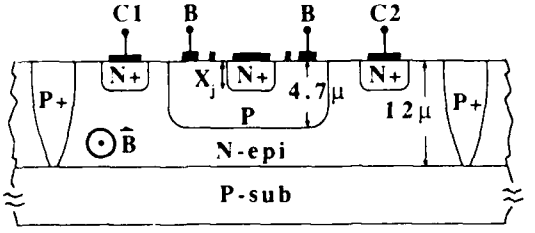

Fig. 2. Dual-collector bipolar MT.

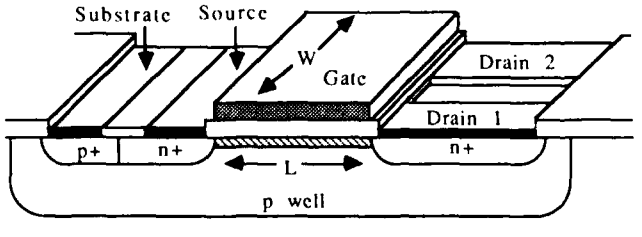

Fig. 3. 3-d view of MAGFET. $W = L = 100$ μm, and drain separation = 20 μm.

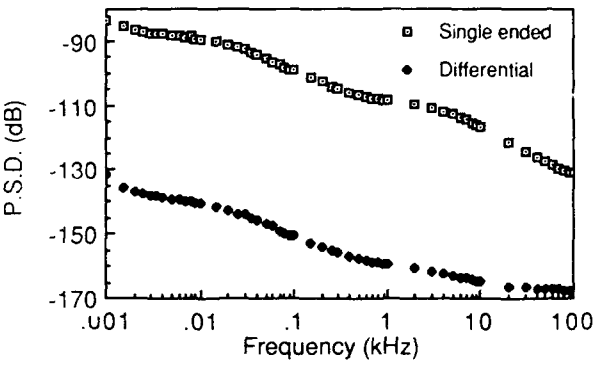

Fig. 4. Differential and single-ended collector noise voltage PSD's for CMOS MT, $I_B = 20$ μA, $I_{C1} = I_{C2} = 975$ μA, $V_{CE} = 4$V, with load resistor, $R_L = 3.3$ kΩ.

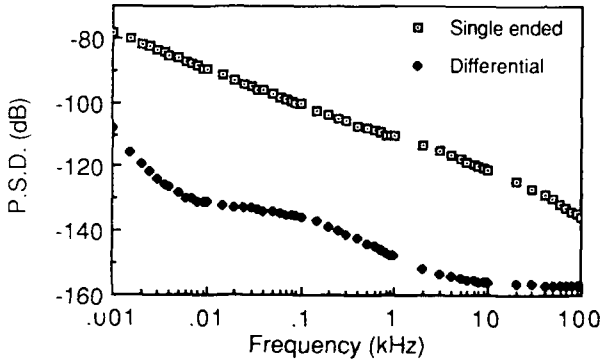

Fig. 5. As in Fig. 4, but for bipolar MT. $I_{C1} = I_{C2} = 760$ μA, $V_{CE} = 7.7$ V, and $R_L = 6.75$ kΩ.

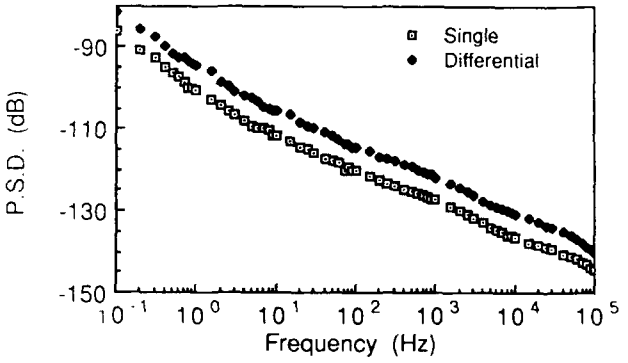

Fig. 6. Differential and single-ended drain noise voltage PSD's for MAGFET. $V_{DS} = 8.5$ V, $V_{GS} = 6.3$ V, $V_{SB} = 0$V, $V_{DD} = 12.7$ V, $R_L = 33.2$kΩ.

	MT	MAGFET
Sensitivity $\Delta I/I.B$	0.06	0.05
Differential resolution B_{min}(nT) f = 1 kHz, Δf = 1 Hz	25	2400
Differential/ Single PSD ratio	0.01	4
Correlation of noise	+99%	-90%

Table I. Comparison of CMOS MT (Fig. 1) with MAGFET (Fig. 3).

BIPOLAR INTEGRATED PRESSURE TRANSDUCER

Ronald E. Brown and Dennis M. Koglin

Delco Electronics Corporation
Kokomo, Indiana 46904

An all-silicon, bipolar, two-chip integrated pressure transducer has been developed. This device uses a piezoresistive pressure cell and a single-signal conditioning integrated circuit. No external compensation components are required for this circuit board mount device.

This device uses a unique temperature compensation circuit differing in basic concept from that used in previous attempts at developing such a device. No special TC resistors are required. The pressure sensing cell has digital adjustment capabilities for zeroing the cell output.

The cell signal is amplified and temperature compensated on a second integrated circuit containing gain, offset, and other digital trims. The parameters which are trimmed are a result of mathematically modeling the pressure cell output over pressure and temperature.

The mathematical representation identified parameters in the empirical model which would require compensation and on which chip this compensation was best accomplished. Laboratory measurements over temperature and pressure have been taken on the pressure cell and conditioning integrated circuit as separate components as well as on the two-chip system. Both cases verify the model of this device. The two-chip pressure sensor tests consisted of operation over the 5 kPa to 120 kPa pressure range and -40°C to +125°C temperature range.

The initial parts are intended for one atmosphere absolute pressure application. Initial parts will be allowed to have a room temperature error of no more than ±2 kPa over the central operating pressure range. The initial temperature multiplier will be 1, between 0°C and +85°C. Operation over the 5 kPa to 120 kPa pressure range and -40°C to +125°C temperature range is the design goal. Work continues on the device to allow tightening the error bands.

This device will be available for the 1990 model year in production quantities for circuit board applications.

Gen II Pressure Transducer
2-Chip Block Diagram

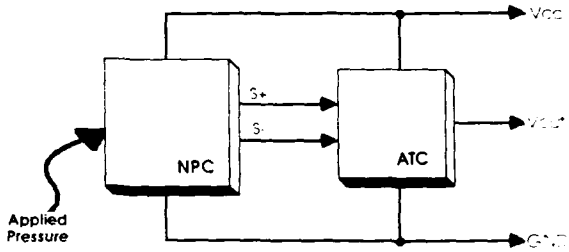

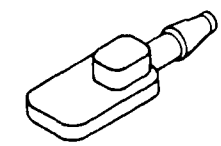

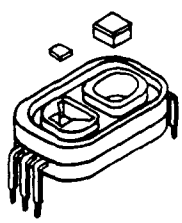

TH0215-4/88/0000-0106

A Broad Range Absolute Pressure Microsensor

S. D. James, R. G. Johnson, R. E. Higashi
Honeywell Sensors and Signal Processing Laboratory
10701 Lyndale Avenue South, Bloomington, MN 55420

Abstract - A microminiature absolute pressure sensor for gaseous media based on thermal effects and with feature size of 10um wide and 90um long has been fabricated in silicon using anisotropic etching techniques. Operation was demonstrated using dry air over a pressure range of .015 to 150psia. The power function output curve represents the change in power required to keep the thermally isolated microstructure at constant temperature. The device is most useful for applications demanding low cost but not requiring high precision.

Introduction

A pressure sensor is a device which has an output which is a function of applied pressure. Traditional pressure sensors use one of four basic technologies[1] which are:

- elastic-member
- gravitational
- electrical (thermal)
- strain gage

The diaphragm pressure sensor is probably the most commonly used sensor type when the application requires an electrical signal with moderate precision, low cost and sensitivity at high pressure. These sensors use integrated resistors, capacitance, or reflected light as a measure of diaphragm deflection as a function of pressure. However, they have inherent limits of overpressure and dynamic range. A common low pressure vacuum sensor is the Pirani gauge. It operates by measuring the power required to keep a wire at constant temperature. However, its range is limited to the high vacuum range of 3 torr (0.06psia) or less. Some thermal conductivity gauges which monitor the pressure dependent convection losses work up to about 14.7 psia.[2] The new microsensor device described here does not use this effect and is most similar to a pirani gauge but has a much larger dynamic range (0.015 to 150psia). It has no diaphragm so there is no inherent overpressure limit.

The microsensor designed and fabricated at the Honeywell Sensors and Signal Processing Laboratory consists of a narrow temperature sensitive resistor embedded in a silicon nitride microbridge film which is suspended over a narrow, anisotropically etched pit. The dimensions of the microbridge structure are typically 90um long, 6um wide and 0.75um thick. The gap between the edge of the microsensor and the substrate is typically 2um. For this gap size the Knudsen number is 1 (transition between the continuum and free molecular regime) at about 0.5psia. Figure 1 shows a SEM micrograph of a microbridge absolute pressure sensor.

This device uses a little-known effect of the dependence of thermal conductance on gas density within a sharply non-linear temperature profile. For linear thermal profiles and mean free paths short compared to the conduction space and structure geometry, the thermal conductance, k, is independent of gas density. However, as the dimension of the heated body is reduced, a highly non-linear temperature gradient forms and the thermal conduction is no longer constant for different gas densities. Output of the device then depends on density (which is directly related to pressure) and thermal conductivity of the media gas.

The device is fabricated on standard <100> silicon so that on-board electronics could be added. The device consists of an undercut silicon nitride bridge with an imbedded NiFe resistor. The cavity under the sensor is a v-groove approximately 25um deep with the characteristic side wall of the <1,1,1> planes. The undercutting thermally isolates the bridge from the substrate and allows thermal conduction only through the air and through the silicon nitride where the bridge is attached to the rest of the die. The energy balance is:

$$q_{gen} = q_{rad} + q_{cond} + q_{conv}$$

where
q_{gen} = heat added to the bridge
q_{rad} = heat loss by radiation
q_{cond} = " " by conduction
q_{conv} = " " by convection

Radiation is considered to be minimal due to the relatively cool temperatures, small area and low emissivity. Convection is reduced by not allowing airflow over the chip (a negligible amount of free convection may still occur). If q_{cond} is the major loss to the system then:

$$q_{gen} = q_{cond} = q_{br} + q_{top} + q_{bottom} + q_{edges}$$

where

q_{br} = losses at point of bridge attachment
q_{top} = losses from top surface
q_{bottom} = losses from bottom surface
q_{edges} = losses from the sharp edges

For comparison the heat conduction is considered simplistically as a function of area of the surface and the temperature gradient by the simple equation:

$$q = k * A_{surf} * dT/dx$$

where
k = thermal conductivity
A_{surf} = surface area of body
dT/dx = temperature gradient (constant for parallel plates)

Thermal conductivity of silicon nitride is about 80 times greater than air. However, the area of the silicon nitride at the bridge attachment point is 1/15th of the area of the bridge edges.

The area of the bottom and top of the bridge compared to the edge area is large (8 times). However, the small gap between the bridge edge and the substrate makes the temperature gradient there close to 25 times as large as the gradient at the bottom/top. Therefore, using this simplistic view it can be seen that of the heat loss from the bridge will occur mostly at the bridge edges. This is the conduction path which changes with gas density and is responsible for the signal beyond the "normal" pirani or thermocouple gauge range.

IH0215-4/88/0000-0107 © 1988 IEEE

The changes of power necessary to heat the thermally isolated microminiature sensor to a constant temperature is monitored. The circuit used to power the sensor consists of a Wheatstone bridge and an error integrator. The resistor embedded in the silicon nitride bridge has a finite temperature coefficient of resistance (0.003/degC). The microbridge structure requires very little power to heat (0.04mW/degC). The bridge is run about 50deg above chip temperature. The bridge voltage is raised until the wheatstone bridge is balanced. The bridge voltage is used as an indication of the power necessary to keep the microbridge structure at constant resistance (and therefore temperature). This power changes with pressure. Figure 2 shows the circuit used to thermostat the bridge. A similar circuit was used to thermostat the chip to hold the substrate temperature constant.

Results

The devices were fabricated using a simple four mask process. Since the sensors are small many can fit on a single 3 inch wafer (approx. 4800). Individual die were mounted in TO headers and placed in a pressure chamber and tested for pressure sensitivity. It was found that the pressure function was an s-shaped curve. The curve starts with a small slope which increases at first and then decreases. The inflection point at the low pressure is caused by conduction losses through the silicon nitride bridge to the substrate which becomes a major heat loss mechanism when the gas media is evacuated. The decrease in sensitivity at higher pressures is theorized to be caused by the mean free path becoming much shorter than the spacing which leaves only the signal due to the large and non-linear temperature profile very near the microsensor edge. The pressure at which the mean free path equals the bridge spacing of 2um is about 0.50psia. However the signal is still measurable up to at least 150psia. Figure 3 shows the response of a microbridge absolute pressure sensor at the high pressure range.

Conclusions

The microbridge absolute pressure sensor fabricated at Honeywell has many features:

- extremely small size (6X90um bridge)
- low power (2mW)
- large dynamic range (0.01 to 150psia)
- unlimited overpressure

It operates using thermal properties and has no moving (deflecting) parts. Unlike the pirani gauge, however, it has a large dynamic range (0.015 to 150psi). It measures pressures in gaseous media (unless it is coupled pneumatically to a liquid system). The sensor can be used for many applications, and can be easily incorporated into existing evacuated or pressurized circuit packages to monitor package integrity.

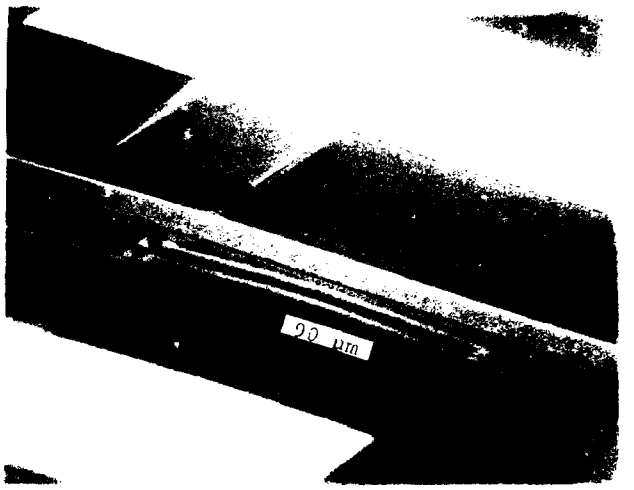

Figure 1- SEM of Honeywell Microbridge Absolute Pressure Sensor.

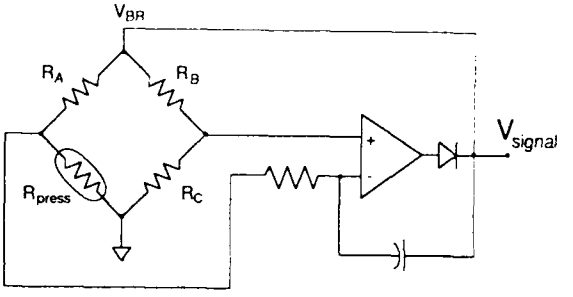

Figure 2- Circuit for Operating Honeywell Absolute Pressure Sensor.

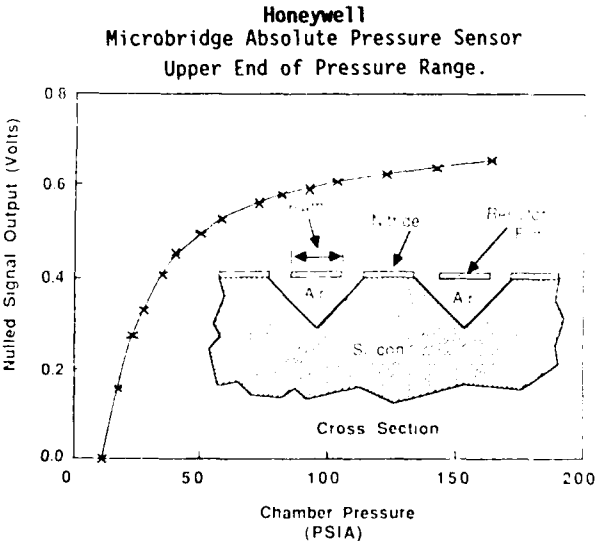

Figure 3- High Pressure Range Data and Cross Section for Pressure Sensor.

References

1 D. M. Considine and S. D. Ross editors, *Handbook of Applied Instrumentation,* McGraw-Hill, New York, 1964.

2 J. F. O'Hanlon, *A User's Guide to Vacuum Technology,* John Wiley & Sons, New York, 1980.

MECHANISMS OF ANODIC BONDING OF SILICON TO PYREX® GLASS

Kevin B. Albaugh
Paul E. Cade
IBM General Technology Division
Essex Junction, VT 05452

Don H. Rasmussen
Department of Chemical Engineering
Clarkson University
Potsdam, NY 13676

The mechanisms of formation of anodic bonds between glasses and metals are examined. Prior workers have suggested electrochemical, electrostatic, and thermal mechanisms for bond formation, but the dominant mechanism has not been clearly defined. The process is found to be an electrochemical analog to thermal glass-to-metal seals, where the metal surface is oxidized into the glass due to the development of large electric fields across the anodic depletion layer.

Introduction

Anodic bonding is commonly used for joining glass to silicon for micromechanical applications (1). The utility of anodic bonding arises from the low process temperature. Since the glass and silicon remain rigid during the process, it is possible to bond glass to a silicon surface preserving grooves in either the glass or silicon, which allows formation of devices such as pressure transducers. The physical processes occurring during bonding are of importance in determining the surface conditions required and the process conditions (temperature, voltage, and time) required to form a permanent, high quality bond. The current vs time transient at constant voltage contains a significant amount of information regarding the process mechanisms, which are predominantly electrochemical.

Experiment

Bonding was accomplished between discs of silicon (57mm diameter wafers) and Pyrex 7740 glass (50 mm diameter, 3.18 mm thick) in an apparatus previously described (2). The temperature range was 250° to 330°C, and the voltage ranged from 500 to 1000 V. The bonding was performed at constant applied voltage after the temperature had stabilized. Constant current could also be used, but was avoided since dielectric breakdown occurs at long times. The apparatus is shown in Fig. 1.

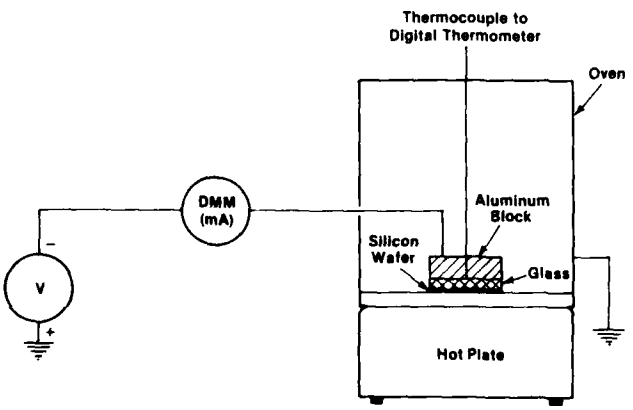

Figure 1. Apparatus

PYREX is a registered trademark of the Corning Glass Works, Inc.

Since no external pressure was applied, the bonding surfaces are joined by electrostatic attraction (3). In this case, bonding occurs by a two-step process: first, the contact area increases due to electrostatic attraction, and second, the permanent bonding forces develop. The extent of bonding is determined visually.

The primary measurements are the current vs time characteristic, the sample temperature measured at the center of the cathode, and the extent of bonding (area bonded/total area).

Current Characteristic

The variation of current with time gives a significant amount of information about the process. The current decays rapidly at the start of the cycle, due to the initial charging of the depletion layer. A model for the transient current response has been developed (4), which treats the depletion layer as a capacitor and the bulk glass as a series resistor. For the short-time regime, the leakage across the depletion layer is neglected. The model current characteristic is shown in Fig. 2, which approximates well the actual response shown in Fig. 3.

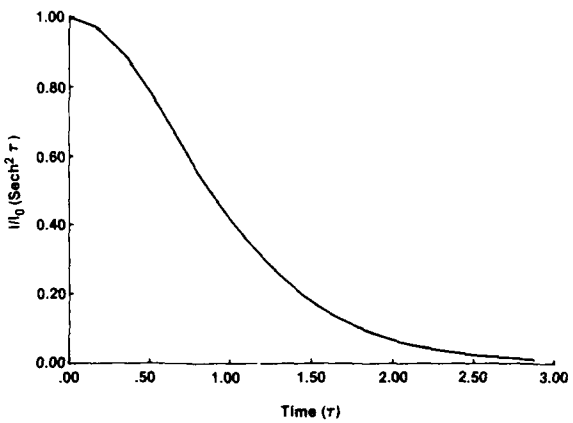

Figure 2. Current response—theoretical

The actual response has an exponential tail which is predicted by the long-time model of Carlson (5-8). This tail is due to leakage within the depletion layer.

The area under the initial charging peak gives the charge removed from the depletion layer. The curvature is determined by the series resistance and the charge concentration in the depletion layer. The charge concentration observed experimentally is very large, and indicates that most of the ionizable material in the depletion layer is removed. Since effectively no current is observed when the applied voltage is removed, the depletion layer is charge neutral, which indicates that any oxygen counterions present in the depletion layer are delivered to the anode.

TH0215-4/88/0000-0109

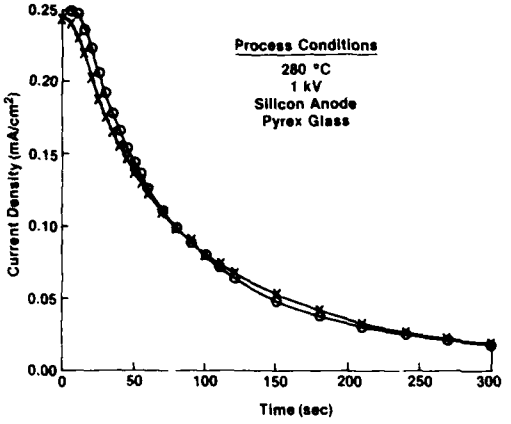

Figure 3. Current response—experimental

The experience with thermal sealing indicates that seals of glass to metal form when the metal surface is oxidized into the glass with proper control over the metal oxide to provide an adherent metal oxide scale. In the case of silicon to glass bonding, one merely needs to oxidize the silicon surface into the glass network, and one would not expect a large amount of oxygen to be delivered to the anode to do so. In the present experiments, bonding occurs after the delivery of 2 mC/cm2 to the anode, which suggests that <20 nm of oxide needs to be grown on the silicon to form a good bond to glass (as long as the surfaces are optically flat).

From the model for the current characteristic, the kinetic parameters for bonding are those that govern the rate of charge transfer: the voltage, temperature, and ion content of the glass. The process window is, as the delivery of oxygen to the anode will occur (albeit at widely varying rates) for a variety of temperatures and applied potentials. High temperature and high bias leads to rapid bonding.

Practical Implications

Surface preparation

The total amount of oxidation is very small for bonds to silicon. In some material systems, such as aluminum/glass or iron/glass, the metal ions are mobile and are transported into the glass, but for silicon/glass a mobile silicon ion does not exist. This means that surface preparation must be very good, since no oxidation of high spots into the glass can occur (9,10). The surfaces remain rigid during the bonding process and so little toleration of point asperities (particles) is possible as well.

A variety of surface cleans were evaluated during the study. Most cleans work quite well, such as acetone rinsing, sulfuric/nitric acid cleans, and chromic etch (11). Merely washing with sodium lauryl sulphate then rinsing is inadequate, since the soap leaves a residue which consumes oxygen at the anode, scavenging it prior to oxidation of silicon. The surface should be free of organic residues and as free of particulates as possible, but does not appear to be particularly sensitive to the presence of other residues (e.g., chromium ion).

Applied Pressure

The two conditions for bonding described above are that the surfaces to be bonded must be in intimate contact, and that after intimate contact sufficient oxidation occurs at the anode to provide permanent bridging bonds. If the surfaces are not in intimate contact at the start of the process, some of the charge transfer is "wasted": any anodic oxidation does not lead to bridging between the anode and the glass. Use of externally applied pressure avoids this difficulty, which is somewhat peculiar to the silicon anode since the total amount of charge transfer available is lower than for systems with mobile metal cations (e.g., aluminum). Even for aluminum, though, the process benefits from relatively large amounts of compression, as large as 70 MPa (12).

Conclusions

The formation of anodic bonds is satisfactorily explained by oxidation of the metal surface into the glass. Sufficient charge transfer occurs to allow the oxidation, and the observation of charge neutrality in the depletion layer indicates that oxygen ions are delivered to the anode in the case of silicon anodes. It is also possible in some cases that metal ions are delivered from the anode to the depletion layer, but this will result in formation of metal oxide as the metal ions combine with oxygen ions remaining in the depletion layer. Electrostatic attraction is important when the parts are not initially brought in intimate contact by an applied pressure. Joule heating of the depletion layer is not required for bonding to occur, and is inconsistent with minimal filling of surface topography on silicon anodes.

REFERENCES

1. Petersen, K. E., Proc. IEEE, V70(5) 1982 p420

2. Albaugh, K. B., Mat. Lett., 4 (11-12) 1986 p465

3. Wallis, G., J. Amer. Ceram. Soc., V53(10) 1970 p563

4. Albaugh, K. B., submitted to J. Electrochem. Soc.

5. Carlson, D. E., et. al, J. Amer. Ceram. Soc., V57(7) 1974 p291

6. Carlson, D. E., J. Amer. Ceram. Soc., V57(11) 1974 p461

7. Carlson, D. E., et. al, J. Amer. Ceram. Soc., V57(7) 1974 p295

8. Carlson, D. E., K. W. Hang and G. F. Stockdale, J. Amer. Ceram. Soc., V55(7 337

9. Borom, M. P., J. Amer. Ceram. Soc., V56(5) 1973 p254

10. Brownlow, J. M., IBM Technical Report RC 7101, May 3, 1978

11. Skoog, D. A., and D. G. West, Fundamentals of Analytical Chemistry, 2nd Ed., Holt, Rinehart, and Winston, NY 1969

12. Arata, Y., A. Ohmori, S. Sano, and I. Okamoto, Trans. JWRI, 13(1) 1984 p35

EDGE EROSION EFFECTS IN DOUBLE SIDED SILICON MICROMACHINING

M. Zanini, M. Mikkor, R. C. Elder, L. W. Cathey, J. L. Bomback, and B. E. Artz

Ford Motor Company
Research Staff
Box 2053, Dearborn, MI 48121

Abstract

Double sided anisotropic etching of silicon wafers produces internal edges when etched cavities from opposing sides meet to form openings through the thickness of the wafers. Rapid erosion of these new edges is observed if the etch is continued. The process is dominated by the appearance of fast etching crystallographic planes. The transformations occurring at such edges are shown and a method to predict shape modifications is described.

Introduction

Wet anisotropic etching is widely used to produce micromachined structures in silicon. Since precise dimensional control of microstructures is becoming more stringent, corner undercutting and edge erosion need to be minimized so as not to adversely affect the resulting shapes. Double sided etching is being used more frequently because of the increasing complexity of new silicon sensors. A double sided etch that is carried all the way through the thickness of the wafer leads to the formation of new internal edges defined by the intersection of two crystallographic planes intersecting at a convex angle. These convex edges are susceptible to further rapid attack as soon as they are formed similar to what is observed at the corners of mesa structures during anisotropic etching. However, while the latter case has been described in detail in the literature[1,2], little has been reported about the effects observed when a double sided etch is taken through the thickness of a wafer. This study describes the shape modifications observed on the edges of openings formed by a double sided etch when etched past the break-through point. A method for predicting the overetching effects of such shapes is described. We will also discuss the implications that our results have on dimensional control of beams and orifices utilized in some micromachined silicon devices.

Experimental

The etch studies were carried out in 30% KOH aqueous solution at 80°C. Four inch, p-type (5-50 ohm-cm), (100) silicon wafers, 625 μm thick, were used with 1000Å of thermal oxide plus 1000Å of LPCVD Si_3N_4 acting as the etch mask. Rectangular openings in the mask (4x7 mm in size, aligned along <110> directions) were formed on both sides of the wafers using a Suss double side aligner and plasma etching. The patterns on either side were displaced by 1 mm relative to each other along the longer edge of the opening, but were not displaced in the orthogonal direction. The wafers were etched in the KOH bath until rectangular holes appeared. Care was taken not to overetch the wafers during this first step. Each wafer was then put back in the etch for periods of time ranging from one to four hours. The wafers were then sawed across the windows with cuts perpendicular to the mask edges to reveal the cross section of each side of the opening. Other wafers were removed from the etch before break-through and a layer of PECVD Si_3N_4 was deposited on one side. The etch was then resumed and continued for a predetermined length of time after break-through. SEM characterization was carried out with a Cambridge 250 MK3 system calibrated with a magnification standard in order to obtain accurate etch rate data.

Results and Discussion

A schematic representation of the two different edge geometries that can be obtained when a double sided etch breaks through in the interior of a (100) wafer is shown in Fig. 1a and 1b. If the top and bottom masks are perfectly aligned, the edge which defines the resulting opening is given by the intersection of two {111} planes and the angle is equal to 109.4°. On the other hand, if the top and bottom masks windows are either staggered or of different size, the resulting opening is defined by edges formed by {100}/{111} planes intersecting at 54.7°. Fig. 2a-k show cross sectional views of the erosion effects observed after the etch-break through on both types of convex edges. The {111}/{111} edge (a) on further etching blunts and a rough {110} vertical surface appears (b). Erosion of the slanted sidewall cavities continues while the rough {110}-like surface moves inward until it reaches the edges of the top and bottom mask (c). Upon further etching, two new {111} planes form starting from the mask edge and tilting inward (d). Finally, a self stopping groove defined by {111}/{111} planes is formed (e).

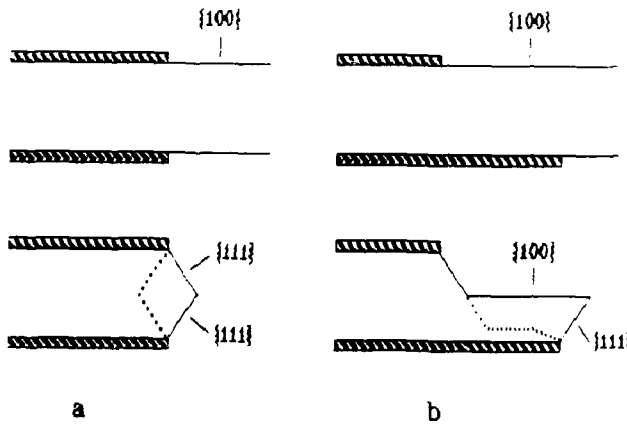

Figure 1. Mask arrangement to produce: (a) {111}/{111} and (b) {100}/{111} convex edges. The dotted lines show the ultimate shape of the edge.

The situation is slightly more complicated at the {111}/{100} edge (f). Blunting of the edge occurs with the appearance of the rough {110} surface as seen in the {111}/{111} case (g). In addition a smooth, well defined {311} plane also forms on the side of the shelf (g) which continues to be thinned (h). Eventually, the {311} plane reaches the mask edge (j) and undercutting occurs at the bottom mask (k) because the {311} is a fast etching plane. Thus, the edge erosion proceeds faster in this case than in the previous example and, more significantly, the etch is no longer limited by the bottom mask.

TH0215-4/88/0000-0111

The etch rates for the {100}, {311}, and {110} planes were derived by measuring the cross section changes as seen in the calibrated SEM micrographs and also independently using a depth gauge. Their values were found to be 1.2, 2.4, and 2.3 micron/min, respectively, in good agreement with other data in the literature[4].

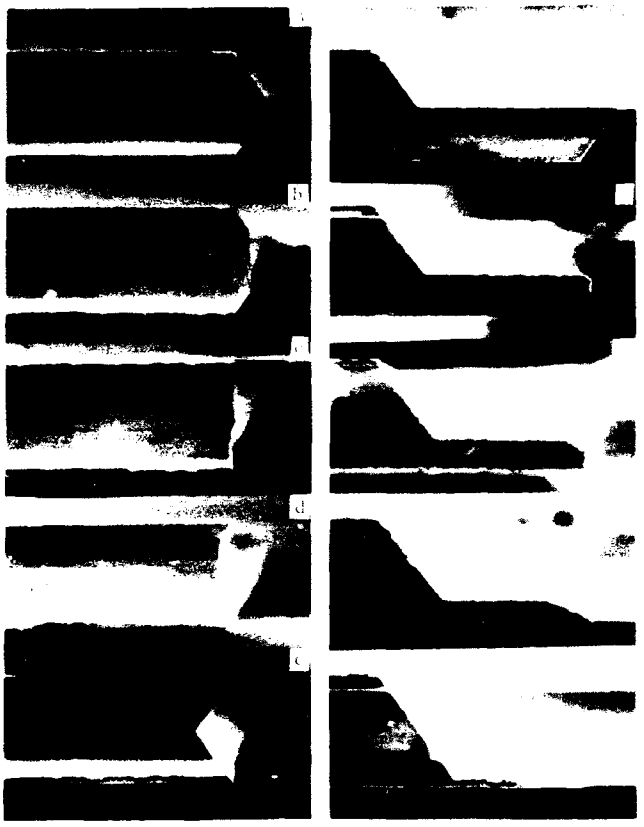

Figure 2. Cross sectional SEM views of the progress of anisotropic etching on the {111}/{111} and {100}/{111} convex corners. Figs. a-e and Figs. f-j, respectively.

The method to predict the intermediate shapes of convex edges during periods of rapid erosion is illustrated in Fig. 3a where the original cross section of a {111}/{111} type edge is shown as a dotted line. Also superimposed is a polar plot of the etch rates of planes in the (110) zone. The polar plot is based on our measured etch rates for the {100}, {110}, {111}, and {311} planes. The exact shape of the plot between these poles is schematic but is in general agreement with previously published results[3]. Normals to the etch rate vectors are constructed between the poles of the two {111} surfaces i.e., between P_1 and P_2. Planes lying between these poles are the only ones with "access" to the edge. The outer envelope of this construction (the solid line) defines the intermediate shape of the edge. In this case, only the {110} plane forms due to its high etch rate.

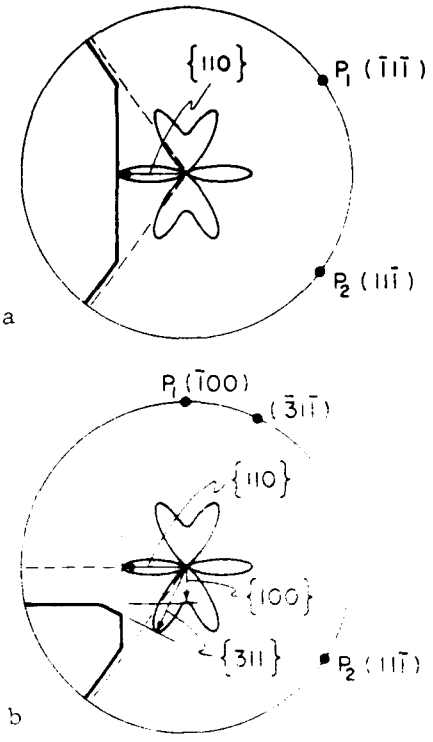

Figure 3. (001) stereographic projection showing the {111}/{111} and {100}/{111} edges. The dotted lines are the initial shapes and the solid lines are the etched shapes. Only planes in the (11) zone lying between poles P_1 and P_2 have access to the edge. A polar plot of the etch rates for these planes is shown schematically. Intermediate shapes are constructed by drawing perpendicular lines through the ends of the etch rate vectors. Only {111} and {110} type planes can participate in (a), while {100} and {311} types come into play in (b). Etching along the {111} is exaggerated.

The construction is shown again in Fig. 3b for a {111}/{100} edge. In this case, {100} and {311} etch planes can be formed producing a faceted edge. However, the number of facets eventually dominating the shape of the edge depends on the relative etch rate of the crystallographic planes involved. These rates vary for different etchants and etching conditions such as temperature and concentration. Fig. 4 shows the cross section of a silicon beam obtained with a double sided etch in EPW ("F" etch, no pyrazine, 111 °C). The larger base of the beam was initially defined by two {111}/{100} convex edges. Continuation of the etch past the break-through point produces {311} facets but no {110} ones because of the lower (110) etch rate in EPW. Faceting can also be avoided by adding a passivation layer on one side of the wafer before break-through occurs.

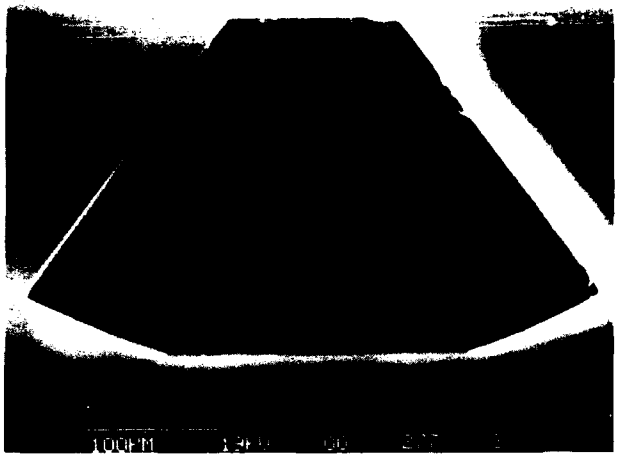

Figure 4. Cross section of a beam obtained with a double sided etch in EPW. No {110} planes are visible in this case because of their low etch rate compare to the {311} in this etchant.

The simple method described here can be contrasted with that of Jaccodine[5] for predicting the shapes of anisotropically etched cavities in partially masked surfaces. There the normals to the cusps (minimum etch rate planes) of the polar etch rate plot define the shapes of etched cavities.

Conclusions

We have shown that unpassivated convex corners produced in a double sided etch are subject to rapid erosion which modifies the shape of the edge. This effect may be either detrimental or advantageous to the precise dimensional control of a micromachined structure depending on its geometry. For example, Kurth reported[6] that using a double sided etch the dimensional variability of the mouth of orifices can be made independent of wafer thickness. We showed that prolonging the etch on such a configuration will remove the internal partial obstruction of the orifice due to the convex edge without affecting the outer dimensions of the orifice. Moreover, orifices with relatively straight walls can be etched through (100) silicon wafers by prolonging the etch to erode the internal edges. On the other hand, the cross sections of beams and cantilevers formed by double sided etching is rapidly changed by edge erosion and an additional passivation layer may be desirable for accurate dimensional control.

References

[1] M. Abu-Zeid, J. Electrochem. Soc. 131, 2138 (1984).

[2] X. Wu and W. H. Ko, Proceedings Transducers '87, Tokyo, 1987, page 126.

[3] D. F. Weirauch, J. Appl. Phys. 46, 1478 (1975).

[4] D. L. Kendall, Ann. Rev. Mater. Sci. 9, 373 (1979).

[5] R. J. Jaccodine, J. Appl. Phys. 33, 2643 (1962).

[6] R. H. Kurth, U. S. Patent 4,169,008

A MINIATURE SILICON ACCELEROMETER WITH BUILT-IN DAMPING

Stephen Terry
IC Sensors, 1701 McCarthy Blvd.
Milpitas, California 95035

Abstract

Silicon micromachining has been utilized to produce a novel, miniature accelerometer comprising a three-layer silicon structure. The center layer contains the accelerometer proof mass supported by a double cantilever suspension. The outside two silicon caps provide protection, mechanical stops for the proof mass, and air damping of its major resonant frequencies. Critical damping is typically provided. Piezo-resistors are used to sense the deflection of the silicon mass. By cross coupling the eight resistors in a Wheatstone bridge, substantial reduction in sensitivity to off-axis acceleration has been achieved. The integral packaging and air damping reduces production costs by simplifying the final assembly steps. This commercially available, low cost accelerometer is expected to find applications in automotive, industrial, and medical markets.

Introduction

The full force of silicon micromachining technology has recently been focused on accelerometers. New and exotic suspension structures, sensing mechanisms, and more sophisticated versions of conventional accelerometers are currently under development. The techniques of silicon micromachining are being applied for the purpose of both fabricating the microstructures and reducing the production costs through the use of wafer-level assembly of the devices. These new devices are aimed at a wide range of applications from inertial navigation to automotive crash sensing.

The silicon micromachined accelerometers with integral packaging began with Roylance[1] at Stanford University in 1975. That device was a single cantilever structure with a silicon mass and piezo-resistive sensing. It was enclosed in etched cavities in Pyrex glass wafers anodically bonded to both surfaces of the silicon wafer. Since then, micromachined accelerometers have been built with capacitive sensing[2], operated in force feedback configurations[3], and built with torsional[3] and diaphragm[2,4] suspension systems. In all cases, damping of the resonant frequencies has either been ignored, achieved with a viscous liquid, or accomplished electrically with a force balance control system.

The IC Sensors model 3021 accelerometer described in this paper is fabricated using silicon micromachining at the wafer level to achieve precise control of the device geometry, to provide protective packaging for the delicate accelerometer structure, and to provide critical air damping.

Device Description

The accelerometer chip used in the 3021 is a sandwich structure of three layers of silicon. As depicted in Figure 1, the center layer is the suspended-mass accelerometer. The outside two layers are caps into which shallow depressions have been etched. These depressions allow the proof mass room to move and serve to provide mechanical stops to protect it from over-acceleration in its sensitive direction. They are also important in providing air damping of the device. This capping is accomplished at the wafer level, and thus the accelerometer mass and flexures are protected during sawing and final packaging.

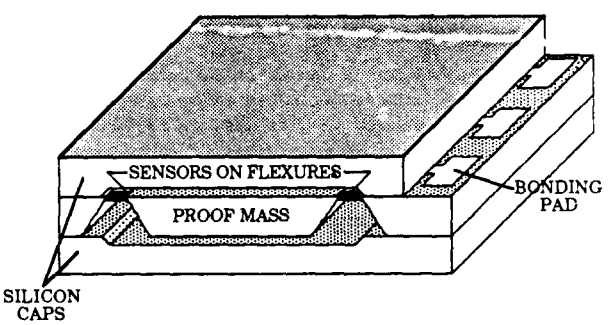

Fig. 1 Cutaway view of 3-layer accelerometer chip

The proof mass is suspended by a double cantilever structure. This suspension was chosen to provide a highly symmetric support for the proof mass, which minimizes the response of the structure to off-axis accelerations. The four flexures contain implanted piezo-resistors to sense deflection of the supports caused by acceleration of the proof mass. To achieve the desired sensitivity for a ±1 g full scale unit, the silicon mass was made 3.6 mm square, and the resulting chip with caps is 7.7 x 7.2 x 1.2 mm. There are a total of eight piezo-resistors to sense strain in the flexures. They are connected in an open Wheatstone bridge with two sensing resistors in each leg of the bridge, giving a total bridge impedance of 3.5 kΩ. As will be discussed in a following section, the interconnection scheme reduces the sensitivity of the device to off-axis accelerations.

The accelerometer chip is mounted on a 15.2 mm square ceramic substrate which is available with ribbon cable or PC mounting pins for the output. With a plastic cap covering the silicon chip for protection, the complete device weighs 1.2 grams. It is designed to be glued down or clamped to the surface which is undergoing acceleration. There is sufficient room under the plastic cap to allow for the mounting of active signal conditioning circuitry.

Because the accelerometer chip is essentially its own package, a minimum weight configuration can be constructed with the silicon package mounted directly on a flex circuit cable with wire bonds to the conductors. This light weight version weighs only 0.2 grams.

TH0215-4/88/0000-0114

The family of devices range in sensitivity from full scale outputs (±50 mV with a 5 V drive) for ±1 g to ±500 g. With built-in over-acceleration stops, all parts, even the ±1 g devices, are capable of surviving 2,000 g shocks from any direction. They are critically damped and depending upon the sensitivity range of the unit, have a flat frequency response from DC to 350 Hz for the low g device and up to 2000 Hz for the high g device. The control of the damping factor to achieve critical damping for this wide range of sensitivities is one of the most significant features of these accelerometers.

Damping

A significant problem in silicon accelerometer design is coping with the high-Q resonances of these structures. When excited by an external vibration at one of the resonant frequencies, the mechanical motion of the mass is amplified by a factor equal to the Q at that resonance. In a vacuum, the Q of a silicon structure can easily be over 1,000. Thus, without some form of damping, silicon accelerometers are very prone to breakage due to excitation of their mechanical resonances. The control of these resonances by properly damping the devices is therefore imperative in making a rugged device and is the key to providing flat frequency response.

Finite element analysis of the double cantilever structure with four supports predicts that there will be three dominant modes of oscillation of the proof mass. As is depicted in Fig. 2, the lowest frequency or fundamental mode of oscillation occurs with the mass rising and falling in the z-direction, the acceleration sensing direction of the device. The rocking of the mass about its axis which is perpendicular to the flexures is mode II and occurs at roughly the first harmonic frequency. The third mode is a torsional oscillation at a frequency which lies between the fundamental and first harmonic.

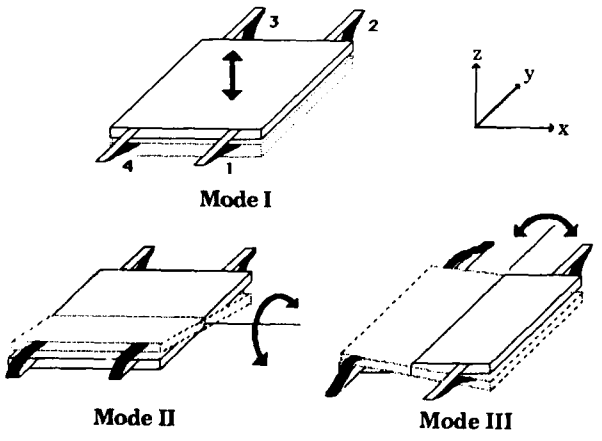

Fig. 2 Fundamental and harmonic motions of the accelerometer structure.

These three modes of oscillation can be observed in devices which have accessible outputs from piezoresistors on each of the flexures. Uncapped devices operated in open air exhibit three resonances with Q's in the range of 20 to 30. A typical spectrum from a ±2 g device is plotted in Fig. 3. By monitoring the phase relationship between the output signals from each flexure, the peaks can be correlated with their respective modes of oscillation.

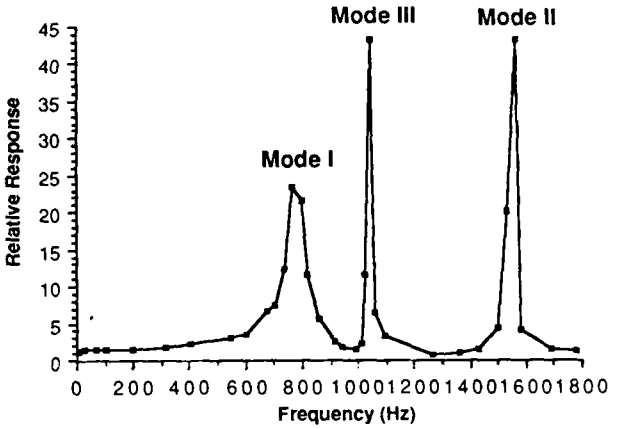

Fig. 3 Undamped accelerometer response

Due to the large surface area of the proof mass, the movement of air which accompanies the deflection of the mass results in significant damping. The uncapped device which produced the spectrum in Fig. 3 could not survive the violent oscillations which would result if it were operated in a vacuum. By the same token, restricting the movement of air around the mass increases the damping and reduces the oscillations. This can be accomplished very effectively by restricting the air to shallow depressions in the silicon caps on the top and bottom sides of the proof mass. Thus, the same depressions which provide room for the mass to move and provide mechanical over-acceleration stops also determine the damping of the device. The depth of the depressions can be accurately controlled to within 1 μm, resulting in less than a 10% variation in the damping factor across a wafer. The damping is proportional to the viscosity of the air which only varies by 25% from its room temperature value between -40° and 125°C. This variation is far less than is experienced by liquids used as damping agents.

In a mechanical system such as this accelerometer, each resonance contributes a term to the transfer function of the form

$$A = \frac{1}{1 + \frac{s}{\omega_0 Q} + \left(\frac{s}{\omega_0}\right)^2} \qquad (1)$$

Experience with the devices indicates that the damping for all three modes of oscillation appears to be about the same. Using this assumption and using the resonant frequencies from the device from Fig. 3, an electrical model with three poles of the form of Eq. 1 yields the expected frequency response of the device. Fig. 4 shows this response for the three poles with critical damping (Q=0.707), and for over-damped and under-damped cases. Experimental spectra obtained from the accelerometers agree quite well with the shape of the theoretical curves.

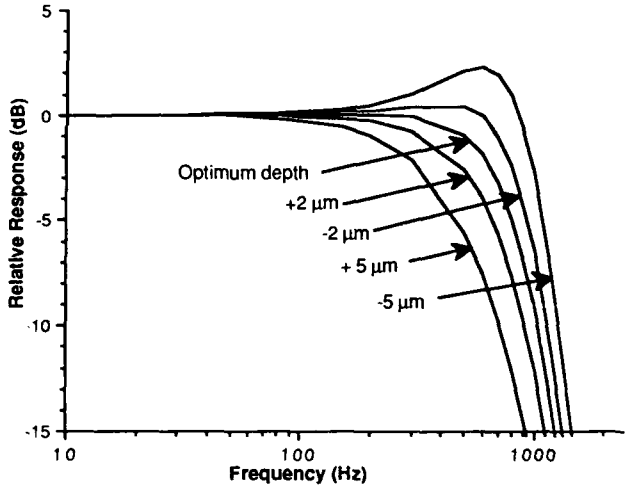

Fig. 4 Response variation due to changes in cavity depth. Typical variation in depth is ±1 µm.

Off-axis sensitivity

The flexures which support the proof mass are at the top surface of the silicon mass. The center of mass of the proof mass, however, is in the midplane of the silicon wafer, 200 µm below the surface. This offset of the center of mass below the center of support leads to movement of the mass when it is subjected to cross-axis acceleration. When it is accelerated along the x-axis or the y-axis, the mass tends to deflect as shown in Fig. 2 for Mode II or Mode III. The electrical response to these deflections can be greatly reduced by the appropriate interconnection of the sensing resistors on the flexures.[5]

There are two resistors on each flexure, one at the mass end and one at the frame end. They are connected in a Wheatstone bridge as shown in Fig. 5.

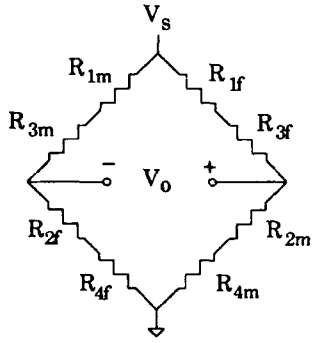

Fig. 5 Connection of sensing resistors. Subscripts refer to flexures shown in Fig. 2 at mass or frame ends.

If the resistors are well matched and the deflection of the mass is about its center of mass, then the equal and opposite responses from the resistors make it theoretically possible to obtain output from the device for z-axis accelerations only.

With actual devices this interconnection scheme eliminates any observable Mode II & III resonances and results in less than a 1% response to off-axis accelerations.

	ΔR with x accel	ΔR with y accel	ΔR with z accel
R_{1m}	↓	↓	↑
R_{1f}	↑	↑	↓
R_{2m}	↓	↑	↑
R_{2f}	↑	↓	↓
R_{3m}	↑	↑	↑
R_{3f}	↓	↓	↓
R_{4m}	↑	↓	↑
R_{4f}	↓	↑	↓
V_{out}	0	0	↑

Table 1 Increase or decrease of resistance from sensing resistors with acceleration.

Conclusions

Silicon micromachining techniques have been used to produce a new, commercially available accelerometer. An integral silicon package provides mechanical protection, over-acceleration stops, and air damping for the device. This critical packaging step utilizes silicon micromachining for precise dimensional control. It is performed at the wafer level, thus reducing production costs by eliminating final assembly steps. Though the accelerometer chip is relatively large, the design can easily be extended to smaller versions for high-g or lower-performance applications. The micromachining concepts incorporated in the design of the three layer package and the air damping can be applied to a whole family of devices with various sensitivities and degrees of off-axis performance. These relatively inexpensive accelerometers should play a major role in the expansion of the markets and applications of micromachined silicon sensors.

Acknowledgements

The author would like to gratefully acknowledge the design, modeling, and fabrication efforts of H. Allen, H. Jerman, and J. Crawford.

References

1. Roylance, L. M., Angell, J. B., "A batch-fabricated silicon accelerometer", *IEEE Transactions on Electron Devices*, Vol. ED-26, No. 12, 1979, p. 1911

2. McArthur, S. P., Holm-Kennedy, J. W., "Air loading on a capacitively sensed membrane supported accelerometer", *IEEE Solid-State Sensors Workshop Digest of Technical Papers*, June 1986,

3. Rudolf, F., Jornod, A., Bencze, P., "Silicon microaccelerometer", *Transducers '87 Digest of Technical Papers*, June 1987, p. 395.

4. Suminto, J. T., Yeh, G., Spear, T. M., Ko, W. H., "Silicon diaphragm capacitive sensor for pressure, flow, acceleration and attitude measurements", *Transducers '87 Digest of Technical Papers*, June 1987, p. 336

5. Sandmaier, H., Kühl, K., Obermeier, E., "A silicon based micromechanical accelerometer with cross acceleration sensitivity compensation", *Transducers '87 Digest of Technical Papers*, June 1987, p. 399.

A CMOS PROCESS FOR HIGH TEMPERATURE SENSORS AND CIRCUITS

R. B. Brown and K.-C. Wu
Electrical Engineering and Computer Science
University of Michigan
Ann Arbor, MI 48109-2122

M. Ghezzo and D. M. Brown
Central Research and Development
General Electric Company
Schenectady, NY 12301

ABSTRACT

Sensor applications from automobile and jet engines to space-based power systems are begging for smart sensors and control circuitry which will operate reliably at temperatures above 200°C. The requirements of these extreme environments can be met by combining high-temperature technologies, design rules, and circuit methods [1]. This paper reports progress in junction-isolated CMOS technology for high temperature operation. Variations on an advanced 1.25μm VLSI process have addressed two of the most serious high-temperature problems in CMOS: refractory metallization has eliminated the problem of electromigration; *and process variations have doubled latchup* holding voltage and current at 300°C.

INTRODUCTION

A number of alternatives to traditional silicon processes are being considered for the implementation of high-temperature circuits [2], including deep-impurity semiconductor technologies, wide-bandgap materials (i.e., GaAs, GaN, GaP, SiC, $B_{12}As_2$, and Diamond), and miniature vacuum devices using thermionic or field emission. Development of these approaches ranges from yet unproven principles, to working (but expensive) large-scale integration. Our efforts are focused on CMOS technologies, which, having high input impedance *and good noise immunity, are advantageous for sensor interface* circuitry. While the unrelenting scaling of features in mainstream CMOS runs counter to the needs of high temperature microelectronics, the processes developed to achieve dense layouts can be very useful (with more conservative design rules) for high-temperature circuits.

HIGH-TEMPERATURE CMOS

The starting point of this work is the GE A/VLSI process [3], developed for 5 volt digital and analog chips with 1.25μm design rules. The twin-tub process includes lightly doped drains, polysilicon gates, and double metal interconnect. The basic process includes some features which suit it well to high temperature applications: 1) thin epitaxial starting material (3.5μm) and retrograde p-wells improve latchup performance by reducing the value of the parasitic lateral resistor and the gain of the parasitic vertical bipolar transistor; 2) a metal electrode layer forms a high-quality metal-to-metal capacitor, facilitating the design of analog circuits, essential to smart sensor chips; and 3) molybdenum interconnect on metal layers 1 and 1.5 (capacitor electrode) prevents electromigration, a serious problem of aluminum at high temperatures.

Several modifications have been made to the standard A/VLSI process to improve its high temperature performance. The first of these addressed the electromigration problem by replacing the standard top level metal (aluminum) with molybdenum. Typically, power rails are routed in top level metal, and the electromigration problem is aggravated both by the additional thermal energy available at high temperatures, and because of additional junction leakage which increases current density in the power traces. Molybdenum has a resistivity of 5.7$\mu\Omega$-cm compared to approximately 3.4$\mu\Omega$-cm for aluminum interconnect alloys, so design rules must accommodate this difference to avoid resistively-coupled noise. On the other hand, the electromigration activation energy for molybdenum is so high as to effectively eliminate this reliability concern. Top metal to bottom metal via resistance in the all-moly system is within 20% of that in the standard process.

Tests were conducted using the basic process to evaluate the contribution of the epi layer to latchup characteristics at high temperature. Conventional bulk wafers and epitaxial wafers were processed with a test vehicle mask set. Latchup data were taken on an inverter structure, with separate contacts for V_{SS}, V_{DD}, V_{IN}, V_{OUT}, p-well, and substrate. The test configuration was a two-terminal circuit formed by hard-wiring the n^+ source (cathode) to the p-well contact (V_{SS}), and the p^+ source (anode) to both the top and backside substrate contacts (V_{DD}). Latchup was induced by forcing a current through this two-terminal circuit.

Fig. 1 shows latchup characteristics over temperature for epi and bulk devices sized at 100%, 75% and 50% of the design rules. For both holding current and holding voltage (which is not shown), bulk curves for the different size structures are close together, while epi curves are spaced apart. Most of the triggering current forced into the test-structure anode on an epi wafer is directly injected into the low resistivity substrate, making it unavailable for forward biasing the lateral PNP transistor. As the anode and cathode are spaced further apart, the percent of lateral current in the epitaxial layer decreases rapidly, due to the epi / substrate resistivity differential. (In bulk wafers, the uniform substrate resistance spreads the current flow more evenly.) As a result, scaling up of design rules is a very efficient method for improving latchup performance in epitaxial CMOS. This advantage is even more pronounced at higher temperatures.

To reduce holding current and simulate different source-to-substrate contact spacings, a 25% undersized device was used in another test, and external resistance was inserted in series between the anode and substrate contact. The well-known deterioration of latchup performance with temperature is seen in Fig. 2, a family of latchup holding current curves for bulk CMOS with different external resistances. Over a temperature range of 25 to 315°C, holding current is reduced by a factor of 10. With external resistance, the reduction is smaller, causing the curves to converge at high temperatures. This effect can be ascribed to the increase in well and substrate resistance at higher temperature; if the substrate resistance already includes external resistance, any further increase due to temperature is less important, and holding current temperature sensitivity is lower. Similar measurements were made on identically processed epi wafers. Temperature sensitivity is low on the epi wafers because the lateral parasitic resistance is low. As seen in Fig. 3, not only were room temperature holding currents 2.7 times higher than in bulk, but the holding current decreased by only a factor of 2 over temperature (compared to a factor of 10). This results in a large ratio of holding currents between epi and bulk at higher temperatures. Again, the use of epi material for latchup immunity is seen to be even more compelling at high temperature than at room temperature

Other modifications were made in a special high-temperature CMOS process: the epitaxial layer thickness was reduced by one third, and doping levels were increased. The thinner epi causes even more of the trigger current to be shunted harmlessly into the substrate. Higher doping levels correspond to lower junction leakage currents and higher intrinsic temperatures; they also cause lower junction breakdown voltages, in this case, reducing drain breakdown by 30% to a still acceptable level of 9 volts. Figs. 4 and 5 compare bulk, epi and the special high-temperature epi (HT-Epi) holding currents and holding voltages. These data are for 1.25μm channel length inverter structures tested as two-terminal devices. (Gates are tied to the cathode.) The high-temperature process has improved both holding current and holding voltage at 300°C by more than a factor of 2 over *the already excellent performance of the standard A/VLSI process.* Holding voltage at 300°C is 4 times better in the special process than in bulk CMOS, and holding current is 30 times better than in the bulk process.

CONCLUSIONS

Integrated sensors and circuits can be designed to operate reliably at high temperatures by taking advantage of scaled CMOS technology developments, together with special process variations designed to improve high temperature performance. In this example, inexpensive process *modifications doubled high-temperature latchup robustness.*

TH0215-4/88/0000-0117

ACKNOWLEDGEMENTS

This work is supported by grants from Ford Scientific Research Laboratories and the Ford Fund, and by the General Electric Corporate Research and Development Center.

REFERENCES

[1] Richard B. Brown, Fred L. Terry, and Kou-Cheng Wu, "High Temperature Microelectronics — Expanding the Applications for Smart Sensors," *IEDM 1987 Tech. Digest*, pp. 274-277.

[2] *High Temperature Electronics Workshop*, organized by Sandia National Laboratories and sponsored by Air Force Wright Aeronautical Laboratories, April 12-14, 1988.

[3] D. Brown, S. Chu, M. Kim, B. Gorowitz, M. Milkovic, T. Nakagawa and T. Vogelsong, "Advanced Analog CMOS Technology," *IEDM 1985 Tech. Digest*, pp. 260-263.

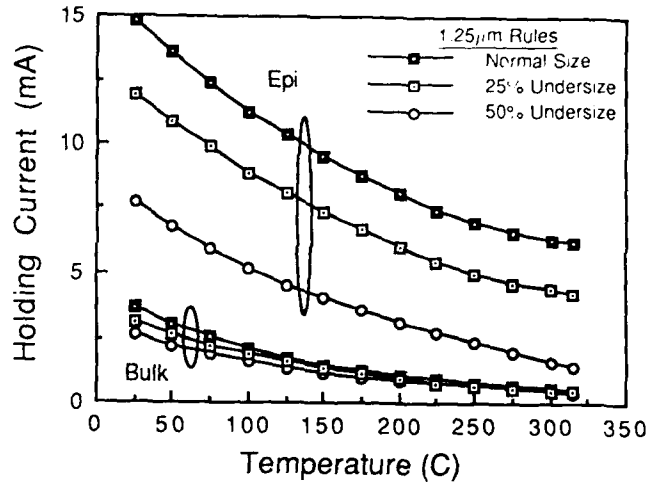

Fig. 1. Comparison of holding current for bulk- and epi-CMOS inverters of three sizes.

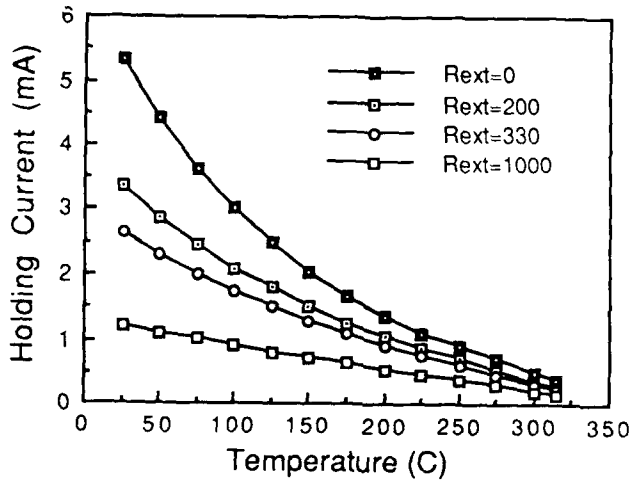

Fig. 2. Holding current of 25% undersized bulk-CMOS inverter versus temperature, with external resistance as a parameter.

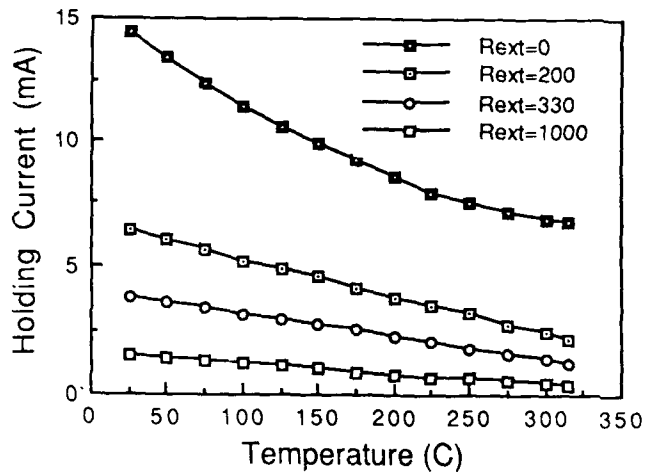

Fig. 3. Holding current of 25% undersized epi-CMOS inverter versus temperature, with external resistance as a parameter.

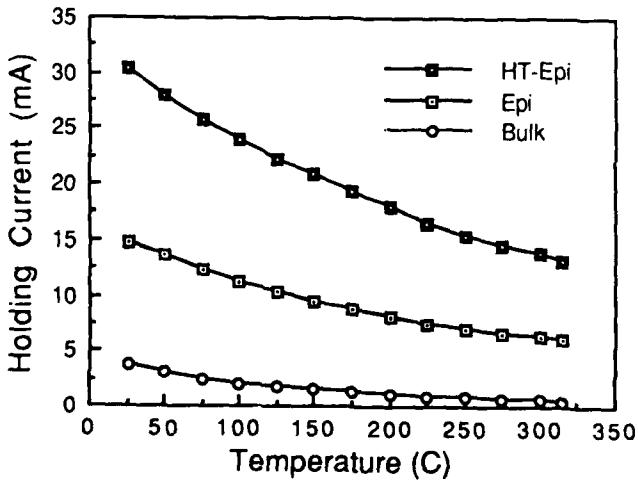

Fig. 4. Comparison of holding current for bulk-CMOS, epi-CMOS, and special high-temperature epi-CMOS inverters.

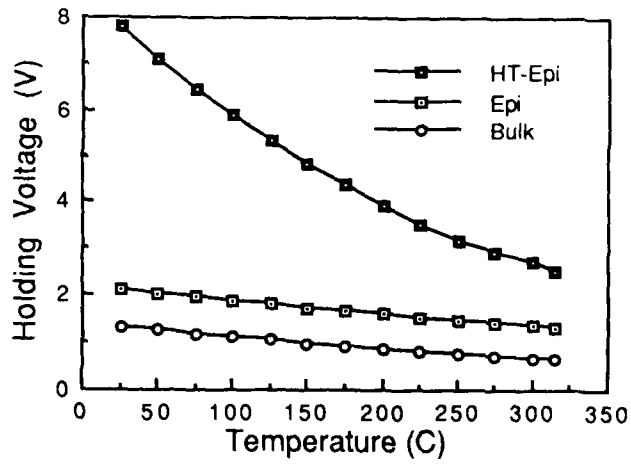

Fig. 5. Comparison of holding voltage for bulk-CMOS, epi-CMOS, and special high-temperature epi-CMOS inverters.

AN ADVANCED SOLID STATE PRESSURE TRANSDUCER FOR HIGH RELIABILITY SSME APPLICATIONS

G.E. Gustafson and J.J. Shea
Solid State Electronic Division
Honeywell, Incorporated
Plymouth, Minnesota, 55441 U.S.A

ABSTRACT

The objective of this research project is to develop a new silicon sensor and packaging technique to advance the state-of -the-art of pressure transducers for the NASA Space Shuttle Main Engine (SSME). This advancement will yield improved reliability, accuracy, and cryogenic temperature operation. This paper describes the silicon sensor, packaging concept, and the results from mechanical and electrical testing of development hardware.

The targeted performance goals for Honeywell SSED's new SSME pressure transducer are challenging. The combination of low temperature, high pressure, and severe vibration and shock associated with the SSME provides an extremely hostile environment in which to operate a high accuracy transducer. The new design is constrained to conform to the external configuration of the transducer currently used on the Space Shuttle Main Engine so that electrical and mechanical interchangability is maintained. In addition to meeting the current requirement, improved frequency response characteristics can be achieved over the current device by flush (versus remote) mounting the Honeywell SSME transducer to the engine. SSME pressure transducer design features are summarized in Table 1. The electrical design goals of the program are listed below.

- Identical / redundant on -chip sensing and compensation functions.
- Operating temperature range of -196° to 121°C (-320 to 250°F)
- Linearity ≤ 0.15% FS
- Hysteresis ≤ 0.1% FS
- Non-Repeatability of Pressure Signal ≤0.05% FS
- Non-Repeatability of Pressure Null ≤0.05% FS
- Spanshift ≤ 0.005% FS
- Nullshift ≤ 0.005% FS
- Zero set to ≤0.25% FS
- Electrical to pressure calibration set point at 80% ± 0.1% FS
- Voltage output of 30 mV; with total error band of ≤ 0.1% FS
- Supply Voltage of 10 Volts D.C.

To achieve the high-accuracy, high-pressure performance objectives, the transducer design concept utilizes packaging materials with similar thermal coefficients of expansion and maintains the transducer pressure seals primarily in compression. (The SSME application calls for a maximum 9.5K psi full scale with 20K psi overpressure). The full scale operating pressure range is changed simply by changing the thickness of the silicon diaphragm. One common package is designed to accommodate a pressure family from 300 PSIA to 9500 PSIA. The sensor capsule assembly is shown in Figure 1 and the complete package design is shown in Figure 2. The mechanical integrity of development hardware was demonstrated over the requirements for temperature (-320°F to 250°F) and vibration (400gs @ 2000Hz).

Silicon test sensors have also been fabricated to evaluate the package concept. The silicon piezoresistor doping concentration was customized for the SSME temperature requirement. Results from testing development hardware of the new package concept show excellent transducer performance over the temperature range of -196° (liquid nitrogen) to 125°C.

The final silicon sensor chip design will provide redundant sensing bridges with integrated, laser-trimmable compensation electronics. The compensation circuit provides a trimmable null, a 30 mV linear full scale signal and passive compensation for span shift and null shift over temperature. Successful completion of this research project will result in the fabrication of deliverable hardware for NASA testing and evaluation.

TABLE 1
Honeywell's SSME Pressure Transducer Design Features

DESIGN FEATURES	DESIGN APPROACH
Sensing Element and Circuit	-- Two sets of sensing elements, and circuits are contained on a single chip. (dual sensing outputs) -- The circuit provides a fully compensated and calibrated linear output voltage proportional to pressure.
Integrated Circuit Protection	-- The integrated circuit on the silicon is protected by the absolute reference cavity.
Method of Calibration	-- Laser circuits trim capability is provided by thin film resistors on the silicon chip.
Pressure Range Change (300psi to 9500 psi F.S.)	-- The operating pressure range is changed simply by changing the thickness of the silicon diaphragm.
Pressure Media (Cryoginic Fluids)	-- To insure highreliability the circuit side of the silicon chip is protected from the pressure media. -- The transducer package materials were selected for pressure media compatibility.
Vibration	-- The attributes of silicon pressure transducers such as small size, low mass, integrated electronics and essentially no moving parts all contribute to high vibration capability. -- The length of the electrical interconnects from the silicon chip to the terminal board will be controlled for high vibration capability.

IH0215-4/88/0000-0119

DESIGN FEATURES	DESIGN APPROACH
Cryogenic Temperature	-- Excellent silicon sensor performance, at liquid nitrogen temperature was successfully demonstrated at NASA/MSFC. -- The implant dose of the ion implant sensor elements is customized for cryogenic temperature performance. -- The transducer package materials were selected for cryogenic temperature compatibility.
High Pressure	-- The transducer design concept maintains the transducer seals primarily in compression and utilizes high strength materials with similar coefficients of expansion.
Acoustic Frequency Response	-- Acoustic modeling software was developed to analyze the frequency response characteristics and will be utilized in the final design to maximum frequency response. -- Pressure port length will be minimized.

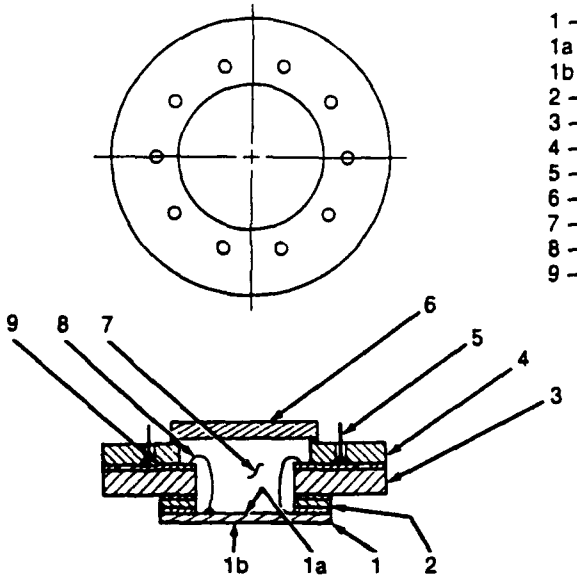

1 — Pressure Sensing Chip
1a — Circuit Side
1b — Backside
2 — Pyrex Washer (Sensor Mount)
3 — Terminal Board #1
4 — Terminal Board #2
5 — Electrical Terminal Pins
6 — Cover Glass
7 — Absolute Reference Cavity
8 — Electrical Wire Bonds
9 — Electrical Feedthroughs

Figure 1

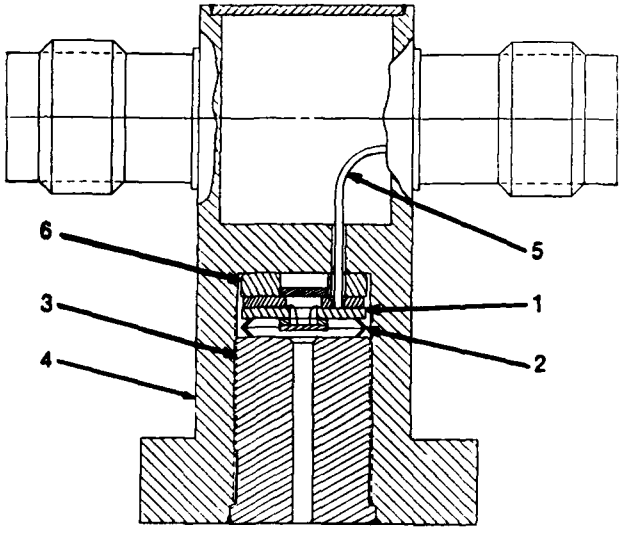

6 — Invar Interface Plate
5 — Connection: Terminal Board-To-External Connector
4 — Stainless Steel Housing
3 — Stainless Steel Plug
2 — Metal V-Ring (Pressure Seal)
1 — Capsule Assembly

Figure 2

DISPOSABLE BLOOD PRESSURE SENSORS WITH DIGITAL ON-CHIP LASER TRIMMING

Janusz Bryzek, Ph.D., Robert Mayer, Phillip Barth, Ph.D.

NovaSensor
1055 Mission Court
Fremont, CA 94539
415-490-9100

Abstract

A monolithic silicon pressure sensor with laser-trimmable calibration networks has been developed for disposable use in invasive blood pressure monitoring. Laser trimming of the novel quasi-digital on-chip resistor networks brings improved performance and short trim times for high production volumes. Incorporation of a small, square diaphragm for pressure sensing provides exceptionally high overpressure capability (10,000 mmHg), while the ability to laser trim after packaging eliminates errors associated with package-induced stresses. The chip offers low cost and high performance and is suitable for a variety of packages.

Introduction

Disposable blood pressure sensors were introduced to the market in 1982. The only technology capable of the required price/performance ratio for this application ($40/1% accuracy) was based on silicon IC processing. The first of these products employed hybrid technology wherein sensing was performed by a silicon monolithic chip while calibration and compensation were performed by a thick-film laser-trimmed circuit. The market for this type of product increased from approximately 40,000 units in 1982 to 6 million units in 1988. This dramatic volume increase, combined with a simultaneous sensor price drop to below $3 in large volume, necessitated a transition to new technology with a higher level of vertical integration on-chip, including laser-trimmable thin-film resistors.

The challenge to chip manufacturers has been to achieve designs with planar or near-planar circuit topology, rapid trim capability, good stability after trimming, high yield both at the die level and at the package level, and low cost. The chip introduced here meets those goals, and is the smallest and most advanced to date for this market.

Integration of additional circuitry on a chip necessitated efforts geared toward:

- developing and combining processes for piezoresistors and temperature-stable laser-trimmable thin-film resistor networks without degradation of the characteristics of either
- optimizing the chip design and fabrication process to improve parameter distributions (die-to-die, wafer-to-wafer, and lot-to-lot), thus simplifying the trimming network
- minimizing chip size to minimize fabrication cost per chip
- designing the logistics of pressure/temperature testing and laser trimming for high throughput and low cost
- designing chip trimming capabilities in either wafer or package form

The packaged, trimmed product must deliver a set of well-controlled parameters. The initial guidelines were provided by the Association for the Advancement of Medical Instrumentation (AAMI) [1]. Marketing issues have pushed the performance even further [2], necessitating trimming for initial offset, offset temperature coefficient, sensitivity and its temperature coefficient, output symmetry and impedance, input impedance, and shunt calibration. Required performance for pressure nonlinearity, offset and sensitivity shift with excitation voltage (over a 1-12 V range), and overpressure capability are provided by design.

Sensor Design

A 900 um square diaphragm was selected with a fully active Wheatstone bridge configuration of strain gages. This small diaphragm size requires a thickness of 12 um to deliver the necessary pressure sensitivity. To provide effective stress transfer, a super shallow (1 um) piezoresistor process was developed using ion implantation.

The doping level for the resistors was selected with the aid of modelling to optimize temperature coefficients and pressure sensitivity [2]. A controllable etch stop technique was selected to obtain a tight sensitivity distribution and predictable, repeatable overpressure performance. A chip size of approximately 2.6 mm square was selected as a compromise between real-estate cost and isolation from package stress.

A new thin-film resistor process with low temperature coefficient of resistance was developed based on sputtered, passivated Si-C_r. A TCR of 20 ppm/^oC was achieved, exceeding the original target of 100 ppm/^oC.

The resistor network implementation is based on quasi-analog digital trimming. This technique allows rapid sequential cutting of links while network resistance is monitored by a comparator, until a threshold resistance value is reached.

The fastest available laser trimmers were developed for trimming and repairing semiconductor memory chips through "link blowing." In that application, metal links are evaporated by a pulse of laser energy which changes a short circuit to an open circuit. The fastest lasers can achieve link-blowing speeds as short as 10 ms. These link-blowing techniques are readily adaptable to sensor technology.

The concept of the resistor design is shown in Figure 1. Resistor R_o is shunted by N parallel resistors (Figure 1a). Initial resistance R_{min} is equal to the parallel combination of all resistors. The laser begins blowing links at link L_1, introducing step changes in the value of effective resistance R, as shown in Figure 1b. When all links are open the maximum value of the network is equal to R_o. Throughout the trimming range R_{min} to R_o, the resistance increases monotonically with each consecutive link blown. This trimming process is equivalent to analog laser

trimming in that it allows monotonic trimming to a required value for parameters such as offset, sensitivity, etc.

To use quasi-analog digital trimming over a broad range of resistance change without an excessive number of links, several parallel resistors networks are placed in series, each of them delivering a different trimming range. The layout of this complex chip is shown in Fig. 2.

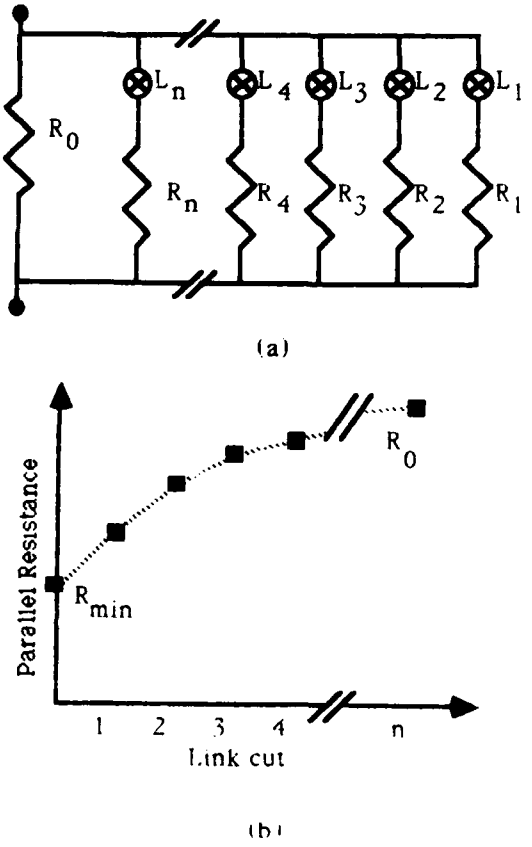

Figure 1. Conceptual illustration of quasi-analog digital trim technique. (a) Parallel network of resistors. (b) Monotonic change of resistance with trimming

Sensor Characteristics

The combination of laser-trimmed calibration and advanced piezoresistor fabrication techniques has resulted in a chip with outstanding performance characteristics including:

Full scale pressure	300 mmHg
Trimmed sensitivity	5 uV/V/mmHg ± 1%
Nonlinearity	<0.2% (terminal-based)
Offset shift	<1mmHg for excitation voltage shift of 1-12 Volts
Backside burst pressure	>10,000 mmHg.
Stability	<0.1 mmHg/8 hours typical

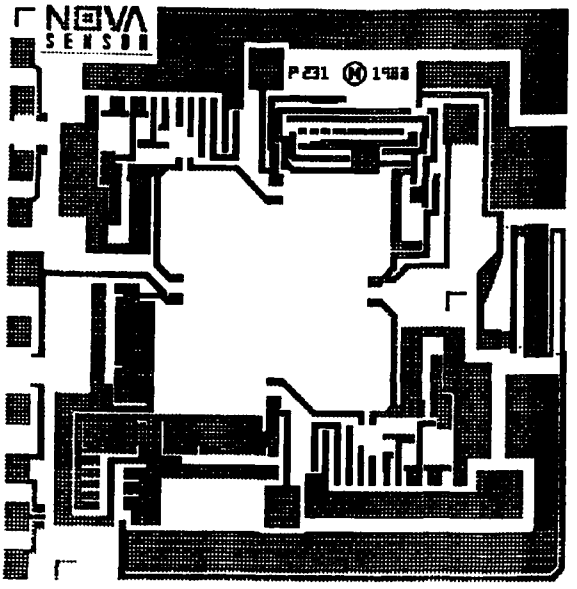

Figure 2. Layout of pressure sensor chip

Packaging

Because laser trimming of the chip can be accomplished after packaging, the effects of package stresses are not important. The sensor has been successfully mounted, tested, and trimmed on a variety of substrate materials including alumina, kovar, and various thermoplastics. Performance on all of these materials has been well within AAMI guidelines. Mounting on almost any substrate material appears practical as long as the material has reasonable dimensional stability in the temperature range expected during packaging and use. The stable performance and good untrimmed temperature characteristics of the sensor allow efficient high-speed testing in the package before and after laser trimming.

Conclusion

The design of the chip and the on-board thin-film resistor network are the result of extensive thermal, mechanical, and electrical modelling (both analytical and finite element modelling) to assure an optimum price/performance ratio. In addition, exceptional backside overpressure capability has been achieved without sacrificing sensitivity or linearity.

The technology used for this sensor design is suitable for a wide variety of additional applications in automotive, HVAC, consumer, and industrial markets. The device establishes a new level of price/performance for blood pressure sensing and has the potential for similar advantages in other applications.

References

[1] ..*erchangeability and Performance of Resistive Bridge Type Blood Pressure Transducers, AAMI Standard, 1986

[2] Janusz Bryzek, **New Generation of Disposable Blood Pressure Sensors**, Sensor Expo Proceedings 1987, Helmers Publishing, Inc., Peterborough, NH, pp 279-284, 1987

[3] J.R. Mallon, A.D. Kurtz, T. Nunn, **Microfabricated Structures for Silicon Piezoresistive Transducers**, *Second International Conference on Solid State* Transducers, Delft, The Netherlands, June 1983.

LOW-COST, HIGH-VOLUME PACKAGING TECHNIQUES FOR SILICON SENSORS AND ACTUATORS

Joseph Mallon, Janusz Bryzek, Jeff Ramsey,
Graham Tomblin, Farzad Pourahmadi

NovaSensor
1055 Mission Court
Fremont, CA 94539
415-490-9100

Abstract

Novel sensor packaging techniques for high volume production at low cost are introduced. Plastic pressure sensor packages for benign to moderate environments provide cost reductions compared to previous packages. Isolated-diaphragm packages suitable for production in high volume with costs approaching plastic-packaged sensors are described.

Introduction

Packaging techniques are widely recognized as a major hurdle in the development and implementation of new sensor designs. In contrast with integrated circuits which are sealed away from the ambient environment as fully as possible, consistent with cost and durability, silicon sensors and actuators must interact with their physical environment, and so must be exposed to that environment.

Sensor are used in a wide range of environments, some at high or low temperatures, many at very high pressures, and some in corrosive gasses or liquids. No one package design is suitable for all applications; specific designs must focus on optimum price-performance ratios. The necessities of coping with these environments along with other customer requirements dictate a wide variety of packages. Efficient production to a cost target on the other hand requires standardization. The solution is a modular packaging approach which employs to the greatest extend possible the packages and techniques of the IC industry.

NovaSensor has developed novel, low-cost packaging techniques for silicon sensors and actuators, which permit the use of these devices in applications which were previously cost-prohibitive. This paper reviews the design philosophy and design process for several such packages, and discusses them against the background of previous packaging techniques with an eye toward future sensor and package developments.

Packaging for Benign and Moderate Environments

Pressure sensor chips in vented TO-style headers are suitable for use in clean, dry environments or moist air. Figure 1 illustrates a typical configuration for a differential pressure sensor in a TO-8 package.

The weakest link in this package is the metallization on top of the sensor chip. Aluminum, typically used for this metallization, will eventually corrode. Gold, platinum, and other noble metals are more corrosion-resistant, but corrosion resistance is still limited by necessary corrosible interlayers. A layer of silicone gel is typically placed over the chip to avoid corrosion of the chip metallization and of the wire bond regions, but this solution is not entirely satisfactory for the most difficult environments. Pressure applied through the bottom port does not encounter the chip metallization, so the backside ambient may be less benign than the frontside ambient. Even so, the package

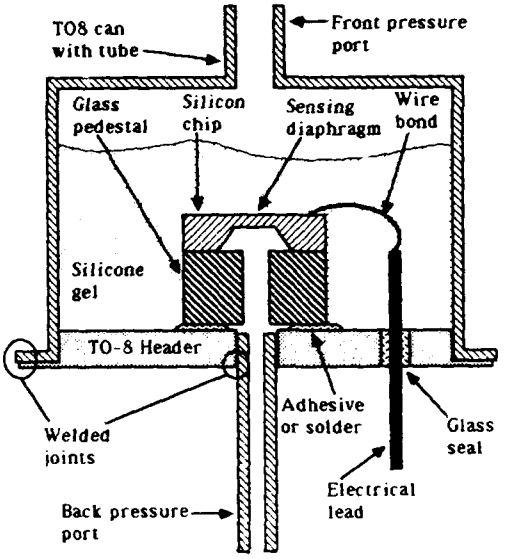

Figure 1. Conceptual drawing of a typical TO-8 pressure sensor package for differential pressure.

may eventually fail from corrosion of the exposed adhesive or solder in very difficult environments.

Sensors mounted directly on hybrid circuit boards, with laser-trimmable resistors on the same board, have been in use for many years, and are suitable for a wide variety of applications. While such hybrid boards can suffer from many problems in severe environments including corrosion and cracking, they have been successful in applications including automotive manifold pressure sensing and disposable blood pressure monitoring.

A major drawback to hybrid packaging for high-volume applications is cost. Just as small plastic-packaged integrated circuits have displaced metal packages and hybrid packages in a host of applications, small plastic sensor packages should displace higher-cost packages.

Shown below in Figure 2 is the first plastic mini-DIP package for silicon pressure sensors. This 6-pin board-mountable package has two fluid ports and is potentially useful for other types of sensors and actuators including flow sensors, miniature valves, and humidity sensors. The package takes advantage of injection molding technology for high volume and low cost. As in TO-style packages, silicone gel provides some protection for the chip metallization and the wire bonds. Pressure ambient applied to the backside of the silicon chip can be less benign than frontside pressure ambients.

The package can be used for differential, gauge, or absolute sensing, while the electrical pins can be

0-0215-4/88/0000-0123 © 1988 IEEE

configured in various ways so that the pressure port can exit through either side of a circuit board. A "gull-wing" option is suitable for surface mounting. Pressure connections are made simply, using flexible tubing which slides over the bayonet-style tube on the package. Electrical compensation of sensors is provided either by laser-trimmed thin film resistors on the sensor chip (minimizing part count) or by external components. Thus, the package accommodates both simple chip designs and more advanced designs.

The design process for this package included finite element modelling (FEM) of stresses in the package's walls and pressure ports. ANSYS from Swanson Associates was run on a MicroVAXII computer for these modelling efforts. Figure 3 shows the FEM model for one of the ports on this package when the internal pressure rises 200 PSI above the outer pressure. Compressive stresses are generated internally while tensile stresses are generated near the attachment point of the port.

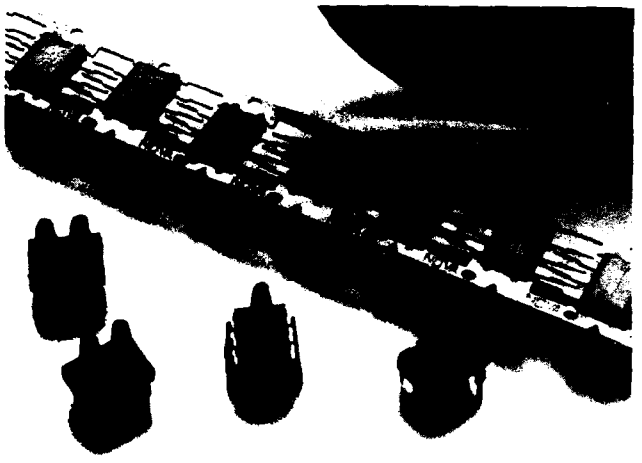

Figure 2. Low cost plastic packaging for circuit-board mounting.

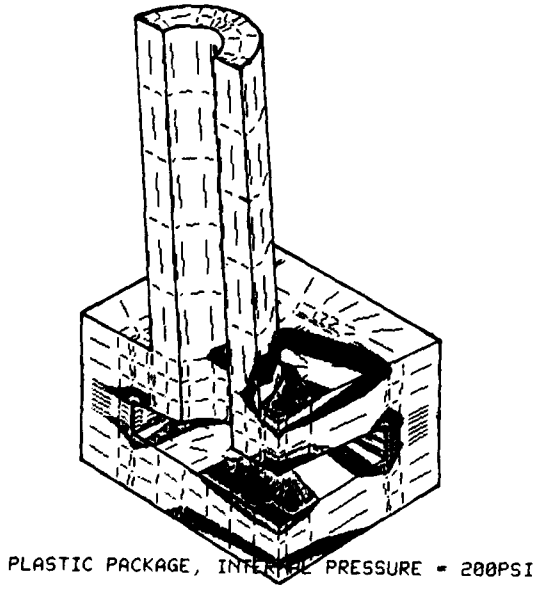

Figure 3. Finite element model of a pressure port on a plastic package.

Packaging for Harsh Environments

More severe environments require a metal isolation diaphragm between the pressure medium and the sensor chip for moisture and corrosion resistance. An incompressible liquid such as silicone oil transmits pressure to the sensor chip. Such packaging has traditionally been expensive, but with proper design and high-volume production the cost can be minimized. A major effort was undertaken to reduce all aspects of cost by efficient design for reasonable mechanical tolerances and efficient, well-fixtured production. Design of the packages required finite element modelling (FEM) to provide maximum performance. Figure 4 depicts three packages resulting from this effort. Hybrid circuit boards mounted on such a package, external of the oil-filled volume, can be laser-trimmed for final transducer calibration.

Sensor chips with laser-trimmable thin-film resistors on board can be used in all of the above packages, as can sensor chips with active electronics and laser trimming. However, it should be noted that final trim of such a chip cannot always be accomplished after the package is completed, so special care is taken to minimize package-induced changes in sensor offset or sensitivity.

Conclusion

Packaging techniques for sensors are evolving in the directions of higher performance, higher volume, and lower cost. The packages shown here are modular subassemblies suitable for easy incorporation into a variety of second-level packages. Thus, customers' needs for configurability are met while retaining the benefits of an efficient modern semiconductor packaging approach.

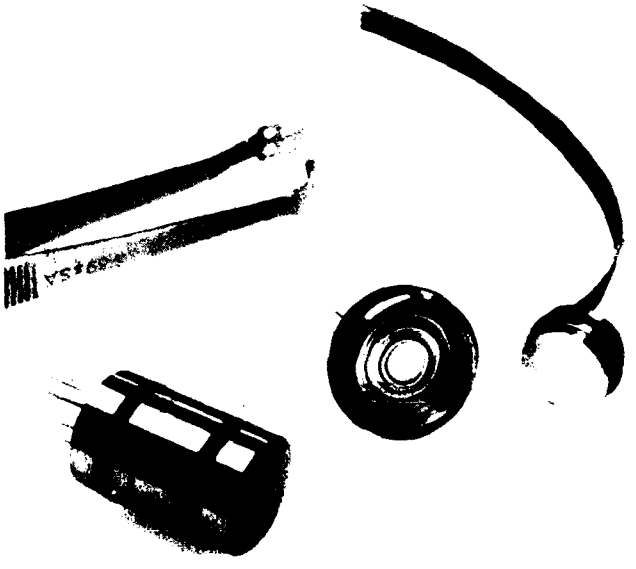

Figure 4. Three low-cost packages for corrosive environments. Stainless steel diaphragms protect the sensor chip from corrosion while silicone oil trasnmits pressure to the chip. Left: Packaging for 10,000 PSI; Middle: Packaging for 1000 PSI; Right: Packaging for 15 PSI.

USE OF TIME DEPENDENT CHEMICAL SENSOR SIGNALS FOR SELECTIVE IDENTIFICATION

Joseph R. Stetter[1] and G. Jordan Maclay[2]

1. Transducer Research Inc., 1228 Olympus Dr., Naperville, IL. 60540
2. Microelectronics Laboratory, Department of Electrical Engineering & Computer Science, University of Illinois, Box 4348, Chicago, IL. 60680

ABSTRACT

A sensor system is described for identifying and quantifying different components in a gas mixture by decoding information from a modulated output signal. The system operates by passing the unknown gas into a reaction chamber containing a heated catalytic filament. The output products from the chamber are detected by an electrochemical sensor. The concentration of the reaction products is modulated by periodic variation of the temperature of the catalytic filament. A theory is presented for analyzing the modulated output signal. The validity of the analysis is confirmed by experiments conducted with benzene, CO, and HCN, and by computer simulations. It appears possible to identify different species in the inlet gas stream provided the species undergo chemical reactions in the reactor that have different activation energies. The signal magnitude at peaks or valleys in the output is directly proportional to concentration even though a steady state condition is not reached. The approach may be generalized to other detector systems.

INTRODUCTION

In the sensor system a periodic non-steady-state sensor signal is generated and this modulated signal is controlled experimentally so as to provide information about specific chemical species present and their concentrations (1,2).

A theory describing the response of the system has been developed for an existing sensor system (1,2) and measurements made to aid in model development. The system consists of a reaction chamber and an electrochemical cell. The gas to be analyzed is exposed to the electrically heated catalytic filament in the reaction chamber that precedes the detector. The rate at which the chemical reaction proceeds depends on the species concentration, the catalyst activity, and the residence time in the chamber. After leaving the reaction chamber, the products of reaction are detected by an electrochemical sensor that produces an output proportional to the product concentration. The concentration of product can be controlled most easily in this case by changing the temperature of catalyst.

MODEL OF REACTION CHAMBER DYNAMICS

The input gas, with component species A and B, flows into the reaction chamber of volume V_o at a rate of u (liters/sec). A reaction takes place in which a reactant C is formed

$$A+B \xrightarrow{k} C$$

where k is the reaction rate constant (liters/mole-sec). The gas in the chamber, which is assumed to be homogeneous and isothermal, exits into an electrochemical sensor where it is detected.

The reaction rate r(t) (moles/liter-sec) is directly proportional to the concentrations C_a and C_b of the reactants:

$$r = k(C_a)(C_b). \tag{1}$$

In the typical trace pollutant detection problem, the concentration of the species to be detected (species A) is several hundred parts per million while the oxygen concentration is 200,000 ppm.

The reaction rate constant, k, is assumed to depend on temperature only

$$k = A \exp(-\Delta E/R_G T) \tag{2}$$

where A is the pre-exponential factor for the particular oxidation, ΔE is the activation energy for conversion of A to C, and R_G is the gas constant per mole. The steady state system response is given by

$$i(\infty) = m\, C_a\, R \tag{3}$$

where the conversion ratio R can be written as

$$R = (1 + u/k\, C_b V_o)^{-1} \tag{4}$$

Note that R depends on the flow rate, u, and the reaction rate k. The constant m is characteristic of the sensor sensitivity for a given oxidation product and k is characteristic of the analyte for a given catalyst and reaction chamber condition.

USE OF PERIODIC VARIATION IN FILAMENT TEMPERATURE

A periodic variation in the filament temperature, such as a sinusoidal variation, can yeild information which can assist in differentiating between different species that produce detectable reaction products (C) from reactions with different rates (e.g. different rate constants and activation energies). For simplicity, in this analysis we assume that the variations in temperature T about T_o which are given, for example, by

$$T = \Delta T \sin(\omega t + \phi) + T_o \tag{5}$$

are sufficiently slow (quasistatic) so that the solution for the steady-state current given by Eq. 3 is valid for all times during the temperature cycle. This assumption is made for mathematical simplicity.

We can write a two term Taylor series expansion for the steady state current as a function of the filament temperature T.

$$i(\infty,T) = i(\infty)\Big|_{T_o} + \frac{di(\infty)}{dT}\Big|_{T_o} \Delta T \tag{6}$$

The first term on the right represents steady state or the dc current i_{dc}, the second term represents the ac current magnitude, i_{ac}, in the small signal approximation in which all higher order terms in ΔT have been omitted.

Differentiating Eq 3, we obtain

$$i_{ac} \equiv \Delta T \frac{di(\infty)}{dT}\Big| = mC_aR(1 - R)\frac{\Delta E}{R_G T}\,\frac{\Delta T}{T} \tag{7}$$

Since $i(\infty) = i_{dc}$, it follows that

$$\frac{i_{ac}}{i_{dc}} = (1 - R)\,\frac{\Delta E}{R_G T}\,\frac{\Delta T}{T}. \tag{8}$$

This ratio is independent of concentration and therefore, this ratio carries the qualitative information required to identify the reacting species, A. It depends only on the flow rate, temperature, ΔT and the activation energy ΔE. It should therefore be possible to distinguish between reactions and components with different activation energies.

The magnitude of the dc signal varies directly with the conversion ratio R (Eq. 4) while the ratio of the ac to dc signal

TH0215-4/88/0000-0125

goes as 1-R. Thus at low conversions the dc signal is reduced but the ratio of ac to dc signal is increased. For a typical case (ΔE = 30 k-cal/mole; T = 900° K, ΔT = 10 C°) we find that i_{ac} / i_{dc} varies from 0.18 for 10% conversion to 0.10 for 50% conversion.

The operating point P_o (u,T) at which the a.c. signal is a maximum corresponds to a dc conversion ratio slightly less than 50%.

Gas mixtures can be analysed by the detector system described if there are independent non-interfering species present and the system response to each is linear. It is more likely that such approximations will be valid if low concentrations and low conversion

MODEL VALIDATION

Figure 1 illustrates a simulation of the derivative of the steady state sensor response to a mixture of species with the activation energies 25, 35, 45 kcal/mole. Since it is assumed that the chemicals give independent responses, the ac sensor response is simply the sum of the individual ac response for each component. The derivative with respect to temperature gives a "spectrum" with peaks corresponding to different activation energies. The peak heights correspond to the magnitude of the ac sensor response, and the location of the peak identifies the operating point P_o and the temperature T_o at which the sensor exhibits the greatest temperature dependence for the species with that particular activation energy ΔE_o. This kind of "spectrum" could be generated experimentally by modulating the temperature in a sine wave while also ramping the temperature from low to high and using phase sensitive detection to monitor only the modulated sensor response.

Modulation of the filament temperature about T_o should not produce a modulated sensor signal for species with activation energy significantly different from ΔE_o. This is illustrated in Figure 2 where the temperature is modulated in a sine wave about T_o for a species with an activation energy ΔE_o of 35 kcal/mole (and A=1.5 x 10^6 cc/mole-sec). The calculated sensor response shows no ac component for compounds with activation energies of 20 and 45 kcal/mole.

CONCLUSION

The computer simulations and theoretical analyses appear to indicate that the appropriate choice of filament temperature, amplitude of temperature modulation, and flow rate will result in the "filtering out" of responses from all species with significantly different rate constants than that of a selected compound to be detected by the sensor system. Experiments are now required to determine the actual variability of k and ΔE from species to species. A more general sensor response model should be incorporated into the theory and faster modulator/detector pairs studied to validate the above arguments.

REFERENCES

(1) Stetter, J.R. and T. Otagawa, "Selective Detection of Chemicals usery Energy Modulated Signals, "Proc. 3rd Int. Conf. on Solid-State Sensors and Actuators (pub. by IEEE, Piscataway N.J. 08854), 77-88 (1985); and G.J. Maclay and J.R. Stetter, "Use of Time-Dependent Chemical Sensor Signals for Selective Identification," Proc. 4th Int. Conf. on Solid State Sensors and Actuators (pub. by IEE of Japan) (1987) 557-560.

(2) T. Otagawa and J.R. Stetter, "A Chemical Concentration Modulation Sensor For Selective Detection of Airborne Chemicals," Sensors and Actuators 11 (1987) 251.

FIGURES

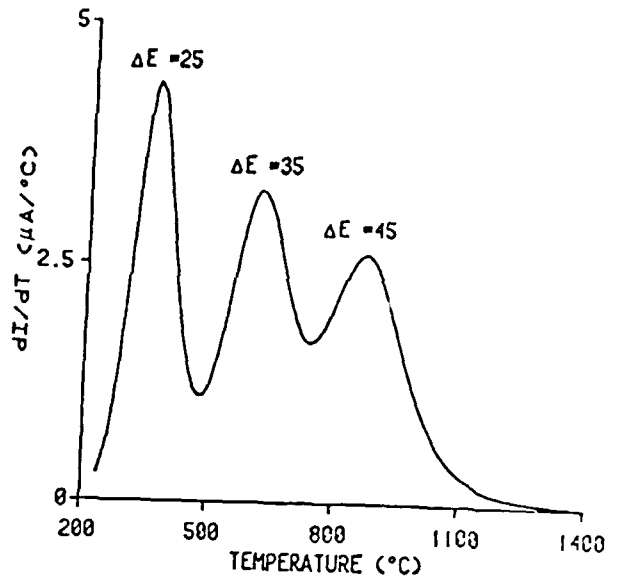

Figure 1. Calculated derivative with respect to temperature for the steady state sensor response to a mixture of species with activation energies of 25, 35, and 45 kcal/mole. The derivative is proportional to the magnitude of the ac sensor response to a small sinusiodal variation of the filament temperature.

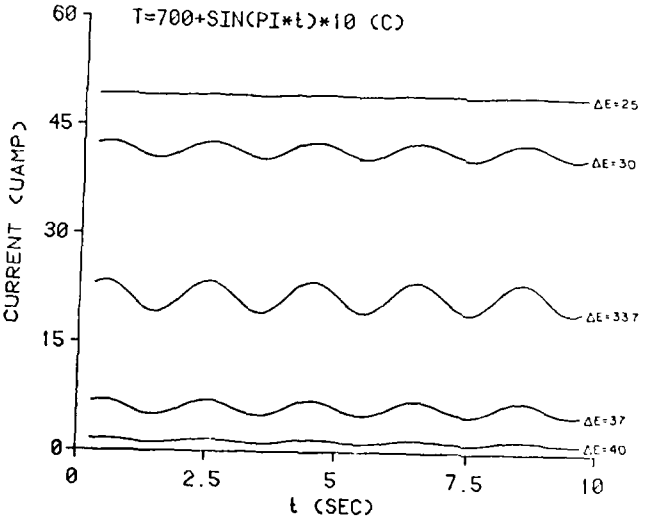

Figure 2. Calculated response of sensor for activation energies from 25 to 45 kcal/mole. The filament temperature varies sinusoidally from 614°C to 634°C, with a period of 2 sec.

TOWARD THE DESIGN OF SUCCESSFUL ELECTRIC MICROMOTORS

Jeffrey H. Lang & Stephen F. Bart

Department of Electrical Engineering and Computer Science
Laboratory for Electromagnetic and Electronic Systems
Massachusetts Institute of Technology
Cambridge, MA, 02139, USA

ABSTRACT

This paper considers various characteristics of electric micromotors, and the relations between those characteristics, in an attempt to organize the process by which successful micromotors can be designed. Special attention is paid to electromechanical characteristics. The resulting organization illuminates the interdisciplinary nature of the physics behind micromotor analysis and design, suggests specific research problems which should be pursued to support micromotor design, and illuminates the interdependence of micromotor design, fabrication and performance. A simple design example which considers the impact of friction torque on the top speed of both variable-capacitance and induction rotary micromotors is provided for illustration.

(1) INTRODUCTION

The surface micromachining of silicon-related materials has recently been applied to the fabrication of very small mechanical structures which exhibit unrestrained motion over at least one degree of freedom, and which do not require assembly of discrete parts [3]. Both linear and rotary structures have been demonstrated. Further, methods of electrification have been proposed for these structures to permit their development as self-propelled actuators [2,4]. Such actuators are the subject of this paper, and are generically refered to here as micromotors.

Much of the initial research aimed at the development of micromotors, and other very small mechanical structures, has focused on understanding fundamental material properties and surface micromachining processes such as internal stress and the resulting strain, tensile strength, adhesion of surfaces, etching rates, the effects of doping and annealing, and so on. This makes considerable sense since knowledge of these properties and processes, and the ability to control them, is critical to the success of any micromachining effort [8]. Eventually, however, the question of what type of micromotor to fabricate must be addressed, and to do so, their electromechanical characteristics must be considered in detail.

The purpose of this paper is to consider electromechanical and related characteristics of micromotors, and the relations between those characteristics, in an attempt to organize the process by which successful micromotors can be designed. The resulting organization illuminates the interdisciplinary nature of the physics behind micromotor analysis and design, suggests specific research problems which should be pursued to support micromotor design, and illuminates the interdependence of micromotor design, fabrication and performance. In this spirit, Section 2 presents a list of important micromotor characteristics. The list is intended to include orthogonal sets of entries between which important relations may exist. The list is certainly not all-inclusive, but rather is meant to be an illustrative focus for the discussion which follows. For further illustration, Section 3 presents a simple design example which studies the impact of friction torque on the top speed of both variable-capacitance and induction rotary micromotors. A summary and conclusions are presented in Section 4.

There are two assumptions upon which this paper is predicated that are worthy of mention. The first assumption is that the micromotors under consideration are electric rather than magnetic in character. The many reasons for this assumption are discussed in [4,2,9]. The second assumption is that the micromotors are fabricated by surface micromaching of silicon-related materials, as outlined in [2,5] for example. Here, surface micromachining refers to the selective etching of multiple layers of deposited thin films. As a consequence, the micromotors under consideration have planar geometries.

(2) A LIST OF CHARACTERISTICS

Some of the more important electromechanical and related characteristics of micromotors are listed in Table 1 for the purposes of discussion. This list is intended to include orthogonal columns of entries which collectively describe micromotors and their performance. The first column lists possible micromotor types as discussed in [4,2] and studied in the references cited therein. It is important to note that each type has a magnetic dual, which has been studied extensively. The second column lists attributes of motor architecture. Each micromotor type is further described by these generic attributes. Each type of micromotor, regardless of its architecture, is fabricated from materials having different functions. These functions are listed in the third column. The success of a material in executing its function(s), is governed by a number of its properites, some of which are listed in the fourth column. These properties may be restricted by the limitations of micromachining fabrication, so possible limitations are also listed. Finally, the ultimate success of a micromotor in its application is judged by one or more performance criteria such as those listed in the fifth column.

Since its columns are orthogonal, Table 1 defines many possible relations between micromotor characteristics. Therefore, one way to interpret Table 1 is as generator of micromotor analysis and design questions. For example, taking the corresponding entry from each column yields the question "How does the conductivity of the conducting rotor effect the torque produced by a rotary induction micromotor?". In this way, relevant micromotor analysis and design questions, and un-

TH0215-4/88/0000-0127

Table 1: Micromotor Characteristics.

Micromotor Types	Micromotor Architectures	Material Functions	Material Properties & Fabrication Limitations	Performance Criteria
Variable-Capacitance Induction Excited-Rotor Permanent-Electret	Rotary Or Linear Number Of Phases & Poles Dimensions Motion Sensing Excitation	Sacrificial Structural Insulation Conduction Lubrication	Mechanical Strength Breakdown Strength Electrical Conductivity Thermal Conductivity Friction & Wear Properties Fabrication Tolerances Permissible Aspect Ratios	Motion Accuracy Force Or Torque Acceleration Top Speed Bandwidth Efficiency Stability Stored Energy

solved research problems, are organized and identified. Hopefully, critical problems which can guide micromotor research will emerge from those suggested by Table 1. Further, the interdisciplinary nature of micromotor analysis and design becomes evident as the entries of Table 1 are examined, as does the interdependence of micromotor design, fabrication and performance. Micromotors are indeed integrated systems which should be treated as such. This is a principle currently followed during the analysis and design of traditional high-performance magnetic-motor drives, and one which is yielding considerable benefits.

Another issue which arises from Table 1 is that of the modeling tools necessary to answer the analysis and design questions posed therein. At least electrical, structural, thermal and fabrication modeling tools are necessary. Whether these tools should be theoretical, numerical or experimental has yet to be determined, however, the need for their development seems clear. In many cases, perhaps for friction or electrical breakdown, for example, even a basic model is lacking, which suggests the initial development of an experimental data base for the purposes of modeling. In any event, compatible levels of modeling sophistication are probably warranted when analyzing the many phenomena involved in answering any given design question. The results of simple-model analyses should indicate where more elaborate modeling is justified.

Finally, Table 1 is certainly not complete; there are surely omissions which will be discovered as micromotor research proceeds. One such omission by condensation is micromot r excitation. If micromotors ever develop to the level of traditional magnetic motors, their performance will likely be significantly limited by their power electronics. Micromotor power electronics therefore probably deserve consideration equal to that given to the micromotors themselves. This emphasizes that micromotor drives, each comprising a micromotor, its power electronics and its controller, should be thought of as a system for design purposes.

(3) A DESIGN EXAMPLE

To further illustrate the discussion of the previous section, this section presents a simple design example which considers the impact of friction torque on the top speed of both variable-capacitance and induction rotary micromotors. The essential geometry of both micromotors is shown in Figure 1. Both micromotors have a disk rotor which rotates about a pin bearing. The rotor is overlapped above by a plate which supports upper stator electrodes. The substrate supports lower stator electrodes. The rotor carries annular insulating bushings which minimize the rotor contact area with the stator; the stator is defined as the plate and substrate. The main difference between the two micromotors is that the rotor of the variable-capacitance micromotor supports electrically-salient highly-conducting electrodes, whereas the rotor of the induction micromotor is a uniform conductor of moderate conductivity. The fabrication details of such micromotors are discussed in [5,2].

All stator electrodes of both micromotors are radially oriented and tangentially disposed in planes parallel to the substrate. These electrodes are electrically excited with a traveling-wave potential that induces charge on the rotor. The rotor charge is dragged along by the stator potential causing the rotor to rotate. A more detailed discussion of the design and operation of variable-capacitance and induction micromotors can be found in [2,4,6] and the many references cited therein. Reference [6] in particular provides a wide variety of electromechanical analyses applicable to micromotors. In addition to being propelled in rotation, the rotor charge is vertically attracted to the upper and lower stator electrodes [4,2]. Although the opposing attractions could balance to create an equilibrium, such an equilibrium is surely unstable; see [2,4,10] and references cited therein. Thus, it is likely that a rotor bushing will be held in contact with the stator as the rotor rotates. This is the source of the friction considered here.

The question of how friction impacts the top speed of a micromotor is one which is contained in Table 1, and as such it is an example of the use of the table. Perhaps more important, however, this question exemplifies the influence that micromachining limitations will have on micromotor performance. As the rotor displaces towards one set of stator electrodes, its attraction to those electrodes increases, while its attraction to the other set decreases. This accounts for the instability of rotor motion perpendicular to the plane of the substrate. When a rotor bushing is in contact with the stator, the differential force of attraction determines the resulting friction torque. There-

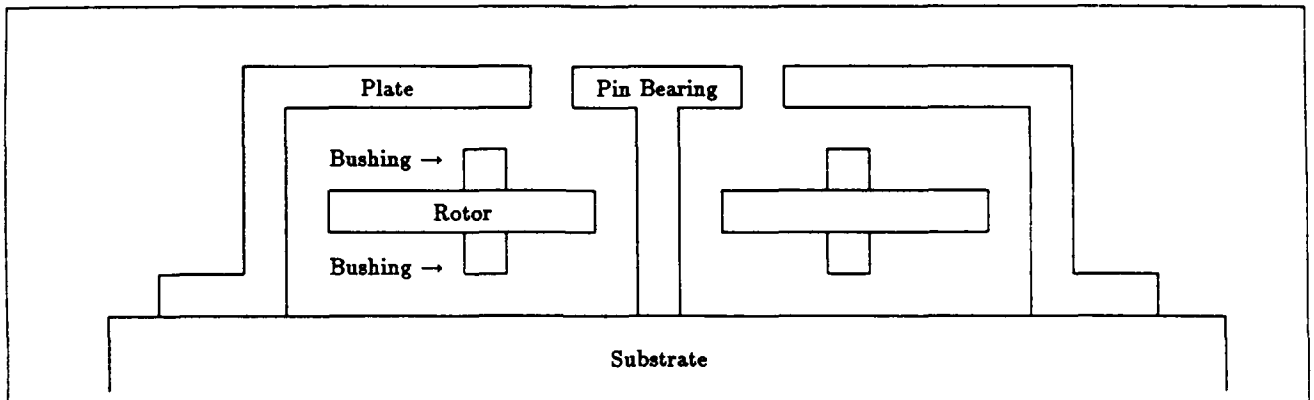

Figure 1: Basic micromotor geometry.

fore, the more the bushing extends into its air gap, the smaller the rotor displacement can be, hence the smaller the friction torque will be. Ideally, both bushings should extend just across their air gaps. Certainly, this is impractical. Space must be left between the bushings and the stator plate and substrate to accomodate micromachining imperfections, warpage of the stator plate and rotor, and so on. Thus, the ability to accurately micromachine will directly influence the performance of the micromotor.

The friction force experienced between two molecularly-flat micromachined surfaces is apparently unstudied. As a starting point for modeling this friction force, consider the expression for kinetic friction between large-area surfaces in which $F_F = \mu F_N$ [1] where F_F is the friction force, F_N is the normal force holding the two surfaces together and μ is the kinetic friction coefficient. Note that this friction model is independent of the contact area of the two surfaces. It should be emphasized that the validity of this model when applied to micromotors is unclear, and that considerable research is warranted. For example, μ is known to have a slight reciprocal dependence on velocity which may be important at the high speeds that are possible with micromotors [7]. Further, the friction force may not be independent of the contact area. Very smooth and clean surfaces often show friction forces that are independent of the normal force and proportional to the contact area [7]. Finally, for highly-cleaned smooth metal surfaces in vacuum, the kinetic friction can become very large and lead to seizure with $\mu > 5$ [1]. Nonetheless, the simple model used here is an appropriate starting point.

The friction torque caused by the friction force acting through the lever arm of the bushing radius can be added to the windage torque and set equal to the micromotor torque of electric origin to yield a top speed for a given micromotor design. As a specific design example, consider the variable-capacitance and induction motors described in detail in [2,4]. Both micromotors have outer and inner stator-electrode radii of 300 μm and 200 μm, respectively, a rotor outer radius of 300 μm, a bushing radius of 100 μm, and nominal air gap separations of 1 μm. In both cases, the stator electrodes are excited through 3 phases with an air-gap potential amplitude of 100 V. The variable-capacitance micromotor has 60 rotor electrodes which match the shape and displacement of the stator electrodes. The induction micromotor has a rotor conductivity of 0.01 S, an excitation frequency of 1 MHs and an excitation spatial periodicity of 18.

Figure 2 shows the top speed of the variable capacitance micromotor as a function of its bushing height normalized to the nominal air gap separations of 1 μm. The kinetic friction coefficient is the parameter for this figure. Figure 3 shows the same results for the induction micromotor. Note that as the normalised bushing height approaches unity, which dictates a perfectly centered rotor, the friction torques vanish, and the top speeds result from balances between micromotor torques of electric origin and windage torques; the windage torque expressions are identical for both micromotors. The top speeds coincide with those given in [2,4]. The fact that the top speeds for both micromotors are equal is a consequence of the selection of micromotor parameters; these parameters are not necessarily optimal.

As the rotor becomes increasingly offset from center due to a smaller bushing height, the friction torque has a different impact on the top speed of the two micromotors. For example, the variable-capacitance micromotor has a greater top speed for large bushing heights, while the induction motor has a greater top speed for small bushing heights, at least for this example. Thus, the achievable bushing height can dictate the choice of micromotor type. At sufficiently small bushing heights, both

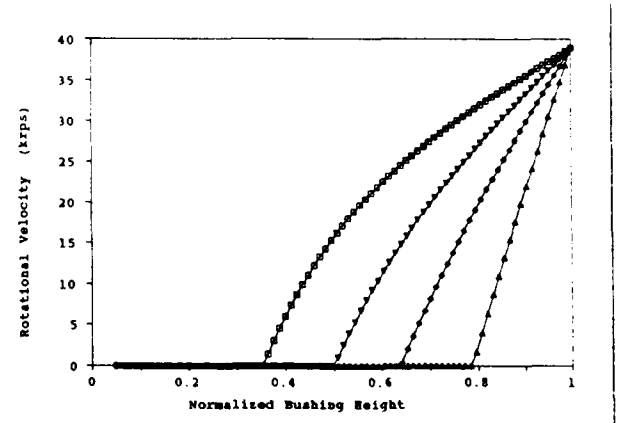

Figure 2: Variable-capacitance micromotor top speed shown as a function of normalised bushing height. Bushing friction is a parameter where □ denotes $\mu = 0.3$, ▽ denotes $\mu = 0.5$, ◇ denotes $\mu = 0.8$, and △ denotes $\mu = 1.5$.

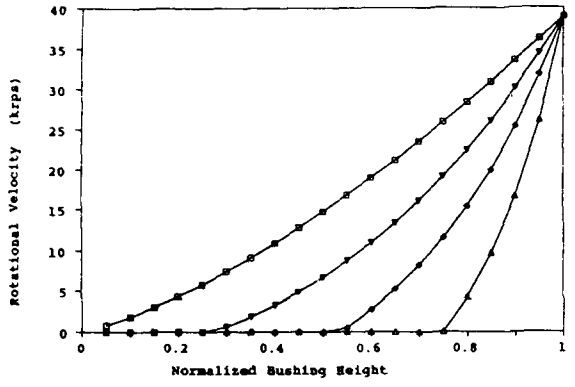

Figure 3: Induction micromotor top speed shown as a function of normalised bushing height. Bushing friction is a parameter where □ denotes $\mu = 0.3$, ▽ denotes $\mu = 0.5$, ◇ denotes $\mu = 0.8$, and △ denotes $\mu = 1.5$.

motors seize, emphasising the importance of tight micromachining tolerances which will permit the fabrication of bushings which extend a sufficient distance across their respective air gaps. Finally, note that top speed is strongly influenced by the kinetic friction coefficient, about which little is known. This indicates that research into the friction encountered in micromotors is certainly worthwhile. Until such research is complete, it is not clear which of the two micromotors is likely to be the most successful.

In summary, while this example has studied a specific design question, and reached conclusions concerning that question, its main value is to illustrate the usefulness of Table 1, and to illustrate the strong interdepence of micromotor design, fabrication and performance. Further, it emphasizes that considerable research, perhaps experimental, is needed before appropriate micromotors can be designed for any given application. Such research might again respond to analysis and design questions posed by Table 1.

(4) SUMMARY AND CONCLUSIONS

This paper considered various characteristics of electric micromotors, and the relations between those characteristics, in an attempt to organize the process by which successful micromotors can be designed. Special attention was paid to electromechanical characteristics. Those characteristics and their relations were summarized in Table 1. This table illuminated the interdisciplinary nature of the physics behind micromotor analysis and design. This table also suggested specific research problems, as well as specific analysis and design questions, which should be pursued to support micromotor design. Further, the table made evident the interdependence of micromotor design, fabrication and performance. A simple design example which considered the impact of friction torque on the top speed of both variable-capacitance and induction rotary micromotors was also provided. This example further illustrated the interdependence of micromotor design, fabrication and performance, as well as the utility of simple-model analyses. Finally, this example illustrated that the proper design of a micromotor is, at this point, perhaps far from obvious.

ACKNOWLEDGEMENTS

The authors wish to thank T. A. Lober, M. Mehregany, M. F. Schlecht, S. D. Senturia, and L. S. Tavrow, all of MIT, for their many contributions to this paper. The development of this paper was supported by the United States National Science Foundation under grant ECS-8614328.

REFERENCES

[1] M. F. Ashby and D. R. H. Jones, *Engineering Materials, 1*, Pergamon Press, 1980.

[2] S. F. Bart, T. A. Lober, R. T. Howe, J. H. Lang and M. F. Schlecht, "Design considerations for microfabricated electric actuators", *Sensors and Actuators, 14*, 3, 269–292, July 1988.

[3] L. S. Fan, Y. C. Tai and R. S. Muller, "Pin joints, gears, springs, cranks and other novel micromechanical structures", *Proceedings of the International Conference on Solid-State Sensors and Actuators*, 849–852, Tokyo, Japan, June 2–5, 1987.

[4] J. H. Lang, M. F. Schlecht and R. T. Howe, "Electric micromotors: electromechanical characteristics", *Proceedings of the IEEE Workshop on Micro Robots and Teleoperators*, Hyannis, MA, November 9–11, 1987. Reprinted in the *Proceedings of the ASME Annual Winter Meeting, DSC-6*, 403-410, Boston, MA, December 13–18, 1987.

[5] T. A. Lober and R. W. Howe, "Surface-micromachining processes for electrostatic microactuator fabrication", *Proceedings of the IEEE Workshop on Solid-State Sensors and Actuators*, Hilton Head Island, SC, June 6–9, 1988.

[6] J. R. Melcher, *Continuum Electromechanics*, MIT Press, 1981.

[7] E. Rabinowicz, *Friction and Wear of Materials*, John Wiley and Sons, 1965

[8] S. D. Senturia, "Can we design microbotic devices without knowing the mechanical properties of materials?", *Proceedings of the IEEE Workshop on Micro Robots and Teleoperators*, Hyannis, MA, November 9–11, 1987.

[9] W. S. N. Trimmer and K. J. Gabriel, "Design considerations for a practical electrostatic micro motor", *Sensors and Actuators, 11*, 2, 189-206, March 1987.

[10] H. H. Woodson and J. R. Melcher, *Electromechanical Dynamics, 1*, John Wiley and Sons, 1968.

THE MODELLING OF ELECTROSTATIC FORCES IN SMALL ELECTROSTATIC ACTUATORS

Richard H. Price,[1] John E. Wood,[2] and Stephen C. Jacobsen[3]

Center for Engineering Design
[1]Department of Physics
[2]Department of Bioengineering
[3]Department of Mechanical and Industrial Engineering
University of Utah
Salt Lake City UT 84112

Abstract. Electrostatic force generation may offer distinct advantages over more familiar magnetostatics at size scales approaching microns. The fabrication of very small electrostatic actuators is becoming technologically feasible, but is extremely difficult, so that mathematical modelling of actuator designs is likely to be very important in the advancement of this technology. Modelling involves difficulties not only in finding solutions (typically numerical) to a mathematical problem, but more important, it requires that the mathematical problem be well formulated. This in turn requires an understanding of, and an intuition for, what electrostatic effects are likely to be relevant, as well as an appreciation for the behavior of materials in electrostatic interactions and for the impact on other machine components (bearings, beam loads, etc.). The well established lore of magnetostatics is not of much use as a guide in this task for several reasons: Magnetic materials tend to be either highly permeable (i.e., ferromagnetic) or to have no magnetic effect. By contrast there are no electrostatically inert materials; the relative dielectric constant ε of any solid (of normal density) is of order 2 or greater, and thus any solid element of an electrostatic configuration has a significant influence on the field. Also, the sources of magnetic fields, currents or magnetization, can be specified with some confidence, while the sources of the electrostatic field, electric charge and polarization, are much more elusive and subject to change. It is the purpose of this paper to point out some of the effects that must be taken into account if a mathematical model is to give an adequate representation of the behavior of an actual system. To do this we sketch a brief list of the types of electrostatic elements and interactions (conductors, dielectrics, compensated and uncompensated electrets, ferroelectrics, image forces, dielectrophoretic forces, etc.) and we use this list as background for discussing some electrostatic effects that may be important in the design or modelling of actuators. For some of these effects, applicable results are reported from experimental investigations carried out with a small (several hundred micron scale) electrostatically actuated device ("SCOFSS") built to study aspects of microelectromechanical design, and of control via electrostatic actuation.

1. INTRODUCTION

On macroscopic size scales, conveniently produced electric fields are much weaker than the magnetic fields in motors. On a size scale of microns, however, this is no longer true. Strong electric fields can be produced by low voltages, and are not limited by the 3×10^6 volt/m coronal discharge point of air. There are strong motivations for using such electrostatic fields as the basis for actuation in small devices. [For recent reviews of these motivations see e.g., Jacobsen, 1987, 1988; Lang, et al., 1987; Trimmer and Gabriel, 1987; and Fujita and Omodaka, 1987.] Not the least of these motivations is the example set by nature: muscular motion arises from electrostatic force, albeit via covalent bonding.

Work on microelectrostatic actuators, wherein a force or torque is transmitted out of the device, is well underway in a number of research groups, but we know of no device to date which can be considered useful. We believe that success will arrive in the next few years, but will require the development of new intuition and insights. Although a formal analogy can be drawn [Lang, et al., 1987; Layland, 1969] between magnetic and electric actuators, in practice most of the intuition of magnetic motors is inapplicable to electrostatic actuators.

Effective actuator design will require considerable effort in modelling and will lead to new intuition. The relationship of understanding to modelling is a two-way street; modelling leads to improved understanding, but the formulation of a model requires understanding for two quite distinct reasons: For one thing, considerable insight is needed to choose configurations that are plausible actuator candidates and that merit study. The second reason is more subtle: Any mathematical model is a simplified approximation of what exists and happens in the real world. If the model is to represent the real world with adequate accuracy, it must be formulated with some understanding of what is and what is not crucial in the interactions. As we shall explain presently, this question is a more difficult one in electrostatics than in magnetostatics.

The differences between electrostatics and magnetostatics can be divided, though not perfectly, into two categories: (i) materials, and (ii) field behavior. Clearly the brief nature of this article allows neither a broad nor a deep review of these subjects. We will be able to discuss only very superficially a number of issues. To reinforce the basic message of this paper, we shall also present several examples of material and conceptual issues for which the obvious answer, or the common knowledge, is wrong.

The discussion will be organized into categories based on the type of electrostatic element involved. In several instances we shall illustrate material and field phenomena with examples of our own laboratory work in electrostatics, especially with an electrostatically driven Small Cantilevered Optical Fiber Servo System (SCOFSS) described elsewhere [Wood, et al., 1987; Price, et al., 1987].

2. ELECTROSTATIC ELEMENTS

2.1 CONDUCTORS

2.1.1 *Conductors and Potentials*

A mathematically ideal conductor has enough mobile charge to shield its interior from electric fields. Electrodes, conducting elements set (by a voltage source) to a specified potential, behave in practice more-or-less in accord with simple idealized theory. A very basic and crucial difference between magnetic and electrostatic modelling is that the production of electric fields by electrodes is very different from the generation of magnetic fields, in which the sources of the field, either the currents or the magnetization of magnetic material, are specified. The electrostatic analogy of fixing the field in this manner would be the specification of electric charge distribution. (See the discussion below of electrets.) When electrodes are used, however, potentials, not charge distributions, are fixed. (Charge distributions on an electrode change, for instance, when a nearby charged armature moves; see the discussion below of image forces.)

This difference is fundamental to a basic design difficulty of electrostatic actuators. With magnetic sources, strong magnetic fields can be created over large regions of space. Consider, for example, a planar solenoid formed by two parallel sheets of oppositely directed current; as long as the sheets are large (compared to the separation between them), the field strength depends only on the surface current density (Amps/cm) in the sheets and not on their separation. Similarly, if electrostatic fields were produced with parallel sheets of fixed charge (parallel planar electrets, see below), the situation would be like that of magnetostatics; provided that the plates were large the field strength would not depend on separation, and the field, in principle, could be produced over a large region. However, for fields generated with electrodes, this is not true. Fixed voltages produce fields highly dependent on geometry. Strong fields require small gaps, and the general design principles of magnetostatics are inapplicable.

TH0215-4/88/0000-0131

The specification of fields via voltages can also give rise to somewhat surprising effects and to errors in models and intuition. Figure 2 shows a simplified description of the SCOFSS apparatus (see Fig. 1) used to study electrostatic actuation. A relatively long (5 cm) and narrow (140 micron diameter) quartz optical fiber is "permanently" negatively charged with implanted electrons. This fiber moves under the influence of the electric fields produced by the conducting strips, of width $2d$, on a silicon substrate, to which the fiber is parallel.

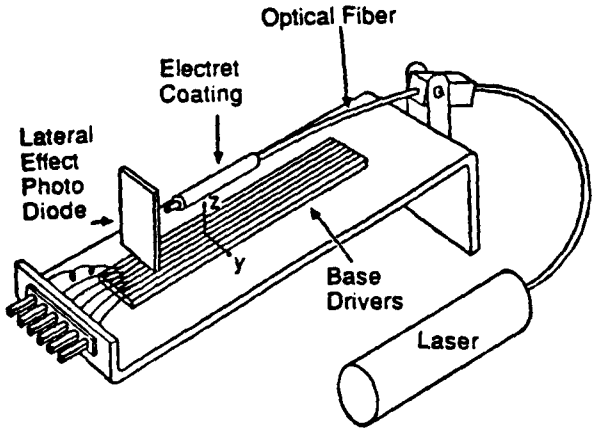

Fig. 1. Schematic of SCOFSS system, with laser source, cantilevered fiber-optic beam (with electret region), lateral-effect photodiode for measuring beam position, and voltage-controlled driver plates.

If the strips were nonconducting, and if positive charge were implanted in strips B and D, with the other strips left uncharged, it is clear that at any fiber height h the effect of the strips would be to attract the fiber. Suppose now that the strips are electrodes, that A, C, E are grounded and that B and D are set to a positive potential. This would induce positive charge on B and D, and would seem to create a field, at least qualitatively the same as that in the example of nonconductive strips. In fact the field produced is quite different; at large heights the field is attractive, as expected, but at small heights, over the center of strip C, the field is repulsive. It turns out that for B and D positive, negative charge is induced in strip C so that the electric field vectors point upward near the surface of C. At a height of $d\sqrt{3}$ above the center of C there is no force due to the imposed voltage. (We have in fact used this no-force condition as a technique for calibrating fiber heights.) This example underscores the fact that by setting the potentials rather than the charges, we are removed by an intuitive step from the sources of the field. Consequently, the charge distributions (which typically get concentrated at corners and edges) do not usually turn out to be what we want them to be for actuation.

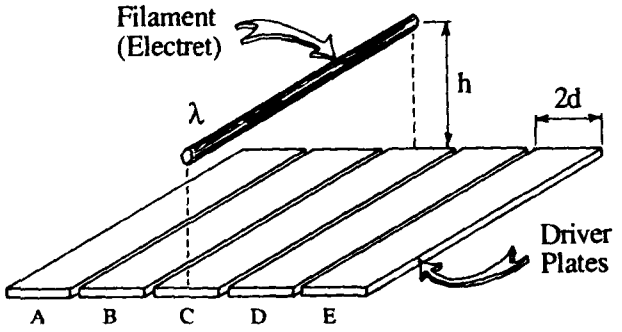

Fig. 2. Fixed-charge filament (electret) interacting with a set of five driver plates.

Conductors with no connection to external reference voltages are said to be floating. If, for example, strip C in Fig.2 had no wire connection, it would be floating and its potential would, in principle, be determined by initial conditions, presumably the condition that the net charge is originally and always zero. The laboratory reality is very different. The floating conductor is capacitively coupled to its environment, and in the real, imperfect, world it is also resistively coupled. The resulting RC time constant is rarely more than one second (see the discussion, below, of insulators) and the conductor therefore will float only for this time before coming to an equilibrium determined by its resistive coupling to the elements of its environment (the other strips, the substrate, etc.). Strip C in Fig. 2, for example, will within several seconds come to a voltage close to that imposed on B and D, but somewhat lower since C is also coupled to low voltage elements in the environment.

When sources (currents and magnetization for magnetostatics, charge density for electrostatics) are specified, there is no ambiguity about the meaning of the source. On the other hand, when a field is created by 10 volts being applied to a conductor, there can be considerable confusion lurking in the question "10 volts with respect to what?" This is especially true because in electrostatics, unlike magnetostatics, we can have monopolar sources. In three-dimensions this does not usually cause a problem since, in practice, it is understood that voltages are specified with respect to spatial infinity. This is no longer the case when (as in SCOFSS) the configuration is very long compared to its transverse dimensions, and can be approximated as two dimensional. For a two-dimensional source with a nonzero monopole, there is an infinite potential difference between spatial infinity and the source of the field.

An example of the confusion that this can cause is the configuration shown in Fig. 3: two long circular cross section wires, of radius a, length L, and separation s. For $L >> s$ the electrostatic configuration can be idealized as two-dimensional. If one wire is charged to voltage V_0 and the other to $-V_0$, it is straightforward to compute the (opposite) charge per unit length induced on the two wires and the force of attraction, per unit length, between them. The well-known result [Jackson, 1975; Prob. 1.7] is

$$\text{force/length} = \frac{1}{2s}\left(\frac{V_0}{\ln(s/a)}\right)^2 . \qquad (1)$$

(This assumes s>>a. The more general answer, without this constraint, can also be given in closed form in terms of elementary functions, but is less instructive here [Jackson, 1975; Prob. 2.4; Price and Phillips, 1988].) This problem which has no source monopole, has no ambiguities. Contrast this with the case that both wires are at $+V_0$. A valid *mathematical* solution of this problem is simply that the potential is V_0 everywhere, but this solution is clearly inappropriate since it predicts no electric fields, and therefore no induced charge and no forces between the wires. Physical intuition dictates that if both wires are charged to $+V_0$ they will repel each other. Yet there seems no mathematical alternative, since the only elements in this electrostatic configuration are the two wires (both at potential V_0) and infinity which must either be at V_0 (the inappropriate solution) or at infinite potential (physically acceptable, but of no help in resolving the question of the charges and forces).

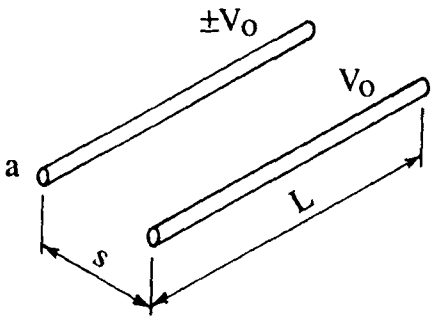

Fig. 3. Interacting conductive rods at potentials $\pm V_0$.

It is amusing how such a simple configuration is so paradoxical, and it is instructive how unexpected is the resolution: Except for the equal potential case, the configuration in Fig. 3 is incompletely defined by the geometry and the wire voltages. The force between the wires is determined by the distance d to the nearest large external conductor and the potential difference between V_0 and that conductor. If V_0 is the difference between the external potential and the common potential of the two wires, the force per unit length is [Price and Phillips, 1988]

$$\text{force/length} = \frac{1}{2s}\left(\frac{V_0}{\ln(s/a) + 2\ln(d/s)}\right)^2 . \qquad (2)$$

The fact that the force depends on passive elements in the environment underscores how unintuitive electrostatics can be. It should be noted that no similar surprise can arise in magnetostatics. When we have isolated the important elements of a magnetic configuration, distant passive elements cannot enter in this subtle way.

Our work in measuring field strengths generated by the SCOFSS electrodes required these insights. For the 200 micron wide by 2 cm long electrodes, our measurements of the potential field in the neighborhood of the electrodes were in good agreement with simple two-dimensional theoretical predictions, only out to about 500 microns. At larger distances the influence of environment (the location and potentials of the mounting hardware, etc.) became significant.

2.1.2 *Conductors and Image Forces*

For the understanding of and design of electromechanical actuators, sensors, etc., it is crucial to understand a phenomenon that is present whenever charges and conductors are present, the phenomenon of image forces.

If, say, a positive charged particle is moved to a location at a distance h above a grounded conductor, negative charge will be induced on the conductor (in order for it to remain at ground) and the negative charge will be concentrated in that position on the conductor closest to the positive charge. If the conductor is an infinite plane (in practice, if its edges are at distances $>> h$) the fields generated by the charge arrangement induced on the plane are exactly the same as the field due to a mirror *image* negative charge located a distance h below the plane. This shows, in particular, that the charged particle will be attracted to the plane with a force that varies as $1/h^2$. If the grounded conductor is spherical, the effects of induced charge can again be represented with an image charge, although with slightly more complexity. For more generally shaped grounded conductors we use the expression "image force" somewhat loosely to describe the attraction of a charged body to the conductor, though the force of attraction cannot always be represented with a simple finite set of fictitious charges.

Image forces are crucial to electrostatic design for a number of reasons, and they have no real analog in magnetostatics. One reason for their importance is that they are unavoidable; any source of field (fixed charge, electrode, etc.) external to a conductor is attracted to the conductor by image forces. In the SCOFSS configuration pictured in Fig. 1, for example, the charged fiber is attracted to the plane of the conducting strips with a force (proportional to the square of the fiber charge) that is independent of the applied voltages. The reason that image forces are particularly of concern in microelectromechanical design is that as distances decrease image forces increase more quickly than controllable forces (e.g., the force of an electrode on an electreted armature) and can overwhelm the controllable forces. Furthermore, relative surface roughness is likely to be a problem in microelectromechanical design. A gap between electrically active elements of 1 or 2 microns may have large fractional variability. If the gap is modelled as constant, it is unlikely that the model will give results in good agreement with reality. Applied fields may perhaps be treated adequately by an approximation of constant average gap, but not image forces. Not only are they strongly distance-dependent, and formally infinite at zero gap, but they are also destabilizing. At small distances the strong image forces act to make the distances smaller yet, and thereby to create a positive feedback loop which ends with surfaces sticking, conductors shorting out, etc.

2.2 DIELECTRICS

2.2.1 *Dielectrics and Polarization*

There is an important difference in material properties for magnetostatics and electrostatics, that can easily be overlooked in modelling. Some materials (due to collective phenomena) have enormously strong magnetic effects; ferromagnetic materials have a small-field incremental, (relative) permeability μ typically in the range $10\text{-}10^4$. Most materials, however, are paramagnetic or diamagnetic, have values of $|\mu - 1|$ smaller than 10^{-2} [Jackson, 1975, Sect. I.4] and, as a good approximation, can be considered to be impermeable, i.e., to be magnetically inert. In modelling magnetic configurations, therefore, it is usually straightforward to recognize which elements must be included as part of the active model, and which elements serve other (structural, etc.) functions. By contrast there is no solid material (of ordinary density) which is electrostatically inert. Molecules have fairly high electrical (as opposed to magnetic) polarizability, and no solid material has a low-frequency relative dielectric constant ϵ less than 2 (the value for Teflon®). Materials used in microfabrication typically have values larger than 2 ($\epsilon = 3.8$ for SiO_2) or much larger ($\epsilon = 27$ for Ta_2O_5). Dielectric materials, even with a dielectric constant as small as 2, have profound effects on external electrical fields. A simple example of this is the interaction of a charged particle with a planar face of a large (compared to the distance to the particle) dielectric. The presence of the particle induces a distribution of polarization in the dielectric which in turn generates a field external to the dielectric. It turns out that the external field thus produced can be represented with an image charge at the same location as if the dielectric were a conductor, but with charge reduced in magnitude by the reduction factor $(\epsilon\text{-}1)/(\epsilon+1)$.

The form of this reduction factor is somewhat specific to the planar geometry, but the nature of the result is general: A dielectric acts qualitatively in the same manner as an uncharged, floating, conductor, but with an effect smaller by a reduction factor. This reduction factor goes to unity in the limit $\epsilon \to \infty$ (the dielectric effectively becomes a conductor); the reduction factor vanishes when $\epsilon \to 1$ (the vacuum limit). The implication of this general behavior is that even for a material with $\epsilon = 2$, the effect on the field due to a dielectric structure is (assuming the planar reduction factor) one third of the effect that a geometrically identical floating conductor would have, and thus this effect cannot be ignored in modelling.

2.2.2 *Dielectrophoretic Forces*

Because dielectrics, at least as idealized here, cannot be electrically charged, the forces on dielectrics differ somewhat in their nature from those on charged materials, or charged conductors. There is no force directly caused by an external electric field. Rather, the electric field induces a polarization in the dielectric (the generalization of image charge) and makes the dielectric element, in effect, an electrical dipole $\mathbf{p}$. Because the energy of interaction is $-\mathbf{p}\cdot\mathbf{E}$, the dipole (i.e., the dielectric material) is drawn to regions of stronger $\mathbf{E}$ field strength. (For exceptions to this see, e.g., Epstein, 1965.) The dielectric material therefore couples not to the $\mathbf{E}$ field, but to the gradient of the $\mathbf{E}$ field with what is called the "dielectrophoretic" (DEP) force. Dielectrophoretic forces can be nonnegligibly strong, and their existence has consequences for modelling. We would like to be able to think of simple charged particles and (as in the case of SCOFSS) fibers, but chargeable materials (in fact all nonconductive materials) are dielectric, and experience DEP forces. These forces may overwhelm the direct E-field-to-charge coupling and produce motions totally different from those predicted by a model which does not include DEP effects. As a rule of thumb the condition for DEP forces to be negligible compared to E-field-to-charge coupling is

$$\left(\frac{\epsilon\text{-}1}{\epsilon+2}\right)\frac{E\ vol}{Q\ d} << 1 , \qquad (3)$$

where "vol" is the volume of the charged particle, Q is its charge, E is the electric field due to external sources, and d is the characteristic length scale on which E changes. If the particle charge is proportional to its volume, this relation suggests that DEP forces increase in importance as actuator size decreases.

2.3 INSULATORS

In simple models of electrostatic configurations, elements appear which are electrically insulated from each other. But in reality perfect insulation is impossible. As pointed out above in connection with conductors, this means that a floating conductive element will have constant charge only for a time small compared to its RC time constant, where C is the typical capacitance between the element and other elements and R is the characteristic resistance through which the element is connected to other elements. Capacitance scales as the first power of length, so that for microchip sizes capacitive coupling will be quite small. The SCOFSS electrodes, for example, are macroscopic (2 cm) in one dimension, but even for these the capacitance is no more than 1-10 picofarads. For a configuration which is micro sized (say 10 microns) in three dimensions, the capacitance will be a small fraction of a picofarad.

These small capacitances mean that even with the highest resistivity materials, fields will not be "static" for indefinite periods. In practice, careful design is needed to achieve RC constants of more than a few seconds. A consequence of this is that truly "static" fields can be produced only by electrodes, not by isolated sources.

Models of actuators which use other elements (floating conductors, dielectrics, etc.) will be valid only if they are meant to operate at frequencies (e.g., commutation rates) well above the reciprocal of the relevant RC constant. For the high resistance considerations of microelectromechanical devices the question of resistivity is a difficult one, involving properties almost impossible to model. The resistivity of a high-resistivity material such as Teflon® depends so strongly on ambient humidity, surface contamination, how the material has been handled, etc. that characterizing resistance with a simple single number, such as $10^{19}\Omega$-cm, is a convenient, but misleading fiction.

The very concept of resistivity -- a linear relationship between electric field and current density, based on a diffusive picture of current flow -- is often inappropriate. At sufficiently high field strength the relationship will be decidedly nonlinear. This is most familiar when it is catastrophic and results in breakdown, arc discharge, etc. In microelectromechanical devices coronal discharge in air is an obvious problem. It has been pointed out by several authors [Lang, et al, 1987; Fujita and Omodaka 1987] that the breakdown strength (e.g., 3×10^6 volt/m for air) characterizing macroscopic lengthscales does not apply to the gaps in microelectromechanical devices, since the avalanche phenomenon responsible for coronal discharge is suppressed by the small (< 10 micron) lengthscales [see von Hippel, 1954]. Air breakdown can be avoided, of course, simply by evacuating all strong field regions in a device. In this case, however, breakdown will occur in a different form: as field emission from the surface of the material, typically at electric field strengths of 10^8-10^9 volts/m. At very small lengthscales still other physical effects enter; in particular, electron wavefunction overlap and tunneling, as in an STM.)

One of the applications of the modelling of actuators is a study of the onset of dielectric breakdown, coronal discharge, field emission, etc. From computations of electric field strengths, predictions can be made whether or where breakdown will occur. Designs can be refined to control breakdown, e.g., by eliminating sharp edges of conductors. The common wisdom is that the electric field strength on a conductor is greatest at the point of greatest curvature. This is a useful rule of thumb, but is in no sense strictly valid [Price and Crowley, 1985]. Surface curvature is an easily computed local quantity whereas electric field strength is nonlocal; it requires a global solution of the electrostatic problem, and is much more difficult to determine, requiring mathematical modelling and, typically, finite element solutions.

It should be noted that the design and modelling difficulties posed by finite resistivity have no analog in standard magnetic devices. While the source (charge) of the electrostatic field can drift through materials of finite resistance, the sources of magnetic fields (currents confined to wires; magnetization in permanent magnets) do not.

2.4 ELECTRETS AND FERROELECTRICS

Charge can be fixed, to some extent, on any nonconducting solid, but there are certain materials in which the charge density that can be achieved is high, and for which the process of charge implantation is relatively controllable. Such materials (typically polymers, e.g., Teflon®, polycarbonate, polyimide, etc.), when charged with electrons, through the use of a scanning electron microscope, a coronal discharge arc, the wet electrode apparatus, etc., are called electrets [Sessler, 1982], and are of considerable interest for microelectromechanical design both because they need no wire connections, and because they hold the promise of high field strengths without small electrode gaps. Especially interesting is the possibility of implanting high spatial resolution charge patterns on electret materials, thereby creating an easily fabricated structure with high field gradients.

A distinction must be made between two types of electrets: compensated and uncompensated. A compensated electret is a sheet of electretable polymer with a metalized coating on one side. During the charging process this metal layer is grounded so that it acquires a positive surface charge density equal in magnitude to that of the negative charge implanted in the polymer. The resulting two-layer sandwich is equivalent to a dipole sheet. Compensated electrets are relatively well studied, have commercial applications (electret microphones, etc.) and are reasonably stable. Because of their dipole structure, however, they are less interesting as armatures or field generators in actuators than are uncompensated electrets.

Relatively little work has been done with uncompensated electrets. In our own work we have been able to achieve surface charge densities of 10 nanocoulombs/cm^2 in Teflon®. This is equivalent to a field of order 10^6 volts/m and it seems clear that air breakdown, along with other means of charge motion and compensation, is involved in limiting the surface field strength [Roos, 1969].

Our own experimental studies with electrets have focussed on high spatial resolution charge density patterns. We found effects suggestive of transient surface conductivity, and of the influence of the dielectric properties of the electreted polymer. At this point we can only be sure that there are physical processes going on which are not part of any simple model of charge trapping in polymers. Certainly an improved understanding of the nature of electrets (especially high spatial resolution, uncompensated electrets) is needed before their fabrication becomes predictable via design tools.

Unlike an electret, a ferroelectric material cannot hold a significant amount of implanted charge. But due to its crystal structure (typically that of perovskite) it can take on a quasipermanent electrical polarization. A ferroelectric is the electrical analog of a permanent magnet. Like a permanent magnet it can have no monopole, but the strength of its dipole field can be imposing. For lithium niobate at saturation polarization, the fields are equivalent to those produced by a surface charge density of 3×10^5 nanocoulombs/cm^2. This is equivalent to a Maxwell pressure of 10^8 psi. The forces that would be produced by such fields in a micromechanical setting are amusing. If a 70 micron radius fiber of lithium niobate were polarized perpendicular to the fiber axis, and placed with the axis 100 microns from a metal plane, the image force of attraction would be 10 tons per centimeter of fiber.

No such forces, or *any* forces, are observed in working with ferroelectrics, but this can be ascribed to the fact that metal electrodes are usually deposited on opposite faces of ferroelectrics during the poling process, and these electrodes, like the metallic layer in a compensated electret, acquire charge so that the external field of the ferroelectric-electrode system vanishes. But ferroelectrics can be poled without attached electrodes. In such a case will enormous forces be produced? Again, too simple a model does not take into account the reality of materials. The extraordinary fields predicted for a saturated ferroelectric would breakdown air and arc from one poled face to the opposite. In vacuum, surface currents or field emission would quickly reduce the external fields. So fields corresponding to surface charge densities of 3×10^5 are impossible, but some uncanceled external field can be maintained. The possibility cannot be ruled out that such a field is usefully strong.

3. CONCLUSIONS

We have reviewed the basic elements of electrostatic devices (conductors, dielectrics, insulators, electrets and ferroelectrics) and have shown that the modelling of electrostatic forces is a very different, and in many ways a more difficult, undertaking than the modelling of magnetic interactions; the difference between the "real-world" behavior of electrostatic configurations and "textbook" models is much greater than for magnetic configurations. Models must take into account the realities of materials, in particular the fact that resistivity is never infinite, and that any structural part of an actuator will affect fields through its dielectric properties. We have seen that in this sense (the behavior of materials) as well as in the most basic conceptual viewpoint (fields determined by potentials rather than by direct sources) electrostatics and magnetostatics are at opposite poles. It would seem that much new understanding is needed for, and will emerge from, the modelling of electrostatic devices that will be carried out in the next few years.

ACKNOWLEDGMENTS

This work was supported by grants from the System Development Foundation and from the Defense Advanced Research Projects Agency.

REFERENCES

Epstein, L. (1965): "Electrostatic Suspension," Am. J. Phys. 33(5):406-407.

Fujita, H. and Omodaka, A. (1987): "Electrostatic Actuators for Micromechatronics," IEEE Micro Robots and Teleoperators Workshop, Hyannis, MA, Nov. 9-11.

Jackson, J.D. (1975): *Classical Electrodynamics*. Wiley, New York.

Jacobsen, S.C. (1987): "Electric Field Machine," U.S. Patent No. 4,642,504, February 10.

Jacobsen, S.C. (1988): "Electric Field Machine," U.S. Patent No. 4,736,127, April 5.

Lang, J.H., Schlecht, M.F. and Howe, R.T. (1987): "Electric Micromotors: Electromechanical Characteristics," IEEE Micro Robots and Teleoperators Workshop, Hyannis, MA, November 9-11.

Layland, M.W. (1969): "Generalized Electrostatic Machine Theory," IEE Proceedings, 116:403-405.

Price, R.H., Jacobsen, S.C. and Khanwilkar, P.S. (1987): "Oscillatory Stabilization of Micromechanical Systems," IEEE Micro Robots and Teleoperators Workshop, Hyannis, MA, November 9-11.

Price, R.H. and Phillips, R.P. (1988): "The Force between Two Charged Wires." Paper in preparation. Note that eq.(2) assumes $d < L$.

Price, R.H. and Crowley, R.J. (1985): "The Lightning-Rod Fallacy," Am. J. Phys. 53(9):843-848.

Roos, J. (1969): "Electrets, Semipermanently Charged Capacitors," J. Appl. Phys. 40(8):3135-3139.

Sessler, G.M. (1982): "Polymeric Electrets," Chap. 6 in *Electrical Properties of Polymers*, Ed. D.A. Seanor, Academic Press, New York.

Trimmer, W.S.N. and Gabriel, K.J. (1987): "Design Considerations for a Practical Electrostatic Micro-Motor," Sensors and Actuators, 11(2):189-206.

von Hippel, A.R. (1954): *Dielectrics and Waves*. J. Wiley, New York.

Wood, J.E., Jacobsen, S.C. and Grace, K.W. (1987): "SCOFSS: a Small Cantilevered Fiber Optic Servo System," IEEE Micro Robots and Teleoperators Workshop, Hyannis, MA, November 9-11.

A CONSTANT FLOW-RATE MICROVALVE ACTUATOR BASED ON SILICON AND MICROMACHINING TECHNOLOGY

Sekwang Park, Wen H. Ko and Joseph M. Prahl
Electronics Design Center
Case Western Reserve University
10900 Euclid Avenue, Cleveland, OH 44106

ABSTRACT

Microactuators play an important role in many diverse areas, especially microrobotics and biomedical applications, where small size and low power consumption are paramount. In patients with hydrocephalus, the imbalance between the production and absorption of cerebrospinal fluid (CSF) can produce abnormally high intracranial pressures. A shunt is used to drain the CSF to the abdominal cavity. However, an overdrainage often occurs when the patient stands up from a lying down position. Furthermore the desired flow rate may change with time. An adjustable device to control the minute flow of this fluid, insensitive to the pressure drop across the microvalve, is critical to the management of hydrocephalic patients. This paper outlines the analysis and development of a clinically useful microvalve using silicon and solid state micromachining technology to meet the needs of the hydrocephalus patients.

I. THEORETICAL ANALYSIS

The flow in this minute passage is modeled as the flow of a viscous fluid (low Reynolds number flow) and the diaphragm deflection is modeled as the deflection of an elastic membrane clamped on both sides of the passage.

The notations used in this paper are followings:

L : Channel length	Y(x,z): Local channel height
Y_o : Channel height	Y_1 : Diaphragm deflection
W : Channel width	P_1 : Inlet pressure
P_2 : Outlet pressure	t : Thickness of diaphragm
Q : Flow rate	ρ : Density of fluid
D_{in} : Diameter of inlet	μ : Viscosity of fluid
ν : Poisson's ratio	E : Elastic Modulus

u : x-directional fluid velocity
v : y-directional fluid velocity
w : z-directional fluid velocity
D : Flexural rigidity of a diaphragm

I-1. Continuity and Momentum Equations

For steady, two dimensional flow of a fluid (z-directional fluid velocity is negligible.) of constant viscosity and density, the continuity and momentum equations are, [1]

$$\frac{\partial u}{\partial x} + \frac{\partial v}{\partial y} = 0 \qquad ---(1)$$

$$\rho\left(u\frac{\partial u}{\partial x} + v\frac{\partial u}{\partial y}\right) = -\frac{\partial P'}{\partial x} + \mu\left(\frac{\partial^2 u}{\partial x^2} + \frac{\partial^2 u}{\partial y^2}\right) \qquad ---(2)$$

$$\rho\left(u\frac{\partial v}{\partial x} + v\frac{\partial v}{\partial y}\right) = -\frac{\partial P'}{\partial y} + \mu\left(\frac{\partial^2 v}{\partial x^2} + \frac{\partial^2 v}{\partial y^2}\right) \qquad ---(3)$$

where $P' = P + \rho gy$

For low Reynolds number flow and $L > W >> Y_o$, the momentum equations become

$$\mu\frac{\partial^2 u}{\partial y^2} = \frac{\partial P'}{\partial x} = \frac{\partial P}{\partial x} \qquad ---(4)$$

$$\frac{\partial P'}{\partial y} = 0 \qquad ---(5)$$

where $P' = P + \rho gy$.

Integrating Equation (4) successively with respect to y,

$$u(x,y) = \frac{y^2}{2\mu}\frac{dP(x)}{dx} + C_1 y + C_2 \qquad -----(6)$$

I-2. Thin Diaphragm Deflection (t << W < L)

As seen in Figure 2, $Y(x,z) = Y_o - Y_1(x,z)$, where $Y_1(x,z)$ is a diaphragm deflection under the pressure P_1-P(x). The deflection of a rectangular thin diaphragm with clamped edges under pressure P_1-P(x) is given by Equation (7). [2,3,4]

$$\frac{\partial^4 Y_1}{\partial x^4} + 2\frac{\partial^4 Y_1}{\partial x^2\,\partial z^2} + \frac{\partial^4 Y_1}{\partial z^4} = \frac{P_1 - P(x)}{D} \qquad ---(7)$$

with boundary conditions

$Y_1 = 0$ for $x = 0, L$ $\qquad$ $Y_1 = 0$ for $z = 0, W$ ---(8)

$\frac{\partial Y_1}{\partial x} = 0$ for $x = 0, L$ $\qquad$ $\frac{\partial Y_1}{\partial z} = 0$ for $z = 0, W$ ---(9)

The solution to Equation (7) is coupled to the solution of the viscous flow equation. However, under the assumption of $L > W$, Equation (7) can be approximated as Equation (10).

$$\frac{\partial^4 Y_1}{\partial z^4} = \frac{P_1 - P(x)}{D} \qquad ----- (10)$$

with boundary conditions

$Y_1 = 0$ for $z = 0, W$ $\qquad$ $\frac{\partial Y_1}{\partial z} = 0$ for $z = 0, W$ ---(11)

$$Y_1(x,z) = \frac{P_1 - P(x)}{24\,D} W^4\left(\frac{z}{W}\right)^2\left[\left(\frac{z}{W}\right) - 1\right]^2 \qquad ---(12)$$

I-3 Differential Equation of the Flow-Rate (Q)

The coefficients C1 and C2 of Equation (6) are determined from the boundary conditions, u=0 at y=0 and u=0 at y=Y(x,z) (no slip at the walls).

$$u(x,y) = \frac{1}{2\mu}\left(-\frac{dP(x)}{dx}\right) Y^2(x,z)\,\frac{y}{Y(x,z)}\left(1 - \frac{y}{Y(x,z)}\right) \qquad ---(13)$$

with the boundary conditions, $P(0) = P_1$, $P(L) = P_2$

and $Q = \int_0^W \int_0^{Y(x,z)} u(x,y)\,dy\,dz = \text{CONSTANT}$

$$Q = \int_0^W \int_0^{Y(x,z)} u(x,y)\,dy\,dz \qquad -----(14)$$

$$= \int_0^1 \frac{W}{12\mu}\left(-\frac{dP(x)}{dx}\right) Y^3(x,z)\,d\left(\frac{z}{W}\right) \qquad ----(15)$$

For normalization of the above equations,

$$\text{let } x' \equiv \frac{x}{L}, \quad z' \equiv \frac{z}{W}, \quad p(x) \equiv \frac{P_1 - P(x)}{P_1 - P(x)}$$

$$Q = \frac{W}{12\mu L}\frac{dp(x)}{dx}(P_1-P_2)Y_o^3\int_0^1\left[1-Ap(x)(z^4-2z^3+z^2)\right]^3 dz \qquad ----(16)$$

$$\text{where } A \equiv \frac{(P_1-P_2)\,W^4}{24\,Y_o\,D} = \frac{(P_1-P_2)W^4(1-\nu^2)}{2\,Y_o\,E\,t^3} \qquad ----(17)$$

A represents a nondimensional pressure difference applied to the microvalve scaled by the stiffness of the diaphragm.

Let the integration of Equation (16) $F(A,x,p)$.

$$F(A,x,p) \equiv \int_0^1 [1- A\,p(x)(z^4-2z^3+z^2)]^3\,dz$$

$$= 2\int_0^C [1- A\,p(x)z^2(2C - z)^2]^3 \qquad ----(18)$$

$C = 0.5$ for $C_1 \geq 0.5$

$C = C_1$ for $0 < C_1 < 0.5$ and $C_1 \equiv \left\{\frac{1}{Ap(x)}\right\}^{1/4}$

C_1 varies with the position of channel.

Thus the differential equation of flow-rate is

$$\frac{dp(x)}{dx} = \frac{12\,Q\,\mu\,L}{(P_1-P_2)Y_o^3\,W}\frac{1}{F(A,x,p)} = \frac{B}{F(A,x,p)} \qquad ---(19)$$

with boundary conditions of

$$p(0)=0, \quad p(1)=1 \qquad -----(20)$$

$$\text{where } B \equiv \frac{12\,\mu\,L\,Q}{(P_1 - P_2)Y_o^3\,W} \qquad -----(21)$$

B is the non-dimensional flow rate scaled by the expected flow.

I-4. NUMERICAL RESULTS OF DIFFERENTIAL EQUATION

The solution of the first order differential Equation (19) should satisfy the boundary conditions given in Equation (20). Since B=1 at A=0 is the maximum value B can obtain, A begins from 0 and is increased to 100. For a given A, the differential Equation (19) can be solved by changing the values of B from 1 to 0. The relationship between A and B is shown in Figure 4, derived from a numerical solution using the 4th order Runge-Kutta method. [5,6] Since A is the pressure difference scaled by the stiffness of the diaphragm and B is a function of A (pressure), the product AB which has no pressure term is considered.

$$AB \equiv \frac{6(1-\nu^2)\,\mu\,L\,W^3\,Q}{Y_o^4\,E\,t^3} \qquad -----(22)$$

AB is the flow-rate scaled by the diaphragm flexibility. When A increases from 0 to 15, AB is in the linear region, making AB proportional to A. If A is greater than 15 , AB begins to saturate because the diaphragm touches the bottom base. Figure 5 shows the relationship between the nondimensional flow-rate (AB) and the nondimensional pressure (A).

II. FABRICATION (Figure 6)

Based on the theoretical analysis and design procedures, silicon has been chosen as a diaphragm material for this study because silicon has been known as a good elastic material and can make use of micromachining technology.

II-1 Top Layer

1. Initial Material : The process begins with a 2" diameter, 0.012" thick, p-type silicon wafer with (100) orientation. The resistivity of the wafer is 2-5 ohms-cm.
2. Standard Degrease
3. Standard Clean
4. Initial Thermal Oxide (7200 Å) , 1100 °C
5. Photostep (Window open for P^+ diffusion)
6. EPW Etching : PSE 300, 112 °C
7. Measurement of channel height (Y_o).
8. Standard Clean
9. P^+ Diffusion : 1100 °C, 4 hour,
10. Boron Glass Removal : Low temperature oxidation
11. Photostep : Hole drilling
12. Diamond drilling : 10 mil diameter,
13. Standard Degrease and Clean.
14. Reoxidation : For a EPW back-etching mask
15. Photostep (Open window for EPW etching)
16. Remove Oxide : BHF dipping for the edge part of wafer

II-2. Bottom Layer

Pyrex glass #7740 : 12 mil thick, 2" diameter
1. Photostep : Hole drilling
2. Diamond Drilling : 25 mil diameter
3. Standard Clean

II-3. Top and Bottom Layer Bonding

1. Electrostatic bonding [7,8] : Top layer of Silicon and #7740 Pyrex glass, 450 °C, 900 V
2. Diamond SAW cutting
3. EPW etching : PSE 300, 112 °C
4. Standard Degrease

II-4. Top Lid, Inlet and Outlet Tube Bonding

III. TEST RESULTS

The valves were fabricated using two different aspect ratios (L/W=2 and 4) of the diaphragm. To verify the control of the flow rate, each valve was designed and fabricated with a different value of Y_o and t. Each was tested with water at room temperature. Before measuring the pressure/flow each valve is flushed with water at a high pressure range (greater than 200 CM-H_2O) to make sure that there are no air bubbles in the water carrying tube. Each data point is the average value of three measurements and has a variation of within 10 %. The variation is mainly the result of measuring error (the balance and pressure gauge error) and the imperfect elastic properties of the thin silicon diaphragm. Test results shown in Figure 7 is the flow rate versus pressure characteristic curve. Nondimensional pressure (A) and nondimensional theoretical flow-rate (AB_t) are calculated from the pressure and flow-rate measurements.

IV. DISCUSSION

IV-1. Correction Coefficient (C)

As seen in Figure 7, these theoretical curves and experimental curves for aspect ratios of L/W=2 and L/W=4 agree favorably as expected. By multiplying a correcting coefficient which is based on a semi-empirical method, the theoretical curves for the valve can be modified. The errors are thought to come from an incorrect estimation of Young's Modulus, a non-uniform thickness of the diaphragm and the simplified diaphragm deflection Equation. Considering these errors the range of correction coefficient (C) is between 0.45 ~ 0.55 for L/W=2 and 0.8 ~ 0.9 for L/W=4. It is considered that a flow-rate can be controlled by changing the inlet hole size, but if it is too small, a pressure drop will occur across the inlet hole. It is also considered that as the outlet hole position is moved away from the edges of the valve, the flow rate will be cut down for the higher ranges of pressure and can flat down the slope of curve.

IV-2. Valve and Field-Effect Transistor Analogy

There is a qualitative analogy between the operational principle of the microvalve and that of a Field-Effect Transitor (FET) even though the flow rate is not perfectly constant independent of a pressure as in a FET. Pressure and flow rate in the hydraulic system have an analogy with voltage and current in electrical system.

$$Q = \frac{B\, Y_o^3\, W}{12\, \mu\, L}\, \Delta P = G_m\, \Delta P \qquad \text{-----(23)}$$

where $G_m \equiv \frac{B\, Y_o^3\, W}{12\, \mu\, L}$ is the conductance of the microvalve. As ΔP increases, B decreases as can be seen in the A and B relationship curve (Figure 4). In other words, a conductance of the microvalve changes according to ΔP. The coductance term G_o in the FET is not exactly analogous to B of the microvalve, but B can be compared to the other terms which varies according to V_G and V_D.

V. CONCLUSION

Computer modeling and prototype testing of a nearly constant flow-rate microvalve which requires no power consumption to maintain the flow-rate has been presented. The parameters of the valve have been obtained by mathematical models with correction factors from the experimental trials. These parameters allow for general design guidelines for a rectangular, thin diaphragm microvalve.
The important criteria for a given size (length and width) are :
1. Channel height (Y_o) --- the nondimensional flow rate (B) with this channel height must be between 0 and 0.2.
2. Diaphragm thickness (t) --- the nondimensional pressure (A) with this diaphragm thickness must be between 5 and 150.

To have the experimental data agree with the theoretical model, using the method of least squares, for the prototype rectangular silicon valve described in this paper the correction coefficient is 0.45 ~ 0.55 for a diphragm aspect ratio of L/W=2 and 0.8 ~ 0.9 for an aspect ratio of L/W=4. The correction factor accounts for the simplified diaphragm deflection equations, incorrect estimated elastic modulus of the diaphragm and variation in the diaphragm material thickness.

REFERENCES

[1] W.H. Li, S.H. Lam, Principles of Fluid Mechanics, Addison-Wesley Publishing Co, Inc., 1964

[2] S. Timoshenko and S. Woinowsky-Kreiger, Theory of Plates and shells, McGraw-Hill, New York, 1959

[3] I.A. Wojtaszak, "The Calculation of Maximum Deflection, Moment, and Shear for Uniformly Loaded Rectangular Plate with Clamped Edges", J. Appl. Mech., Vol 4, 1937

[4] S. P. Timoshenko, "Bending of Rectangular Plates with Clamped Edges", Proceedings of the Fifth International Congress for Applied Mechanics, 1939

[5] S. Conte, et. al, Elementary Numerical Analysis, McGraw-Hill Book Co., 1980

[6] Graham de Vahl Davis, Numerical Methods in Engineering & Science, Allen & Unwin, 1986

[7] Kurt E. Petersen, "Silicon as a Mechanical Material", Proceedings of the IEEE, Vol. 70, No. 5, May 1982

[8] T.A. Knecht, "Bonding Techniques for Solid State Presure Sensors", Transducers '87, pp 95-98, June 1987, The 4th International Conference on Solid-State Sensors and Actuators.

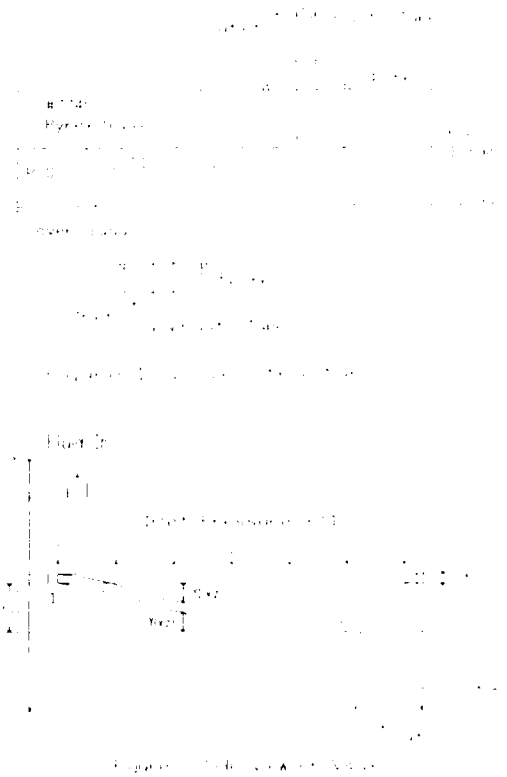

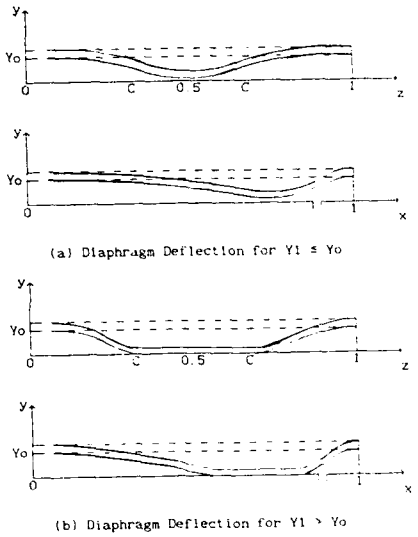

Figure 3. Diaphragm Deflection

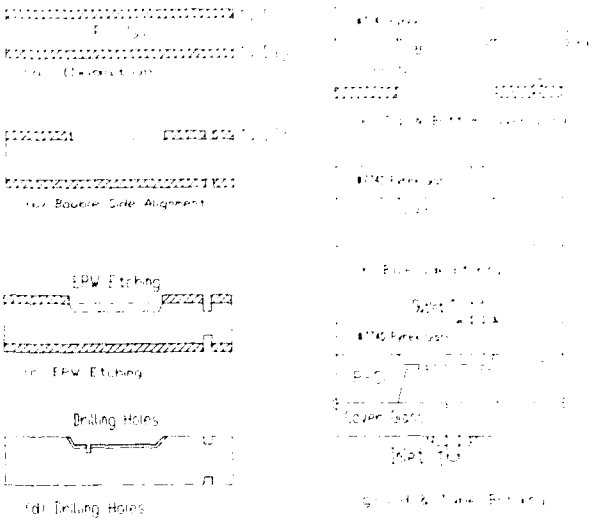

Figure 6 Fabrication Process

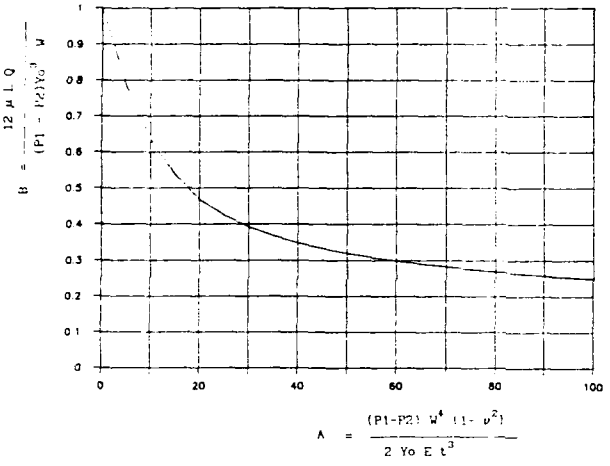

Figure 4 Relationship Between B and A

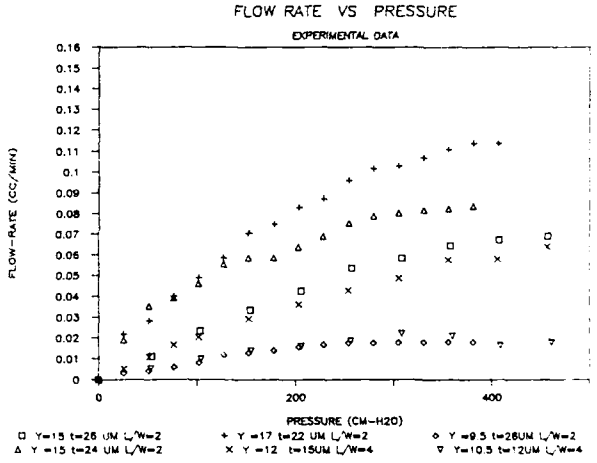

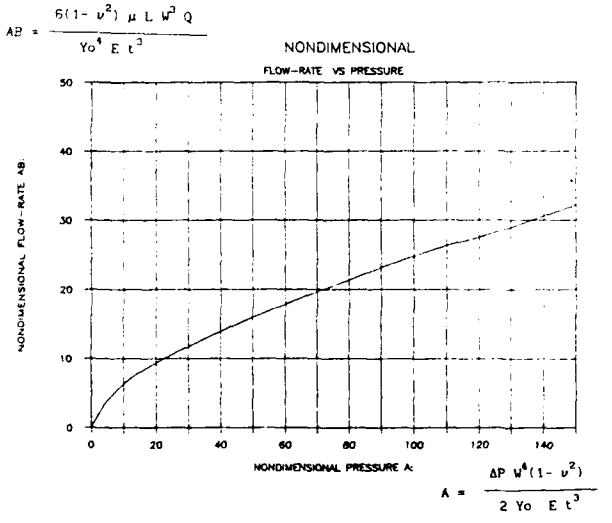

Figure 5 Nondimensional Flow Rate (AB) versus Pressure (A) (Theoretical Curve)

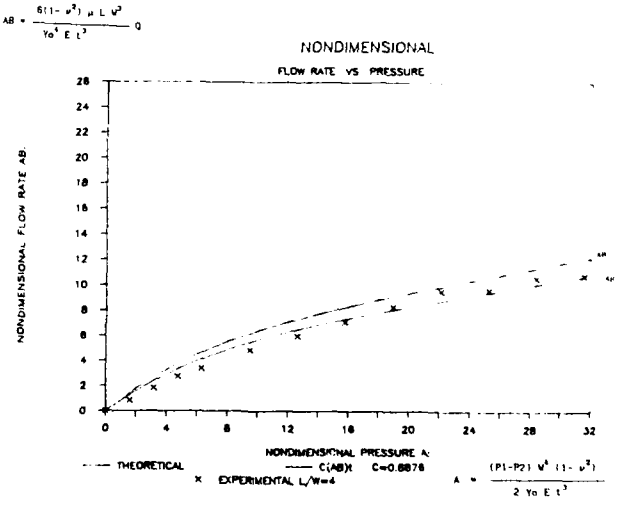

Figure 7. Flow-Rate vs. Presssure Curve

A NEW SILICON-ON-GLASS PROCESS FOR INTEGRATED SENSORS

L. J. Spangler and K. D. Wise

Center for Integrated Sensors and Circuits
Solid-State Electronics Laboratory
University of Michigan
Ann Arbor, Michigan 48109-2122

ABSTRACT

This paper reports a process for the formation of high-performance thin single-crystal silicon films on glass substrates. The process utilizes the electrostatic bonding of a silicon wafer to glass and subsequent etching of the silicon to form films having thicknesses controlled from less than 2 μm to over 20 μm. The use of Corning 1729 glass substrates yields an excellent thermal expansion match to the silicon film and allows the use of post-bond processing temperatures for the films of as high as 800°C, allowing the formation of both MOS and bipolar device structures. Thus, integrated circuitry can be incorporated in dissolved-wafer sensing structures. A variety of related processes are also possible where some or all of the silicon device processing is performed at high temperature before bonding to the glass.

INTRODUCTION

For many sensing applications, the use of a substrate which is electrically insulating, thermally insulating, or optically transparent is desirable. In most such applications, monolithic active circuitry is also useful with the transducer array to allow signal amplification, multiplexing, or package simplification. Recently, an ultraminiature silicon-on-glass capacitive pressure sensor was reported [1] for application in a biomedical catheter. This sensor was based on a simple four-mask single-sided bulk-silicon process featuring a batch wafer-to-glass electrostatic seal and subsequent unmasked wafer dissolution. The process reported here significantly extends that work by allowing the monolithic integration of high-performance circuitry in such dissolved wafer-processes. The process produces higher-quality silicon films than do recrystallized SOI processes [2] and has the added advantage of allowing the use of relatively thick silicon films which can be pre- and post-bond processed to produce structures not possible using other techniques. This approach appears very attractive for applications such as active-matrix LC displays, large-area tactile imagers, and ultra-miniature presure/flow sensors which require active readout electronics and/or distributed signal processing.

PROCESS DESCRIPTION

The overall process for creating the SOI film is shown in Fig. 1. The process begins with a <100>-oriented silicon wafer having an epitaxial layer in which the eventual devices will be created. A silicon etch-stop is realized at the epi-substrate junction using any of several techniques. Two approaches have been used in this research. In the first, a heavily-doped diffused boron buried layer is used between the epi film and a lightly-doped substrate. Epitaxial growth should be optimized here to minimize out-diffusion into the film and dislocations due to boron-induced stress in the buried layer. The second approach has utilized a heavily-doped (n- or p-type, > $10^{18}cm^{-3}$) substrate with an epitaxial layer of the desired thickness and resistivity grown directly on it. Such p/p+ "CMOS" wafers are widely available for use in CMOS VLSI. An electrochemical etch-stop at an n-p epi-substrate junction or an ion-implanted etch-stop might also be used.

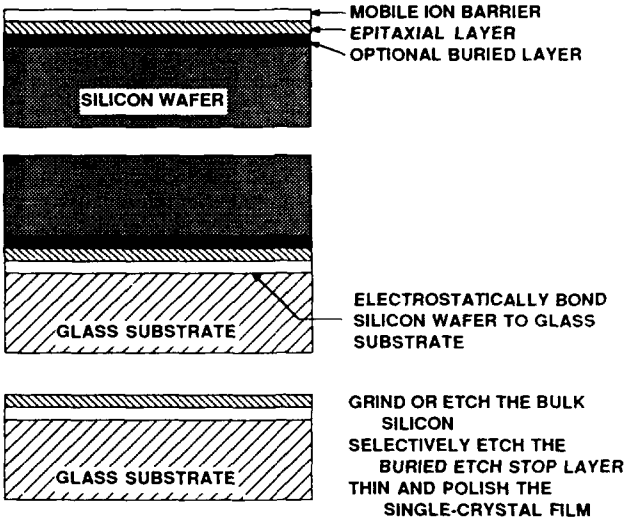

Fig. 1: Process Flow for Producing Single-Crystal Silicon Films on Glass.

After formation of the epitaxial layer and etch-stop, the silicon wafer is electrostatically bonded to a glass substrate. Both Corning 1729 and 7740 substrates have been used. Corning type 1729 glass offers a better match to the thermal expansion coefficient of silicon than do other glasses [3], including 7740, and its high anneal point (853°C) allows device fabrication after bonding. Figure 2 shows the time required to achieve a bonded area of approximately one square inch for various bonding voltages and glass thicknesses using a point contact for the potential on the glass. While the required voltage is generally higher for 1729 glass than for 7740, scaling the 1729 glass thickness shown to 0.5mm should reduce the voltage by nearly a factor of two,

0215-4/88/0000-0140

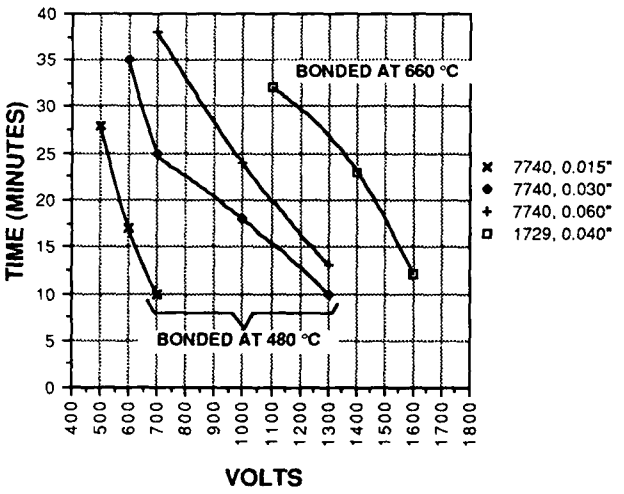

Fig. 2: Bonding Times and Voltages associated with forming a Bonded Area of One Square Inch for Various Glass Thicknesses.

placing it in a range similar to that for 7740. In alkali-containing glasses such as 7740, the mobile alkali cations drift toward the anode (silicon), causing an increased fraction of the applied potential to be dropped near the silicon-glass bonding interface and resulting in a lower bond voltage [2]. In a low-sodium glass such as 1729, the voltage distribution in the glass is thought to be more uniform, increasing the required potental but also allowing the voltage to scale more directly with thickness. While sodium thus plays an important role in determining the potential distribution in the bonding materials, it is not thought to otherwise contribute to the bond formation. Oxygen ions generated from defects in the glass, particularly E-centers, are thought to drift towards the anode, where they form an irreversible bond with the silicon [2]. Due to the high local forces generated by the electrostatic field, a bonded area coverage of over 99.8 percent on three-inch wafers has typically been observed.

As with 7740 electrostatic bonds, the 1729 silicon bond is stronger than the silicon itself, with fracture occurring in the bulk of the silicon wafer rather than at the interface. This supports the idea that oxygen from the glass acts as the bridging atom between the two bonding surfaces since the Si-O bond is about 2.5 times stronger than the Si-Si bond.

In device applications, a stress-compensated multilayer film of silicon dioxide, silicon nitride, and silicon dioxide [4] is deposited on the silicon surface via pyrolytic CVD prior to bonding to the glass. This film functions as a mobile ion barrier, preventing sodium migration into the silicon during subsequent device processing. Electrostatic bonds between dielectrically-coated silicon wafers and 1729 glass have typically been performed at 670°C, and subsequent heating to as much as 850°C has not noticeably altered the bond or its strength.

After bonding, the silicon wafer is subjected to an unmasked etch to the etch-stop. With a boron etch-stop, an EDP final etch [5] has been used, whereas with a heavily-doped substrate, an 8:3:1 acetic, nitric, hydrofluoric etch has been employed [6]. The EDP etch effectively reduces the etch rate to zero, while the 8:3:1 etch slows by a factor of at least 100 when encountering lightly-doped material, effectively yielding an etch-stop as well. In this work, these etching processes have allowed the formation of 75mm SOI wafers. The boron etch-stop has yielded slightly better silicon film thickness uniformity, while the "CMOS" substrates have yielded better epitaxial film quality. Figure 3 shows the contour plot for an SOI film formed using a 27 μm-thick epitaxial layer and the boron etch-stop process. The plot was derived from surface profilometry after preferentially removing the buried layer with a chemical etch. Over most of the wafer area, the film thickness is uniform to within five percent, and some of the variation noted is likely due to nonuniformity in the epi and buried-layer thicknesses themselves.

Following the removal of the silicon bulk, the remaining SOI film is polished and etched to remove the etch-stop layer (if present) and yield the final film. While this step contributes additional film nonuniformities (in our work, about ten percent of the etched thickness), the overall process is capable of producing final films which are uniform in thickness to within ten percent or better (e.g., ±0.5 μm on a 5 μm final film), which is adequate for most sensing applications.

X-ray diffraction measurements have shown these SOI films to be <100>-oriented and single-crystal, essentially identical to the starting substrates. Surface defect-sensitive etchants have indicated defect densities similar to those of the starting material as well. Hall measurements on 1.2-5μm-thick films produced using the boron etch-stop on 1729 glass with an ion barrier have produced n-type mobilities of 893 and p-type mobilities of 354 as compared with values of 1105 and 342 obtained in the bulk, respectively.

DEVICE STRUCTURES

A wide variety of device structures are possible with this process or variations of it. One of the principal advantages of this process over other SOI approaches is that high-temperature processing of the silicon is possible prior to bonding so that unique structures can be created using the ability to double-side process the film. Figure 4 shows an MOS structure realized using single-sided processing of the film. Both n- and p- channel MOSFETs have been realized having this structure. The n-channel devices resulted in electron surface mobilities of 640 cm^2/V-sec, the highest ever reported for an SOI transistor on glass [7]. The off-state drain leakage current was less than 0.1pA/μm. The upper limit of 800°C on post-bond processing temperature allows relatively standard gate oxidation processes to be used as well as the activation of ion-implanted dopants.

Figure 5 shows a bipolar transistor structure realized using double-sided film processing. A high-temperature diffusion was used prior to bonding to form a highly doped n^+ layer next to the ion barrier. Standard processing was then used to form the film, after which the p-type base was implanted using boron and a polysilicon emitter was formed using CVD. As with the MOS devices above, device islands were

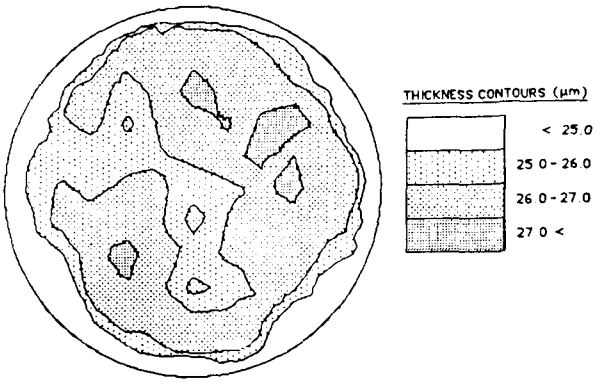

Fig. 3: Thickness Contours for an SOI Film on a Three-Inch Glass Wafer. The SOI film has a mean thickness of 26.8μm after removal of the boron etch-stop layer.

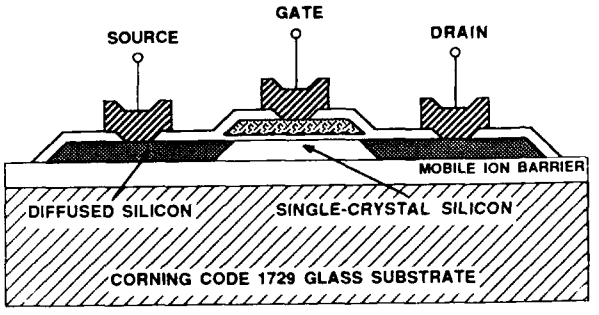

Fig. 4: An MOS Transistor Structure Formed in Single-Crystal Silicon on Glass.

formed using a selective anisotropic etch, and deposited oxides were used to passivate the device. Aluminum was used for interconnect. These devices have not yet been fully functional due to difficulties with the polysilicon emitter technology; however, the entire process has been run without other difficulty. As the island thickness increases, thicker resists are required for post-island processing, limiting feature sizes to 5 μm and above. These are adequate for most sensing applications.

Figure 6 shows the proposed process for an ultaminiature silicon pressure sensor with on-chip electronics. A "CMOS" wafer is deep diffused with boron to form a rim for the transducer, while a shallow high-temperature boron diffusion is used for the recessed diaphragm. A barrier dielectric is deposited and the wafer is sealed to the glass, after which the bulk of the wafer is dissolved to the etch-stop. Relatively-standard device processing (<800°C) is then used to form readout circuitry [1] in the remaining circuit islands. All of the individual steps in this fabrication sequence have been successfully run separately, and the overall combined process is now being implemented.

A variety of other alternative processes could also be implemented with this approach to sensor fabrication. Particularly attractive for some applications are those in which most or all of the circuit processing is done prior to glass bonding, so that the devices are on the lower surface of the silicon, next to the glass. In this case an electrostatic bond to the glass via deposited pillars or other elevated areas on the silicon is required along with a conducting shield to protect the devices from the electrostatic fields encountered during bonding. Such structures are more complex than that shown in Fig. 6 but avoid the necessity of processing the glass wafers. When an encapsulating layer of CVD silicon nitride is used over the glass, however, no cross-contamination problems have been observed, and the ability to perform double-sided processing on semiconducting SOI films of almost arbitrary thickness allows the formation of a number of structures impossible to realize using other techniques.

ACKNOWLEDGMENTS

The authors wish to thank Dr. Khalil Najafi and Ms. Qian Shi of the Solid-State Electronics Laboratory, University of Michigan, for their assistance. The encouragement, assistance, and financial support provided by the General Motors Research Laboratories is also gratefully acknowledged.

REFERENCES

1. H. L. Chau and K. D. Wise, "An Ultraminiature Solid-State Pressure Sensor for a Cardiovascular Catheter," Digest 4th Int. Conf. on Solid-State Sensors and Actuators (Transducers '87), IEE Japan, Tokyo, June 1987, pp. 344-347.

2. L. J. Spangler, "A Process Technology for Single-Crystal Silicon-on-Insulator Sensors and Circuits," Ph.D. Dissertation, The University of Michigan, April 1988.

3. F. P. Fehlner, W. H. Dumbaugh, and R. A. Miller, "Refractory Glass Substrates for Thin-Film Transistors," Proc. 6th Annual Int. Display Research Conf., Tokyo, 1986, pg. 100.

4. I. H. Choi and K. D. Wise, "A Silicon Thermopile-Based Infrared Sensing Array for Use in Automated Manufacturing," IEEE Trans. Elect. Dev., 33, pp. 72-79, January 1986.

5. A. Reisman, etal., "The Controlled Etching of Silicon in Catalyzed Ethylenediamine-Pyrocatechol-Water Solutons," J. Electrochem. Soc., 126, pg. 1406, Aug. 1979.

6. H. Muraoka, T. Ohhashi, and Y. Sumitomo, "Controlled Preferential Etching Technology," in Semiconductor Silicon 1973, Princeton, N. J.: Electrochem. Soc., pg. 327.

7. L. J. Spangler and K. D. Wise, "A Technology for High-Performance Single-Crystal Silicon-on-Insulator Transistors," IEEE Electr. Dev. Lett., 8, pp. 137-139, April 1987.

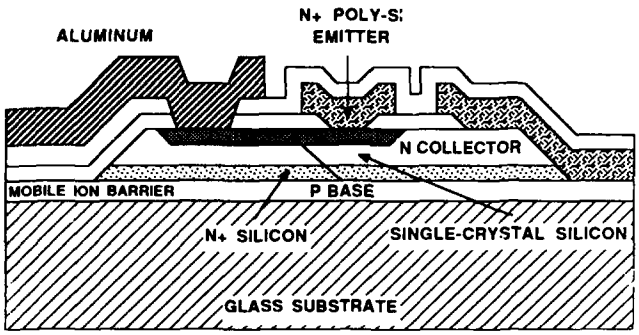

Fig. 5: A Vertical NPN Bipolar Transistor Structure on Glass. The n+ buried collector is formed using a pre-bond diffusion from the front of the silicon wafer.

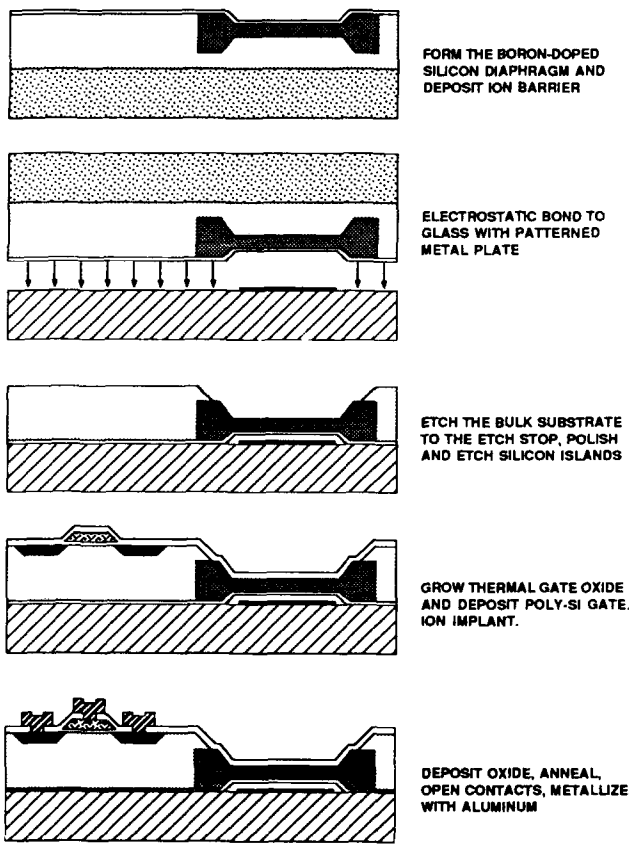

Fig. 6: A Proposed Process for an Active Ultraminiature Capacitive Pressure Sensor on Glass.

SILICON FUSION BONDING FOR PRESSURE SENSORS

Kurt Petersen, Phillip Barth, John Poydock,
Joe Brown, Joseph Mallon Jr., Janusz Bryzek

NovaSensor
1055 Mission Court
Fremont, CA 94539
(415) 490-9100

ABSTRACT

Two novel processes for fabricating silicon piezoresistive pressure sensors are presented in this paper. The chips described here are used to demonstrate an important new silicon/silicon bonding technique, Silicon Fusion Bonding (SFB). Using this technique, single crystal silicon wafers can be reliably bonded with near-perfect interfaces without the use of intermediate layers. Pressure transducers fabricated with SFB exhibit greatly improved performance over devices made with conventional processes. SFB is also applicable to many other micromechanical structures.

INTRODUCTION

Micromachining technology is often severely constrained 1) because of the structural limitations imposed by the traditional backside etching process and 2) because few practical methods have yet been demonstrated for true silicon/silicon direct bonding. Devices fabricated using techniques such as thermomigration of aluminum, eutectic bonding, anodic bonding to thin films of pyrex, intermediate glass frits and "glues" suffer from thermal expansion mismatches, fatigue and creep of the bonding layer, complex and difficult assembly methods, unreliable bonds and/or expensive processes. In addition, none of these processes provide the performance and versatility required for advanced micromechanical applications. For example, the (backside) cavity sidewalls slope outward from the diaphragm in anisotropically etched pressure sensor chips, forcing the overall chip area to be substantially larger than the active sensing diaphragm area. Another problem area is that narrow, hermetic gaps between two single crystal wafers are difficult to fabricate with precision because of the intermediate layers required. Finally, the most exciting class of new micromechanical structures, which have recently been developed, are actually thin film movable structures that are incompatible with current silicon/silicon bonding techniques.

Workers have addressed these problem by fabricating beams [1], diaphragms [2], and (recently) more complex structures such as mechanical springs and levers [3] from polycrystalline silicon using sacrificial-spacer etching. The silicon/silicon bonding technique described here has been previously discussed in several papers [4, 5, 6, 7]. SFB (Silicon Fusion Bonding) is a very powerful process for creating a wide range of all single crystal mechanical structures, that can replace polysilicon in many of the currently used sacrificial-etching methods. In this paper, several pressure sensor designs will be presented that illustrate the practical implications of this technology. Another paper at this meeting describes an acceleration sensor realized with the same processing techniques [8].

FABRICATION OF LOW PRESSURE SENSORS

One important application of silicon/silicon bonded sensors is ultra-miniature catheter-tip transducer chips for in vivo pressure measurements. A typical chip currently in use for this product is shown as Design 1 in Figure 1. This device has dimensions of 2400 μm by 1200 μm by 175 μm thick. It has a 650 μm square active diaphragm which is 8.0 μm thick. Diaphragm thickness is controlled to within 0.5 μm by an etch-stop process. The silicon wafer is anodically bonded to a glass constraint wafer which is only 125 μm thick. Much of the processing of this product requires lithography, etching, bonding, and general handling of these extremely thin wafers. A piezoresistive half-bridge is located on two edges of the diaphragm for a pressure sensitivity of 18 μV/V/mmHg. Linearity of these chips is better than about 1.2 % of the full scale output. These chips have been in production at NovaSensor for about a year and a half.

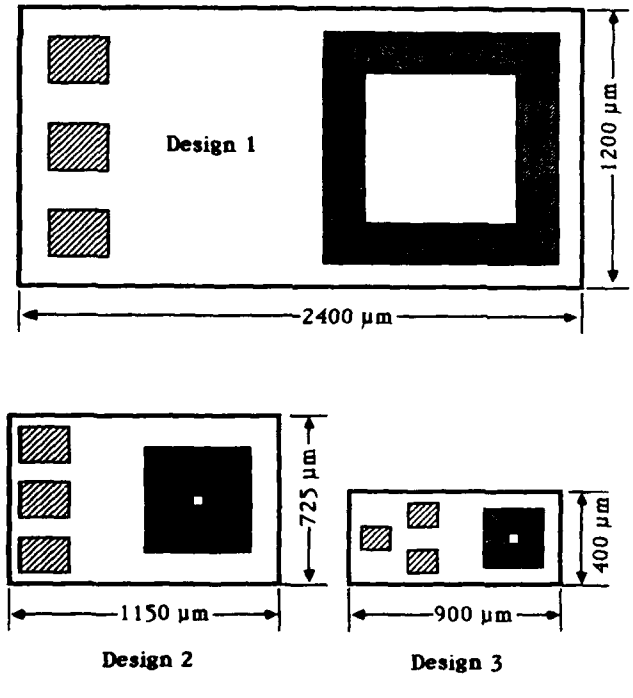

Figure 1 The three designs shown schematically here represent three generations of cathetar-tip sensors fabricated at NovaSensor. Design 1 uses a "conventional" silicon pressure sensor process sequence. Designs 2 and 3 use the SFB process.

TH215-4/88/0000-0144 © 1988 IEEE

A new generation of silicon fusion bonded (SFB) chips makes it possible to fabricate much smaller chips with equivalent or better overall performance. Schematic drawings of these chips are shown in Figure 1 and the fabrication procedure is outlined in Figure 2. The bottom, constraint substrate is first anisotropically etched with a square hole which has the desired dimensions of the diaphragm. In the most recent generation of chips, the bottom wafer has a (standard) thickness of 525 μm and the diaphragm is 250 μm square, so the anisotropic etch forms a pyramidal hole with a depth of about 175 μm. At the same time the pattern for these holes is defined, an alignment pattern is produced on the backside of the wafer in a double-sided aligner. Next, the etched constraint wafer is SFB bonded to a top wafer consisting of a p-type substrate with an n-type epi layer. The thickness of the epi layer corresponds to the required thickness of the final diaphragm for the sensor.

The bulk of the second wafer is removed by a controlled-etch process, leaving a bonded-on single crystal layer of silicon which forms the sensor diaphragm. Next, resistors are ion-implanted, contact vias are etched, and metal is deposited and etched. These patterns are aligned to the buried cavity using a double-sided mask aligner, referenced to the marks previously patterned on the backside of the wafer at the same time as the cavity. All these operations have a high yield because they are performed on wafers which are standard thickness. In the final step, the constraint wafer is ground and polished back to the desired thickness of the device; about 140 μm. The bottom "tip" of the anisotropically etched cavity is truncated during this polishing operation, thereby exposing the backside of the diaphragm for a gauge pressure measurement.

In an optional configuration, the initial cavity need not be etched to completion. Figures 3 and 4 show SEM's of a device with a sealed reference cavity only 30 μm deep. This design can be directly compared to the polysilicon sacrificial-layer pressure sensor techniques currently under investigation [2].

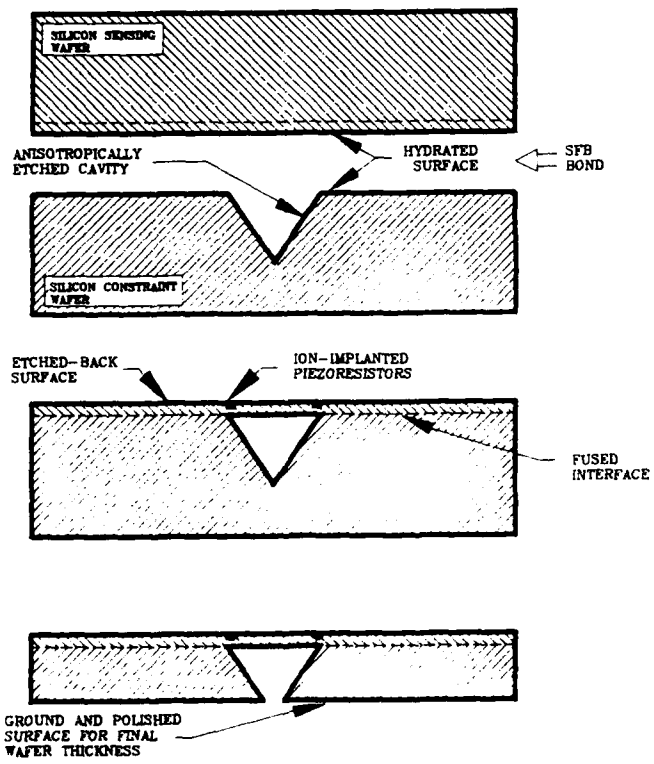

Figure 2 Fabrication process of SFB bonded low pressure sensor suitable for ultra-miniature cathetar-tip applications.

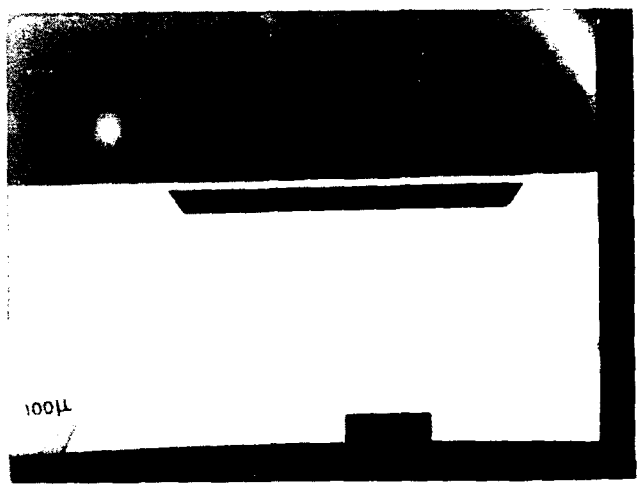

Figure 3 SEM cross-section of a test structure consisting of a 30 μm deep cavity anisotropically etched in the constraint wafer, and a 6 μm thick, 400 μm wide diaphragm suspended over the reference cavity. The fabrication procedure follows the general sequence outlined in Figure 1.

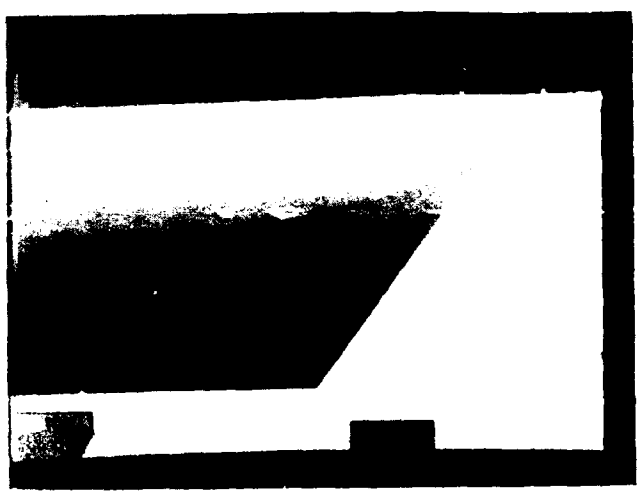

Figure 4 Magnified SEM cross-section of the bond region, reference cavity, and 6μm diaphragm in Figure 2.

Despite the fact that all dimensions of this chip are about half those of the conventional chip described above, the pressure sensitivity of the SFB chip is identical to the larger device and its linearity is actually improved to 0.5% of full scale. The implementation of SFB technology increases wafer yield because the wafers are not as thin (fragile) during most wafer processing steps. In addition, of course, the small size of these chips is advantageous since each wafer contains almost 16,000 chips.

A comparison of conventional and SFB technology (as applied to ultra-miniature catheter-tip transducers) is shown in Figure 5. For the same diaphragm dimensions and the same overall thickness of the chip, the SFB device is almost 50% smaller. In this special application, chip size is critical. SFB fabrication techniques make it possible to realize extremely small chip dimensions, which may permit this catheter-tip pressure sensor to be used with less risk to the patient in many situations.

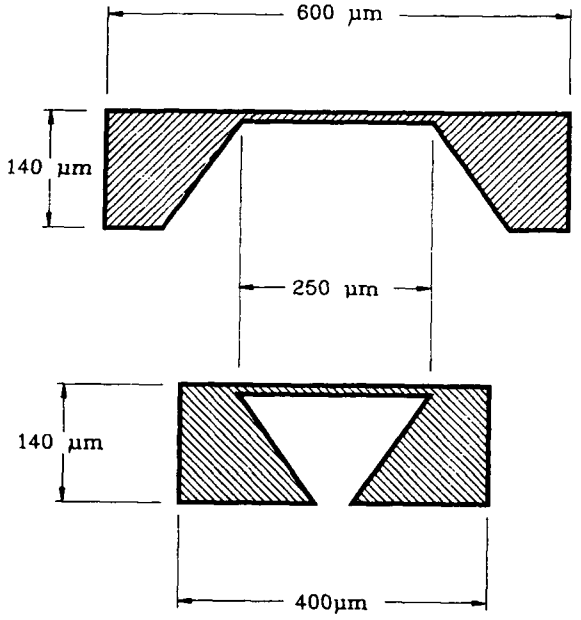

Figure 5 Comparison of miniature, low pressure silicon sensors fabricated using a "conventional" process, and the SFB process described here. For the same diaphragm dimensions and design groundrules, the SFB process results in a chip which is 50% smaller than the conventional process.

FABRICATION OF HIGH PRESSURE SENSORS

High pressure absolute sensors have been constructed in a modified SFB process to create much thicker diaphragms and to provide a larger mass of silicon in the constraint wafer, thereby optimizing materials compatibility and minimizing thermal mismatch problems.

First, the oxidized constraint wafer is aligned and exposed on both sides. The bottom surface has a "marker" pattern which will be used as an alignment reference later in the process in a manner similar to the low pressure sensor. The top surface has a round cavity pattern which will correspond to the diameter of the sensing diaphragm. After the oxide is wet etched, the silicon is plasma etched in CF_4 or anisotropically etched in KOH or EDP on both sides of the wafer simultaneously to a depth of about 10 µm.

Next, all photoresist and oxide layers are stripped from the constraint wafer and the top surface of this wafer (the surface with the round depression) is bonded to another n-type wafer at 1100°C. This operation is illustrated in the top part of Figure 6. After bonding, the top wafer is mechanically ground and polished back to a thickness corresponding to the desired pressure range. For a 900 um diaphragm with a thickness of 200 µm, this chip will result in a pressure sensor with a full scale output of 130 mV at 4000 psi. Linearity is exceptional at about 0.2% of full scale.

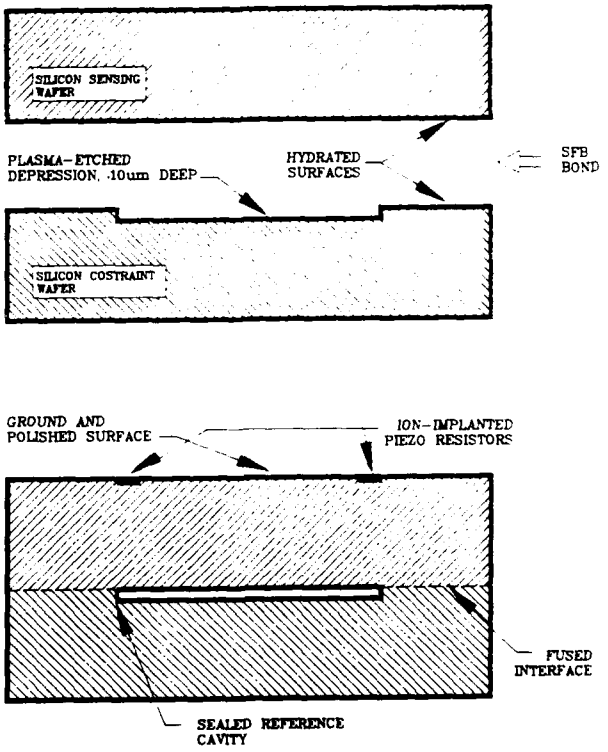

Figure 6 Fabrication process for SFB bonded high pressure sensors suitable for pressure ranges from 1,000 psi to 10,000 psi.

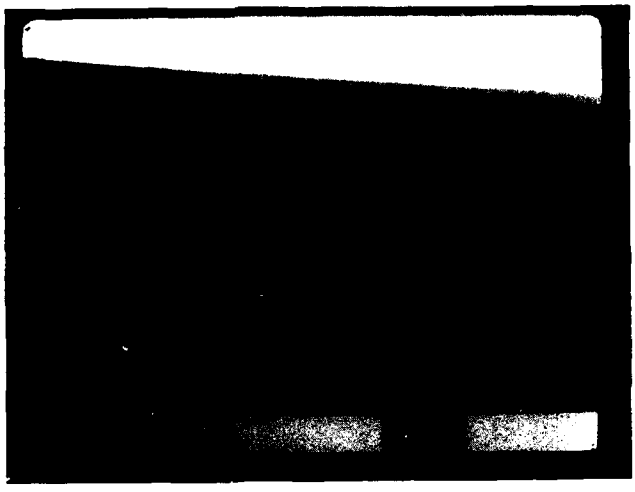

Figure 7 SEM cross-section of a silicon/ silicon bonded reference cavity of the type used in the high pressure sensor. The narrow cavity is only 2 μm deep in this figure. After plasma-etching the shallow cavity, the top wafer is SFB bonded as outlined in Figure 6.

Finally, an insulator is deposited, piezoresistors are implanted and annealed, contact holes are opened, and metal is deposited and etched. This completes the process for the pressure sensor. No back-side etching and no anodic bonding are required. In addition, 100% of the bulk of the chip is single crystal silicon. A monolithic single crystal silicon sensor chip provides important performance advantages in temperature coefficient of offset. The SFB chip, a total silicon thickness of over 600 μm, exhibits a very low temperature coefficient of bridge offset of about 0.3%/100°C of full scale output. A similar chip made with conventional backside etching and anodic glass/silicon bonding for the constraint, exhibits a typical TC of zero higher by a factor of 3.

CONCLUSION

The successful development of these two products shows that SFB bonding can be applied on a commercial basis. Not only are the processes employed here simpler than those currently used to build conventional pressure transducers for the same applications, but the yields are higher, the costs are lower, and the chip performance is improved compared to conventional technologies.

Beyond the two devices shown here, the potential of SFB bonding in other micromechanical structures is enormous. This process eliminates most of the disadvantages of previous silicon/silicon bonding methods. It is hermetic; it does not require any intermediate bonding layers; it accurately preserves any pattern previously etched in either or both bonded wafers; it has a high yield strength, as much as double that of anodic bonds; it can be used to create vacuum reference cavities; it can be used in place of sacrificial layer technology in many applications; it eliminates thermal expansion and Young's modulus mismatches in bonded wafer structures. The interface itself is a true single-crystal/single-crystal boundary. We have demonstrated, for example, that pn junctions with low leakage and sharp break-down voltages can be formed by bonding a wafer with a p-type diffusion to an n-type wafer.

We have only begun to exploit this extremely powerful new technology. During the next few years, silicon fusion bonding will revolutionize the field of silicon microstructures and will have a vast impact on high performance silicon microsensors.

ACKNOWLEDGEMENTS

The authors would like to acknowledge the important contributions of Ted Vermeulen, Rose Scimeca, Van Nguyen, and Terry Cookson in the development of SFB for silicon sensor applications.

REFERENCES

1] R.T. Howe and R.S. Muller, **Integrated Resonant-Microbridge Vapor Sensor**, International Electron Devices Meeting, December 1984, pg. 381.

2] H. Guckel, D.W. Burns, C.R. Rutigliano, D.K. Showers, and, J. Uglow, **Fine Grained Polysilicon and Its Application to Planar Pressure Transducers**, International Conference on Solid-State Sensors and Actuators, June 1987, pg. 277.

3] L.S. Fan, Y.C. Tai, R.S. Muller, **Pin Joints, Gears, Springs, Cranks, and Other Novel Micromechanical Structures**, International Conference on Solid-State Sensors and Actuators, June 1987, pg. 843.

4] J. Lasky, S. Stiffler, F. White, and J. Abernathey, **Silicon-on-Insulator (SOI) by Bonding and Etch-back**, International Electron Devices Meeting, December 1985, pg. 684.

5] H. Ohashi, K. Furukawa, M. Atsuta, A. Nakagawa, and K. Imamura, **Study of Si-Wafer Directly Bonded Interface Effect on Power Device Characteristics**, International Electron Devices Meeting, December 1987, pg. 678.

6] L. Tenerz, and B. Hok, **Silicon Microcavities Fabricated with a New Technique**, Electronics Letters, 22, pg. 615, (1986).

7] J. Ohura, T. Tsukakoshi, K. Fukuda, M. Shimbo, and H. Ohashi, **A Dielectrically Isolated Photodiode Array by Silicon-Wafer Direct Bonding**, IEEE Electron Device Letters, EDL-8, pg. 454, (1987).

8] P.W. Barth, F. Pourahmadi, R. Mayer, J. Poydock, K. Petersen, **A Monolithic Silicon Accelerometer with Integral Air Damping and Over Range Protection**, Solid-State Sensors Workshop, Hilton Head, S.C., 1988.

POLYSILICON MICROBRIDGE FABRICATION USING STANDARD CMOS TECHNOLOGY

M. Parameswaran, H. P. Baltes and A. M. Robinson

Dept. of Electrical Engineering and The Alberta Microelectronic Centre
The University of Alberta, Edmonton, Canada T6G 2G7

ABSTRACT

We describe a technique for fabricating polysilicon microbridges using a standard industrial CMOS process. The introduction of new layout methodologies enables us to fabricate CMOS compatible microbridge structures requiring only one additional postprocessing step. This step involves etching of the field oxide below the polysilicon layer in CMOS process which is equivalent to the sacrificial layer that is typical of any microbridge fabrication procedure.

INTRODUCTION

Within the last decade, there has been a growing interest to fabricate micromechanical structures for sensor applications using silicon micromachining technology [1]. In particular, polysilicon micromechanical structures have become popular primarily because of the favourable mechanical properties of the polysilicon material [2]. Its capability to form resilient, deformable mechanical structures has been demonstrated by Howe, through its application in vapour sensing [3]. In view of integrating the micromechanical structures with pertinent circuitry, efforts are in progress to suitably modify the standard planar integrated circuit (IC) technology [4,5]. These modifications comprise of additional steps or altering selected steps in the processing sequence, thereby customising the process for a specific application. For purposes of low cost mass production as well as high reliability, it is desirable to use CMOS processing technology for the fabrication of polysilicon based micromechanical structures. By incorporating additional lithographic steps for the etching of the sacrificial layers, polysilicon microstructures can be realised using standard CMOS process. Hence, attempts to use the standard technology with a minimum number of postprocessing steps will be most economical for commercial production.

In this paper, the technique employed in fabricating polysilicon microbridge structures using an industrial CMOS (CMOS-3DLM) process is presented. This processing service is offered by Northern Telecom Canada, to the students of Canadian universities [6]. In our attempt to fabricate the microbridge, we have introduced some unconventional layout design procedures and one additional postprocessing step.

LAYOUT DESIGN

Figure 1(A) shows the layout of a simple circuit in which a polysilicon layer is placed over two diffusions (layout terminologies are used). The cross-sectional view of the circuit shown in Figure 1(B) helps to examine the physical formation of these various layers more clearly. In this view, one can see the poly being separated by a thin gate oxide over the diffusion area and by a thick field oxide everywhere else. By removing the field oxide below the poly, we obtain the desired bridge structure.

In the standard CMOS process, a layer of oxide (usually PSG or BPSG) is used to insulate the polysilicon and the other underlying layers prior to metallization. Deposition of the passivation layer follows the metallization step. These additional layers deposited over the polysilicon should be removed in order to obtain a free-standing bridge structure. This is achieved by introducing some unconventional layout designs (see Figure 2) viz., a contact-cut and a pad-opening over the region where the microbridge is to be formed.

The dimensions of the contact-cut and pad-opening should be over-sized on the breadth side of the poly layer. These openings provide access to the region below the polysilicon for an isotropic oxide etchant to remove the field-oxide thereby forming the microbridge as illustrated in Figure 3. Since the transistors are formed by the self aligned technique, the gate material (polysilicon in this case) is also exposed to ion implantation during the source and drain definition step. Hence, the region where the polysilicon eventually becomes a microbridge is masked from ion implantation with the use of P+ and N+ mask layers [6]. This step is again an unconventionl method of layout design specially adopted for the microbridge fabrication in standard CMOS technology.

TH0215-4/88/0000-0148

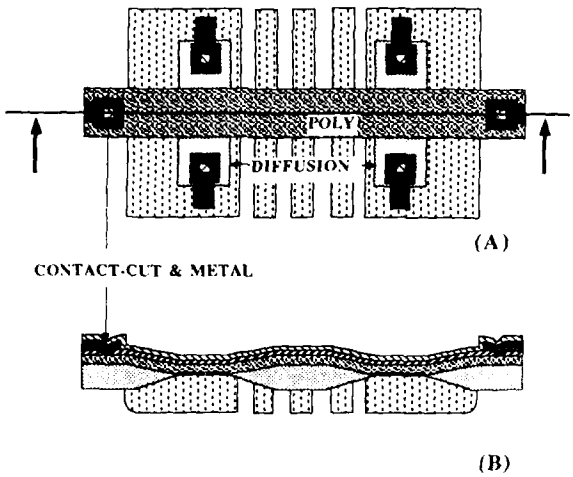

Figure 1. Layout and cross-sectional view of standard design.

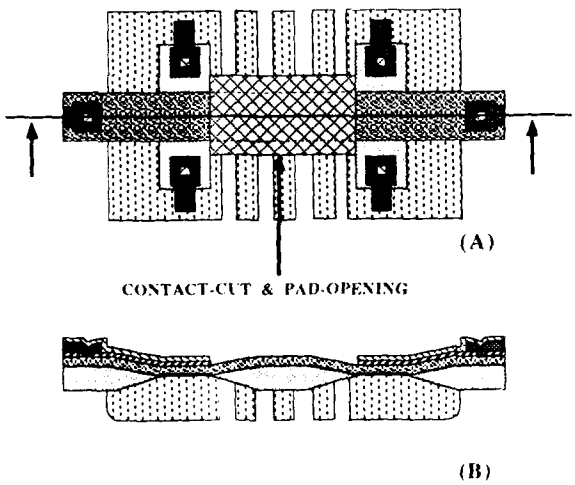

Figure 2. Layout and cross-sectional view of modified design.

POSTPROCESSING

The removal of field oxide below the poly is performed by a lithographic step after the CMOS processing sequence. This includes spinning the die with a 1 µm thick photoresist, soft-baking for 45 seconds at 90°C and creating a opening directly above the microbridge (see Figure 3(A)). Isotropic etching of the oxide below the poly is performed with buffered oxide etch (BOE). Depending on the bridge geometry the etch time required is 35-45 minutes at 27 °C. To determine this time, the bridge was destroyed and inspected for oxide residues in the space underneath using a scanning electron microscope. Figure 4 shows the oxide residues of a sample etched for 20 minutes. Figure 5 and 6 show the scanning electron micrographs of two completed microbridge structures (30 µm × 102 µm and 47 µm × 180 µm).

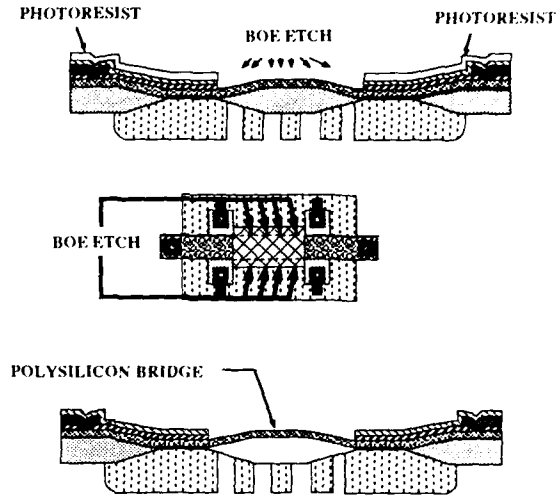

Figure 3. Postprocessing for obtaining the microbridge.

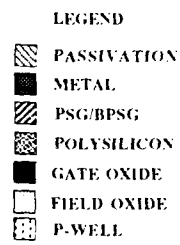

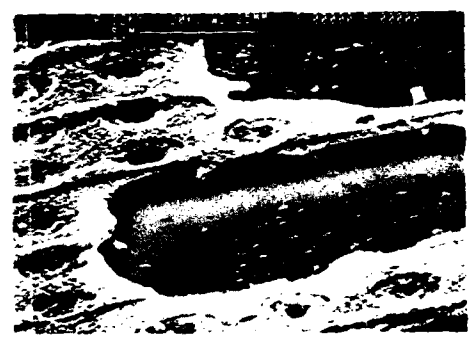

Figure 4. SEM photograph of structure obtained with etch time of 20 minutes.

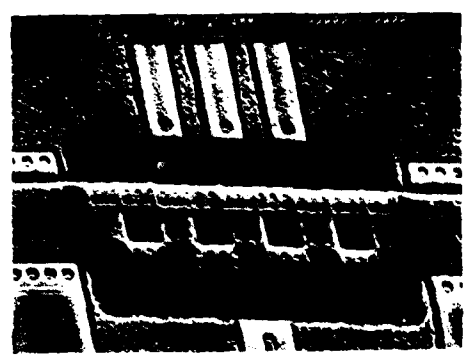

Figure 5. SEM photograph of 30 µm ×102 µm microbridge.

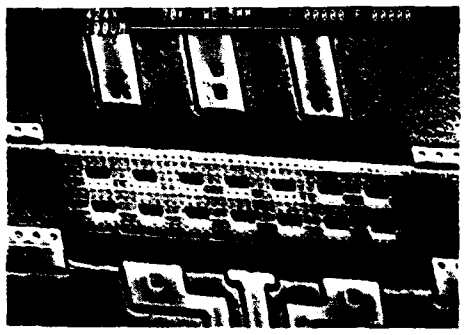

Figure 6. SEM photograph of 47 μm × 180 μm microbridge.

STRESS-RELIEF CONSIDERATIONS

Built-in stress in CVD thin films, especially in polysilicon is very common and has to be given due consideration [4,7]. The resulting bridge structure could otherwise exhibit buckling or deformation from the expected regular shape. To relieve the built-in stress, a high temperature anneal is used. The exact temperature and duration of the anneal depend on various factors such as deposition temperature, thickness, dopant concentration etc., and have to be determined expermentally [8]. The two high temperature cycles in the CMOS-3DLM process, taking place after the deposition of the polysilicon (990 °C for 45 minutes and 950 °C for 30 minutes) aid relieving the built-in stress but do not guarantee complete stress relief in polysilicon, since the typical CMOS process is not optimised for the purposes of creating micromechanical structures. Consequently, this latest attempt resulted in poor yield. Private communications with the process engineers suggest that incorporating one additional anneal step after the deposition of polysilicon will not seriously alter the CMOS process sequence, if the diffusion (well-diffusion) time, which is done prior to the deposition of polysilicon, is properly adjusted.

CONCLUSION

We have presented a technique to fabricate polysilicon microbridge structures that is highly compatible with CMOS technology and requiring only one additional postprocessing step. It is anticipated that the reliability of the microbridge with integrated electronics, fabricated using this technique will be comparable to that of a typical standard IC process. With the proper stress relief measures, low cost fabrication of microbridges appears feasible. The fabrication of annealed bridges using standard IC technology is currently in progress.

ACKNOWLEDGEMENTS

We gratefully acknowledge the services of the Canadian Microelectronic Corporation (CMC) in arranging the chip fabrication. We wish to thank G. Fitzpatrick and M. Buchbinder for the technical assistance. This work was supported by the Natural Science and Engineering Research Council of Canada (NSERC).

REFERENCES

[1] K. E. Petersen, "Silicon As A Mechanical Material", *Proc. of IEEE.*, V 70 (5), May 1982, pp. 419-457.

[2] Long-Sheng Fan, Yu-Chong Tai and R. S. Muller, "Pin Joints, Gears, Springs, Cranks and other Novel Micromechanical Structures", *Digest of Technical Papers, 4th int. Conf. on Solid State Sensors and Actuators* (Transducers'87), Japan, June 1987, pp. 849-852.

[3] R. T. Howe, "Integrated Silicon Electromechanical Vapour Sensor", Ph.D Thesis, Department of Electrical Engineering and Computer Sciences, Univeristy of California, Berkeley, CA, 1984.

[4] H. Guckel and D. W. Burns, "A Technology for Transducers", *Digest of Technical Paper, Int Conf. on Solid State Sensors and Actuators* (Transducers'85), Japan, June 1985, pp. 90-92.

[5] H. Guckel, D. W. Burns, C. R. Rutigliano, D. K. Showers and J. Uglow, "Fine Grained Polysilicon and its Application to Planar Pressure Transducers", *Digest of Technical Paper, Int. Conf. on Solid State Sensors and Actuators* (Transducers'87), Japan, June 1987, pp. 277-282.

[6] *"Guide to the Integrated Circuit Implementation Services of the Canadian Microelectronic Corporation"* , Carruthers Hall, Queens University, Kingston, Canada, 1987.

[7] R. T. Howe and R. S. Muller, "Polycrystalline Silicon Micromechanical Beams", *J. Electrochem. Soc.*, Vol. 130, No. 6, June 1983, pp.1420-1423.

[8] S. P. Murarka and T. F. Retajczyk, Jr, "Effect of Phosphorus Doping On Stress in Silicon and Polycrystalline Silicon", *J. Appl. Phys.*, 54 (4), April 1983, pp. 2069-2072.

PREFERRED CRYSTALLOGRAPHIC DIRECTIONS OF PORE PROPAGATION IN POROUS SILICON LAYERS

S.-F. Chuang† and R. L. Smith
† Department of Materials Science and Engineering
Department of Electrical Engineering and Computer Science
Massachusetts Institute of Technology
60 Vassar Street, Cambridge, MA 02139

Abstract

The results presented here demonstrate that pores propagate along preferred crystallographic directions within both n and p type silicon substrates. In addition to this, pores were surprisingly found not to have a round shape. Instead, they are confined by well-defined crystallographic planes. The results from plane-view TEM technique provide quantitative information on the pore size and pore-to-pore distance distributions. These indicate that morphologies are most sensitive to the silicon substrate characteristics.

Introduction

Porous silicon is formed by anodically biasing silicon in the presence of hydrofluoric acid. The resulting film contains micropores, whose diameter and density depend on the formation conditions and silicon substrate. Diameters can range from 10 Å to several thousand Å. Mechanisms for pore initiation and propagation have not yet been elucidated. A comprehensive study of formation, including substrate orientation, dopant type and concentration dependence, is currently being investigated. The objective of this study is to assemble from electrochemical behavior and morphology results, a formation model. Given a model of formation, it is proposed that this material will be formable with controlled porosity and/or morphology, for application to catalysis and ion or molecular separation. In addition, controlled porosity is necessary to control the density of resultant oxidized films. These films can then serve as thick electrical or thermal insulators in integrated circuit or microsensor applications.

Experimental

Both n and p type silicon wafers with various orientations were investigated in this study. An aluminum film, about 3000 Å in thickness, was deposited on the backside of the wafers and annealed in nitrogen. The anodizations were performed in aqueous HF solutions and under controlled current conditions. Both cross-sectional and plane-view TEM techniques were used to investigate the detailed morphologies.

Results and Discussion

It was observed that pores propagated normal to the surface in n-type, [100] orientation silicon, i.e. in the <100> direction, and short branches appeared normal to these, also in [100] directions. Since current flow is normal to the surface, it was not clear if this was the result of crystallographic preferential etching or not. Conclusive evidence is shown in Figure 1, which is a cross-sectional TEM photomicrograph of an n-type, [110] oriented sample of 0.82 Ω-cm resistivity. The formation current density is 80 mA/cm^2 and the HF concentration is 49 wt. %. The direction of current flow is from top of the photo to bottom. The direction normal to the surface shown in the photo, was determined by electron diffraction to be <$\bar{1}$12>. From this information and the relative, two dimensional, projection of the crystallographic directions shown in Figure 2, it is concluded that the pores are indeed propagating preferentially along [100] directions. In addition, the pores propagate in a branching manner. This is also observed in [100] silicon samples. The density of pores at the surface is lower than in the bulk and this increase is due to pore branching. Pore propagation is via a sequence of branching, termination and new pore initiation from branches. A uniform and saturated pore density occurs a few thousand Å distance below the surface. This bulk density can be varied with dopant concentration, HF concentration and formation current density.

Porous silicon layers which form in p-type substrates have much smaller pore diameters and higher pore densities. This makes elucidation of pore propagation directions and singular pore morphology much more difficult for p-type substrates. However, it has been observed that the interface between the porous silicon layer and the substrate is microscopically rough at lower formation current density; also, pore-to-pore distance is longer at lower HF concentration. In this formation regime, individual pores (≤ 50 Å diameter) have been resolved in the interface region. In p-type [100] silicon, the pores were found to propagate normal to the interface, while in p-type [110] silicon, the pores are found to propagate in a manner quite similar to that occurring in n-type [110] silicon. It is thereby concluded that preferred pore propagation along <100> directions is a general phenomenon, and not silicon type specific.

The pore shape in n-type porous silicon layers was revealed by plane-view TEM technique. Figure 3 is a plane-view TEM photomicrograph of the near surface region of an n-type [100] porous silicon layer. The formation current density is 10 mA/cm and the HF concentration is 10%. The pores were found to have a square shape instead of the round, conventionally conceived, shape. The upper right corner of Figure 3 is the electron diffraction pattern after the calibration of the rotation angle between diffraction pattern and the image. The [100] directions were found to be normal to the pore walls. Therefore, the well-defined crystallographic planes composing the pore walls are {100} planes. This phenomenon was unexpected and has not as yet been explained.

Pore initiation was found to be sensitive to silicon surface defects. In the lower left corner of Figure 3, we can observe a pore with a different orientation from the other pores. The extra spots in the diffraction pattern suggest that this pore might have initiated at a twin on the surface. Figure 4 is also a plane-view TEM photomicrograph of the surface of an n-type [100] porous silicon layer. The formation current density is 10 mA/cm^2 and the HF concentration is 49 wt. %. Many large pores initiated along a straight line, corresponding to a surface scratch.

The plane-view TEM technique provides a good method to quantitatively evaluate the influence of various formation parameters on the pore size and pore-to-pore distance distributions. Figure 5 is an illustration of a pore size distribution histogram. The sample was formed at 10 mA/cm^2,10 wt.% HF. Figure 6 is the pore-to-pore distance distribution histogram of the same sample. The pore diameters are sensitive to HF concentration and current density. The pore-to-pore spacing is most sensitive to the substrate doping. Spacing, as well as branch lengths, decrease with increasing doping. This is particularly observable on n-type samples. The n-type silicon is reverse biased during anodization, therefore it is proposed that the branch length and spacing are a function of depletion depth, or more generally speaking, the diffusion length of charge carriers in the silicon bulk to the pore tips. Depletion depths have been estimated, assuming all of the applied voltage is dropped in the semiconductor side of the silicon/solution interface. The values obtained are the same order of magnitude as the pore to pore spacing observed in n-type samples.

Conclusion

Pores were found to propagate along [100] directions within both n- and p-type silicon. The initiation of pores is found to be sensitive to surface defects. Pores propagate via a sequence of branching, branch termination, and reinitiation along branches. A steady state distribution of pore diameter and density is quickly obtained. Formation rate and porous film morphology are relatively constant with increasing thickness (10's of microns) for a constant current density. These results indicate that propagation is determined by diffusion of charge carriers in the silicon to the silicon/ HF

TH0215-4/88/0000-0151

solution interface, rather than (or in addition to) diffusion of HF down the pores.

Acknowledgement

Partial fellowship support from the Foxboro company for S.-F. Chuang is gratefully acknowledged. Helpful discussions with Dr. Scott D. Collins is also acknowledged.

Figure 1.--- Cross-sectional TEM photomicrograph of a porous silicon layer formed in n-type, [110] oriented silicon wafer. The direction normal to the surface is <$\bar{1}$12>.

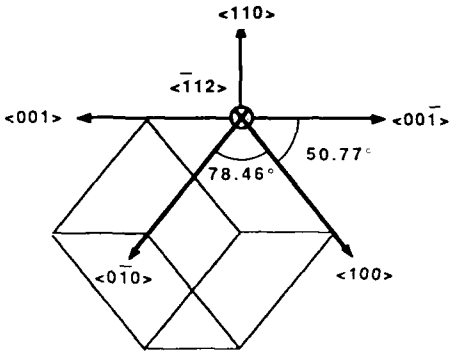

Figure 2.--- Two dimensional projection of the crystallographic directions relative to Figure 1.

Figure 3.--- Plane-view TEM photomicrograph of the near surface region of a porous silicon layer formed in n-type, [100] oriented silicon wafer. The upper right corner is the electron diffraction pattern.

Figure 4.--- Plane-view TEM photomicrograph of the surface of a porous silicon layer formed in n-type [100] oriented silicon wafer.

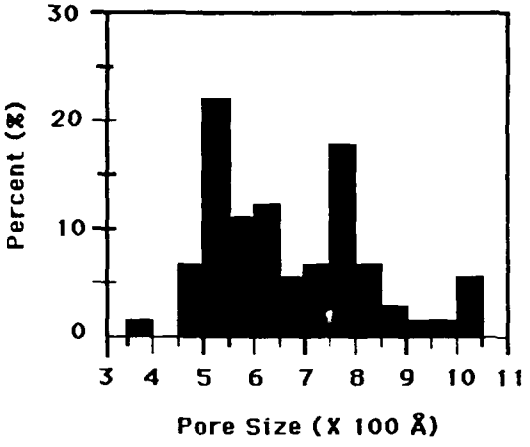

Figure 5.--- Pore size distribution histogram of a porous silicon layer formed in n-type, [100] oriented silicon wafer. The formation current density is 10mA/cm and HF concentrationis 10wt%.

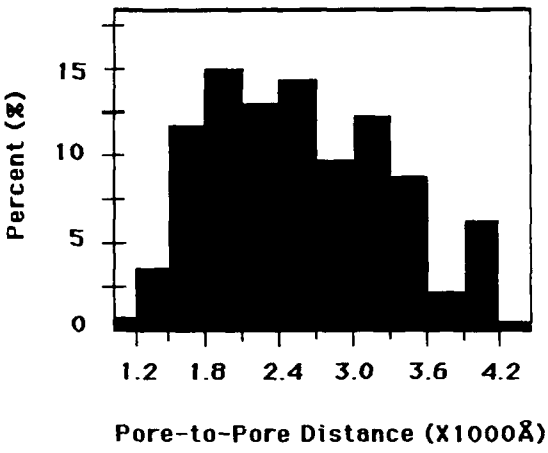

Figure 6.--- Pore-to-pore distance distribution histogram of the same sample as in Figure 5. The distances were measured from pore edge to pore edge.